

**Document Version**

Final published version

**Citation (APA)**

Xu, Y. (2026). *Natural Weathering Reshapes Nanoplastic Aggregation and Deposition Dynamics: Implications for Nanoplastic Removal during Riverbank Filtration*. [Dissertation (TU Delft), Delft University of Technology]. <https://doi.org/10.4233/uuid:cf262798-9e85-42be-bdf9-3af28e7612c5>

**Important note**

To cite this publication, please use the final published version (if applicable).  
Please check the document version above.

**Copyright**

In case the licence states "Dutch Copyright Act (Article 25fa)", this publication was made available Green Open Access via the TU Delft Institutional Repository pursuant to Dutch Copyright Act (Article 25fa, the Taverne amendment). This provision does not affect copyright ownership.  
Unless copyright is transferred by contract or statute, it remains with the copyright holder.

**Sharing and reuse**

Other than for strictly personal use, it is not permitted to download, forward or distribute the text or part of it, without the consent of the author(s) and/or copyright holder(s), unless the work is under an open content license such as Creative Commons.

**Takedown policy**

Please contact us and provide details if you believe this document breaches copyrights.  
We will remove access to the work immediately and investigate your claim.

# Natural Weathering Reshapes Nanoplastic Aggregation and Deposition Dynamics: Implications for Nanoplastic Removal During Riverbank Filtration



Yanghui Xu

## **Propositions**

Accompanying the thesis

### **Natural Weathering Reshapes Nanoplastic Aggregation and Deposition Dynamics: Implications for Nanoplastic Removal During Riverbank Filtration**

by Yanghui Xu

1. Natural weathering of nanoplastics adds complexity to evaluating their transport and fate in natural systems (this thesis).
2. A two-stage dynamic provides an accurate description of nanoplastic transport in natural porous media (this thesis).
3. Weathering of sand by natural biofilms enhances nanoplastic retention during filtration (this thesis).
4. Accounting for spatial heterogeneity of aquifers enables an accurate prediction of nanoplastic breakthrough (this thesis).
5. Model nanoplastics cannot capture the wide variety of particle types, shapes, sizes and aging conditions.
6. The development of novel water treatment technologies must be grounded in the real-world characteristics of environmentally relevant nanoplastics.
7. Even if plastic production stops today, the ongoing accumulation and long-term burial of plastic debris in sediments threatens ecosystem and human health.
8. Poorly biodegradable plastic debris may be more persistent, but they can be less toxic than the so-called “biodegradable” ones.
9. “Is it true just because it has always been so?” —Xun Lu
10. There is no perfect plan, and outcomes often go beyond your expectations—so don’t wait. Just do it. You’ll find your way through trial, error, adaptation, and persistence.

These propositions are regarded as opposable and defensible and have been approved as such by the promoters, Prof dr.ir. L. C. Rietveld and Dr.ir. K.M. Lompe.

# **Natural Weathering Reshapes Nanoplastic Aggregation and Deposition Dynamics: Implications for Nanoplastic Removal During Riverbank Filtration**

## **Dissertation**

For the purpose of obtaining the degree of doctor

at Delft University of Technology

by the authority of the Rector Magnificus,

Prof.dr.ir. H. Bijl,

chair of the Board for Doctorates,

to be defended publicly on

Tuesday 14 April 2026 at 10:00 o'clock

by

**Yanghui XU**

This dissertation has been approved by the promotor and the copromotor.

Composition of the doctoral committee:

Rector Magnificus	Chairperson
Prof.dr.ir. J.P. van der Hoek	Delft University of Technology, promotor
Prof.dr.ir. L.C. Rietveld	Delft University of Technology, promotor
Dr.ir. K.M. Lompe	Delft University of Technology, copromotor

Independent members:

Prof.dr.ir. T.A. Boogaard	Delft University of Technology
Prof.dr. S. Krause	University of Birmingham, United Kingdom
Prof.dr. M. Teixidó Planes	Consejo Superior de Investigaciones Científicas, Spain
Dr.ir. C. Bertelkamp	Puur Water & Natuur, the Netherlands
Prof.dr.ir. M.K. de Kreuk	Delft University of Technology, reserve member

Other members:

Prof.dr.ir. G. Liu	Delft University of Technology / Chinese Academy of Sciences, China
--------------------	--

This research was conducted at the Sanitary Engineering Section, Department of Water Management, Faculty of Civil Engineering, Delft University of Technology, The Netherlands, and was financially supported by the China Scholarship Council.

Cover by: Yanghui Xu

Keywords: Nanoplastics; Riverbank filtration; Natural weathering; Aggregation; Deposition

Copyright © 2026 by Yanghui Xu

ISBN/EAN: 978-94-6518-258-2

An electronic version of this dissertation is available at <http://repository.tudelft.nl/>

# Table of Contents

<b>Chapter 1 Introduction.....</b>	<b>1</b>
<b>1.1. Microplastics and Nanoplastics as Emerging Contaminants .....</b>	<b>2</b>
1.1.1. Pollution of Microplastics and Nanoplastics in Surface water and Groundwater .....	2
1.1.2. Nanoplastics Pose Higher Environmental and Health Risks Than Microplastics .....	3
<b>1.2. Weathering Produces Secondary Microplastics and Nanoplastics .....</b>	<b>4</b>
<b>1.3. Nanoplastics Exhibit Distinct Transport Patterns From Microplastics .....</b>	<b>5</b>
1.3.1. Fate of Microplastics and Nanoplastics in Aquatic Environments.....	5
1.3.2. Aggregation and Colloidal Stability of Nanoplastics .....	6
1.3.3. Nanoplastic Transport and Deposition in Porous Media .....	8
<b>1.4. Riverbank Filtration as Barrier of Colloidal Contaminants.....</b>	<b>9</b>
<b>1.5. Research Outline.....</b>	<b>10</b>
1.5.1. Research Objective .....	10
1.5.2. Research Gaps .....	10
1.5.3. Research Questions and Outline .....	11
<b>Chapter 2 Photo-oxidation of Micro- and Nano-plastics: Physical, Chemical and Biological Effects in Environments .....</b>	<b>13</b>
<b>Abstract .....</b>	<b>14</b>
<b>2.1. Introduction .....</b>	<b>14</b>
<b>2.2. Photo-Oxidation of MNPs .....</b>	<b>16</b>
<b>2.3. Physical Behavior of MNPs After Photo-Oxidation.....</b>	<b>17</b>
2.3.1. Adsorption of Contaminants .....	17
2.3.2. Colloidal Stability in Water Media.....	20
2.3.3. Transport Behavior in Porous Media .....	23
<b>2.4. Photochemical Processes With Coexisting Constituents .....</b>	<b>26</b>
2.4.1 Effects of Natural Substances on the Photo-Oxidation of MNPs .....	26
2.4.2. Effects of MNPs on the Photochemical Transformations of Other Contaminants .....	28
<b>2.5. Biological Effects of Photoaged MNPs .....</b>	<b>30</b>
2.5.1. Toxicity to Aquatic Organisms .....	30
2.5.2. Effects on Microorganisms .....	32
2.5.3. Potential Impacts on Plants .....	35
<b>2.6. Future Perspectives .....</b>	<b>37</b>
<b>Chapter 3 Natural Organic Matter Stabilizes Pristine Nanoplastics but Destabilizes Photochemical Weathered Nanoplastics in Monovalent Electrolyte Solutions.....</b>	<b>41</b>
<b>Abstract .....</b>	<b>42</b>

<b>3.1. Introduction .....</b>	<b>42</b>
<b>3.2. Materials and Methods.....</b>	<b>44</b>
3.2.1. Materials .....	44
3.2.2. NOM Fractions Preparation.....	45
3.2.3. Accelerated Photooxidation Experiments.....	45
3.2.4. Adsorption Experiments .....	46
3.2.5. Aggregation Kinetics Measurements.....	47
3.2.6. Characterization .....	47
3.2.7. DLVO and Steric (Polymer-Mediated) Interaction Energy.....	48
<b>3.3. Results and Discussion .....</b>	<b>48</b>
3.3.1. Photochemical Weathering Modifies NPs .....	48
3.3.2. NOM Adsorption Modifies Pristine and Photoaged NPs .....	50
3.3.3. Photochemical Weathering Stabilizes NPs .....	53
3.3.4. NOM Stabilizes Pristine NPs but Destabilizes Photoaged NPs.....	53
3.3.5. Molecular Weight-Dependent Stabilization and Destabilization Capacity.....	59
<b>3.4. Environmental Implications.....</b>	<b>60</b>
<b>Chapter 4 Weathering of Nanoplastics Reduces the Effect of Sand Surface Heterogeneity on Irreversible and Reversible Deposition in Saturated Porous Media</b>	<b>63</b>
<b>Abstract .....</b>	<b>64</b>
<b>4.1. Introduction .....</b>	<b>64</b>
<b>4.2. Materials and Methods.....</b>	<b>66</b>
4.2.1. Materials .....	66
4.2.2. Preparation of Weathered Nanoplastics .....	67
4.2.3. Column Transport Experiments.....	67
4.2.4. Adsorption and Desorption Experiments.....	68
4.2.5. Characterization .....	68
4.2.6. Modelling .....	68
4.2.7. DLVO and XDLVO Interaction Energy.....	71
<b>4.3. Results and Discussion .....</b>	<b>71</b>
4.3.1. Two-Stage Deposition of Nanoplastics.....	71
4.3.2. Sand Surface Heterogeneity Creates Favorable Deposition Sites .....	75
4.3.3. UV Weathering Reduces Surface Heterogeneity Effects.....	77
4.3.4. NOM Reduces Surface Heterogeneity Effects.....	81
4.3.5. NOM Molecular Weight-Dependent Deposition of Nanoplastics .....	82
<b>4.4. Environmental Implications.....</b>	<b>83</b>
<b>Chapter 5 Beyond Classic Colloid Filtration: the Role of Natural Weathering and Biofilm Spatial Heterogeneity in Nanoplastic Transport and Predictive Modeling During Riverbank Filtration .....</b>	<b>85</b>
<b>Abstract .....</b>	<b>86</b>
<b>5.1. Introduction .....</b>	<b>86</b>
<b>5.2. Materials and Methods.....</b>	<b>88</b>

5.2.1. Biofilm Inoculation and Development in Laboratory .....	88
5.2.2. Biofilm Characterization .....	89
5.2.3. Nanoplastic Transport Experiments .....	91
5.2.4. Nanoplastic Characterization .....	92
5.2.5. Modelling .....	92
5.2.6. Interaction Energy Calculation .....	95
<b>5.3. Results and Discussions .....</b>	<b>95</b>
5.3.1. Surface Heterogeneity Drives Two-Stage Transport Dynamics of NPs .....	95
5.3.2. Biofilm Facilitates Both Favorable and Unfavorable Attachment of NPs .....	98
5.3.3. Spatial Heterogeneity of Biofilms Determines NP Retention .....	101
5.3.4. Eco-Corona Reduces Favorable but Enhances Unfavorable Attachment .....	102
5.3.5. Refinement of NP Transport Prediction in Filtration-Based Processes.....	105
<b>5.4. Summary .....</b>	<b>107</b>
<b>Chapter 6 Conclusion and Perspectives .....</b>	<b>109</b>
6.1. Conclusion and Implications for Environmental Science and Engineering.....	110
6.2. Limitations and Future Perspectives .....	113
<b>Supplementary Materials.....</b>	<b>115</b>
<b>Bibliography .....</b>	<b>187</b>
<b>Acknowledgement .....</b>	<b>209</b>
<b>Curriculum Vitae .....</b>	<b>211</b>
<b>List of Publications .....</b>	<b>212</b>



## Summary

Nanoplastics (NPs) are emerging colloidal contaminants that may pose risks to ecosystems and human health. Their environmental fate and associated risks are governed by colloidal processes, including aggregation (particle–particle interactions) in the water phase, and deposition (particle–surface interactions) within porous media. These processes are particularly critical in systems such as riverbank filtration (RBF), a widely used natural treatment method for drinking water production. NPs do not remain in their pristine state but undergo natural weathering processes including UV-induced weathering and eco-corona formation due to natural organic matter (NOM) adsorption. Porous media, such as sand grains, also undergo natural weathering such as the development of spatially heterogeneous biofilms. These weathering processes can alter the surface properties of both NPs and porous media, consequently influencing NP aggregation and deposition dynamics. Understanding how natural weathering modulates NP behavior during RBF will improve the prediction of NP environmental fate and support more accurate risk assessments under realistic conditions.

First, current knowledge on the influence of UV weathering on the transport, fate and ecological risks of NPs and microplastics has been reviewed, as well as their interactions with co-occurring environmental contaminants. UV weathering typically increases surface O-containing functional groups and negative charges, and hydrophilicity of NPs. With respect to NP aggregation and deposition, these physicochemical alterations collectively reduce NP aggregation and deposition. Additionally, UV weathering tends to reduce the thickness of the eco-corona, thereby attenuating the influence of NOM on NP aggregation behavior. Together, these findings from literature offer valuable insights into the role of UV weathering in modulating the colloidal stability and mobility of NPs in the environment.

In the following, using model Suwannee river NOM, a contrasting role of the eco-corona in the aggregation behavior of non-weathered versus UV-weathered NPs was elucidated. This was primarily because UV weathering altered the interaction patterns between NOM and NPs, as well as the conformational structure of the eco-corona. For non-weathered NPs, hydrophobic NOM components primarily bound with NPs via hydrophobic and  $\pi$ - $\pi$  interactions, while extended hydrophilic NOM segments provide steric repulsion, inhibiting aggregation. In contrast, for UV-weathered NPs, hydrogen bonding promoted binding of hydrophilic NOM segments to multiple particles, increasing aggregation through polymer bridging. Both the stabilizing and destabilizing effects of NOM increased with its concentration and molecular weight. It highlights the destabilizing role of NOM in weathered NPs, offering new perspectives on environmental colloidal chemistry and the fate of NPs in complex aquatic environments.

Then the transport and deposition mechanisms of non-weathered versus weathered NPs in porous media were examined, challenging the assumptions of classical clean bed filtration theory. It revealed that the inherent physical and chemical heterogeneity of sand grains drove a two-stage deposition process: an initial stage characterized by both rapid, irreversible and reversible attachment onto heterogeneous surface domains until site saturation was reached, followed by a slower, predominantly irreversible attachment onto more homogeneous regions of the grain surfaces. Both UV-induced weathering and NOM coating made them more negatively charged, reducing the extent of both irreversible and reversible deposition compared to non-weathered NPs. As a result, these weathering processes effectively reshaped NP transport dynamics and screened the retardation effects imposed by surface

heterogeneity. These findings provide valuable insights into how sand surface heterogeneity and NP weathering influence NP transport and deposition in saturated porous media.

Finally, weathering of sand grains was studied, particularly the development of spatially heterogeneous natural biofilms, affecting NP transport during RBF. NP transport was characterized by a two-stage dynamic: an initial stage dominated by favorable attachment, leading to strong retention and delayed breakthrough, followed by a later stage characterized by unfavorable attachment. Natural biofilms, particularly in the upper layer of the sand column, enhanced both favorable and unfavorable NP attachment, with both attachment stages decreasing with depth and positively correlating with biofilm biomass. In addition, natural eco-corona formation on NPs in river water suppressed initial favorable deposition while enhancing unfavorable deposition, ultimately reducing the overall transport potential of NPs through RBF. It suggests naturally weathered NPs may break through earlier than non-weathered NPs, but with reduced long-term leaching potential and a lower risk of groundwater contamination.

Overall, the dissertation reveals that the critical role of natural weathering in shaping NP aggregation and deposition dynamics. It underscores the necessity of incorporating not only environmentally weathered NPs but also naturally aged aquifer media in experimental designs to more accurately represent real-world environmental conditions. This enables more reliable prediction of NP mobility in RBF systems and provides essential mechanistic insights to guide the development of engineered filtration and decontamination strategies tailored to mitigate NP contamination in drinking water supplies.

# Chapter 1

Introduction

## 1.1. Microplastics and Nanoplastics as Emerging Contaminants

### 1.1.1. Pollution of Microplastics and Nanoplastics in Surface water and Groundwater

The global production of plastics has risen exponentially since the mid-20th century, reaching nearly 400 million tons annually by 2018 [1]. This surge in production is driven by the lightweight, durable, and versatile properties of plastics, which have revolutionized modern industries and daily life [2]. However, this convenience comes at an environmental cost, as plastic waste is pervasive, poorly biodegradable, and accumulates across diverse ecosystems, from landfills to the ocean floor [3]. Over time, larger plastic debris undergoes degradation through processes like photooxidation, abrasion, and microbial activity, fragmenting into tiny particles [4]. These smaller plastic particles have first drawn scientific attention in the 1970s when they were identified as an important component of ocean floor debris [5]. The term “microplastics (MPs),” introduced by Thompson et al. [6], have further heightened awareness by describing the accumulation of microscopic plastic particles in marine sediments and water columns, broadening the scope of research on these emerging pollutants. A commonly accepted classification defines MPs as plastic particles ranging from 1  $\mu\text{m}$  to 5 mm. However, the degradation of plastics does not halt at this stage; MPs can further break down into even smaller particles known as nanoplastics (NPs), which are typically less than 1  $\mu\text{m}$  in size [7].

Available data on MPs in surface water reveal a wide range of contamination levels, although they are often reported in inconsistent units. In concordance with global production, polyethylene (PE), polyethylene terephthalate (PET), polypropylene (PP), polystyrene (PS), polyvinyl chloride (PVC), polyamide (PA), and polycarbonate (PC) are frequently detected in environments [8-10]. An average MP concentration of 1,597 to 12,611 items/ $\text{m}^3$ , with a mean value of  $2,516.7 \pm 911.7$  items/ $\text{m}^3$  has been reported for the Yangtze River in China [11]. MP concentrations in European rivers typically range from 0–30 items/ $\text{m}^3$ , with occasional hotspots reaching thousands or even hundreds of thousands of items/ $\text{m}^3$  [12]. Excluding outliers, averages are 608 and 145 items/ $\text{m}^3$  for the Elbe and Rhine, respectively [13, 14]. These findings indicate that MPs are pervasive contaminants in freshwater environments. However, due to the challenges in detecting NPs in natural freshwater environments, few studies have reported on their pollution levels in surface waters. NP concentrations ranged from 0.283 to 0.793  $\text{mg}/\text{m}^3$  from upstream to downstream along the Fuhe River in China, likely influenced by high pollution inputs from urban areas [10]. NPs were also detected in all Swedish lakes and streams (mean 563  $\text{mg}/\text{m}^3$ ), including PE, PVC, PP, and PET, while in Siberia, they were found in 7/12 water bodies at lower concentrations (mean 51  $\text{mg}/\text{m}^3$ ) with only PVC and PS polymers detected [15].

Although studies on groundwater MPs and NPs (MNPs) contamination are limited, a few documented cases provide insights. In four groundwater boreholes of the North West of South Africa, reported microplastic concentrations averaged 41.7 items/m<sup>3</sup> for fragments < 600 µm and 125 items/m<sup>3</sup> for fibers ranging from 20 µm to > 1.5 mm [16]. In Holdorf, Germany, MP concentrations in three 30 m deep wells ranged from 0 to 7 items/m<sup>3</sup>, with an average of 0.7 items/m<sup>3</sup>, predominantly between 50–150 µm [17]. In contrast, Panno et al. have studied springs and wells (< 65 m) in karst aquifers in Illinois, USA, detecting MP fibers (> 0.45 µm) in 16 out of 17 samples, with an average concentration of 6400 items/m<sup>3</sup> and a maximum of 15200 items/m<sup>3</sup> [18]. The more open structure of karst systems, featuring crevices, conduits, and sinkholes, likely facilitates MP entry, with septic releases and runoff identified as major sources. Bäuerlein et al. have reported MP concentrations ranging from 231 to 12,882 items/m<sup>3</sup> in groundwater and riverbank-filtered groundwater in the Netherlands [19]. Similarly, low concentrations of NPs, ranging from 0.021 to 0.203 mg/m<sup>3</sup>, have been detected in riverbank groundwater [10].

### 1.1.2. Nanoplastics Pose Higher Environmental and Health Risks Than Microplastics

Fibers and fragments make up the majority of MPs identified in organisms [20], and their presence has potential environmental and health risks. Physically, the ingestion of MPs can cause blockages and damage to the gastrointestinal tract, leading to false satiety, malnutrition, and even death [21]. Plasticizers and other chemical additives can leach from MPs, causing severe biological effects, including endocrine disruption and adverse impacts on steroid hormones, lipid metabolism, and thyroid function [22, 23]. Toxic monomers found in polymers like PVC, PS, and PC further exacerbate the problem, being linked to reproductive abnormalities and carcinogenic effects [24]. Moreover, once inside the gastrointestinal system, MPs not only release their chemical components but also any persistent, toxic organic micro-pollutant adsorbed on the MPs [25, 26].

In vitro and in vivo studies have demonstrated that MPs, but especially NPs can cause serious health impacts on the human body, including physical stress, cell damage, apoptosis, necrosis, inflammation, oxidative stress, and immune responses [27-29]. NPs typically pose a higher potential for biological effects due to the following reasons. First, their small size enables them to traverse cellular barriers, potentially leading to greater interference with biological systems and increased risks to organisms [30]. Second, NPs possess a larger surface area-to-volume ratio compared to the larger MPs, enabling them to adsorb more toxic organic micro-pollutants [31], and facilitating easier interactions with the tissues and organs of organisms [32, 33]. Several studies have highlighted various pathways through which MNPs enter the human food chain, including ingestion by animals in their natural habitats [34], contamination during food production processes [35], and leaching from plastic packaging of food and beverages [36].

## 1.2. Weathering Produces Secondary Microplastics and Nanoplastics

MNPs in environments are categorized based on their sources into primary and secondary types [37]. Primary MNPs are directly released into the environment in their original small sizes as a result of industrial processes and specific applications [38]. These include particulate emissions from industrial production, cosmetic and cleaning products like toothpaste, raw materials for plastic goods manufacturing, and textile fibers shed during washing or drying [39]. Often referred to as "microspheres" or "microbeads," these MPs come in a range of shapes, sizes, and compositions [40]. It has been reported that PE accounts for more than 90% of the microspheres used in cosmetics, with other polymers such as PP, polymethylmethacrylate (PMMA), PS, and PET also being utilized [41, 42]. The presence of polymeric NPs have also been revealed in exfoliants, likely an unintended by-products of MP degradation during production, as their small size prevents them from functioning as exfoliating agents [41].

Secondary MNPs, on the other hand, are generated from the weathering or degradation of larger plastic debris through exposure to physical, chemical, biological, and microbial processes [43-48]. Mechanical breakdown involves disintegration and abrasion caused by interactions between plastics and environmental factors such as sediments, pebbles, waves, and tidal forces in aquatic systems [49]. Thermal degradation of plastics occurs when the bond dissociation energy is exceeded, leading to bond breakage [50]. On land, plastics are particularly vulnerable to thermal degradation in areas such as beaches, where high surface temperatures can accelerate the process [51]. Solar radiation is the most effective pathway for plastic degradation [52]. UV-induced oxidative degradation can create a fragile, brittle surface layer prone to fissures and cracks, leading to the formation of polymer MPs and NPs through fractures caused by moisture-induced stress, temperature fluctuations, and abrasion by beach sand grains [52]. Photodegradation has resulted in a 5% weight loss of an expanded polystyrene box, within one month, generating approximately  $6.7 \times 10^7$  particles/cm<sup>2</sup> of MNPs in regions at a latitude of 34°N [53]. Biological weathering of MPs occurs primarily through microbial degradation and the processes of ingestion and digestion by organisms. Although slow and limited, the biodegradation of plastics may occur through enzymatic depolymerization followed by microbial assimilation and mineralization [54, 55]. The degradation of MPs through ingestion was also documented, showing that Antarctic krill (*Euphausia superba*) can fragment ingested MPs (31.5 μm) into smaller NPs (less than 1 μm) under acute static renewal conditions [7]. Marine and freshwater rotifers also can break down PS, PE, and photo-aged MPs, releasing tiny particles during ingestion [56].

These weathering processes not only break down large plastics into smaller MPs or NPs but also alter the physicochemical properties of the primary materials [57, 58]. Beyond surface

fissuring and progressive fragmentation, UV irradiation induces chromatic shifts in MNPs, typically manifesting as a transition from white to yellow or black hues [53], with intensifying pigmentation correlating with prolonged solar exposure. Furthermore, UV weathering can promote the surface functionalization of MNPs through the introduction of oxygenated groups, including hydroxyl and carbonyl functionalities [59]. This formation of oxygen functional groups is also linked to an increase in the surface hydrophilicity and polarity of the MNPs [60].

Biofouling, also referred to as the plastisphere, being the specialized ecosystems that develop on MPs, represents a distinct form of MNP weathering [61]. The plastisphere comprises bacteria, fungi, viruses, archaea, algae, protozoa and extracellular polymeric substances (EPS), that maintain dynamic interactions with the surrounding environment [62]. Plastisphere formation has been shown to change MP density, thereby altering their buoyancy [63]. The plastisphere increases the effective density of MPs without a proportional increase in volume, even leading to the sedimentation of previously buoyant particles [64]. However, due to their smaller size, NPs exhibit a limited capacity for extensive biofilm formation, but their surfaces can readily adsorb various components of natural organic matter (NOM), including humic substances, proteins, and EPS, resulting in the development of an eco-corona [65]. This organic layer influences the physicochemical properties of NPs, changing their interfacial characteristics, aggregation behavior, and transport dynamics in aquatic environments (*Figure 1.1*) [66, 67].

### 1.3. Nanoplastics Exhibit Distinct Transport Patterns From Microplastics

#### 1.3.1. Fate of Microplastics and Nanoplastics in Aquatic Environments

The transport and fate of MNPs are strongly influenced by their hydrodynamic behavior, including aggregation, settlement, resuspension, and horizontal transport [68]. Polymer density plays a crucial role in determining the deposition and mobility of MPs within aquatic ecosystems. Settling and sedimentation of MPs are primarily governed by gravitational forces, with high-density MPs tending to settle near riverbeds, while low-density MPs remain buoyant and float near the surface [69]. For instance, low-density polymers like PP and PE typically float, whereas high-density polymers such as PVC tend to settle. MP transport occurs through gravity-driven vertical movement or horizontal displacement due to settling within aquatic systems [70]. NPs, due to their distinct size characteristics, exhibit a different transport behavior compared to MPs. The colloidal nature of NPs means that Brownian motion (diffusion) often dominates over sedimentation and buoyancy forces, resulting in limited vertical transport in the water column compared to MPs of the same material [71]. According to Stokes' law, a 1 mm PVC MP would settle in water at a rate of approximately 22 cm/s, whereas a 100 nm PVC NP would settle at an estimated rate of only 7 cm/year [71]. Consequently, NPs are more likely

to remain homogeneously dispersed in aqueous systems unless aggregation occurs, which causes them to behave as larger particles. The distinct size properties of MPs and NPs also result in different transport processes in porous media, such as soils and sediments [60]. Physical straining or filtration plays a critical role in controlling the transport of MPs in porous media. It has been suggested that MPs larger than 10  $\mu\text{m}$  are typically filtered out, while smaller particles have a higher potential to pass through soil pores and arrive in deep soil layers [72]. The density of MPs also influences their movement; low-density MPs are less likely to move downward due to buoyancy [73]. The mobility of NPs in porous media generally aligns with colloidal filtration theory [74], where the classic Derjaguin-Landau-Verwey-Overbeek (DLVO) interactions predominantly govern NP deposition [75].

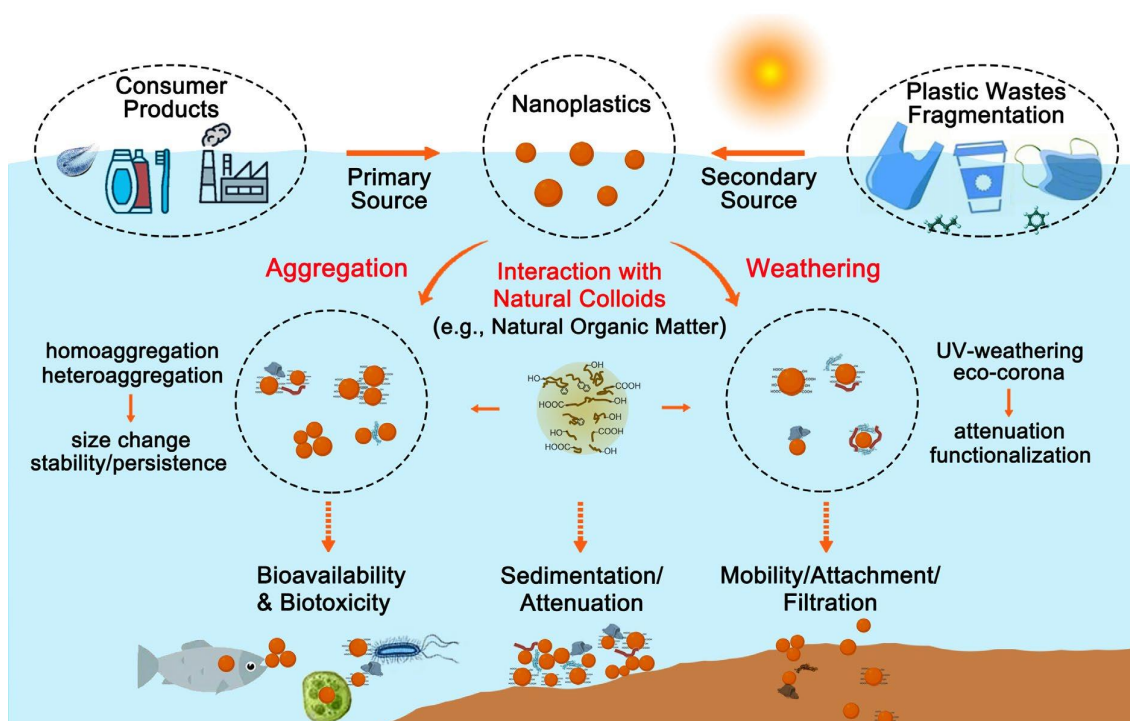


*Figure 1.1. Schematic illustration of NP weathering, transport, and fate in aquatic environments.*

### 1.3.2. Aggregation and Colloidal Stability of Nanoplastics

The aggregation and stability of NPs are primarily governed by DLVO interactions, including electrostatic and van der Waals forces, which are strongly influenced by water chemistry (e.g., pH, ionic strength, and ion valence) in aquatic environments. Typically, NPs carry a negative charge while a decrease in pH or an increase in ionic strength can compress the electrical double layer and lower the energy barrier, allowing particles to interact and aggregate due to

Van der Waals attraction [76, 77]. Therefore, NPs, generally, exhibit minimal aggregation in freshwater but undergo a stronger aggregation in seawater [78]. Multivalent cations (e.g.,  $\text{Ca}^{2+}$ ,  $\text{Mg}^{2+}$ , and  $\text{Fe}^{3+}$ ) are more effective at screening surface charges than monovalent cations (e.g.,  $\text{Na}^+$  and  $\text{K}^+$ ) at equivalent mass concentrations [76, 77]. Beyond this charge screening effect, these multivalent cations can also serve as cationic bridges, linking particles together and promoting aggregation [79].

NOM is widespread in aquatic environments and consists of a complex mixture of organic compounds, including humic acids (HA), microbial excretions, proteins, and polysaccharides [65]. When NPs interact with NOM, they can develop a diverse organic coating on their surfaces, referred to as an eco-corona [80]. This eco-corona can alter the physicochemical properties of NPs, thereby influencing their stability [65]. In monovalent electrolyte solutions, NOM generally stabilizes NPs through steric repulsion or electrostatic repulsion [81]. However, in divalent electrolyte solutions (e.g.,  $\text{Ca}^{2+}$ ), the interaction between  $\text{Ca}^{2+}$  and adsorbed NOM can enhance aggregation via  $\text{Ca}^{2+}$ -facilitated polymer bridging [76, 77, 82]. NPs are typically less stable in solutions containing both high concentrations of cations and NOM compared to solutions with either cations or NOM [83]. A study has demonstrated that a combination of 10 mM cations and 5 mg/L NOM caused extensive aggregation and nearly complete removal of 50–100 nm NPs from suspension, while NPs remained stable when only one of these components was present [84]. The role of NOM in NP stability is also influenced by the source and composition of the NOM. In NaCl solutions, the most pronounced stabilization effect was observed with bovine serum albumin (BSA, a model protein), which has exhibited the largest hydrodynamic adsorption layer thickness of 21.9 nm, followed by HA, EPS, and sodium alginate (SA, a model polysaccharide) [82]. In contrast, in  $\text{CaCl}_2$  solutions, SA has caused considerable destabilization of NPs through bridging with  $\text{Ca}^{2+}$ , with the destabilizing effect increasing as concentrations of SA and  $\text{CaCl}_2$  rose. The destabilization effect of the other three macromolecules followed the order: BSA > HA > EPS [82].

Inorganic colloids, such as clay and metal oxides, also influence the stability of NPs. Electrostatic interactions typically dominate, depending on the zeta potential of the minerals. Minerals and NPs with similar charges may repel each other, thereby stabilizing the NPs. As reported, bentonite clay, which carries a net negative charge at pH 6.0, can help stabilizing NPs [85]. However, high ionic strength can reduce this electrostatic repulsion between similarly charged particles, and sorbed multivalent cations may facilitate cation bridging, which enhances aggregation [85]. Similarly, montmorillonite and kaolinite, both negatively charged, had no effect on the stability of NPs colloidal suspensions [86]. In contrast, the presence of positively charged goethite or magnetite reduced NP stability due to a strong electrostatic attraction between the NPs and the iron oxides [86].

### 1.3.3. Nanoplastic Transport and Deposition in Porous Media

NPs can migrate from the topsoil to the saturated zone through infiltration driven by rainfall or irrigation. Additionally, NPs may be introduced into aquifers through intentional injection activities. The transport and deposition of NPs are highly influenced by factors such as flow rates, flow orientations, degree of water saturation [87], solution chemistry (i.e., pH, ionic strength and valence) [88], and the co-existence of environmental colloids such as NOM [88, 89], and bacteria [90]. Wu et al. have found that as pH increases, the electrostatic repulsion between soil particles and negatively charged PS NPs also increases, which enhances the mobility of PS NPs due to the greater negative charge density resulting from the deprotonation of clay minerals [91]. In addition, divalent cations have facilitated the deposition of NPs on sand surfaces through cation bridging [92], with deposition decreasing in the order  $Cs^+ > K^+ > Na^+$  and  $Ba^{2+} > Ca^{2+} \geq Mg^{2+}$  [93]. NPs coated with NOM have exhibited lower attachment efficiencies compared to uncoated NPs due to increased electrostatic repulsion [88, 94], or the introduction of additional steric repulsion [67, 89]. Specifically, the transport of PS NPs in saturated porous media has greatly been enhanced by the eco-corona formed from the larger-sized EPS of Gram-negative *Escherichia coli* MG1655, compared to the eco-coronas derived from soil HA and fulvic acids [67]. The negatively charged BSA has enhanced NP transport, while the positively charged lysozyme has triggered the aggregation of NPs into large clusters, inhibiting their movement through electrostatic adsorption and bridging effects [89].

The transport of NPs in porous media is also strongly associated with the characteristics of the porous media itself, including grain size, surface properties, moisture content, and mineral composition. Studies have shown that as the particle size of the media increases, NP deposition decreases [95], primarily due to the reduced specific surface area and fewer adhesion sites for NPs on the larger media surfaces [96]. Most studies on NP migration in porous media use bare quartz sand columns, but real-world porous media are often more complex, with varying media properties, affecting NP mobility. Metal oxides, particularly manganese, aluminum, and iron oxides, are key deposits, formed during soil development. Under typical pH conditions, these metal oxides are positively charged, facilitating the retention of negatively charged NPs through electrostatic attraction [88, 94].

Studies on the role of biofilms on NP transport in porous media have been limited to biofilms cultivated with *Pseudomonas aeruginosa*, *Escherichia coli*, or *Bacillus subtilis* [97, 98]. It has, e.g., been found that biofilms (*Escherichia coli*) increased the retention of PS NPs in porous media by enhancing media surface roughness, narrowing flow paths, and forming hydrogen bonds between extracellular polymers and PS NPs [97]. Mitzel et al. have also revealed that biofilm-coated quartz sand retained more PS NPs than uncoated sand, but the deposition mechanisms differed between hydrophilic (*P. aeruginosa* 9027) and hydrophobic (*P.*

*aeruginosa* PAO1) biofilm-coated surfaces [98]. NP transport was variable in sand coated with a hydrophilic biofilm, while transport remained constant over time in sand coated with a more hydrophobic biofilm [98].

#### 1.4. Riverbank Filtration as Barrier of Colloidal Contaminants

Managed aquifer recharge systems, including riverbank filtration (RBF), soil-aquifer treatment, and aquifer recharge and recovery, have globally been used to enhance the availability of local water supplies, because of their high production potential, proximity to areas of demand, and ease and economics of extraction [99, 100]. RBF has been practiced in Europe for more than 100 years, particularly in countries such as Switzerland, where 80% of drinking water comes from RBF wells, 50% in France, 48% in Finland, 40% in Hungary, 16% in Germany, and 7% in the Netherlands [101, 102]. RBF has also been used for nearly half a century in the United States, especially in the states of Ohio, Kentucky, Indiana, Illinois, among others [103]. Nowadays, some Asian countries (e.g., China, India, and South Korea) have started developing RBF for drinking water production [94, 104].

During RBF, the removal of pollutants through physical, chemical, and biological processes can take place between surface water and groundwater and with substrates [105, 106]. Using its natural filtration function, RBF is efficient in removing colloidal pollutants in rivers, such as turbidity [103], pathogenic micro-organisms [107, 108], and engineered nanoparticles [109]. Most studies have focused on the attenuation of pathogenic micro-organisms (i.e., viruses, bacteria, and protozoa) during RBF, with the main removal mechanisms being inactivation, straining, and attachment to the aquifer grains (adsorption) [103]. Inactivation can happen with the disruption of coat proteins and the degradation of nucleic acids [103]. Depending on the particle size and that of the pore throats, physical straining is the most important removal mechanism of microbial particles [108]. Flocculation with other colloids in the water might increase in particle size and density, enhancing the removal of pathogenic micro-organisms [101]. Finally, surface interactions such as electrostatic interaction, hydrogen bonding and hydrophobic interaction, may also take place between pathogenic microorganisms and soil particles, contributing to their removal [110]. The removal mechanisms of engineered NPs in RBF systems have been found to be similar to bio-colloids, although limited studies on their removal in realistic RBF systems exist [109, 111]. Bäuerlein et al. have reported MP concentrations ranging from 231 to 12,882 particles/m<sup>3</sup> in river water and RBF-treated groundwater in the Netherlands, with MP levels reduced by 78% to 98% through RBF [19]. The observed lower NP concentrations in riverbank groundwater (0.021–0.203 mg/m<sup>3</sup>) compared to surface water (0.283–0.793 mg/m<sup>3</sup>), was also likely due to the filtration efficiency

of the RBF [10]. Although RBF potentially contributes to the attenuation of MNPs, low levels can still be detected in filtered groundwater, indicating that the removal is incomplete.

## 1.5. Research Outline

### 1.5.1. Research Objective

Understanding the transport and fate of NPs in natural waters and during RBF is critical for ensuring clean water production. However, the weathering of NPs in natural waters through processes such as UV exposure and eco-corona formation, as well as the weathering of sand grains by natural biofilms in RBF sediments add complexity to understand their behavior.

Therefore, the overall objective of this dissertation is to explore how these natural weathering processes change NP character in natural waters and influence their transport dynamics during RBF, and to translate these insights into an improved predictive model, simulating the fate of NP during RBF.

### 1.5.2. Research Gaps

(1) Weathering, particularly UV-induced weathering, serves as a pivotal driver in the generation of secondary MNPs, which exhibit divergent transport dynamics and environmental fate compared to their primary counterparts. However, a thorough review of research on the physical, chemical, and biological impacts of UV-weathered MNPs in both aquatic and terrestrial ecosystems is missing.

(2) The aggregation dynamics of NPs are profoundly modulated by weathering processes, including UV-induced degradation and the formation of eco-coronas through NOM. Studies utilizing commercially available NPs, representative of primary NPs, have demonstrated that NOM adsorption affects NP aggregation. However, UV-weathered NPs, which mimic environmentally relevant particles, exhibit distinct surface properties that may enable the formation of a distinct eco-corona. How UV weathering affects the interaction of NPs with NOM and, consequently, alters NP aggregation, remains largely unexplored.

(3) Natural filtration systems, such as RBF, play a crucial role in enhancing water quality by retaining contaminants, including NPs, within sediment matrices. Understanding the transport and deposition mechanisms of NPs in porous media is fundamental to assess their removal efficiency and potential risks in these processes. While existing studies have offered valuable insights into how UV weathering and NOM adsorption increase or reduce NP transport, a comprehensive understanding of their transport dynamics and mechanisms remains lacking.

(4) Natural sand grains can also undergo weathering processes, such as biofilm formation, which are critical for contaminant attenuation during RBF. However, their role in NP removal

remains incompletely understood. Previous studies on NP mobility in porous media have predominantly employed simplified, homogeneous biofilms cultivated from model bacteria (e.g., *Pseudomonas aeruginosa*, *Escherichia coli*). In addition, in natural RBF systems, biofilms exhibit pronounced spatial heterogeneity along infiltration gradients due to oxygen and nutrient depletion, leading to stratified microbial communities (aerobic, anoxic, anaerobic zones). Model studies have not yet addressed the impact of spatial heterogeneity in sand grains. Bridging this knowledge gap is critical to refining predictive frameworks for NP transport in RBF systems, ensuring they account for the spatial heterogeneity and dynamic interactions inherent in natural biofilms under environmentally realistic scenarios.

### 1.5.3. Research Questions and Outline

*RQ 1. What is the current knowledge and perspectives on the role of UV weathering in shaping MNP transport, fate, and ecological risks across ecosystems?*

In [Chapter 2](#), current knowledge and existing discrepancies regarding the effects of UV weathering on the physical behavior (contaminant adsorption dynamics, colloidal stability, and mobility of MNPs and associated pollutants), chemical processes (photochemical interactions with co-existing constituents), and biological impacts (ecotoxicological risks to aquatic organisms, biofilm formation dynamics, planktonic microbial activity, and structural/functional shifts in soil/sediment microbial communities) of MNPs in ecosystems are critically evaluated.

*RQ 2. What is the role of NOM in the aggregation dynamics of non-weathered NPs versus UV-weathered NPs?*

[Chapter 3](#) focuses on NP aggregation studies. The effects of weathering are reported, including UV-induced oxidation and NOM adsorption, on the physicochemical properties of PS NPs. Furthermore, the distinct role of NOM in regulating the colloidal stability of non-weathered and UV-weathered NPs are described. For this purpose, PS NPs were UV-aged using an artificial accelerated photooxidation method. Bulk Suwannee River NOM and its molecular weight (MW) fractions (< 3 kDa, 3–10 kDa, 10–30 kDa, and 30 kDa–0.05  $\mu\text{m}$ ) were prepared. Aggregation behavior of non-weathered and UV-weathered NPs was monitored using time-resolved dynamic light scattering (DLS), both in the absence and presence of NOM fractions, and DLVO and polymer-mediated steric models were applied to predict and understand the size-dependent roles of NOM in NP aggregation.

*RQ 3. How do the deposition mechanisms differ between non-weathered and weathered NPs in saturated porous media?*

[Chapter 4](#) aims to elucidate the deposition mechanisms of non-weathered and weathered NPs in saturated porous media. Therefore, commercial PS NPs were used as a model for non-

weathered NPs. To simulate environmental aging, these NPs were exposed to UV irradiation using a mercury lamp, producing UV-weathered PS NPs. Additionally, Suwannee River NOM was incubated with both non-weathered and UV-weathered PS NPs to generate NOM-weathered NPs. To further study the influence of NOM characteristics, NOM was fractionated by MW, and each fraction was used to assess how NOM size modified NP surface properties and affected deposition behavior. Breakthrough curves were obtained for both non-weathered and weathered NPs in saturated porous media. Deposition mechanisms were interpreted using two modeling approaches: the two-site kinetic model and the equilibrium-kinetic model. These were further supported by DLVO and extended DLVO (XDLVO) theories to reveal the interaction forces and underlying mechanisms governing NP deposition.

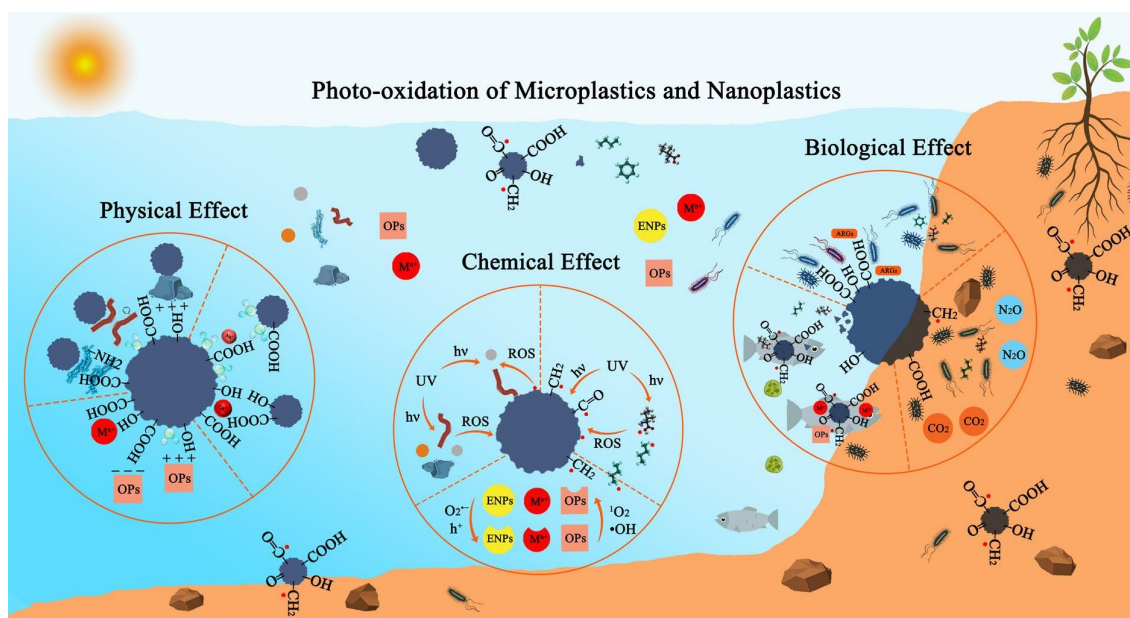
*RQ 4. What is the effect of spatial heterogeneity of biofilm during riverbank filtration on the transport of NPs?*

**Chapter 5** aims to elucidate how the spatial heterogeneity of biofilms influences NP transport and removal, with the goal of improving predictive models for RBF systems. To this end, we constructed multiple long columns packed with clean quartz sand and continuously fed them with river water collected from an RBF site in the Netherlands, enabling biofilm development over periods of 1, 3, and 6 months. After biofilm maturation, each long column was segmented into short sections representing distinct depth intervals, which were subsequently used for NP transport experiments. We first investigated how biofilm-induced heterogeneity affects NP transport dynamics. We then analyzed the relationship between spatial biofilm characteristics and NP retention or mobility. In addition, we compared the transport behavior of pristine NPs in synthetic water with that of environmentally weathered NPs in natural river water to assess the impact of eco-corona formation and a natural water matrix on NP mobility. Finally, we employed transport modeling approaches that incorporate biofilm heterogeneity to better predict NP retention and transport in RBF systems.

**Chapter 6** summarizes the overall conclusions and implications of the thesis, discusses the research's limitations, and outlines directions for future work.

## Chapter 2

### Photo-oxidation of Micro- and Nano-plastics: Physical, Chemical and Biological Effects in Environments



This Chapter is based on

Xu, Y.; Ou, Q.; van der Hoek, J. P.; Liu, G.; Lompe, K. M., Photo-oxidation of Micro- and Nanoplastics: Physical, Chemical, and Biological Effects in Environments. *Environ Sci Technol* **2024**, *58*, (2), 991–1009.

## Abstract

Micro- and nano-plastics (MNPs) are attracting increasing attention due to their persistence and potential ecological risks. This review critically summarizes the effects of photo-oxidation on the physical, chemical, and biological behaviors of MNPs in aquatic and terrestrial environments. The core of this paper explores how photo-oxidation-induced surface property changes in MNPs affect their adsorption toward contaminants, the stability and mobility of MNPs in water and porous media, as well as the transport of pollutants such as organic pollutants (OPs) and heavy metals (HMs). It then reviews the photochemical processes of MNPs with co-existing constituents, highlighting critical factors affecting the photo-oxidation of MNPs, and the contribution of MNPs to the photo-transformation of other contaminants. The distinct biological effects and mechanism of aged MNPs are pointed out, in terms of the toxicity to aquatic organisms, biofilm formation, planktonic microbial growth, and soil and sediment microbial community and function. Furthermore, the research gaps and perspectives are put forward, regarding the underlying interaction mechanisms of MNPs with co-existing natural constituents and pollutants under photo-oxidation conditions, the combined effects of photo-oxidation and natural constituents on the fate of MNPs, and the microbiological effect of photo-aged MNPs, especially the biotransformation of pollutants.

## 2.1. Introduction

With the high production and wide use of plastics, and the lack of effective waste disposal and recycling methods, plastics are increasingly accumulating in the environment [112]. It is estimated that 19 to 23 million metric tons (11%) of global plastic entered aquatic ecosystems in 2016, and annual emissions may reach 53 million metric tons per year by 2030 [113]. In recent decades, small plastic particles called microplastics (MPs; 1  $\mu\text{m}$ –5 mm in size) have attracted widespread attention in the world [114]. A part of the MPs in the aquatic environment comes from the direct discharge of wastewater treatment plants and overland runoff, and the other part mainly comes from the mechanical, chemical, and/or biological degradation processes of large pieces of plastics [43-48]. Nanoplastics (NPs) are considered an extension of MPs but considerably differ from MPs in terms of transport characteristics, interactions with environmental constituents, bioavailability, and ecological risks [115, 116].

In the environment, Micro- and nano-plastics (MNPs) can undergo a series of weathering processes, mainly including mechanical fragmentation, photo-oxidation, thermal-degradation, and biodegradation [117]. Photo-oxidation by sunlight is considered to be the most critical cause of polymer aging, which increasingly attracted attention over the past years [118]. Up to March 2023, the total number of publications was 1892 based on the search results of the Web of Science with the following keywords: microplastic\* or nanoplastic\* and photo\* or light\*

or ultraviolet\* or UV\*. The number of publications continuously increased from 68 in 2018 to 611 in 2022. Photo-oxidation of MNPs is a complex process involving free radicals such as alkyl, peroxy, alkoxy and hydroxyl radicals ( $\cdot\text{OH}$ ) [119], usually resulting in the change of physicochemical properties of MNPs, and inducing their fragmentation and leaching of organic matter like polymer molecules and additives [120]. Photo-oxidation of MNPs in the environment is highly influenced by coexisting natural constituents of the surrounding matrix (e.g., ions, minerals, and natural organic matter or NOM) [121, 122]. Notably, the presence of environmental constituents such as anions, cations, and minerals may accelerate the photo-oxidation of MNPs by promoting the generation of reactive oxygen species (ROS) [122-124]. On the other hand, some constituents like anions and NOM may inhibit the photo-oxidation of MNPs by either shielding light or scavenging ROS, although some debates exist [125-127].

The modification of surface properties after photo-oxidation, such as increased O-containing functional groups and decreased hydrophobicity, can change the fate of MNPs in the environment [128, 129]. For instance, the effect of photo-oxidation generally increased colloidal stability and mobility of NPs in water and porous media [129-131], but this effect might be different depending on the water chemistry (e.g., salt types) [128, 132], the presence of NOM [83, 133], and minerals in environments [128, 129, 134]. As carriers of environmental contaminants, MNPs can adsorb the surrounding chemical substances and mediate their transport in the environment [60]. The photo-oxidation of MNPs may enhance or reduce the adsorption capacity toward pollutants [135], and thus change the mobility of pollutants [60, 136]. Liu et al. reported that the photo-aged PS NPs increased the mobility of both nonpolar (pyrene) and polar contaminants (4-nonylphenol) in saturated loamy sand compared to pristine NPs due to increased binding with contaminants [136]. In addition to affecting the adsorption behavior of other contaminants, the photo-oxidation of MNPs may also produce environmentally persistent free radicals (EPFRs) and ROS, and mediate the photo-chemical transformation of pollutants, such as organic pollutants (OPs) [137, 138], heavy metals (HMs) [139], and engineered nanoparticles (ENPs) [140, 141]. The modified surface properties, the generated EPFRs and ROS, and the leached polymer molecules and additives of MNPs after photo-oxidation can also change their toxicities to organisms and affect microorganisms in the surrounding matrix, such as biofilm formation on MPs [142], the growth of planktonic microbes [143, 144], as well as the microbial community in soil and sediment systems [145, 146]. All in all, photo-oxidation can influence the physical, chemical, and biological processes of MNPs in aquatic and terrestrial environments.

Currently, several reviews have summarized the weathering processes of MPs and corresponding effects on the environmental behavior of MPs, mainly considering the different weathering processes and mechanisms, and the effect of weathering on the properties,

adsorption, and toxicity of MPs [58, 117, 147-149]. However, few of them have thoroughly considered the physical, chemical, and biological effects of photo-oxidation of MNPs in the environment. In the last two years, an increasing number of studies have focused on understanding the process of photo-oxidation and its impact on different types of MNPs, as well as the effect of environmental constituents on this process [122, 124, 126, 150-152]. Furthermore, research on the influence of photo-oxidation of MNPs on the adsorption and photo-chemical transformation of other pollutants has gained more attention [151-154]. The biological effect of photo-oxidized MNPs on organism activity, especially microbial community composition and function has also become a subject of interest among scholars [142, 144, 155]. More importantly, the photo-oxidation process and the physical, chemical, and biological behavior of MNPs are mutually associated and inseparable. Thus, it is necessary to give a critical review of recent research on the physical, chemical, and biological effects of photo-aged MNPs in aquatic and terrestrial environments.

Firstly, this article introduces the photo-oxidation process and physicochemical changes of MNPs. Secondly, the physical effect of photo-oxidation of MNPs on the adsorption behavior toward pollutants, the colloidal stability of MNPs, as well as the transport behavior of MNPs and associated pollutants in porous media are discussed. Next, it dissects the effect of critical factors on the photo-oxidation of MNPs, and the mediated role of MNPs in the photo-transformation of environmental pollutants. Moreover, this article assesses the effect of photo-oxidation of MNPs on the toxicity and its mechanism to organisms, plants and the microbiological effect on a variety of environmental microorganisms. Finally, knowledge gaps are pointed out and avenues for future research are suggested.

## 2.2. Photo-Oxidation of MNPs

Sunlight irradiation is the most important aging process for MNPs in the environment [156]. Sunlight is mainly composed of infrared (wavelength  $\lambda$  between 700 nm and 1 mm), visible ( $\lambda = 400\text{--}700$  nm), and UV ( $\lambda = 100\text{--}400$  nm) [157]. The UV fraction of light irradiation with high energy plays a critical role in the weathering of MNPs [158]. It is estimated that the global average solar irradiance received on Earth is 16.4–34 mW/cm<sup>2</sup> over a 24-hour day [159]. The photo-oxidation of MNPs has been extensively studied in experiments to accelerate aging with artificial light sources, mainly gas discharge lamps such as xenon, mercury, fluorescent and metal halide lamp, with UV intensities ranging from a few to tens of mW/cm<sup>2</sup> [117, 125, 158, 160]. The extent of photo-oxidation is determined by the UV dose (kJ/cm<sup>2</sup>) that is a product of solar irradiance (mW/cm<sup>2</sup>) and exposure time. Photo-oxidation experiments on MNPs are typically carried out in aqueous and aerial environments, commonly involving the participation of oxygen (O<sub>2</sub>) and water [161]. Notably, in the laboratory, the mechanical agitation is typically

combined with UV radiation to simulate hydraulic disturbance and to facilitate the mixing of samples. This can accelerate the photo-oxidation and disintegration to some extent by exposing the sample to more oxygen and UV radiation, as well as mechanical fragmentation.

The photo-oxidation first occurs on the surface of MNPs and produces highly reactive organic radicals and ROS that are involved in the radical reactions [158]. In some cases, photo-oxidation can also lead to the formation of relatively stable EPFRs [161]. Typically, along with the generation of alcohols, ketones, olefins, and aldehydes, carboxylic acids and esters, vinyl groups and O-containing functional groups, such as carbonyl, carboxyl and hydroxyl groups can be formed during the photo-oxidation of MNPs [162]. The yellowing of the polymer is a typical sign of the generation of the chromophore [53]. At the same time, significant changes in surface properties can be observed, including increased surface roughness, specific surface area (SSA), polarity, hydrophilicity, negative charges [60, 117]. With further oxidation with time, it gradually develops to the inner layer [163]. The molecular weight of the polymer is reduced, the original physical properties are modified, and the material becomes fragile and more prone to fragmentation. Finally, the photo-oxidation can result in the leaching of DOC and additives [164], and further mineralization [165].

## 2.3. Physical Behavior of MNPs After Photo-Oxidation

### 2.3.1. Adsorption of Contaminants

MNPs can act as vectors of environmental contaminants, such as OPs and HMs, and thus affect the transport of contaminants by MNPs in the environment and induce ecological risks [43]. The effect of photo-oxidation on the adsorption behavior of MNPs is studied using batch adsorption experiments by determining adsorption kinetics and adsorption isotherms. The Langmuir and Freundlich models are the most commonly used models to describe adsorption of contaminants on pristine and aged MNPs, indicating mono- or multi-layer adsorption processes on heterogeneous surfaces [135, 166, 167]. The influence of photo-oxidation on the adsorption behavior of contaminants on MNPs mainly depends on three mechanisms (*Figure 2.1*): (1) the increase in surface roughness and SSA of aged MNPs could provide more adsorption sites for contaminants [166, 168], (2) decreased hydrophobicity and increased O-containing functional groups can change adsorption affinity of contaminants to MNPs mediated by hydrophobic or hydrophilic interaction [151, 169], and (3) increased electronegativity of aged MNPs could influence the electrostatic interaction between MNPs and charged OPs and HMs [170, 171].

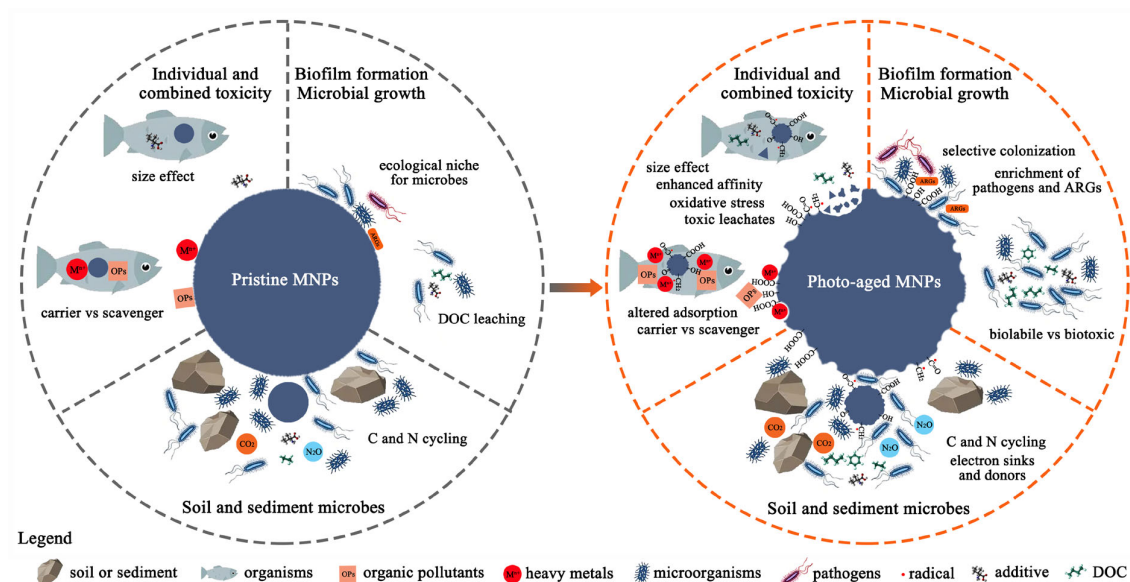


**Figure 2.1.** Effect of photo-oxidation of MNPs on the homo-aggregation, hetero-aggregation, and adsorption behaviors towards pollutants.

**Organic pollutants.** Various forces including hydrophobic interaction,  $\pi$ - $\pi$  bond, electrostatic interaction, and H-bond may mediate the interaction between MNPs and OPs (See [Table S1](#) for details on the adsorption capacity and mechanism of photo-aged MNPs towards OPs) [172]. The hydrophobicity of hydrophobic OPs can be evaluated with the partition coefficient of n-octanol/water ( $\log K_{ow}$ ), which is linearly correlated with their adsorption on MNPs via hydrophobic interaction [135, 173]. Generally, due to the increase of O-containing functional groups, the hydrophobic interaction between MNPs and hydrophobic OPs will decrease with the photo-oxidation [174].  $\pi$ - $\pi$  bond commonly occurs between aromatic MNPs (e.g., PS, PET, and PC) and OPs with C=C bonds or benzene rings [166]. As typical aromatic polymers, photo-oxidation of PS MNPs can lead to a decrease in aromatic components and an increase in O-containing groups [175]. Liu et al. reported that the adsorption of bisphenol A on aged PS MPs was reduced due to the decrease of the hydrophobic interaction and  $\pi$ - $\pi$  bonds [152]. For hydrophilic and polar OPs with abundant O- or N-containing groups, the H-bonds control their adsorption process on aged MNPs [176]. Several studies reported that the adsorption ability of MNPs for hydrophilic compounds enhanced after photo-oxidation as they can form strong H-bonds [170, 172, 177]. For example, Fan et al. found that the maximum adsorption capacity ( $Q_{max}$ ) of antibiotic on aged PLA and PVC MPs ( $1.29 \text{ kJ/cm}^2$ ) were 1.2–2.2 times and 1.3–1.6 times higher than on the pristine MNPs, respectively [177]. For charged OPs, electrostatic interaction also affects their adsorption on MNPs [170]. MNPs are commonly negatively charged under environmental pH conditions, and photo-oxidation could increase

the negative charges of MNPs due to the increase in O-containing functional groups [167]. Theoretically, photo-oxidation can decrease or increase the interaction between MNPs and negatively or positively charged OPs via electrostatic repulsion or attraction [167].

However, the actual situations are more complex and depend on many factors such as the physicochemical properties of OPs, oxidation degree, and polymer type of MNPs. For example, the adsorption of benzalkonium chlorides (BAC) on pristine/photoaged MPs was related to the length of the saturated fat chains: the adsorption capacity of relatively hydrophobic BAC<sub>14</sub> and BAC<sub>16</sub> on aged PE MPs decreased by 19% compared with pristine PE MPs, but that of relatively hydrophilic BAC<sub>12</sub> increased by 22% due to hydrophilic interaction and weak chemical interactions [135]. Therefore, during photo-oxidation, the adsorption of OPs on MNPs is not determined by one force, but the result of a variety of forces. Liu et al. reported that hydrophobic and  $\pi$ - $\pi$  interaction controlled the adsorption of atorvastatin and amlodipine on pristine PS MPs while electrostatic interaction and hydrogen bonding controlled their adsorption on aged PS MPs [167]. Particularly, the adsorption capacity of atorvastatin on PS MPs decreased first and then increased with prolonged oxidation time, indicating the change of dominant forces [167]. Thus, the UV dose also plays an important role in the adsorption of OPs on the surface of MNPs. In addition to oxidation time, the oxidation degree of MNPs could be affected by the light source and polymer type of MNPs. For instance, Liu et al. and Fan et al. reported that the adsorption capacity of ciprofloxacin (CIP) on aged MPs (e.g., PS, PVC, and PLA) was higher than on pristine MPs [170, 177]. Lin et al. found that the adsorption of CIP reduced on PS, PE, PET and PVC MPs after UV treatment, but increased on PVC MPs after vacuum UV treatment [166]. The distinct adsorption phenomenon of CIP on aged PVC MPs in different publications might be related to different oxidation degrees of MPs and influenced by UV treatment time and polymer type. Similarly, Wang et al. suggested that the order of adsorption capacity of atrazine on pristine MPs was PS > PE > PP, while that on aged MPs was aged PE > aged PP > aged PS, which was explained by varying degrees of increase in surface roughness and SSA of aged MPs [172]. Overall, photo-oxidation changes the adsorption of OPs on MNPs by influencing forces such as hydrophobic interaction and H-bond, which is also dependent on the oxidation degree and physicochemical properties of OPs.

**Heavy metals.** Different from OPs, photo-oxidation typically promotes the adsorption performance of MNPs to HMs [118, 168, 169, 178-180]. First of all, photo-oxidation can enhance the surface roughness and SSA of MNPs, and thus promote the adsorption of HMs [118, 180]. With increasing aging time, the surface of PS NPs significantly generated pores and became rough, and the adsorption of five heavy metal ions (Pb<sup>2+</sup>, Cu<sup>2+</sup>, Cd<sup>2+</sup>, Ni<sup>2+</sup>, and Zn<sup>2+</sup>) was enhanced [118]. The increase in surface negative charges after UV irradiation also facilitates the adsorption of HMs due to enhanced electrostatic attraction. For example, the

average zeta potential of tire wear particles (TWP) reduced from  $-8.0$  to  $-14.6$  mV and PP MPs from  $-5.4$  to  $-9.5$  mV after a UV dose of  $0.86$  kJ/cm<sup>2</sup>, and thus the orders of adsorption capacity of MPs towards Cd<sup>2+</sup> and Pb<sup>2+</sup> followed aged TWP > aged PP > pristine TWP > pristine PP [178]. At the same time, the surface O-containing functional groups of aged MPs can strongly adsorb HMs via ion complexation [168].

HMs do not exist alone and may coexist with other contaminants like OPs. Several studies also reported the synergistic or competitive adsorption of HMs and OPs on aged MNPs [181, 182]. Xue et al. suggested that the photo-oxidation promoted the co-adsorption of Cu(II) and oxytetracycline (OTC) on thermoplastic polyurethanes (TPU) MPs, due to the increased surface roughness and functional groups [182]. The synergistic effect was due to the bridging role of Cu(II) and the production of Cu(II)-OTC complex [182]. Zhou et al. also reported that rough surface and O-containing functional groups on aged PS and PVC MPs were responsible for the adsorption of CIP and HMs, while CIP had negative and positive impacts on the adsorption of Cu(II) and Cr(VI) by aged MPs [181]. The negative impact of CIP on the adsorption of Cu(II) may be due to the competitive adsorption and high steric hindrance effect, while non-specific interactions between CIP-Cr(VI) complexes and the heterogeneous surface of aged MPs as well as CIP bridging promoted the adsorption of Cr(VI) on aged MPs [181].

Generally, HMs are characterized by positive charges and high complexing capacity with negative charged groups while OPs exhibit complexity due to variations in hydrophobicity and charge. Therefore, the photo-oxidation typically increases the adsorption capacity of MNPs towards HMs via electrostatic attraction and ion complexation. However, the effect of photo-oxidation on the adsorption of OPs varies, influenced by diverse forces such as hydrophobic interaction, electrostatic interaction,  $\pi$ - $\pi$  bonds, and H-bonds, depending on the polymer type and oxidation degree of MNPs and physicochemical properties of OPs.

### 2.3.2. Colloidal Stability in Water Media

Colloidal stability including homo-aggregation (aggregation with themselves) and hetero-aggregation (aggregation with other colloids) is critical to evaluate the fate, transport and potential toxicity of MNPs, especially NPs, in aquatic environments [115, 116]. Dynamic light scattering (DLS) is a widely used technique to determine the aggregation process and colloidal stability of MNPs by measuring the change in hydrodynamic size of MNPs over time. The initial stage of NP aggregation, characterized by an increase in aggregation rate with increasing ionic strength, is referred to as the reaction-limited stage [82]. The subsequent stage that the aggregation rate of NPs reaches a maximum and remains constant as ionic strength is further increased is known as the diffusion-limited stage [175]. The critical coagulation concentration (CCC) is the ionic strength at which the transition from the reaction-limited stage to the

diffusion-limited stage occurs. CCC can be used as an indicator of the stability of NPs in solution, with higher CCC values indicating greater stability [183]. By modifying the surface properties of NPs and affecting their interaction with environmental substances, photo-oxidation can also influence their homo-aggregation and hetero-aggregation behaviors (See [Table S2](#) for details on the influence of photo-oxidation on the colloidal stability of NPs).

**Stability in the presence of monovalent and divalent cations.** The photo-oxidation can influence the aggregation behavior of NPs by changing their interaction forces [128, 132]. Liu et al. reported that the CCC values of PS NPs exhibited a linear increase from 450 to 760 mM as the UV-radiation time was extended from 0 to 24 h ( $R^2=0.975$ ) in the presence of NaCl [128]. Generally, the zeta potential of NPs became more negative with longer exposure to UV irradiation, which enhanced the electrostatic repulsion between NPs and colloidal stability of PS NPs in monovalent solutions [128]. Mao et al. suggested that reduced hydrophobicity of aged PS NPs was responsible for the reduced aggregation due to enhanced hydration repulsion [130, 175]. That is, photo-aged NPs contained more hydrophilic O-containing groups that easily form H bonds with water, and this hydration layer blocked the aggregation of NPs [133, 175]. In addition, photo-oxidized NPs could release organic molecules into solution, which may also induce the stabilization of PS NPs due to steric repulsion [128]. Therefore, increased electrostatic repulsion, hydration force, and steric hindrance could explain the increased stability of NPs in the presence of monovalent cations after photo-oxidation. Cases are different in the presence of divalent cations. The O-containing functional groups of UV-irradiated NPs could bridge with  $\text{Ca}^{2+}$ , which significantly reduced their stability in  $\text{CaCl}_2$  solutions [128, 133]. According to Liu et al., a negative linear correlation ( $R^2=0.811$ ) was observed between the CCC values and UV exposure time [128].

In contrast, several studies concluded that photo-oxidation did not promote the aggregation of PS NPs in the presence of monovalent cations [132, 184]. Zhang et al. showed that simulated sunlight irradiation for 2 h exhibited a negligible effect on the aggregation of PS NPs [184]. Wang et al. reported that pristine PS NPs are coated with sulfate groups, which were degraded first by photo-oxidation, thereby reducing the negative charges of PS NPs and enhancing their aggregation [132]. The discrepancies may be attributed to differences in aggregation experiment design. Different from traditional aggregation studies, Zhang et al. studied the aggregation of NPs in phosphate buffer solutions (PBS, 1.0 mM) by observing the change in hydrodynamic size over 7 days in a oscillator [184]. It might be difficult to observe a significant difference at low ionic strength due to the high stability of PS NPs [132]. Wang et al. studied the aggregation of NPs under low-intensity UV exposure ( $0.0007 \text{ kJ/cm}^2$ ), which induced slower polymer oxidation than in other studies [128, 133]. Therefore, the stability of PS NPs may first decrease and then increase in monovalent cationic solutions with the destruction of

sulfate groups and subsequent generation of O-containing groups during the photo-oxidation process [128, 132]. Similarly, the decreased stability of PS NPs-NH<sub>2</sub> was also observed after photo-oxidation due to the first oxidation of surface sulfate and amine groups [132]. Thus, it is essential to take into account the impact of UV dose that may affect the outcome when designing relevant experiments. Notably, Zhang et al. observed that the hydrodynamic size of pristine PS NPs increased from 99 to 299, 444 and 833 nm after photo-oxidation under UV dose of 39.5, 78.9 and 157.8 kJ/cm<sup>2</sup>, respectively, which was explained by the crosslinking of PS• or PSOO• and subsequent production of PS-PS or PSOOPS [185]. As reported, if O<sub>2</sub> content is insufficient to react with these radicals, crosslinking reactions are more likely to occur instead of direct chain scission [186]. Given that the details of the aging experiments, such as the concentrations of dissolved O<sub>2</sub> and PS NPs, were not clearly defined [185], further investigation is necessary to determine whether the crosslinking of PS NPs could occur and lead to the aggregation of NPs under UV exposure.

In addition, several studies compared the aggregation behavior of normal PS NPs with carboxyl-functionalized PS NPs (PS-COOH) that may simulate surface properties of photo-oxidized PS NPs to some extent [77, 183]. However, the reported CCC values of PS-COOH in NaCl solutions were not higher than those of bare PS NPs (191 mM vs 264 mM, and 308 mM vs 310 mM), suggesting that PS-COOH may exhibit lower stability [77, 183]. Therefore, although conducting experiments with PS-COOH can be useful in exploring relevant mechanisms, it is important to recognize that these particles may differ from UV-aged NPs in important ways. Firstly, UV exposure can induce changes in the physicochemical properties of PS NPs that may not be fully replicated by carboxyl-functionalization alone. Secondly, commercial PS and PS-COOH particles may be manufactured differently, which can make direct comparisons between the two difficult or unreliable.

**Stability in the presence of natural colloids.** In addition to influencing the homo-aggregation of individual NPs, photo-oxidation can also affect the interaction or hetero-aggregation of NPs with other environmental colloids. Adsorption of environmental and biological macromolecules on NP surfaces is well-studied to enhance the stability of NPs in monovalent cationic solutions due to steric repulsion [82, 183]. The photo-oxidation of NPs were reported to reduce their adsorption capacity toward organic molecules (e.g., HA, lysozyme, and alginate) and the thickness of adsorption layer, thereby decreasing the inhibitory effect of steric repulsion on subsequent aggregation of NPs [83, 133, 175]. However, as opposed to HA, the inhibitory effect of bovine serum albumin (BSA) on the aggregation of PS NPs was strengthened after photo-oxidation due to stronger hydrogen bonding and electrostatic attraction between O-containing functional groups on aged NPs with amide groups of BSA [83]. Dissolved black carbon (DBC) was reported to enhance the aggregation of PS NPs in monovalent cationic

solutions as the strong interaction between aromatic constituents of DBC and PS NPs partially screened negative charges of PS NPs; the photo-oxidation decreased the interaction between DBC and PS NPs, and decreased the promoting effect of DBC on the aggregation of PS NPs [175].

Photo-oxidation can also alter the interaction between natural minerals and NPs, affecting their aggregation and sedimentation in environments. Zhang et al. suggested that positively charged iron oxides (e.g., goethite and magnetite) showed stronger interactions with aged PS NPs than pristine PS NPs due to increased electrostatic attraction and ligand exchange [134]. Although the aged PS NPs were more negatively charged than pristine PS NPs, the enhanced adsorption of aged PS NPs on negatively charged clay minerals (e.g., kaolinite and montmorillonite) was also observed, which was attributed to strong ligand exchange between O-containing functional groups with hydroxyl groups on mineral surfaces [134, 187, 188]. Consequently, the stronger interaction between aged PS NPs and minerals compared to pristine NPs, makes the aged NPs more susceptible to hetero-aggregation, adsorption and co-precipitation with the minerals [134]. Therefore, the photo-oxidation of NPs can enhance or reduce the interaction or hetero-aggregation with natural colloids depending on distinct interfacial interaction, and further affect the aggregation of NPs in complex water media.

However, NPs were unlikely to undergo photo-oxidation alone, as the co-existing natural substances might take part in the photo-oxidation of NPs complex systems. These natural colloids may undergo photo-transformation or affect the photo-oxidation of NPs, and subsequently affect the stability of NPs. For example, HA might compete with NPs for photons and undergo photo-degradation, and the destruction of adsorbed HA increased (in NaCl) or decreased (in CaCl<sub>2</sub>) the aggregation of NPs [83]. However, light irradiation induced the flocculation of BSA molecules that wrapped and integrated NPs, resulting in the formation of large aggregates [83]. Giri et al. observed a significant increase in the hydrodynamic diameter when NPs were photo-oxidized (48 h) with microalgae extracellular polymeric substances (EPS), compared to the case that NPs were aged in the lake water medium alone (without EPS), which was explained by the formation of EPS layer on NPs during the photo-oxidation process [189]. Although the mechanism was not mentioned, the increased particle size might contribute to the hetero-aggregation between NPs and photo-flocculated EPS [83, 190].

### 2.3.3. Transport Behavior in Porous Media

Soil and sediment are not only a sink of MNPs, but may also represent potential sources of MNPs pollution in groundwater systems [60, 191, 192]. The transport and deposition process of MNPs in soil and sediment were commonly studied using porous media transport experiments and quartz crystal microbalance with dissipation (QCM-D) [97, 193-195].

Although no studies have reported this, photo-oxidation of MNPs may decrease the particle size and thus increase its migration into the pore throat of soil and sediment media. Photo-oxidation can also influence the mobility of MNPs in porous media by changing the surface properties of MNPs and hence the interaction between MNPs and soil media [129, 136, 175]. In addition, MNPs in soils are likely to adsorb a variety of contaminants such as OPs, HMs, and ENPs, and affect their transport in soils [43, 196, 197]. As reviewed above, by changing their adsorption capacity towards these contaminants, photo-oxidation of MNPs might increase or reduce the mobility of contaminants.

**Enhanced mobility of MNPs.** Typically, photo-oxidation can increase the mobility of MNPs in porous media [129, 136]. Consistent with the predictions of the classic DLVO theory, Ren et al. demonstrated that photo-aged PS MPs displayed increased mobility in both sandy and clay loam soils, attributed to a more negative charge compared to pristine MPs [129]. The widely used DLVO theory that takes into consideration van der Waals forces and electrostatic interactions, is instrumental in predicting the mobility of charged ENPs in porous media [198, 199]. Unlike common hydrophilic ENPs, such as ZnO [199], TiO<sub>2</sub> [199] and graphene oxide [200]. MNPs exhibit hydrophobic characteristics, and photo-oxidation generally leads to a reduction in their hydrophobic nature [120, 201]. In certain cases, the DLVO theory fails to accurately predict the mobility of MNPs in porous media [136, 202]. Liu et al. indicated that the contribution from increased negative charge was relatively small, whereas photoaging-induced increase in hydrophilicity was the primary cause for the enhanced mobility of PS NPs [136]. Thus, the DLVO theory was less suitable to explain the transport behavior of PS NPs than the XDLVO that considers the hydrophobic effect [136]. Feng et al. observed contrasting effects of photo-oxidation on the transport of two MPs (PE and PTFE) in shore substrates over tidal cycles [202]. Aged PE MPs that were more negatively charged and more hydrophilic compared to pristine MPs, demonstrated greater transport in porous media, aligning with the predictions of both the DLVO and XDLVO theory [202]. Conversely, aged PTFE MPs exhibited enhanced retention in porous media despite a decline in negative charges [202]. This discrepancy was explained with increased surface roughness of aged PTFE MPs [202], but the notable increase in hydrophobicity also suggests that hydrophobic effects might contribute as another potential cause [136]. Hence, although surface charge plays a role, the alteration in other polymer properties after photo-oxidation, particularly hydrophobicity, are of crucial importance. It is essential to consider other non-DLVO interactions when assessing the impact of photo-oxidation on the mobility of MNPs.

The presence of other environmental substances also may affect the mobility of aged MNPs in porous media by influencing the interaction between MNPs and media. The presence of HA in either solution or silica surface inhibited the deposition of PS NPs on the silica surface

mainly due to additional steric repulsion, but this inhibitory effect was weakened after the photo-oxidation of PS NPs [175]. Similarly, photo-oxidation also reduced the promoting effect of DBC on the deposition behavior of PS NPs on silica surfaces due to the weak interaction between DBC and aged PS NPs [175]. The positively charged Fe minerals may enhance the retention of aged MNPs in porous media due to electrostatic attraction and complexation [129, 134], but the actual effect may be related to the content of minerals and the aging degree of MNPs. Although current studies provided important information on the possible effect of natural colloids on the transport of pristine and aged MNPs in porous media, it is still limited to understand the combined effect of photo-oxidation and natural colloids such as NOM, minerals, bacteria, and biofilms on the mobility of MNPs in porous media.

**Mediated transport of contaminants.** MNPs in soils are likely to adsorb a variety of contaminants such as OPs, HMs, and ENPs, and affect their transport in soils [43, 196, 197]. As reviewed above, by altering their adsorption capacity towards contaminants, photo-oxidation of MNPs might alter the mobility of contaminants in porous media. The effects may be distinct for two different cases: (i) MNPs and contaminants coexisted in aquatic media and co-transported, and (ii) MNPs were retained in soil media followed by the introduction of contaminants. In terms of the co-transport case, Liu et al. reported that the photo-oxidation of PS NPs increased the contaminant-mobilizing ability of PS NPs in saturated loamy sand due to increased binding with both nonpolar (pyrene) and polar contaminants (4-nonylphenol) [136]. Considering that photo-oxidation can promote or inhibit the adsorption of OPs depending on various factors, the mobility of OPs may be enhanced or reduced after the photo-oxidation of MNPs, although limited studies have investigated this. Similarly, due to the increase in O-containing functional groups, the promotion effect of UV-aged PS NPs on the transport of Pb(II) and Cd(II) was stronger than that of the pristine NPs [131]. Furthermore, as carriers, aged PS NPs were more capable of freeing HMs retained in porous media [131].

For the case that MNPs were pre-deposited on soil media, Hu et al. found that UV irradiation of PS, PVC and PE MPs enhanced their positive effect on the adsorption of 17 $\beta$ -estradiol in soil, indicating that the input of aged MPs into soil might reduce the mobility of 17 $\beta$ -estradiol by enhancing the adsorption capacity of the soil [203]. Similarly, after being incubated with sediments, aged PE MPs also showed higher retention capacity towards Pb(II) than pristine PE MPs due to enhanced electrostatic attraction [179]. However, photo-oxidation of PLA MPs might increase the mobility of Pb(II) in sediments as aged PLA MPs changed the microbial community in sediments and further altered the zeta potential of the mixture of MPs and sediments [179]. Therefore, the effect of photo-oxidation of MNPs on the mobility of contaminants in porous media may be complex, depending on factors such as transport mode,

polymer type, size and oxidation degree of MNPs, soil properties, and indirect factors like biological effects.

## 2.4. Photochemical Processes With Coexisting Constituents

The photo-oxidation of MNPs involves the direct absorption of specific wavelengths of light energy, leading to the generation of excited states of electrons and alkyl radicals [158]. As the process progresses, produced highly reactive organic radicals such as alkyl, peroxy, alkoxy radicals can facilitate self-catalyzed reactions [158, 204]. In particular, the generation of  $\bullet\text{OH}$  with strong oxidation potential and high electrophilicity further accelerates the photo-oxidation of MNPs [119]. In addition, aromatic MNPs (e.g., PS, PET and PC) are capable of producing an excited triplet state ( $^3\text{MNP}^*$ ) upon exposure to UV radiation [205]. The  $^3\text{MNP}^*$  can transfer energy to dissolved  $\text{O}_2$  and water molecules to produce other ROS such as  $^1\text{O}_2$  and  $\text{O}_2^{\bullet-}$ , accelerating photo-oxidation of aromatic MNPs [201, 205, 206]. However, in the real environments, MNPs do not undergo photo-oxidation in isolation but rather in the presence of various environmental components, such as inorganic ions, natural colloids, and dissolved organic matter (DOM). Under UV irradiation, these co-existing components can also undergo photo-chemical processes, absorbing photons and either consuming or producing ROS [127, 207]. For example, the abundant chromophores in DOM can absorb UV energy, which forms higher energy excited states ( $^3\text{DOM}^*$ ) that can initiate reactions with dissolved oxygen and water molecules, resulting in the production of ROS through energy transfer [208, 209]. Mediating by these photo-chemical processes, the co-existing components can either accelerate or inhibit the photo-oxidation process of MNPs, as illustrated in [Table S3](#) (highlighting critical factors influencing the photo-oxidation of MNPs) and [Figure 2.2](#).

### 2.4.1 Effects of Natural Substances on the Photo-Oxidation of MNPs

Inorganic ions in aquatic environments may influence UV penetration depth and free radical reactions, and thus induce a different degree of photo-oxidation of MNPs [210, 211]. Some studies found that MPs (e.g., PP, PE, and PS) were degraded more efficiently in ultrapure water compared with seawater due to high salt concentrations induce the high refractive index of water and salt crystals formed on MP surfaces [210, 211]. The role of inorganic ions in free radical reactions is still of a matter of dispute. Studies indicated that  $\text{Cl}^-$  can effectively capture  $\bullet\text{OH}$  radicals and inhibit the formation of  $\text{O}_2^{\bullet-}$ , thus weakening the role of ROS in the photo-oxidation of MPs (e.g., PVC and PP) [121, 127]. However, Zhu et al. reported that  $\text{NO}_3^-$ ,  $\text{Br}^-$  and  $\text{Cl}^-$  accelerated the indirect photo-oxidation of PS MPs by reacting with  $^3\text{PS}^*$  to promote the formation of reactive halide radicals and  $\bullet\text{OH}$ ; although  $\text{HCO}_3^-$  scavenged  $\bullet\text{OH}$ ,  $\text{HCO}_3^-$  had no inhibitory effect on PS aging due to the oxidation role of generated  $\text{CO}_3^{\bullet-}$  [124]. The distinct roles of halide ions in the photo-oxidation of MPs may be related to different polymer

types. Halide ions exhibit ROS-scavenging effects that inhibit the photo-oxidation of aliphatic MNPs (e.g., PP, PE, and PVC) [121, 127]. In contrast, for aromatic MNPs (e.g., PS, PET and PC), halide ions can react with the excited state  $^3\text{MNP}^*$ , generating highly reactive halide radicals that promote photo-oxidation and enhance the production of  $\bullet\text{OH}$  [124].

As the main inorganic colloidal component in aquatic environments, natural minerals may take part in the photo-oxidation process of MPs. All reported minerals including kaolinite, montmorillonite, goethite, hematite, and pyrite can promote the photo-oxidation of MPs [122, 150, 212], but mechanisms are distinct. The presence of kaolinite and montmorillonite could stabilize the MP radical cations and prevent their recombination with hydrated electrons, thus promoting the generation of  $\bullet\text{OH}$  and photo-degradation of PVC and PET MPs [122]. Under UV irradiation, the surface Fe(II) phases of goethite and hematite could catalyze the generation of  $\text{H}_2\text{O}_2$  and  $\text{Fe}^{2+}$ , leading to the initiation of the light-driven Fenton reaction [150]. This process produced a large amount of  $\bullet\text{OH}$  and accelerated the photo-oxidation of PP and PE MPs [150]. Similarly, the photo-oxidation of PS MPs and the transformation of intermediates were accelerated in the presence of pyrite due to the generation of ROS, especially  $\bullet\text{OH}$  [212].

DOM which contains chromophores such as carbonyl, carboxyl, hydroxyl, and benzene rings, serves as important photosensitizers in natural waters [213, 214]. There is a dispute regarding the influence of DOM on the photo-oxidation of MNPs. As both ROS scavengers (e.g.,  $\bullet\text{OH}$  and  $\text{O}_2^{\bullet-}$ ) and optical light filters, humic acid (HA) and fulvic acid (FA) were reported to inhibit the photo-oxidation of PP MPs [126]. The aging process of PS MPs was accelerated in the presence of HA and FA [121, 184], and FA exhibited a more significant promoting effect than HA due to their more active carboxyl structure that produce more  $\bullet\text{OH}$  [215]. However, Cao et al. indicated that HA/FA accelerated the photoaging of aliphatic PP MPs due to the generation of  $\bullet\text{OH}$  by DOM photosensitization, while it inhibited or had only a minor effect on the photo-oxidation of aromatic PS and PC MPs/NPs [216]. The explanation provided was that PS NPs with large SSA can adsorb sufficient DOM via  $\pi$ - $\pi$  interactions, delaying photoaging by competing for photon absorption sites, while released phenolic compounds from aromatic MPs weaken the photoaging process by quenching  $\bullet\text{OH}$  [216]. While largely unclear, the varying impacts of DOM on the photo-oxidation of MNPs might be related to DOM photosensitization and light shielding ability, which can be influenced by molecular characteristics of DOM and adsorption extent of DOM on MNPs. Therefore, the physico-chemical properties of MNPs (e.g., size, type, hydrophobicity, and crystal structure) and DOM (e.g., molecular weight distribution, hydrophobicity and functional groups) potentially determine the role of DOM in the photo-oxidation of MNPs.

Therefore, MNPs not only undergo the photo-oxidation process but also interact with a wide range of environmental components that may affect their photo-reactivity in different ways. Depending on their specific roles, these constituents may either act as inhibitors, impeding the photo-oxidation of MNPs, or promoters, accelerating it. The dual nature of their impact is contingent on whether they function as scavengers, competing for photons or ROS, or as photosensitizers, actively promoting the generation of ROS during the photo-oxidation of MNPs. This intricate interplay underscores the complexity of the environmental factors that modulate the photo-degradation of MNPs. Notably, most studies studied the photo-oxidation of MNPs under controlled conditions that can provide valuable insights into the mechanisms involved, but it may not fully reflect the complex interactions and photo-transformations that occur in real-world environments.

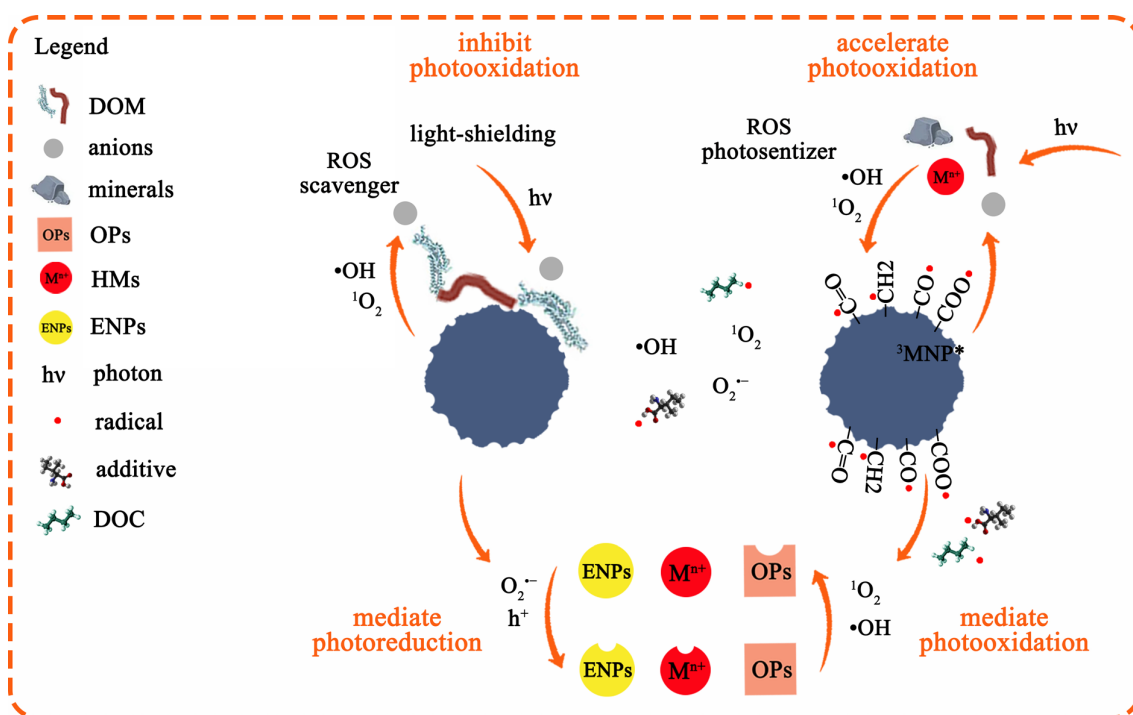


**Figure 2.2.** The photochemical processes of MNPs with co-existing natural constituents and pollutants.

#### 2.4.2. Effects of MNPs on the Photochemical Transformations of Other Contaminants

When exposed to sunlight, OPs can undergo spontaneous photo-transformation, representing an important process of their attenuation in natural waters [217]. The mechanism is direct photolysis and indirect photo-transformation induced by environmental components, such as anions, cations, and DOM. The reactive intermediates such as <sup>3</sup>DOM\* and ROS generated from this photosensitization process can participate in the photo-degradation of OPs [218-220].

On the one hand, MNPs that usually show good optical absorption characteristics, may compete for photons with OPs and thus inhibit the direct photolysis of OPs due to the light screening/shielding (see [Table S4](#) for details on the role of MNPs in the photo-transformation of pollutants) [137, 154, 221, 222]. On the other hand, MNPs can also take part in the indirect photo-transformation of OPs by generating ESPRs, ROS and  $^3\text{MNP}^*$  and by providing more surfaces for pollutant adsorption and photo-reactions (Table S4). For example, Zhang et al. reported that the degradation of sulfamethoxazole (SMX) was decreased in the presence PS MPs and even more so in the presence of aged PS MPs [137], as the optical absorption capacity of PS MPs gradually increased with the photo-aging time after the formation of new chromophores, such as carbonyl groups and conjugated double bonds [137]. Additional studies also noted that the presence of photo-aged MNPs resulted in decreased degradation of OPs compared to pristine ones [138, 154, 222, 223]. However, most studies reported that MNPs had a promoting effect on the photo-oxidation of OPs [153, 222, 224-227]. Wang et al. indicated that the photo-degradation efficiency of atorvastatin (ATV) increased from 19.82% to 50.27% in the presence of 0.01 g/L and 0.5 g/L PS MPs, respectively [226].  $^1\text{O}_2$  generated from photosensitization of PS MPs was the main reason; besides, the role of  $^3\text{PS}^*$  became important in the presence of aged MPs because  $^1\text{O}_2$  can be generated from the  $^3\text{PS}^*$  [226]. The light-screening and photosensitization effects induced by MNPs can occur simultaneously, where the former inhibits the direct photo-degradation of pollutants, while the latter promotes indirect photo-degradation [221]. The MNPs-mediated photo-transformation of OPs may differ depending on the properties of OPs. Wang et al. reported that the catalytic effect of MPs was strongly dependent on the electron-donating ability of functional groups of OPs [227]. Additionally, different types of MNPs also have a different effect on the photo-transformation of pollutants. The photolysis of 2,2',4,4'-tetrabromodiphenyl ether was inhibited by aged PS MPs compared with pristine ones as the aged PS caused more light-shielding effect, while aged PP and PE increased pollutant degradation because the fragmentation of aged MPs provided more contact surfaces for pollutants and light [154].

The photo-oxidation of MNPs can also mediate the oxidation or reduction of HMs (Table S4). Up to now, limited publications have studied the photo-transformation of HMs in the presence of MPs. On the one hand, the photo-reduction of HMs (e.g., Cr(VI) and Ag(I)) was accelerated in the presence of MNPs by processes such as  $\text{O}_2^{\bullet-}$  production [139, 228, 229], or electron shuttling by carbonyl groups on oxidized MPs [229]. On the other hand, the photo-oxidation of certain HMs such as Mn(II) can be accelerated in the presence of MNPs due to the generation of  $\text{ROO}^\bullet$  and  $\text{O}_2^{\bullet-}$  radicals [230]. The photo-oxidation of MNPs can also induce the dissolution of ENPs, such as nano-Ag and nano-ZnO [140, 141], due to the generation of  $^1\text{O}_2$ ,  $\bullet\text{OH}$ , and/or acid release [141]. Simultaneously, reductive  $\text{O}_2^{\bullet-}$  could also reduce the released Ag(I) to

secondary nano-Ag [141]. It is important to note that the role of photo-oxidation in the transformation of metal and metalloid species is reversible and interchangeable, likely depending on the redox potential of the system. These findings highlight the complex interplay between photo-oxidation processes and the fate of MNPs and associated contaminants in environmental systems.

## 2.5. Biological Effects of Photoaged MNPs

### 2.5.1. Toxicity to Aquatic Organisms

**Enhanced or reduced toxicity of MNPs.** The toxicity of MNPs to aquatic organisms in environments can be changed after the photo-oxidation (see [Figure 2.3](#) and [Table S5](#) for details on the biological effects of photo-oxidized MNPs on organisms and microbes). The majority of the studies (6 out of 8 publications) reported that the photo-aging of MNPs can enhance their biological toxicity, mainly originating from four reasons: (i) the fragmentation of MNPs after photo-degradation can generate smaller-sized particles with an irregular shape, which enhance the toxicity of MNPs to organisms due to size and surface area effects. These small particles can be ingested and bio-accumulated in organisms through sorption, endocytosis, and phagocytosis compared to virgin MPs [148, 231, 232]. In addition, these fragments with larger surface roughness and surface-specific area show higher affinity to the tissues and cells and restrained the nutrients absorbed into the cells [232, 233]. (ii) The photo-aging of MNPs can enhance the surface O-containing functional groups and negative charges, which may increase the interaction between MPs and proteins in biota via hydrogen bonding and electrostatic interaction [233, 234]. (iii) Aged MNPs can also result in more oxidative stress due to the generation of EPFRs and ROS [235-237], which led to higher cytotoxicity compared to pristine ones [238]. (iv) The enhanced toxicity of photo-aged MNPs to organisms may be attributed to the leachates including additives and MNP-derived intermediates [37, 239, 240]. The bioaccumulation of the leached endogenous toxicants (mainly phthalates) from photodegraded PS MPs contributed to the exacerbated hepatotoxicity of Grouper [236]. Luo et al. demonstrated that longer radiation time led to more release of Cr and Pb from commercial lead chromate pigmented MPs, exhibiting more inhibitory effects on the cell growth and photosynthesis of *Microcystis aeruginosa* [241].

However, few studies concluded the opposite results that photo-oxidation could alleviate the toxicity of MNPs to organisms [189, 235]. Zou et al. indicated that pristine small-sized PA MPs (8.13  $\mu\text{m}$ ) with a high aggregation potential tended to accumulate in organisms, while photo-aged ones with higher stability were more easily to be excreted by zebrafish larvae [235]. Such a distinct result may be also related to the larger particle size of pristine MPs, which were easily intercepted by the intestinal villi and difficult to be excreted directly by the larvae [231].

However, Giri et al. found that the UV radiation significantly enhanced the hydrodynamic size of PS NPs in media containing EPS due to photo-induced agglomeration of PS NPs and EPS, and this mitigated the toxic effects of PS NPs on freshwater microalgae [189].

Therefore, size and surface area effects, the formation of O-containing groups, the generation of EPFRs, and the leachates from photo-oxidized MNPs are responsible for their higher biotoxicity compared to pristine ones but there are cases where size changes explain the lower toxicity of photoaged MNPs. In real environments, the bio-toxicity change of aged MNPs may result from a combination of multiple causes [231, 232, 236], and can also be affected by the co-existing environmental substrates.

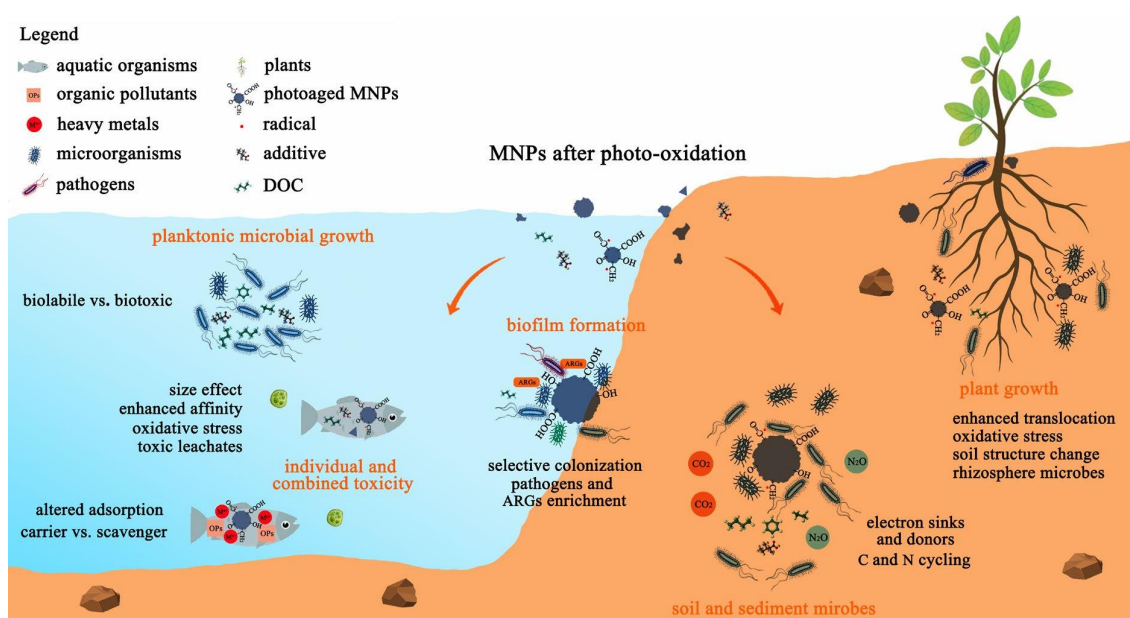


Figure 2.3. Biological effects of MNPs after photo-oxidation.

**Combined toxicity with environmental contaminants.** As vectors for environmental contaminants, MNPs can affect their migration and bioaccumulation in organisms via ingestion [242, 243]. The photo-oxidation can change the interaction between MNPs and contaminants by surface modification, which may further affect their combined risk in environments. Several studies have investigated the effect of photo-oxidation on the combined toxicity of MNPs and pollutants, such as HMs, OPs, and ENPs to organisms. Studies indicated that aged MPs can decrease the bioavailability of coexisting HMs ( $\text{Cu}^{2+}$  and  $\text{Cd}^{2+}$ ) to microalgae *C. vulgaris* due to their strong adsorption capacity towards HMs [234, 244]. Another reason for decreased bioavailability may be that photo-oxidation increased the aggregation and sedimentation of MPs with HMs, and reduced the concentration of HMs and MPs in the aquatic phase, thus

limiting their inhibitory effect on organisms [244, 245]. The opposite results were reported in terms of the combined toxicity of MNPs and metal nanoparticles, such as nano-ZnO and nano-Ag [140, 141]. PS MNPs increased the sunlight-induced dissolution of nanoparticles, and served as vectors for dissolved metal ions, significantly increasing the ion-related toxicity of nanoparticles [140, 141].

However, cases can be complicated for the combined effect of OPs and MNPs after photo-oxidation due to the different role of MNPs (carrier vs. scavenger) in the bioaccumulation of OPs, as well as possible increase or decrease in the adsorption capacity of aged MNPs towards OPs [166, 170, 177]. On the one hand, MNPs can facilitate the mobility of OPs, and photo-oxidation enhance or reduce the bioaccumulation of OPs depending on the changed adsorption capacity [246, 247]. For example, the stress of tilapia caused by PS MPs and propranolol (PRP) was alleviated while that by MPs and sulfamethoxazole (SMX) was exacerbated after photo-oxidation of MPs, as aged MPs adsorbed less PRP but more SMX compared to pristine ones [247]. On the other hand, pristine or aged MNPs may serve as a scavenger for OPs, reducing their bio-uptake [248]. Kim et al. suggested that the aged PE MPs reduced the toxicity of BAC<sub>12</sub> but enhanced the toxicity of BAC<sub>16</sub> as the adsorption of BAC<sub>12</sub> was increased but that of relatively hydrophobic BAC<sub>16</sub> was decreased after the aging of MPs [135].

Therefore, the effect of photo-oxidation on the combined toxicity of MNPs and contaminants depends on both the roles of MNPs as carrier or scavenger, and adsorption capacity of pristine/photoaged MNPs. If MNPs act as carriers, the toxicity resulting from the combined effect of MNPs and contaminants is positively linked to the contaminants' adsorption capacity on pristine/photo-aged MNPs. Conversely, if MNPs act as scavengers, the combined toxicity is inversely related to the contaminants' adsorption capacity on pristine/photo-aged MNPs. However, whether and how photo-oxidation can affect the combined toxicity of MNPs and contaminants needs to be studied in more detail. Current studies lack a consistent approach to assess these effects, and the results may be distinct given the polymer type, size, and the aging degree of MNPs. Moreover, in addition to altering the interaction between MNPs and contaminants and bioaccumulation, photo-oxidation may also affect the chemical transformation of these contaminants. Thus, knowledge regarding the possible role of photochemical effects is needed to understand the ecological risks of co-existed MPs and pollutants in the environment.

### 2.5.2. Effects on Microorganisms

**Biofilm formation.** Biofilm can be formed on the surface of MPs due to the accumulation of a large number of microbial communities in the aquatic environment [44, 249]. MP biofilm is

distinctive and considered a new ecological niche, influenced by MP surface characteristics and the surrounding environmental matrix [250, 251]. As an important process modifying the surface properties of MPs, photo-oxidation has been studied to affect the formation of biofilm and microbial community composition. Due to the increase in surface roughness and SSA, aged MPs were more conducive to microbial adhesion [252, 253]. The formation of O-containing groups and increased hydrophilicity of MPs after photo-oxidation also may select hydrophilic microorganisms to colonize [142]. Additionally, the leaching of degraded polymer from photo-aged MPs as a carbon source, as well as the enhanced adsorption of nutrients may affect the colonization of microorganisms [44, 250]. Studies indicated that the total biomass, detected operational taxonomic unit (OTU) number and  $\alpha$  diversity of biofilm communities increased with the aging of MPs [254, 255], and the relative abundance of some families of the microbial community is significantly altered after the aging treatment of MPs [142, 254, 256]. Simultaneously, the genes associated with the biofilm formation were reported to be significantly expressed in photo-aged MPs [255]. In addition to providing novel substrates for biofilm formation, MPs can potentially facilitate the enrichment and spread of antibiotic-resistance genes (ARGs) and opportunistic human pathogens [257, 258]. Compared with pristine MPs, photo-aged PS MPs enhanced selective ARG enrichment and ARG transfer due to increased proximal ARG donor-recipient adsorption and release of chemicals from MPs [246, 259]. Shan et al. suggested that photo-aged PP MPs were more conducive to the expression of genes related to human pathogens [254], while the abundance of pathogen-related genes decreased with the aging of PE and PVC MPs [255]. Different polymer types and photo-oxidation conditions may be the reason for the inconsistent results. Although these studies provide important information on the potential ecological and health risks of biofilm on aged MPs in aquatic ecosystems, detailed mechanisms underlying them remain to be determined.

**DOC leaching and planktonic microbial growth.** MNPs are likely to contribute to the DOC pool in aquatic environments via leaching [143]. Although plastic-fragments do leach DOC in the dark, light irradiation can stimulate the release of the plastic-derived DOC at levels more than 10 times higher than in the dark [260-262]. The leached DOC from photo-oxidized MNPs shows low molecular weight and varies depending on polymer type [144, 260, 263]. Plastic-derived DOC usually shows high lability and bioavailability [144, 262, 263]. The bioavailability of the leached DOC depends on the plastic source and type [262]. Among the post-consumer plastics, the bioavailability of ePS DOC (disposable lunch box) was the highest ( $76 \pm 8\%$ ), followed by PP DOC (facial cleanser bottle) ( $59 \pm 8\%$ ) and PE DOC (shampoo bottle) ( $46 \pm 8\%$ ) [262]. Similarly, leached DOC from plastic shopping bags was chemically distinct and more bioavailable than NOM in lakes [144]. However, Romera-Castillo et al. reported that the

bioavailable fraction of the leached DOC under artificial solar radiation was (insignificantly) lower than that in the dark ( $55\% \pm 5\%$  in the light treatments vs.  $61\% \pm 3\%$  in the dark). They observed a lower bacterial abundance in the light treatments, which was explained by the possible generation of microbial inhibitors like ROS [143]. In addition, harmful additives may be a source of the inhibitory effect of DOC [262]. The harmful additives in the leachates from high-density PE (HDPE) bags and PVC matting were reported to strongly inhibit the growth of *Prochlorococcus* and photosynthetic capacity [264]. Sheridan also suggested that high plastic leachate concentrations may further impair bacterial growth due to large quantities of toxic compounds (e.g., oxybenzone) [144]. Therefore, the plastic leachates after photo-oxidation can be biolabile or biotoxic, and how planktonic microbes respond to plastic leachates depends on their source and level, as well as the capacity of local microbial communities to utilize these leachates.

**Changing microbial communities in soil and sediment.** Soil and sediment are major sinks of MNPs in aquatic and terrestrial ecosystems [265]. As the primary life forms in soil and sediment systems, the microorganism is the main participator in many biogeochemical processes such as organic matter mineralization and nutrient cycling [265, 266]. The greatest attention has focused on the effect of MNPs on the microbial community and function in soil and sediment systems, including microbial growth and viability [267], microbial activity and enzyme activity [268, 269], community structure and function [270-275]. Indirect mechanisms of these impacts come from changes in soil physicochemical parameters, including bulk density [276], porosity [277], soil aggregation [278-280], water-holding capacity [281, 282] and pH [266, 279]. Direct interactions of MNPs with soil and sediment microorganisms are related to biofilm formation on MP surface [268, 283], plastic leachate impact [270], ROS-induced oxidative stress [284], and combined impacts with other chemicals [285, 286]. The photo-oxidation of MNPs generally alters surface properties [142], leaching of toxic substances and DOC [144, 262], and ROS production [143], and subsequently changes their stability [128, 132] and mobility [129, 136], adsorption [166, 168] and transformations of contaminants [154]. These effects of photoaged MNPs potentially lead to distinct alterations in microbial community and activity, although the specific response of soil characteristics and microorganisms to the photo-oxidation of MNPs remains largely unclear [146, 287].

For example, Liu et al. reported the photo-aged tire wear particles (TWPs) were more toxic than pristine TWPs, which is attributed to the increased adsorption of released heavy metals due to the increase in specific surface area and the transition of positive to negative charge after photo-oxidation [287]. The high levels of ROS produced by photoaged MNPs may induce oxidative stress in cells and subsequently suppress enzyme activity [288-290]. Despite enzymes like superoxide dismutase, catalase, and peroxidase can scavenge ROS [291],

research indicated that high ROS levels from UV-aged MPs may induce structural changes and denaturation in functional enzymes [292], suppressing soil microbial enzyme activity (e.g., fluorescein diacetate hydrolase) [146]. The polymer degradation byproducts from the aged MPs can be metabolized as substrates for specific microorganisms, which may result in a shift in microbial community composition [146]. Aged PP and PS microfibers were shown to reduce the abundance of *Sphingomonadales* (oligotrophic bacteria) and increase the abundance of *Burkholderiales* (eutrophic bacteria) in soil compared with pristine MPs [146], potentially due to the restriction of the growth rate of oligotrophs by eutrophs [293]. Furthermore, the photoaged MNPs may affect microbial metabolism processes such as carbon and nitrogen cycling. Chen et al. suggested that pristine PS MPs inhibited sediment bioavailability and CO<sub>2</sub> emission, but this effect was decreased with the aging of MPs, which was explained by the utilization of DOC by sediment microbes as the carbon source to promote organic carbon mineralization [145]. Rillig et al. speculated that aged MPs contain O-containing functional groups (e.g., ketones) that are redox active, which may serve as electron sinks and donors for microbes, and increase microbial metabolism efficiency [294]. Although photo-aged PE MPs did not significantly influence soil CO<sub>2</sub> and N<sub>2</sub>O emissions compared with pristine MPs, aged MPs significantly increased soil NO<sub>3</sub><sup>-</sup> content and amoA gene abundance [295]. It indicated that aged PE may increase the nitrification rate and then provide more substrates for denitrification, potentially increasing the emission of soil N<sub>2</sub>O [295, 296]. Although several studies provided some insights on the effects of photo-oxidation of MNPs on microbial community and function in soil and sediment, the processes and mechanisms are complicated and depend on various factors such as plastic properties, aging degree, and local microorganisms.

### 2.5.3. Potential Impacts on Plants

While the risks of MNPs to aquatic and terrestrial plants have been extensively documented [297, 298], the potential impacts of photo-aged MNPs on plants remain largely unexplored, and there is a dearth of information in this regard. The direct impacts of MNPs on plants include blockage of cell connections or pores in the cell wall [299, 300], and the uptake, translocation, and accumulation in different plant parts such as roots, shoots, and leaves [301, 302]. The translocation of MNPs potentially posing toxic effects on various physiological and biochemical processes in plants, including inhibition of seed germination and plant development, biomass reduction, disruption of photosynthesis, oxidative damage, and genotoxicity [299, 303, 304]. Surface properties (e.g., particle size, charge, and hydrophobicity) of MNPs play vital roles in the translocation of MNPs [303]. Smaller sizes of MNPs increase the likelihood of entering seed pores and obstructing voids [299], and facilitating translocation in the vascular system and the cell walls of root tissues [301, 302]. Besides, the translocation of MNPs within the

plant appears to favor negatively charged particles, likely attributed to electrostatic repulsions between MNPs and the electronegative cell walls [305, 306]. The translocation within plants could also be influenced by the aggregation states of MNPs [307]. For instance, the growth medium and root exudates promoted the formation of large aggregates, restricting the uptake of positively charged PS NPs; conversely, negatively charged NPs tended to remain stable and can penetrate into root tissues [307]. As discussed in sections 2.3.2 and 2.3.3, the typically more negative charges, hydrophilic nature, and smaller size contribute to the higher stability and mobility of photoaged MNPs in water and soil media compared to pristine ones [128, 129]. It can be expected that the photo-oxidation has the potential to increase the uptake and translocation of MNPs by plants, thereby inducing more adverse effects.

Apart from the physical blockage that can potentially inhibit water and nutrient adsorption [299, 300, 308], the physiological and biochemical responses of plants after MNPs exposure may arise from plastic leachates [309], and oxidative stress [300, 310]. For instance, Pflugmacher et al. highlighted the considerable toxicity of plastic leachates that induced a 77% decrease in the plant germination rate [309]. Therefore, the photoaging can increase the leaching of toxic additives [311, 312], potentially leading to adverse effects on plants. Besides, serving as scavengers or carriers of environmental pollutants [166, 170, 177], the photoaged MNPs may exert distinct impacts on plant growth in contaminated soils. The excessive ingestion of MNPs by plants can also lead to the production of ROS, causing irreversible damage to plant tissue and disrupting photosynthesis [299, 304, 307]. Photoaged MNPs may induce more oxidative stress as they can produce more ROS or EPFRs [313, 314], which exhibit specific toxicological properties, such as DNA damage, lipid peroxidation, protein oxidation, and inflammation [313, 315]. Although not previously reported, it is plausible that photoaged MNPs may result in more toxic effects through these chemical mechanisms.

Indirect impacts of MNPs on plants may also occur through alterations in soil physico-chemical characteristics, such as pH [279], water holding capacity [281, 282], and soil structure [278-280], as well as soil-dwelling microbes [281, 298]. Boots et al. indicated that the presence of HDPE MPs reduced the root growth of *Lolium perenne*, potentially attributed to the changes in soil pH and the size distribution of water-stable soil aggregates [279]. Due to the formation of hydrophilic O-containing functional groups and DOC leaching, the photoaged MNPs potentially increase water and organic matter content, pH and cation exchange ability in soils [316, 317]. These effects can indirectly impact plant growth such as seed germination and root growth [281, 318, 319]. Furthermore, these changes in soil characteristics may impact soil fertility by influencing the growth of microbial communities in the rhizosphere—a crucial interface where plants interact with soil microorganisms [319-321]. Recent findings suggested that polyester MPs enhanced microbial activity in both bulk soil and the rhizosphere [281].

Additionally, the treatment with polyester promoted soil microbe colonization on spring onion roots, and the potential mycorrhizal symbiosis may facilitate the growth of plants subjected to polyester [281]. The introduction of photo-oxidized MNPs into the soil adds another layer of complexity. They may exert distinct effects on soil microbial communities, which play a crucial role in plant-microbe interactions, and nutrient cycling and availability, potentially influencing plant health. In conclusion, our understanding of the potential risks of pristine and photoaged MNPs to plant ecosystems is currently limited, necessitating further comprehensive research.

## 2.6. Future Perspectives

**Relate the adsorption capacity of MNPs to the photo-oxidation degree and the physico-chemical properties of pollutants.** Increasing studies have evaluated the effect of photo-oxidation of MNPs on their adsorption capacity toward contaminants, especially OPs. Generally, the photo-oxidation of MNPs may enhance the adsorption of hydrophobic OPs and reduce the adsorption of hydrophilic OPs due to enhanced O-containing functional groups [174, 176]. However, in some cases, it is complex and depends on many factors including polymer types of MNPs, oxidation degree and physicochemical properties of OPs [166, 170, 177]. There is a lack of knowledge to evaluate the effects of the photo-oxidation degree and the physicochemical properties of OPs on their adsorption processes on MNPs. Integrating experimental data with advanced analytical methods, such as molecular dynamic simulations [322], and machine learning [323, 324], offers a comprehensive approach for understanding the adsorption mechanism of MNPs after photo-oxidation, and establish the multi-dimensional relationship between the adsorption capacity of MNPs, the photo-oxidation degree (e.g., the carbonyl index and hydroxyl index, and the physico-chemical properties of pollutants (e.g., molecular weight, log  $K_{ow}$ , zeta potential, type and number of functional groups).

**Study the combined effect of photo-oxidation and natural colloids on the fate of MNPs.** The stability and mobility of MNPs in water and porous media are well reported to be influenced by the photo-oxidation process and co-existing natural colloids. However, in real-world environments, the effect of photo-oxidation and natural colloids can co-exist. On the one hand, the photo-oxidation of MNPs may change their interaction with natural colloids (e.g., NOM, minerals and bacteria), and these colloids may have different effects on the stability and mobility of pristine and aged MNPs [83, 133, 175]. On the other hand, MNPs are unlikely to undergo photo-oxidation alone, and the presence of natural colloids may take part in the photo-oxidation of MNPs and further affect the stability and mobility of MNPs in environments [122, 150, 212]. More work is needed to better understand the combined effect of the photo-oxidation process and natural colloids on the fate of MNPs in aquatic and terrestrial environments. A well-structured experiment combining photo-oxidation with environmental

transport and fate studies can be complemented by state-of-the-art particle detection techniques such as dynamic light scattering, nanoparticle tracking analysis, in-situ microscopy, and Fourier Transform Infrared Spectroscopy (FTIR), as well as ROS detection techniques like electron paramagnetic resonance spectroscopy.

[Link the photochemical transformation of pollutants in the presence of MNPs to the physicochemical properties of pollutants.](#) By generating ESPRs and ROS or light-screening effect, the coexisting MNPs may promote or inhibit the photo-transformation of OPs. Although the promoting and inhibitory mechanisms have been studied for several OPs, the reasons why MNPs play different roles in the photo-transformation of different types of OPs are unclear. In fact, the adsorption and photo-transformation of OPs can occur simultaneously, and the chemical structure of OPs and the adsorption process may contribute to the distinct effect of MNPs on the photo-degradation of OPs [227]. Limited studies have considered the relationship between adsorption and photo-degradation of OPs in the presence of MNPs. Thus, more research should associate the physicochemical characteristics of OPs such as hydrophobicity, electronegativity, and functional groups with their photo-transformation process in the presence of MNPs, potentially utilizing molecular dynamic simulations [325], and machine learning [326, 327].

[Pay attention to the effect of photoaged MNPs on the biotransformation of pollutants.](#) As reviewed, the photo-oxidation of MNPs significantly influences the physical adsorption and photochemical transformation of environmental pollutants. However, apart from the physicochemical process, microbial biotransformation of pollutants such OPs and HMs under aerobic or anaerobic conditions is also critical [328, 329]. Like the role of DOM in the biotransformation of pollutants [330-332], the photo-oxidation of MNPs is likely to affect the biotransformation of pollutants via several mechanisms: (1) the photo-oxidation may change the adsorption capacity of MNPs toward pollutants, and alter their bioavailability by microorganisms [333], (2) the high lability and bioavailability of DOC from oxidized MNPs may promote the co-metabolic transformation of OPs [144, 262], and (3) photo-aged MPs or intermediates containing redox-active functional groups may serve as electron sinks and donors for microbes, and mediate the biotransformation of pollutants [294, 330]. So far, there has been no research on this topic, which should be paid more attention to in the future. There is potential for comprehensive investigations combining microcosm studies with advanced techniques such as metabolomics, proteomics, mass spectrometry, and electron paramagnetic resonance spectroscopy, to quantitatively assess the metabolism processes of OPs under the impact of photoaged MNPs.

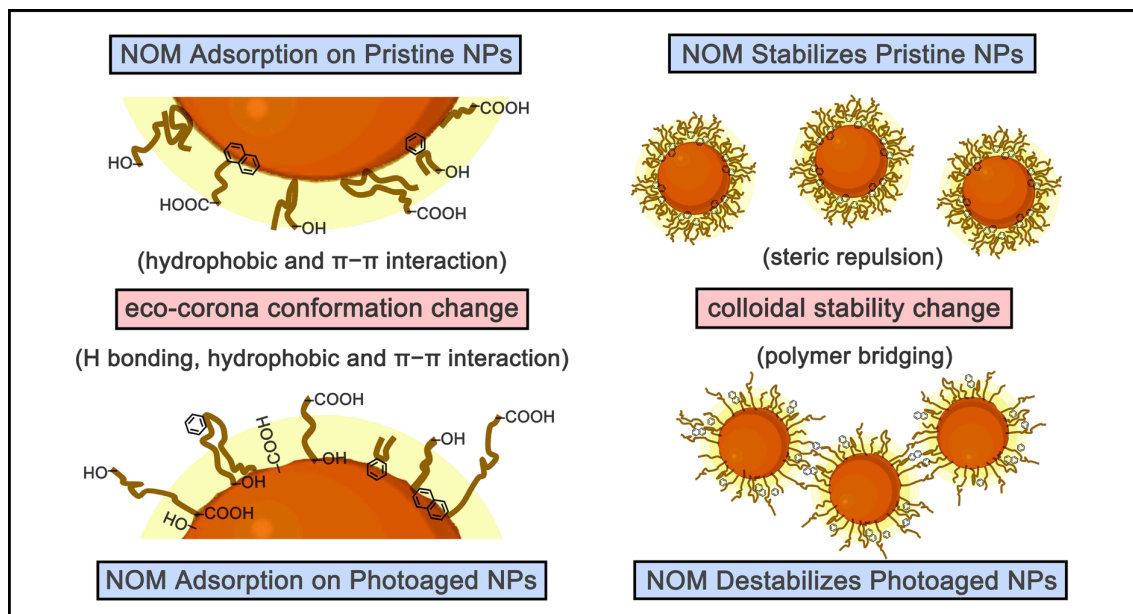
---

**Focus on the interaction between photoaged MNPs and plants.** The interaction between plants and MNPs is an emerging area of study with ecological importance. While the impacts of MNPs on plants have been explored to some extent, the effects of photo-oxidation on these impacts remain unclear. Techniques such as confocal microscopy and FTIR imaging spectroscopy holds the potential to detect the interactions between photoaged MNPs and plants, allowing for the visualization of spatial distribution and potential impacts [334]. Additionally, advanced analytical methods like metagenomes and proteomics, coupled with plant physiology and biochemistry analyses and staining techniques, can be employed to probe the intricate biological responses of both plants and rhizosphere microbes when exposed to photoaged MNPs. Moreover, exploring plant interactions with pristine/weathered MNPs holds promise for addressing the adverse impacts of plastic contamination, contributing to the development of strategies for a cleaner and healthier planet.



# Chapter 3

## Natural Organic Matter Stabilizes Pristine Nanoplastics but Destabilizes Photochemical Weathered Nanoplastics in Monovalent Electrolyte Solutions



This Chapter is based on

Xu, Y.; Wang, X.; van der Hoek, J. P.; Liu, G.; Lompe, K. M., Natural Organic Matter Stabilizes Pristine Nanoplastics but Destabilizes Photochemical Weathered Nanoplastics in Monovalent Electrolyte Solutions. *Environ Sci Technol* 2025, 59, (3), 1822–1834.

## Abstract

Photochemical weathering and eco-corona formation through NOM adsorption play vital roles in the aggregation tendencies of NPs in aquatic environments. However, it remains unclear how photochemical weathering alters the adsorption patterns of NOM and the conformation of the eco-corona, subsequently affecting the aggregation tendencies of NPs. This study examined the effect of Suwannee River NOM adsorption on the aggregation kinetics of pristine and photoaged PS NPs in monovalent electrolyte solutions. The results showed that photochemical weathering influenced the conformation of the eco-corona, which, in turn, determined NP stability in the presence of NOM. Hydrophobic components of NOM predominantly bound to pristine NPs through hydrophobic and  $\pi$ - $\pi$  interactions, and extended hydrophilic segments in water hindered NP aggregation via steric repulsion. Conversely, hydrogen bonding facilitated the binding of these hydrophilic segments to multiple photoaged NPs, thereby destabilizing them through polymer bridging. Additionally, the stabilization and destabilization capacity of NOM increased with its concentration and molecular weight (MW). These findings shed light on the destabilizing role of NOM on weathered NPs, offering new perspectives on environmental colloidal chemistry and the fate of NPs in complex aquatic environments.

## 3.1. Introduction

The extensive production and widespread use of plastics contribute substantially to the accumulation of plastic debris in aquatic ecosystems, comprising a substantial portion of marine litter, ranging from 60% to 80% [43, 335-337]. Over time, these plastic materials undergo a series of processes such as chemical degradation, biodegradation, photodegradation, thermal degradation, and mechanical abrasion, breaking them down into minute particles at the nanoscale ( $< 1 \mu\text{m}$ ) termed as NPs [43, 130, 338-340]. Once entering the aquatic environment, NPs may be exposed to a series of physicochemical processes, such as sunlight-induced photooxidation [128], aggregation [82, 341], deposition [97, 136] and adsorption [134, 342], which are closely linked to their fate, bioavailability, and biotoxicity [43, 343].

The colloidal stability and aggregation tendencies of NPs have emerged as a recent focal point of research interest, often drawing insights from the chemistry of other colloids such as natural colloids and engineered  $\text{TiO}_2$  nanoparticles [344, 345]. The aggregation or flocculation of colloids is typically controlled by soluble polymers, such as engineered synthetic polymers like polyethylene glycol and polyacrylamide [346, 347]. Similarly, in environmental systems, natural polymer such as natural organic matter (NOM) plays a vital role in the aggregation of colloids and nanoparticles [348]. The role of soluble polymers in the aggregation of

nanoparticles is often studied in monovalent electrolyte solutions [188, 349, 350]. These soluble polymers can induce either attractive or repulsive interactions depending on their adsorption capacity on the nanoparticle surface [346]. If the polymer fails to adsorb onto the nanoparticle surface, the exclusion of polymers from the space between the nanoparticles can create osmotic forces known as depletion attractions, which push larger nanoparticles together and promote their aggregation [351]. On the other hand, if the polymer fully coats the nanoparticle surface, it can stabilize the nanoparticles through steric repulsion [349]. However, if the added polymer adheres to the colloid surface, various segments of the same polymer may attach to different nanoparticles, leading to particle aggregation via polymer bridging [348]. In environmental systems, the stabilization of nanoparticles by NOM through steric repulsion typically occurs [188, 350], while destabilization via depletion attraction or polymer bridging is less observed [175, 352-354]. One study demonstrated that citrate-stabilized Au nanoparticles were destabilized by fulvic acid (FA) via bridging flocculation driven by hydrophobic interactions between adsorbed FA molecules [354]. In some cases, destabilization of nanoparticles by NOM might occur via electrostatic patch-charge attraction if the nanoparticles (e.g., ferrihydrite and TiO<sub>2</sub>) and NOM have opposite charges [355, 356], and via cation bridging in the presence of multivalent cations, such as calcium ions [357, 358].

NOM, an ubiquitous natural polymer in aquatic environments, consists of heterogeneous organic compounds, including humic acids (HA), FA, proteins, and polysaccharides [65, 359]. NPs and NOM in environments can interact through diverse attractions such as van der Waals interactions, electrostatic interactions, hydrophobic interactions, hydrogen bonding, and  $\pi$ - $\pi$  interactions [83, 360]. The adsorption of NOM on NPs often results in the formation of an organic coating on the NP surface, referred to as an eco-corona [80]. This eco-corona can alter the physicochemical properties of NPs, affecting their aggregation behaviors in aquatic environments [65]. The eco-corona often enhances the stability of NPs in monovalent electrolyte solutions, primarily due to steric repulsion [81-83]. Photochemical weathering is another key process that modifies the surface of NPs, typically rendering them more hydrophilic and negatively charged [136, 148]. By altering the interactions between NOM and NPs, photochemical weathering can influence the formation and characteristics of the eco-corona [360]. Using a quartz crystal microbalance with dissipation, a study indicated that photochemical weathering decreased the adsorbed mass of HA, FA, and Suwannee River NOM on plastic surfaces in synthetic freshwater [360]. Additionally, studies demonstrated that photooxidation resulted in a decrease in the hydrophobic and  $\pi$ - $\pi$  interactions between PS NPs and HA, consequently weakening the stabilization capacity of HA on PS NPs in monovalent solutions [83, 133]. These findings provide insights into the stabilizing effect of the eco-corona on both pristine NPs and those subjected to photochemical weathering.

Nevertheless, NOM comprises chemically diverse polymers with varying MW and chemical structures [65, 361, 362]. The high MW fraction of NOM typically consists of abundant hydrophobic and aromatic components, whereas the low MW fraction contains a higher proportion of hydrophilic O-containing groups [361, 363]. By influencing the adsorption pattern of NOM on NPs, photochemical weathering has the potential to change not only the mass/thickness but also the fractionation and spatial arrangement of the eco-corona on NPs [364], and potentially leads to distinct stability outcomes. For instance, the photochemical weathered NPs might not adsorb specific fractions of NOM, leading to depletion attraction and potential destabilization of the NPs. Alternatively, hydrogen bonding might dominate the adsorption of NOM on weathered NPs, allowing various hydrophilic segments of NOM to attach to different NPs, thereby destabilizing NPs via polymer bridging. Further investigation is necessary to determine whether these processes could occur and have distinct effects on NP stability.

The main purpose of this study is to investigate the interaction between NOM and pristine/photoaged NPs and their effects on NP aggregation. To address this knowledge gap, the aggregation tendencies of pristine and photochemically weathered PS NPs were studied both in the absence and presence of Suwanee River NOM, as well as NOM fractions fractionated by MW. PS NPs were aged using the artificial accelerated photooxidation method to harvest photoaged NPs. Bulk NOM ( $< 0.05 \mu\text{m}$ ) and NOM fractions ( $< 3 \text{ kDa}$ ,  $3\text{--}10 \text{ kDa}$ ,  $10\text{--}30 \text{ kDa}$  and  $30 \text{ kDa}\text{--}0.05 \mu\text{m}$ ) were prepared for adsorption tests in stirred batch reactors using pristine and photoaged NPs. Time-resolved dynamic light scattering (DLS) was used to observe the effects of bulk NOM and NOM fractions on the aggregation kinetics of pristine and photoaged NPs in sodium chloride solutions.

## 3.2. Materials and Methods

### 3.2.1. Materials

A PS stock solution with a concentration of 50% w/v and a NP nominal size of 100 nm was purchased from Zhichuan Intelligent Technology (Suzhou) Co., Ltd. PS NPs were chosen for their occurrence in natural waters [10], and widespread use in aggregation studies [128, 130, 133], facilitating comparison with existing research. According to the manufacturer, the PS NPs were unfunctionalized but contained the surfactant sodium dodecyl sulfate (SDS). To reduce the interference with this surfactant, the prepared PS suspension (5 g/L) was washed four times using ultrapure water through ultracentrifugation ( $22000 \times g$ , 30 min) and sonication (40 kHz, 5 min) until the total organic carbon (TOC) in the supernatant was negligible ( $0.38 \pm 0.11 \text{ mg C/L}$ ). The hydrodynamic sizes of unwashed and washed NPs were measured as  $161.5 \pm 1.3 \text{ nm}$  and  $159.8 \pm 0.7 \text{ nm}$ , with polydispersity indices of 0.063 and 0.057, respectively,

indicating that the cleaning process did not induce aggregation of PS NPs. Suwannee River NOM was purchased from the International Humic Substances Society (IHSS). The polyvinylidene fluoride (PVDF) ultrafiltration membranes were purchased from RisingSun Membrane Technology (Beijing) Co., Ltd.

### 3.2.2. NOM Fractions Preparation

To prepare the NOM stock solution, 200 mg of NOM was dissolved in 200 mL of ultrapure water under sonication. The pH was then adjusted to 10 using 0.1 M NaOH to enhance NOM dissolution and prevent aggregation [360]. The solution underwent stirring at 200 rpm for 24 hours to facilitate solubilization. A stainless steel Amicon stirred cell (100 mL) ultrafiltration system equipped with a 0.05  $\mu\text{m}$  membrane disc (PVDF) was employed to remove any undissolved NOM and collect bulk NOM. NOM with a size below 0.05  $\mu\text{m}$ , which accounts for the majority of NOM [365, 366], was selected for easy separation from the larger NPs (100 nm) after the adsorption experiment using 0.1  $\mu\text{m}$  filters. Following this procedure, NOM fractions were separated via successive filtration through 30, 10, and 3 kDa membrane discs (PVDF) to collect NOM fractions with MWs ranging from 30 kDa–0.05  $\mu\text{m}$ , 10–30 kDa, 3–10 kDa, and < 3 kDa. After the initial ultrafiltration, the membrane was rinsed with 5 mL of ultrapure water and then subjected to filtration again. This procedure was repeated twice to achieve improved separation performance and minimize loss. The concentrated retentate was collected and then diluted with ultrapure water. The harvested NOM fractions were filtered using 0.1  $\mu\text{m}$  PES filters for further use, aimed at removing any particulates resulting from the ultrafiltration procedure. The TOC concentrations of the final bulk NOM and NOM fractions measured with TOC analysis (Shimadzu, ASI-V) were as follows: 343 mg/L for bulk NOM (< 0.05  $\mu\text{m}$ ), 244 mg/L for NOM (30 kDa–0.05  $\mu\text{m}$ ), 101 mg/L for NOM (10–30 kDa), 243 mg/L for NOM (3–10 kDa), and 131 mg/L for NOM (< 3 kDa). The entire procedure resulted in a 12.2 % loss, with the proportions being 39.2 % (< 3 kDa), 17.1% (3–10 kDa), 6.8% (10–30 kDa), and 19.2% (30 kDa–0.05  $\mu\text{m}$ ). The resulting pH of the stock solutions was 7.1 for bulk NOM, 7.6 for < 3 kDa, 7.1 for 3–10 kDa, 7.2 for 10–30 kDa, and 7.2 for 30 kDa–0.05  $\mu\text{m}$  fractions. These NOM solutions were diluted to achieve a consistent DOC concentration of 1–10 mg/L for the adsorption experiments and the aggregation experiments.

### 3.2.3. Accelerated Photooxidation Experiments

A mercury lamp (500 W) emitting UV light with an intensity of approximately 35 mW/cm<sup>2</sup> was employed to age PS NPs. The spectrum of the mercury lamp is shown in [Figure S1](#). The accelerating factor of the lamp was assessed by comparing the aging extent of PS NPs under real sunlight exposure in the Netherlands (see details in [Text S1](#), [Figure S1](#) and [Figure S2](#)). Pristine PS NPs, with a concentration of 300 mg/L (200 mL), were introduced into a 300 mL

transparent quartz reactor placed on a magnetic stirrer. The lamp, positioned within a circulation-cooled quartz tube, was placed inside the quartz reactor. The PS NPs were aged for 2, 4, and 8 days, corresponding to approximately 40, 80, and 160 days of sunlight exposure in the Netherlands. The particle number concentrations of both pristine and photoaged NPs were considered the same as photoaging did not cause obvious fragmentation of NPs (see Results and Discussion). To eliminate the interference of the leached dissolved organic carbon from plastic photodegradation in subsequent experiments, the aged NPs were washed four times using ultrapure water through ultracentrifugation (Eppendorf, Centrifuge 5910 Ri) at 15000 rpm ( $22000 \times g$ ) for 30 min and sonication (DK-3000H) at 40 kHz for 5 min. The washed pristine and aged NPs for 2, 4, and 8 days were labelled as PS<sub>0</sub>, PS<sub>2</sub>, PS<sub>4</sub>, and PS<sub>8</sub>, respectively (*Figure S3*). Due to changes in NP concentration during the washing process, the concentration of washed aged NPs was determined using UV absorbance at 289 nm and adjusted to match the UV<sub>289</sub> of the unwashed aged NPs. For subsequent adsorption and aggregation experiments, approximately  $4.68 \times 10^{12}$  particles/L of pristine (10 mg/L) and photoaged NPs were used by diluting the stock solutions to match their corresponding UV<sub>289</sub> (0.952, 0.927, 0.916 and 0.902 for PS<sub>0</sub>, PS<sub>2</sub>, PS<sub>4</sub>, and PS<sub>8</sub>, respectively). The dilution resulted in final pH values of 5.7, 5.9, 5.8, and 6.0 for PS<sub>0</sub>, PS<sub>2</sub>, PS<sub>4</sub>, and PS<sub>8</sub>, respectively. The corresponding TOC concentrations for PS<sub>0</sub>, PS<sub>2</sub>, PS<sub>4</sub>, and PS<sub>8</sub> were measured as 29.2 mg C/L, 26.8 mg C/L, 24.7 mg C/L, and 23.6 mg C/L, respectively (*Table S6*). High concentrations of the NPs were used for better observation of experimental phenomena.

#### 3.2.4. Adsorption Experiments

Batch adsorption experiments were carried out to examine the adsorption of bulk NOM and NOM fractions onto pristine and photoaged NPs. Pristine or photoaged NPs (10 mg/L) were mixed with bulk NOM or NOM fractions (2 mg/L) in 10 and 100 mM NaCl solutions within 50 mL centrifuge tubes. At these NaCl concentrations, no aggregation occurred, making them suitable for testing NOM adsorption. The pH was adjusted to  $6.0 \pm 0.1$  using 0.1 M HCl and NaOH to reflect environmentally relevant conditions [76, 82]. The centrifuge tubes were agitated at 100 rpm in a shaker at room temperature for 24 h (preliminary tests indicated that equilibrium was reached after this duration) [367]. Following this, the solution was filtered through 0.1  $\mu\text{m}$  PES filters (pre-washed with 10 mL ultrapure water) to separate NPs and NOM. For each solution, the first 3 mL of filtrate was discarded, and the remaining filtrate was used to test NOM removal. Preliminary experiments indicated that NOM adsorption on filters was negligible, and NOM adsorption by NPs had minimal impact on the specific absorbance of its UV spectra (*Figure S4*). The concentrations of NOM before and after adsorption were determined using UV absorbance at 280 nm, an index that reflects the aromaticity of NOM and is commonly used for its quantification [355, 362, 368]. Control samples of the washed

NPs were compared with a blank sample, confirming no contributions from the NPs to the UV absorbance in the filtrate (*Figure S5*). Duplicates were performed to assess the reduction in NOM concentration ( $1-A/A_0$ ) after adsorption onto pristine and photoaged NPs ( $A_0$  and  $A$  mean UV absorbance at 280 nm before and after adsorption).

### 3.2.5. Aggregation Kinetics Measurements

Time-resolved dynamic light scattering (DLS) technique was used to examine the aggregation kinetics of NPs in NaCl solutions utilizing a Malvern Zetasizer instrument (Nano ZS, Malvern, UK). The NOM and NP samples were pre-mixed in ultrapure water, and the pH was adjusted to  $6.0 \pm 0.1$  using 0.1 M HCl and NaOH. The concentration of NPs was 10 mg/L, a common concentration for aggregation kinetic studies [76, 77, 82, 128]. Bulk NOM ( $< 0.05 \mu\text{m}$ ) was adjusted to concentrations ranging from 1 to 10 mg C/L to examine the effect of NOM concentration on NP aggregation, within the typical range found in natural waters [81, 82, 369]. To further investigate the impact of NOM MW, a representative concentration of 2 mg/L was selected for different NOM fractions. The concentration of monovalent electrolyte solution (NaCl) ranged from 100 mM to 1000 mM. A relatively wide range of NaCl concentrations was tested to estimate the critical coagulation concentration (CCC) values and gain a better understanding of the aggregation tendencies of NPs. Duplicates or triplicates were conducted for each sample. Details on the detection and calculation for the aggregation kinetics can be found in the Supporting Information (*Text S2*). The Zetasizer instrument provided the intensity-weighted hydrodynamic size of NPs. To gain more insights into the aggregation kinetics, the intensity, volume, and number-weighted hydrodynamic sizes were analyzed using the Litesizer DLS 700 instrument (Anton Paar, Austria).

### 3.2.6. Characterization

The UV-vis spectroscopy (G10S UV-Vis, Thermo Fisher Scientific) and three-dimensional excitation-emission matrix (3D-EEM) fluorescence spectroscopy (Horiba Scientific) were employed to characterize the chemical properties of bulk NOM and NOM fractions. The hydrodynamic size and zeta potential of NPs in the absence and presence of NOM were measured using the Zetasizer Nano ZS90 (Malvern Instruments, UK). The size and morphology of pristine/photoaged NPs in ultrapure water were examined using a scanning electron microscope (SEM, Quattro, FEI) and a transmission electron microscope (TEM, Tecnai G20, FEI Corp, USA). Attenuated total reflectance Fourier transform infrared spectroscopy (ATR-FTIR, Nicolet iN10, Thermo Fisher Scientific) was used to detect the surface functional groups of NPs and NOM, as well as their interactions [130]. Detailed characterization methods are provided in *Text S3*.

### 3.2.7. DLVO and Steric (Polymer-Mediated) Interaction Energy.

The classical Derjaguin-Landau-Verwey-Overbeek (DLVO) theory was used to describe the interaction forces between NPs including van der Waals and electrostatic double layer interactions [188, 370]. In the presence of NOM, the extended DLVO (XDLVO) theory considering a steric (polymer-mediated) model was used to investigate interaction energies between NPs. This model takes into account repulsive steric interaction that arises when the adsorbed NOM forms a brush-like layer around the NPs, as well as attractive steric interaction (i.e., polymer bridging) that can occur when the polymer is able to adsorb onto multiple NPs simultaneously [347, 371]. Detailed calculations of DLVO and polymer-mediated interaction energies are provided in [Text S4](#), and [Table S7](#), [Table S8](#), [Table S9](#), and [Table S10](#).

## 3.3. Results and Discussion

### 3.3.1. Photochemical Weathering Modifies NPs

The FTIR spectra and the corresponding functional groups with their respective absorption wavenumbers are presented in [Figure 3.1a](#) and [Table S11](#). As the photoaging time prolonged, a decrease in the intensity of peaks at 696, 753, 1028, 1452, 1494, 1601, 2850, 2920, and 3026  $\text{cm}^{-1}$  was observed, indicating the degradation of aliphatic segments and benzene rings of pristine PS NPs under UV exposure. Notably, the new peaks at around 1717 and 3453  $\text{cm}^{-1}$  appeared after the photochemical weathering of PS NPs, attributed to the stretching vibrations of carboxyl (C=O) and hydroxyl (-OH) groups [372]. This is consistent with previous studies indicating that photochemical weathering can degrade initial hydrophobic aromatic and aliphatic components while generating hydrophilic O-containing functional groups [83, 343]. PS NPs had a specific UV absorbance at around 289 nm, which is attributed to the  $\pi-\pi^*$  transition of the benzenoid ring [373]. Photochemical weathering led to a reduction in UV absorbance at 289 nm ([Table S6](#)) [374], likely due to the destruction of the benzene ring structure [132]. The initial zeta potential of the pristine NPs (washed to remove SDS as described in the methods) was already low ( $-50.3 \pm 1.4$  mV in 10 mM NaCl), most likely due to sulfate groups generated during their synthesis [128, 132]. The zeta potential decreased further as a result of aging to  $-63.8 \pm 0.8$  mV,  $-65.7 \pm 0.5$  mV and  $-70.6 \pm 1.0$  mV in 10 mM NaCl after photoaging for 2, 4 and 8 days, respectively. Additionally, the hydrodynamic size decreased from the initial value of  $159.8 \pm 0.7$  nm to  $156.4 \pm 0.9$  nm,  $153.0 \pm 0.8$  nm, and  $151.7 \pm 1.7$  nm after photoaging for 2, 4, and 8 days, respectively ([Figure 3.2c](#)). Similarly, TEM results indicated that the particle sizes for PS<sub>0</sub>, PS<sub>2</sub>, PS<sub>4</sub>, and PS<sub>8</sub> were  $159.2 \pm 3.0$  nm,  $155.7 \pm 4.2$  nm,  $152.7 \pm 4.5$  nm, and  $150.4 \pm 4.9$  nm, respectively. The SEM and TEM images also showed that both pristine and photoaged NPs generally exhibited a regular spherical

morphology (*Figure S6 and Figure S7*), indicating that photoaging occurred primarily at the surface of the NPs without inducing obvious fragmentation.

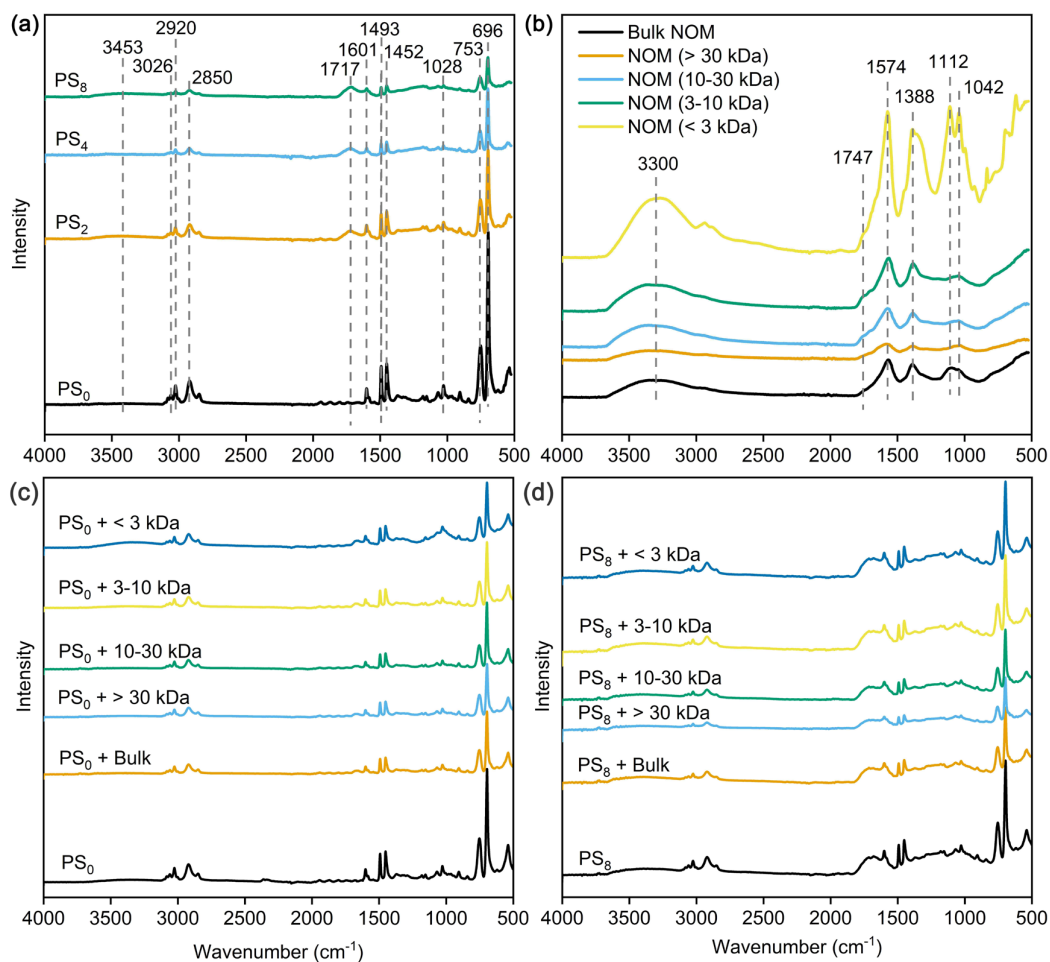


**Figure 3.1.** FTIR spectra of pristine and photoaged NPs (a), bulk NOM and NOM fractions (b),  $\text{PS}_0$  before and after adsorption with bulk NOM and NOM fractions in 100 mM NaCl (c), and  $\text{PS}_8$  before and after adsorption with bulk NOM and NOM fractions at 100 mM NaCl. Subscripts 0, 2, 4 and 8 mean aging times of 0, 2, 4 and 8 d.

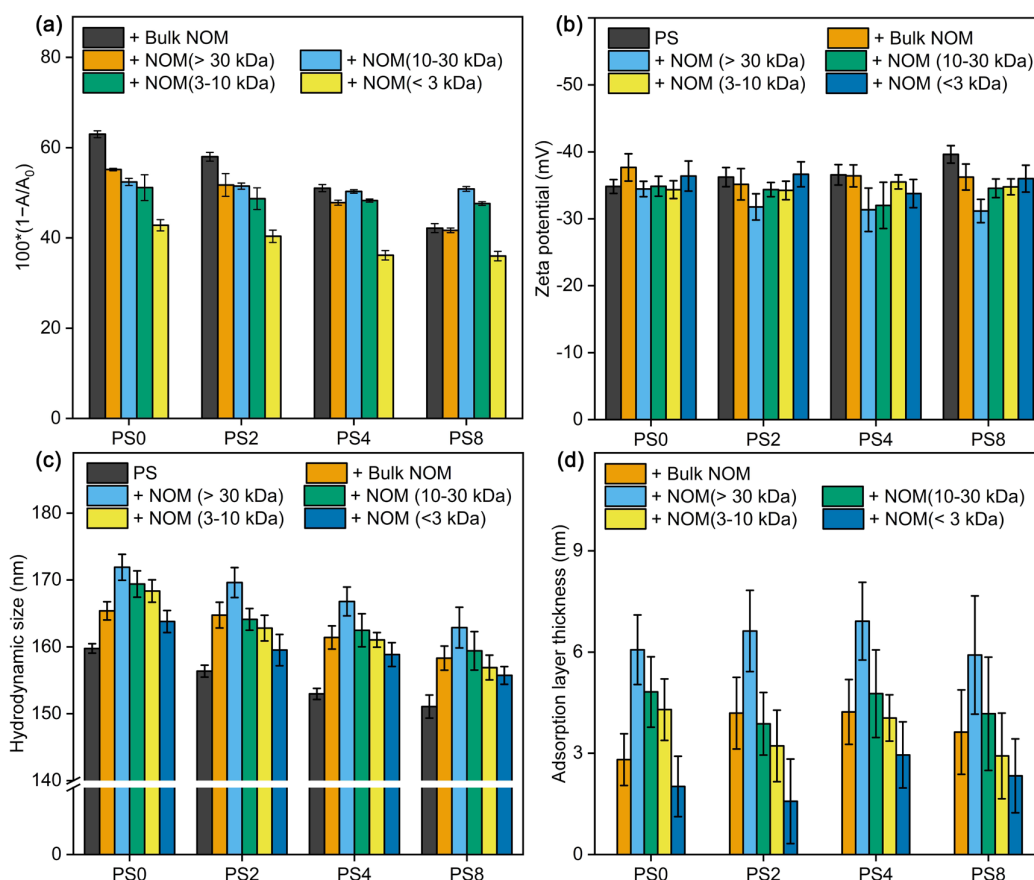


**Figure 3.2.** (a). The zeta potential of pristine and photoaged NPs with and without bulk NOM and NOM fractions (2 mg/L) in 100 mM NaCl after 24 h ( $n = 10$ ). (b). The removal ( $UV_{280}$  reduction) of bulk NOM and NOM fractions (2 mg/L) after adsorption (24 h) on pristine and photoaged NPs in 100 mM NaCl ( $n = 2$ ). (c) The hydrodynamic size of pristine and photoaged NPs with and without bulk NOM and NOM fractions (2 mg/L) in 100 mM NaCl after 24 h ( $n = 10$ ) (d). The adsorption layer thickness of bulk NOM and NOM fractions (2 mg/L) on pristine and photoaged NPs in 100 mM NaCl after 24 h. Error bars represent the mean  $\pm$  1.96 SE (95% confidence interval). Subscripts 0, 2, 4 and 8 mean aging times of 0, 2, 4 and 8 d.

### 3.3.2. NOM Adsorption Modifies Pristine and Photoaged NPs

As observed in the FTIR spectra and corresponding specific wavenumbers (Figure 3.1b and Table S12), both bulk NOM and NOM fractions exhibited peaks at 1042, 1112, 1388, 1574, 1747 and 3300  $\text{cm}^{-1}$ , indicating the presence of  $-\text{OH}$  and  $\text{C}=\text{O}$  groups [355, 367, 375, 376]. Typically, lower MW NOM showed more pronounced absorption peaks across all bands, indicating a higher abundance of  $-\text{OH}$  and  $\text{C}=\text{O}$  groups [355]. As depicted in the UV-vis spectra (Figure S8), NOM with higher MW contained abundant aromatic components, evidenced by the increased absorbance at 254 nm with increasing MW [355]. The UV

extinction coefficients ( $SUVA_{254}$ ) were as follows:  $0.056 \text{ L mg}^{-1} \text{ cm}^{-1}$  for bulk NOM ( $< 0.05 \mu\text{m}$ ),  $0.085 \text{ L mg}^{-1} \text{ cm}^{-1}$  for NOM (30 kDa– $0.05 \mu\text{m}$ ),  $0.071 \text{ L mg}^{-1} \text{ cm}^{-1}$  for NOM (10–30 kDa),  $0.065 \text{ L mg}^{-1} \text{ cm}^{-1}$  for NOM (3–10 kDa), and  $0.038 \text{ L mg}^{-1} \text{ cm}^{-1}$  for NOM ( $< 3 \text{ kDa}$ ), respectively. The corresponding aromaticity values were estimated to be 26.0%, 36.6%, 31.6%, 29.2%, and 19.2%, respectively [377]. Conversely, the lower MW NOM fractions exhibited stronger fluorescence intensities at  $Ex = 300\text{--}350 \text{ nm}/Em = 400\text{--}500 \text{ nm}$  and  $Ex = 250\text{--}275 \text{ nm}/Em = 380\text{--}500 \text{ nm}$  (Figure S9). This may be attributed to the higher abundance of aromatic carboxylic and hydroxyl groups in the lower MW NOM fractions [359, 378, 379]. These findings aligned with previous research, indicating that higher MW NOM fractions contain more aromatic structures, whereas lower MW fractions are richer in hydrophilic C=O and –OH groups [380, 381].

FTIR analysis revealed that NOM may adsorb onto pristine and photoaged NPs through different interaction mechanisms (Figure 3.1c,d and Figure S10). For pristine NPs, the adsorption of NOM reduced the intensities of aliphatic segments at  $2850$  and  $2920 \text{ cm}^{-1}$  and benzene rings at  $1452$ ,  $1492$ , and  $3026 \text{ cm}^{-1}$  (Figure 3.1c), indicating NOM likely interacted with these components via hydrophobic and  $\pi\text{-}\pi$  interactions. Notably, higher MW NOM appeared to reduce these intensities more substantially (Figure 3.1c), likely due to its more hydrophobic aromatic structures (Figure S8). Additionally, higher MW NOM could generate stronger van der Waals forces with NPs [382, 383], might contributing to this phenomenon. The adsorption of NOM also led to the appearance of C=O and –OH functional groups at  $1737$  and  $3280 \text{ cm}^{-1}$  on pristine NPs (Figure 3.1d), likely attributed to the signals from unbonded groups, including –OH and C=O groups of NOM (Figure 3.1b). Generally, pristine NPs with lower MW NOM adsorption showed higher intensities for C=O ( $1737 \text{ cm}^{-1}$ ) and –OH ( $3280 \text{ cm}^{-1}$ ) groups, likely due to their higher abundance and more pronounced response from these functional groups (Figure 3.1b). However, for photoaged NPs, the adsorption of NOM reduced the intensities of not only the original aliphatic segments ( $2850$  and  $2920 \text{ cm}^{-1}$ ) and benzene rings ( $1452$ ,  $1492$ , and  $3026 \text{ cm}^{-1}$ ) but also the newly generated C=O ( $1737 \text{ cm}^{-1}$ ) and –OH ( $3280 \text{ cm}^{-1}$ ) (Figure 3.1d and Figure S10). This suggests that multiple forces likely contributed to the interaction between NOM and photoaged NPs: the hydrophobic aromatic components of NOM may bind to hydrophobic sites (aliphatic segments at  $2850$  and  $2920 \text{ cm}^{-1}$  and benzene rings at  $1452$ ,  $1492$ , and  $3026 \text{ cm}^{-1}$ ) on photoaged NPs via hydrophobic and  $\pi\text{-}\pi$  interactions, while the oxygen-containing groups (C=O and –OH groups at  $1737$  and  $3280 \text{ cm}^{-1}$ ) on photoaged NPs may interact with the hydrophilic –OH and C=O groups of NOM via hydrogen bonding. Notably, higher MW NOM exhibited a greater capacity to reduce the intensities of both hydrophobic and hydrophilic groups on photoaged NPs (Figure 3.1d). This may be attributed to the stronger van der Waals forces between higher MW NOM and NPs

[382, 383], which could also enable hydrophobic and  $\pi$ - $\pi$  interactions, as well as hydrogen bonding. Overall, we hypothesize that the adsorption of NOM on NPs was likely governed by a combination of van der Waals forces, hydrogen bonding, hydrophobic and  $\pi$ - $\pi$  interactions, influenced by the NOM MW and the extent of NP photoaging [343].

The effects of bulk NOM and NOM fractions on the change in zeta potential of pristine and photoaged NPs at 10, 100 mM and 500 mM NaCl are illustrated in [Figure S11](#), [Figure 3.2a](#) and [Figure S12](#), respectively. At 100 mM NaCl, there were no visible differences between pristine and photoaged NPs, as well as between NPs with and without NOM ([Figure 3.2a](#) and [Figure S12](#)). However, at 10 mM NaCl, the surface charges of pristine NPs became more negative in the presence of bulk NOM and NOM fractions ([Figure S11](#)). This phenomenon, widely observed for engineered nanoparticles, was attributed to the charge superposition of the adsorbed NOM [357, 380]. However, the presence of NOM reduced the negative charges of photoaged NPs, especially for PS<sub>4</sub> and PS<sub>8</sub>. While no existing studies have documented this phenomenon, we propose that NOM was likely to interact with these hydrophilic O-containing functional groups on photoaged NPs via hydrogen bonding ([Figure 3.1d](#)), thereby shielding the negative charges or O-containing functional groups on the surface of the photoaged NPs.

[Figure S12](#) and [Figure 3.2b](#) illustrate the UV<sub>280</sub> reduction for bulk NOM and NOM fractions post-adsorption at 10 mM and 100 mM NaCl solution, respectively. For pristine NPs, there was a  $9.2 \pm 1.6$  % reduction in the UV<sub>280</sub> of bulk NOM at 10 mM NaCl, indicating NOM sorption onto the NPs ([Figure S13](#)). However, the addition of both bulk NOM and NOM fractions did not lead to visible change in the hydrodynamic size of both pristine and photoaged NPs at 10 mM NaCl ([Figure S14](#)). At 100 mM NaCl, the adsorption of bulk NOM on PS<sub>0</sub>, PS<sub>2</sub>, PS<sub>4</sub> and PS<sub>8</sub> increased importantly to  $63.0 \pm 0.8$  %,  $58.0 \pm 1.0$  %,  $51.0 \pm 0.8$  %, and  $42.2 \pm 1.0$  %, respectively. Meanwhile, there was an important increase in hydrodynamic size from the initial values of  $159.8 \pm 0.7$ ,  $156.4 \pm 0.9$ ,  $153.0 \pm 0.8$ , and  $151.1 \pm 1.7$  nm for PS<sub>0</sub>, PS<sub>2</sub>, PS<sub>4</sub>, and PS<sub>8</sub> to  $165.4 \pm 1.4$ ,  $164.8 \pm 1.9$ ,  $161.4 \pm 1.7$ , and  $158.3 \pm 1.8$  nm, respectively, when exposed to bulk NOM ([Figure 3.2c](#)). This was attributed to NOM adsorption rather than NOM aggregation as no NOM aggregates were detected by DLS at 100 mM NaCl ([Figure S15](#)). The increased adsorption of bulk NOM at higher salt concentration can be attributed to the compaction of the electrostatic layer between the NPs and NOM. Notably, at 100 mM NaCl, the adsorption at UV<sub>280</sub> decreased with the aging of NPs. Similar trends were observed across various NOM fractions, suggesting that photochemical weathering reduced the adsorption of NOM across all fractions. Generally, NOM with relatively high MW exhibited relatively high adsorption on both PS<sub>0</sub> and PS<sub>2</sub>. However, for the more aged PS<sub>4</sub> and PS<sub>8</sub>, the adsorption of NOM (> 30 kDa) was not the highest compared to lower MW NOM fractions. [Figure 3.2d](#) shows the

adsorption layer thickness determined by comparing the hydrodynamic sizes of the NPs before and after NOM adsorption. Generally, the mean adsorption layer thickness of NOM fractions increased with their MW, indicating that higher MW fractions formed thicker layers on both pristine and photoaged NPs. Notably, although bulk NOM showed higher adsorption on the NPs compared to NOM > 30 kDa, the mean adsorption layer thickness of bulk NOM was generally lower than that of NOM > 30 kDa. Thus, there was no consistent correlation between the mean adsorption layer thickness and the adsorption capacity. The surface coverage of NOM on NPs was estimated based on the adsorption amount and assumed NOM size ([Table S9](#)). The results indicated that surface coverage of NOM decreased with the photoaging of NPs, and higher MW NOM exhibited lower surface coverage, potentially due to spatial constraints between NOM molecules [384].

### 3.3.3. Photochemical Weathering Stabilizes NPs

The effect of photochemical weathering on the aggregation tendency of NPs was examined in monovalent solutions ([Figure S16](#)). As ionic strength increased, the attachment efficiency of both pristine and photoaged NPs increased, due to the charge screening effect of  $\text{Na}^+$ , which reduced the electrostatic repulsion between the NPs [128]. The CCC value of pristine NPs was measured at 550 mM NaCl, indicating their high stability. However, for photoaged NPs, the CCC values exceeded 1000 mM, indicating photoaged NPs were much more stable than pristine ones. At equivalent NaCl concentrations, the attachment efficiencies decreased with prolonged photoaging, indicating a reduction in NP stability as the extent of aging increased. Notably, the zeta potential of pristine NPs became increasingly negative with prolonged photoaging, consequently intensifying the electrostatic repulsion among photoaged NPs. Therefore, it can be inferred that electrostatic interaction played a pivotal role in stabilizing NPs following photoaging, in line with the previous studies [128]. The DLVO theory predicted high energy barriers ( $> 20 k_B T$ ) for both pristine and photoaged NPs at 100 mM NaCl. However, at 500 mM NaCl, no energy barrier was observed for  $\text{PS}_0$ , while energy barriers of 12.5  $k_B T$ , 28.4  $k_B T$ , and 31.5  $k_B T$  were noted for  $\text{PS}_2$ ,  $\text{PS}_4$ , and  $\text{PS}_8$ , respectively ([Figure S17](#)). One study also suggested that the stabilization of NPs may be induced by the release of dissolved organic molecules due to steric repulsion [128]. However, in this study, both pristine and photoaged NPs underwent a washing step to remove dissolved organic molecules, and thus these molecules were not responsible for the enhanced stability observed in our findings.

### 3.3.4. NOM Stabilizes Pristine NPs but Destabilizes Photoaged NPs

The effect of bulk NOM on the hydrodynamic size change of pristine and photoaged NPs in 500 mM NaCl is shown in [Figure 3.3a-3.3d](#) and [Figure S18-Figure S21](#). The presence of bulk NOM slowed down the rate of increase in the hydrodynamic size of pristine NPs ([Figure 3.3a](#)).

The Litesizer measurements indicated that the intensity, volume, and number-weighted hydrodynamic sizes all decreased in the presence of bulk NOM (*Figure S18* and *Figure S19*), suggesting that bulk NOM hindered the aggregation of pristine NPs under this condition. Additionally, the inhibitory effect of bulk NOM on NP aggregation increased with rising NOM concentration (*Figure 3.3a*). *Figure 3.4a* further illustrates the change in attachment efficiency with varying NaCl concentrations. As observed, in the presence of bulk NOM, the CCC value of pristine NPs increased from 550 mM to around 630 mM NaCl, suggesting that NOM enhanced the stability of NPs in monovalent solutions. The electrostatic interaction had a negligible effect, as evidenced by no important difference in the zeta potentials of pristine NPs with and without NOM (*Figure S13*). We hypothesize the electro-steric repulsion induced by the adsorption layer might be a primary factor stabilizing the pristine NPs [83]. As reported, the adsorption of the NOM layer can disrupt the original ionic diffuse layer of particles, leading to an expansion of the ionic diffuse layer, which may enhance the stability of NPs [385]. Additionally, based on the theoretical interaction energy profiles at 500 mM NaCl, a high energy barrier was present between pristine NPs in the presence of NOM (*Figure S22a*). This barrier resulted from the additional long-range steric repulsion that occurred when the separation distance decreased to less than twice the thickness of the NOM adsorption layer. The stabilization of NPs and engineered nanoparticles by NOM via steric repulsion has also been extensively documented in previous studies [81, 82, 363].

Nevertheless, the addition of NOM increased the hydrodynamic size of photoaged NPs (*Figure 3.3b-3.3d*). This phenomenon was not due to NOM aggregation as DLS did not detect NOM aggregates (*Figure S15*). The intensity, volume, and number-weighted size distributions of photoaged NPs with and without NOM over time were examined at 500 mM NaCl (*Figure S20* and *Figure S21*). All three types of size distributions generally exhibited uniform single peaks with minimal variation from each other and showed similar trends over time, indicating that the majority of photoaged NPs aggregated in the presence of NOM. The attachment efficiencies of photoaged NPs at all tested NaCl concentrations also increased after the addition of NOM (*Figure 3.4b-3.4d*), suggesting that NOM destabilized photoaged NPs. Notably, the aggregation of photoaged NPs occurred under relatively high NaCl concentrations, where NOM had minimal effect on the zeta potential of NPs (*Figure S13*), suggesting other forces rather than electrostatic interaction were at play. It has been reported that in addition to steric repulsion, soluble polymers can induce destabilization of colloids/nanoparticles through depletion attraction [349, 351], or polymer bridging [348, 386]. As NOM was adsorbed on photoaged NPs (*Figure 3.2b*), it is unlikely that depletion attraction was the mechanism responsible for the destabilization of photoaged NPs by NOM. In this study, we hypothesize that NOM might serve as a bridging agent among the photoaged NPs, thereby promoting their

aggregation. The XDLVO theory, which considers steric attractive interaction (i.e., polymer bridging), accurately predicted this destabilization phenomenon (*Figure S22b-S22d*). The long-range polymer bridging created a deep primary energy minimum as the separation distance decreased to less than the thickness of the NOM layer. At relatively low salt concentrations (e.g., 100 mM), the strong electrostatic repulsion created a substantial energy barrier between the photoaged NPs, preventing them from coming close enough for polymer bridging to occur (*Figure S22b1-S22d1*). However, at higher salt concentration (e.g., 500 mM), the electrical double layer was compressed, allowing the NPs to approach each other and enabling polymer bridging to take effect (*Figure S22b2-S22d2*). Few studies have reported polymer bridging by NOM in environmental colloid chemistry [353, 354]. Nason et al. reported that Pony Lake fulvic acid (PLFA, > 2 mg/L) destabilized citrate-stabilized Au nanoparticles in 80 mM KCl, which was explained by bridging flocculation driven by hydrophobic interactions between adsorbed PLFA molecules on adjacent Au nanoparticles [354]. Pradel et al. demonstrated that sodium alginate, a model polysaccharide could bridge pristine PS NPs by binding multiple particles together, while the resulting clusters were further stabilized through steric repulsion [353].

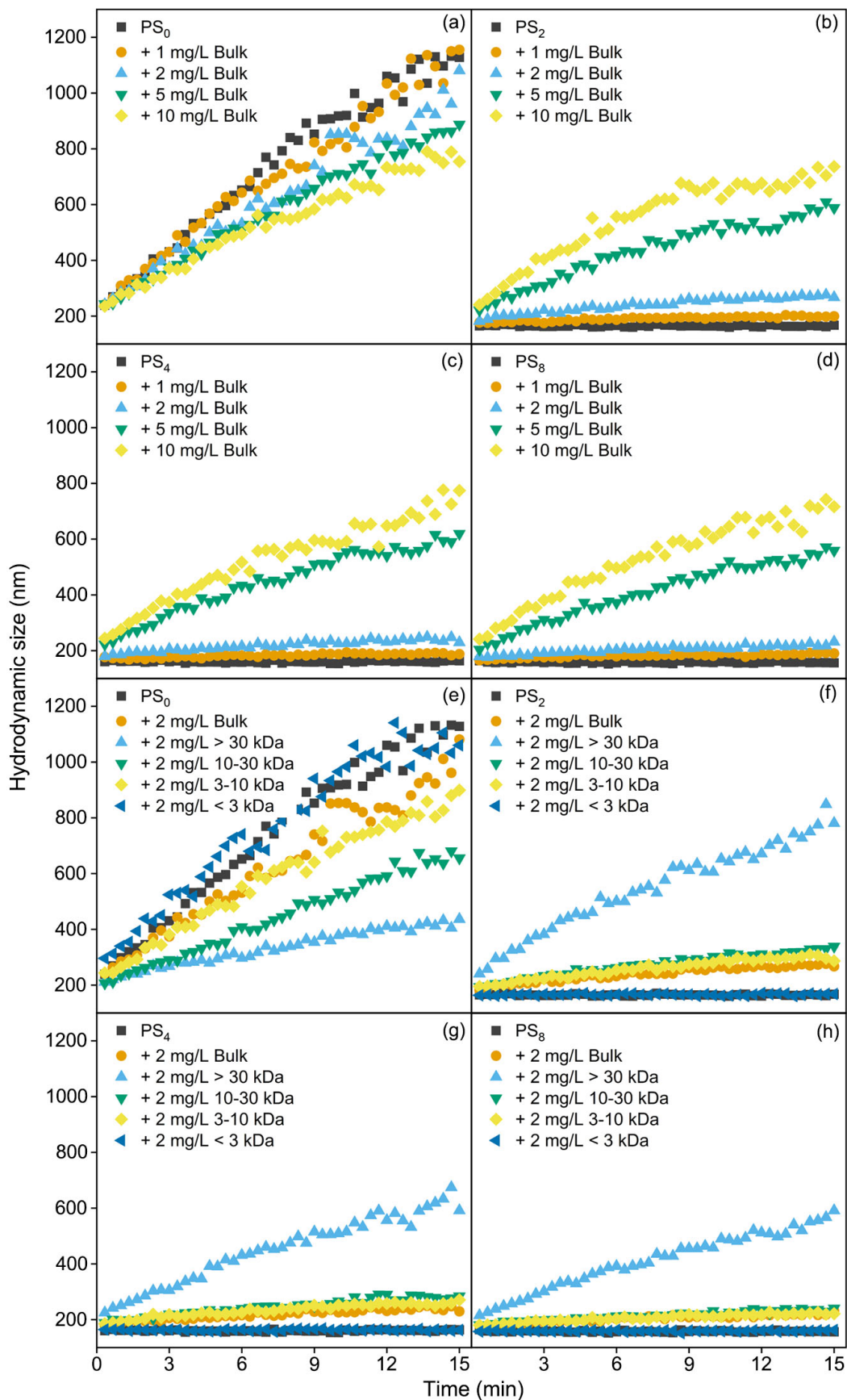


**Figure 3.3.** The effect of bulk NOM concentration (1, 2, 5, and 10 mg/L) and different MW NOM fractions (2 mg/L) on the hydrodynamic size (intensity weighted) change of pristine and photoaged NPs at 500 mM NaCl. Subscripts 0, 2, 4 and 8 mean aging times of 0, 2, 4 and 8 d.

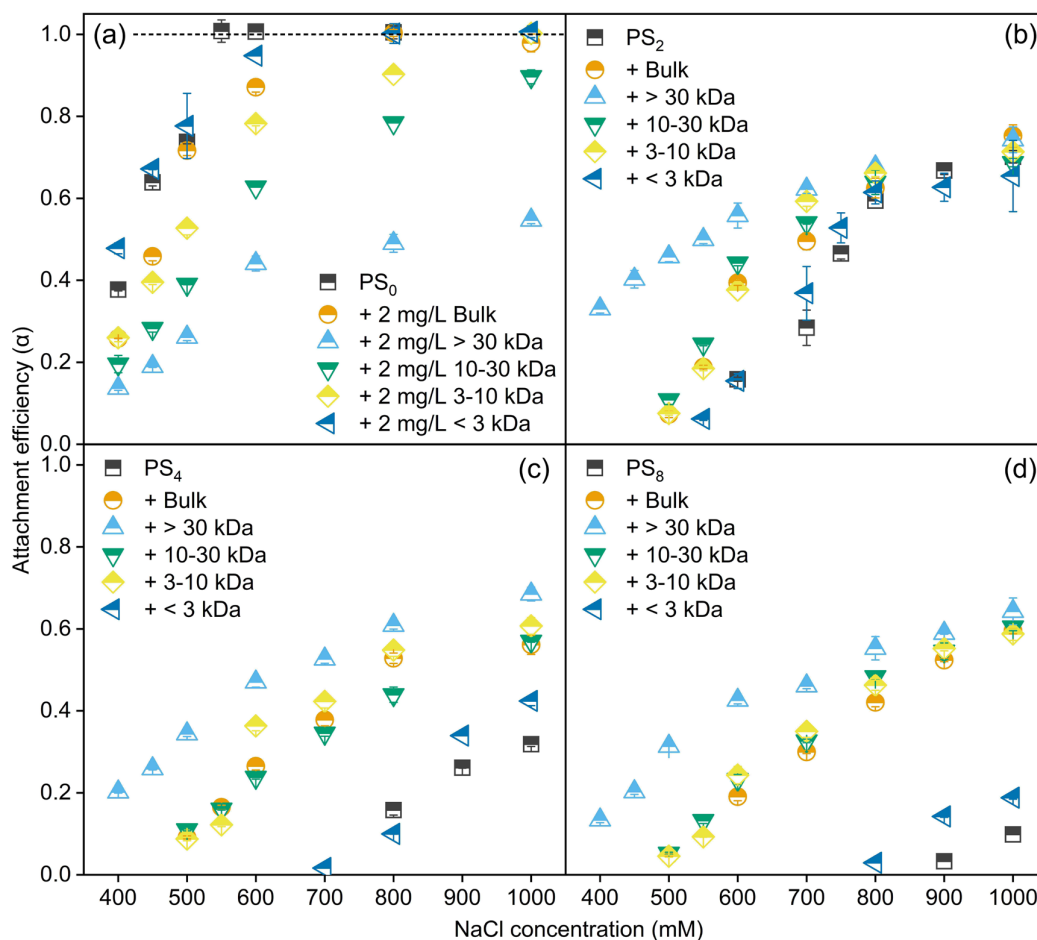


**Figure 3.4.** The aggregation kinetics of pristine and photoaged NPs without and with NOM (2 mg/L) in NaCl solutions. Subscripts 0, 2, 4 and 8 mean aging times of 0, 2, 4 and 8 d. Error bars represent the mean  $\pm$  SD ( $n = 2$  or 3).

As reported, steric stabilization occurs with high adsorbed amounts, but polymer bridging requires sufficient unoccupied surface area on particles for the attachment of polymer chain segments from other particles [386]. Typically, an optimal polymer dosage corresponds to low adsorbed amounts, and an excess of polymer can lead to restabilization [386]. In this study, although photoaging reduced the amount of NOM adsorbed and the surface coverage on NPs (Table S9), low MW NOM fractions (e.g., < 10 kDa) at 2 mg/L still exceeded 100% surface

coverage on photoaged NPs. Furthermore, the destabilization capacity of NOM on photoaged NPs increased with the concentration of NOM (*Figure 3.3b-3.3d*). It suggests that the adsorbed amount or surface coverage did not solely determine the distinct role of NOM in the stability of pristine and photoaged NPs. We propose that the unique adsorption configurations of NOM on pristine and photoaged NPs might play a crucial role.

It is commonly believed that NOM in solution has a micelle-like structure, with hydrophilic moieties exposed on the external part and the hydrophobic domain hidden in the inner part [387-389]. Conformational rearrangements could occur, enabling favorable moieties to adsorb onto solid surfaces [389-391]. The hydrophobic components of NOM might tend to bind with the surfaces of pristine NPs through hydrophobic and  $\pi$ - $\pi$  interactions (*Figure 3.1c*), while hydrophilic segments might extend into the surrounding solution (*Figure 3.5*) [372, 392]. These hydrophilic segments might inhibit NP aggregation through steric repulsion. Compared to pristine NPs, the surface of photoaged NPs was more heterogeneous, containing both aromatic segments and O-containing functional groups (*Figure 3.1a*). This surface heterogeneity may allow NOM to adsorb through both hydrophobic and hydrophilic interactions (*Figure 3.1d*). The hydrophobic and  $\pi$ - $\pi$  interactions likely facilitate the adsorption of the hydrophobic components of NOM onto the non-oxidized regions of the photoaged NPs, while hydrogen bonding may occur between the hydrophilic segments of NOM and the oxidized regions on the photoaged NPs (*Figure 3.5*). Additionally, the remaining hydrophobic or hydrophilic segments of NOM in solution may bind with the heterogeneous regions on other photoaged NPs, effectively bridging two or more photoaged NPs. In previous studies, the presence of HA stabilized both pristine and photoaged PS NPs in monovalent solutions, but the stabilization capacity was weakened on photoaged NPs due to less HA adsorption [83, 175]. The distinct effect of NOM on photoaged NPs observed in this study compared to previous studies may be attributed to differences in aging extent. Earlier studies likely involved less photoaged NPs, with aging times of one day or less, and CCC values that were determinable and below 1000 mM [83, 133]. HA adsorption on these photoaged NPs was likely dominated by hydrophobic and  $\pi$ - $\pi$  interactions, with minimal hydrogen bonding. In contrast, the increased oxidation in this study may reduce these hydrophobic interactions while enhancing hydrogen bonding between NOM and photoaged NPs. Thus, we propose that sufficient surface hydrogen bonding donors (O-containing functional groups) on photoaged NPs are essential for the formation of polymer bridging.

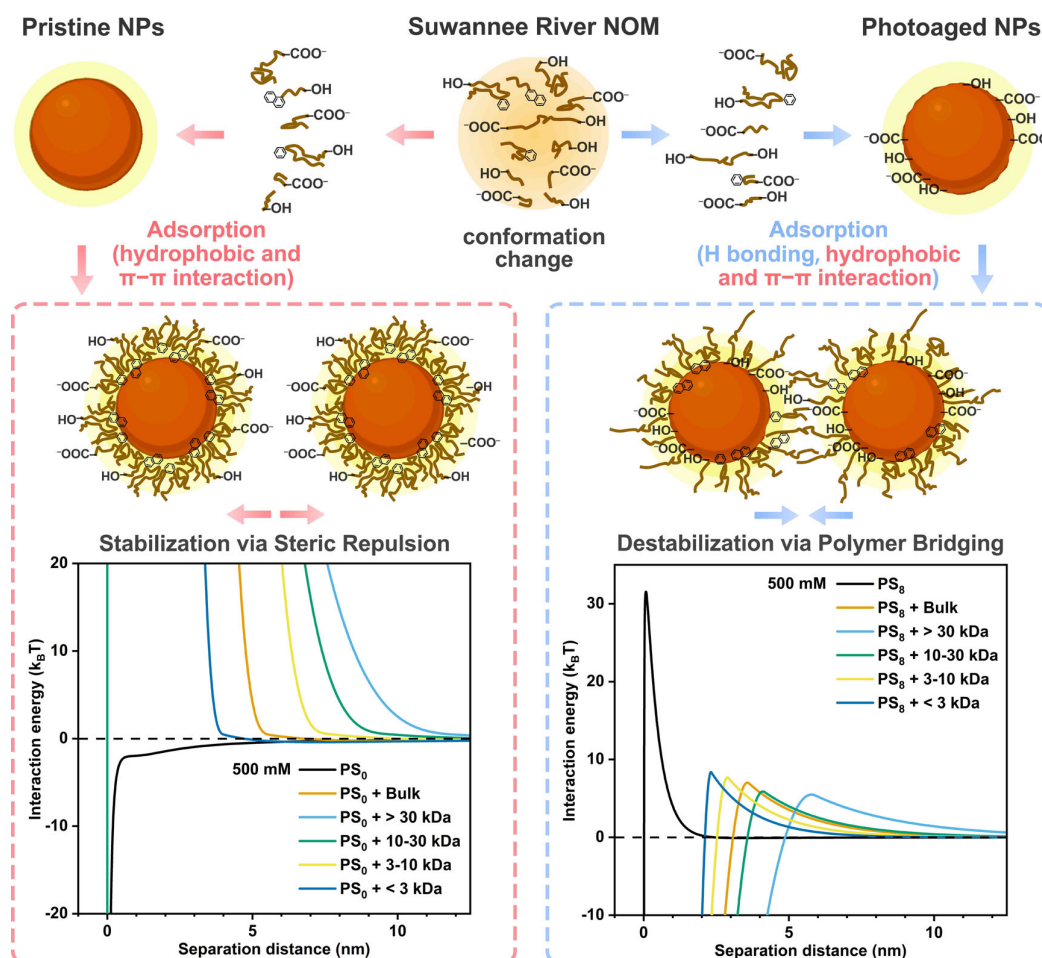


**Figure 3.5.** Schematic diagram illustrating the mechanisms of NOM adsorption and the stabilization or destabilization of NPs by NOM, as well as the DLVO and steric model interaction energy curves at 500 mM NaCl.

### 3.3.5. Molecular Weight-Dependent Stabilization and Destabilization Capacity

NOM, being a heterogeneous mixture of components with varying MW and chemical properties, exhibits chemical heterogeneity among its fractions [393]. This molecular heterogeneity plays a crucial role in determining the formation of an eco-corona, which subsequently impacts the stability of nanoparticles [360, 363]. The impact of MW-fractionated NOM on the hydrodynamic size change of pristine NPs in a 500 mM NaCl solution is depicted in Figure 3e-3h. Compared to pristine NPs in the absence of NOM fractions, NOM with relatively large MWs (i.e., > 30 kDa, 10–30 kDa, and 3–10 kDa) notably inhibited the increase in the hydrodynamic size of NPs, while NOM with MW below 3 kDa seemed to promote the increase in hydrodynamic size in the initial stage. At all tested NaCl concentrations, NOM with relatively large MWs (i.e., > 30 kDa, 10–30 kDa, and 3–10 kDa) inhibited the aggregation of pristine NPs (Figure 3.4b-3.4d). Notably, although NOM < 3 kDa exhibited some

destabilization on pristine NPs under relatively low NaCl concentrations ( $\leq 500$  mM), the CCC value of pristine NPs with NOM  $< 3$  kDa was higher than that of pristine NPs alone (610 mM vs. 550 mM). Generally, the stabilization capacity of NOM fractions increased with the increase in MW. Due to higher aromaticity and fewer carbonyl groups, NOM with higher MW exhibited higher adsorption capacity on pristine NPs (*Figure 3.2b*). Additionally, the larger size of high-MW NOM contributed to the formation of a thicker adsorption layer on the NPs (*Figure 3.2d*). According to the steric model (*Figure 3.5* and *Figure S22a*), higher MW NOM could generate longer-range steric repulsion, producing a high energy barrier at a larger separation distance, thus demonstrating stronger stabilization capacity.

For photoaged NPs, NOM  $< 3$  kDa did not induce obvious changes in the hydrodynamic size at 500 mM NaCl, whereas NOM with larger molecular weights, particularly NOM  $> 30$  kDa, caused an increase in the hydrodynamic size of PS<sub>2</sub>, PS<sub>4</sub> and PS<sub>8</sub> (*Figure 3.3f-3.3h*). The attachment efficiencies of photoaged NPs in the presence of NOM fractions were further investigated across a wide range of NaCl concentrations. Generally, similar to bulk NOM, all NOM fractions destabilized the photoaged NPs. Notably, the destabilization capacity of NOM fractions increased with increasing MW. NOM with relatively large MW generally formed a thicker adsorption layer on photoaged NPs (*Figure 3.2d*). Based on the theoretical calculations of the steric model, the adsorption layer thickness largely determined the separation distance at which polymer bridging occurs (*Figure 3.5* and *Figure S22b-S22d*). NOM with a relatively large MW could serve as a “large bridge”, binding photoaged NPs at a relatively far distance (*Figure 3.5*). Thus, the destabilization of photoaged NPs was strongly dependent on the MW of NOM.

### 3.4. Environmental Implications

The aggregation behavior and colloidal stability of NPs are highly impacted by natural weathering processes, such as photochemical weathering [128], and eco-corona formation [81, 82]. This study revealed that the role of photochemical weathering and eco-corona in the colloidal stability of NPs was more complicated than what we previously expected [83]. Although both photoaging and NOM adsorption are known to stabilize NPs in monovalent electrolyte solutions [81, 82, 128], our study highlighted that NOM stabilized pristine NPs most likely via steric repulsion but destabilized photoaged NPs via polymer bridging in monovalent electrolyte solutions. The modification of NPs through photochemical weathering likely impacts eco-corona formation [394, 395]. Although photoaging reduces the amount of eco-corona on NPs [360], this is not the primary reason for the destabilization of photoaged NPs. We propose that distinct interaction between NOM and pristine/photoaged NPs induced distinct eco-corona conformation on pristine and photoaged NPs, thus leading to distinct

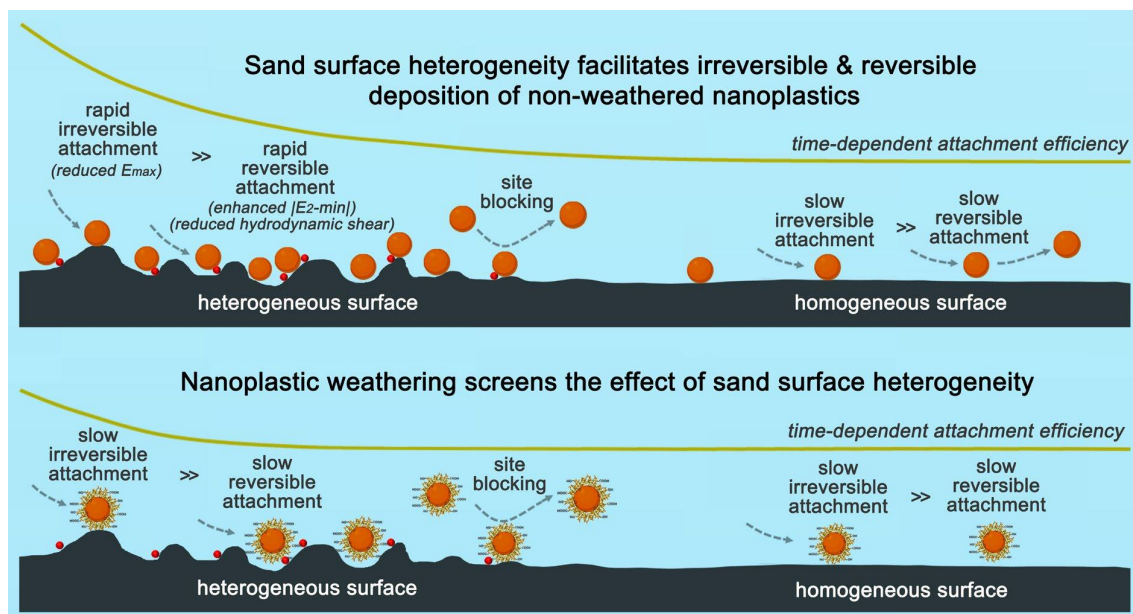
stability effects. In monovalent solutions, NOM typically stabilizes NPs or engineered nanoparticles via steric repulsion [81, 82, 393], while the destabilization phenomenon of NOM usually occurs in the presence of multivalent cations (e.g., calcium) via cation bridging [357, 396]. This study highlighted the destabilization role of NOM in monovalent solutions in environmental colloid chemistry, providing new insights into the stability and fate of NPs and engineered nanoparticles in complex aquatic conditions. NOM is diverse in terms of molecular size and properties [393]. NOM with relatively high molecular weights typically exhibits relatively high aromaticity and hydrophobicity, but low hydrophilicity [363]. In this study, higher molecular weight NOM fractions displayed greater adsorption on both pristine and photoaged NPs, indicating that the photoaging did not notably change the adsorption preference of NPs based on NOM size. In addition, despite their lower abundance, NOM with relatively high molecular weights played a dominant role in either stabilizing pristine NPs or destabilizing photoaged NPs. This highlights the importance of considering the heterogeneity in molecular size distribution of environmental NOM when interpreting its effects on the transport and fate of NPs.

It should be noted that, commercial PS NPs used in this study are highly stable, which makes it challenging to observe aggregation behaviors under typical freshwater conditions. To address this, high salinity conditions were chosen to better observe and understand the interactions and aggregation behaviors of NPs. Thus, the findings are relevant to estuarine or marine ecosystems, where elevated salinity levels are common. However, the underlying mechanisms observed in this study, such as the interactions of NOM with pristine and weathered NPs and the resulting aggregation processes, are fundamental and may also apply to less stable NPs or scenarios in freshwater systems. This suggests that while specific outcomes may vary, the broader insights provided by this research could contribute to understanding NP behavior across a range of aquatic environments.



# Chapter 4

## Weathering of Nanoplastics Reduces the Effect of Sand Surface Heterogeneity on Irreversible and Reversible Deposition in Saturated Porous Media



## Abstract

The deposition of nanoplastics (NPs) in porous media is strongly influenced by natural weathering processes, such as UV exposure and adsorption of natural organic matter (NOM), but the deposition mechanisms of both, non-weathered and weathered NPs, remain poorly understood. In this study the effect of NOM on the transport of non-weathered polystyrene (PS) NPs and UV-weathered PS NPs was examined in saturated porous media under low ionic strength conditions. It revealed that the physical and chemical heterogeneity of the sand surface created favorable attachment sites, leading to site blocking and retardation of NPs. NPs followed a non-steady-state, two-stage transport dynamic: rapid, irreversible, and reversible or pseudo-equilibrium attachment on heterogeneous areas until site saturation, followed by slow, irreversible attachment on relatively homogeneous surfaces. Both UV weathering and NOM coating generated more negatively charged NPs, reducing the irreversible and reversible deposition of NPs. These weathering processes reshaped NP transport dynamics and masked the retardation effects induced by sand surface heterogeneity. Moreover, the impact of NOM on NP deposition varied depending on the extent of UV weathering and the molecular weight of the NOM.

## 4.1. Introduction

The massive production and pervasive use of plastics lead to plastic debris accumulating in the environment [113, 397], with projections suggesting that up to 12 Gt of plastic waste could enter natural ecosystems by 2050 [398]. Over the past decades, microplastics have drawn great attention due to their persistence in the environment and toxic effects on aquatic organisms [399, 400]. Recently, however, nanoplastics (NPs,  $< 1 \mu\text{m}$ ) have attracted increasing attention [401]. NPs originate from two main sources: primary NPs, which are intentionally manufactured for commercial and industrial applications [402], and secondary NPs that are formed through the degradation of larger plastic particles, e.g. by UV-induced breakdown [403]. Both *in vitro* and *in vivo* studies have shown that NPs can pose serious health risks to humans, including physical stress, cellular damage, apoptosis, necrosis, inflammation, oxidative stress, and immune responses [27-29, 404]. NPs have been detected in various water sources, including surface water, groundwater, and riverbank filtrate (RBF) [10]. Especially, the presence of NPs in RBF raises concerns about its effectiveness in removing these particles.

Studies on NP transport and deposition often draw upon established knowledge of colloid transport in porous media [405]. The classical clean bed filtration theory (CFT) is the most commonly used approach for describing the filtration of colloidal particles [406]. The CFT assumes that collector surfaces are perfectly smooth and uniformly charged, with the

deposition rate being constant. A first-order kinetic model is typically employed to describe deposition, where colloids break through without retardation (i.e., breakthrough occurs at or before the first pore volume) and the breakthrough curve (BTC) remains a steady-state plateau [407]. The classic Derjaguin-Landau-Verwey-Overbeek (DLVO) theory is commonly used to explain the deposition phenomena [408]. Under unfavorable conditions, where repulsive interactions are present, colloids typically deposit in the primary minimum by overcoming the energy barrier [409]. However, discrepancies between theoretical predictions and experimental results are often observed, particularly under unfavorable conditions [409, 410]. For instance, colloids are not expected to deposit onto collector surfaces at typically low ionic strengths due to the presence of a high energy barrier, yet particle deposition is frequently observed [410, 411]. Tufenkji and Elimelech have suggested that some colloids undergo "slow" deposition by overcoming the repulsive energy barrier to reach the primary energy minimum, while others deposit "fast" due to a relatively deep secondary energy minimum [410, 411]. Non-steady-state breakthrough, driven by mechanisms such as site blocking, is also commonly seen in experiments [412, 413]. This is usually explained by the physical and chemical heterogeneity of the collector surface, resulting in varying deposition rates [407, 414]. Particularly retardation, which deviates from the CFT, has been observed in the case of colloids [415, 416]. While retardation is associated with "equilibrium adsorption" during the transport of reactive solutes [417], this concept cannot directly be applied to colloid transport as colloids are typically thermodynamically unstable [418]. In addition, the transport of NPs in porous media has extensively been studied using commercially available NPs, such as PS NPs [67, 88, 89, 94, 97, 98, 129, 136, 419]. The deposition of NPs in previous studies typically occurred under unfavorable conditions and deviated from CFT theory [67, 89, 129, 420, 421], but limited research has been dedicated to the reasons behind these deviations [422, 423].

Moreover, NPs exposed to aquatic environments do not maintain their original state or properties, but, instead, undergo natural weathering processes such as oxidation by UV-light and coating with organic macromolecules [117]. For example, secondary NPs may have been UV-weathered [53, 424], while primary NPs may undergo UV weathering when exposed to environmental conditions [128]. Typically, UV weathering generates a range of oxygen-containing functional groups on the NP surface, making them more hydrophilic and negatively charged [136, 148]. Furthermore, a coating of natural organic matter (NOM), which includes various organic components such as humic acids, fulvic acids, proteins, and polysaccharides [65, 359], can be formed as an "eco-corona" on NPs, serving as another weathering factor that modifies their surface properties [83, 360]. Depending on the source and component, NOM may increase or decrease the negative charges of the surface of NPs [88, 89, 94]. The modification of NPs by these weathering processes can alter their interactions with collector

surfaces and thus influence their transport in porous media [67, 88, 89, 94, 129, 136]. For instance, some authors have reported that NOM adsorption can enhance NP transport by increasing electrostatic repulsion [88, 94], or by inducing additional steric repulsion [67, 89]. However, weathering processes may not only enhance the transport capacity of NPs, but may also lead to distinct transport dynamics. Non-steady-state breakthrough and retardation, deviating from CFT, are often observed during transport of non-weathered NPs, whereas weathered NPs tend to show steady-state breakthrough with reduced or negligible retardation compared to pristine particles [67, 421]. Despite these observations, this aspect has not been explicitly studied. Overall, the mechanisms behind these deviations from CFT, as well as how weathering reshapes NP transport dynamics in porous media, remain poorly understood.

Therefore, the main objective of this study is to elucidate the transport mechanisms of non-weathered and weathered NPs in saturated porous media. Commercial PS NPs, representing non-weathered NPs, were UV-aged using a mercury lamp to produce UV-weathered PS NPs. Suwanee River NOM was incubated with both non-weathered and UV-weathered PS NPs to generate NOM-weathered NPs. NOM was further split into different MW fractions to study how NOM size modifies NPs and affects their deposition. BTCs for non-weathered and weathered NPs in saturated porous media were obtained by filtering over clean quartz sand columns. Finally, a two-site kinetic model and an equilibrium-kinetic model, combined with DLVO and extended DLVO (XDLVO) theory, were used to elucidate the mechanisms driving the deposition of non-weathered and weathered NPs.

## 4.2. Materials and Methods

### 4.2.1. Materials

The preparation of PS NPs could be found in [Chapter 3](#). The used quartz sand had a diameter of 0.4–0.8 mm, and was purchased online from vidaXL. For comparison, two other types of quartz sand were obtained from Sigma-Aldrich: Sigma-1, with a size range of 0.2–0.8 mm, and Sigma-2 with a narrower range of 0.21–0.30 mm. The vidaXL sand and the Sigma-1 sand were then sieved using stainless steel screens (30 and 40 mesh) to obtain 0.425–0.6 mm vidaXL sand, 0.425–0.6 mm Sigma-1 sand, and 0.2–0.425 mm Sigma-1 sand. The sand was then cleaned to remove possible organic residues and metals by sequentially soaking it in concentrated NaOH for 24 h, followed by washing with concentrated HCl for 24 hours. After cleaning, the sand was thoroughly rinsed with ultrapure water until the pH stabilized at approximately 6.5. Finally, the cleaned quartz sand was heated at 550 °C for 5 h.

#### 4.2.2. Preparation of Weathered Nanoplastics

The UV-weathered PS NPs were prepared by aging PS NPs under a 500 W mercury lamp (35 mW/cm<sup>2</sup>) for 2, 4 and 8 days [425]. Detailed procedures are provided in [Chapter 3](#).

NOM-weathered NPs were prepared by mixing NOM (2 mg C/L) with pristine or UV-weathered NPs in 10 mM NaCl, with the pH adjusted to  $6.0 \pm 0.1$  using 0.1 M HCl and NaOH. 10 mM NaCl was selected to represent typical surface water with low ionic strength. Bulk NOM (< 0.05  $\mu\text{m}$ ) and NOM fractions with MWs ranging from 30 kDa–0.05  $\mu\text{m}$ , 10–30 kDa, 3–10 kDa, and < 3 kDa were prepared, as detailed in [Chapter 3](#). To obtain stable NOM-weathered NPs, the mixture was allowed to react for 24 hours to approximately reach equilibrium [425].

#### 4.2.3. Column Transport Experiments

A polymethyl methacrylate column with a height of 9 cm and an inner diameter of 2 cm was used to study NP transport in the porous media (see the setup in [Figure S24](#)). The ratio between the column diameter and sand grain diameter was 33, which falls within the recommended range of 20–50, ensuring minimal wall effects and preferential flow paths [426]. To prevent sand loss from the bottom and ensure a uniform flow distribution at the top, a stainless steel mesh with a 200  $\mu\text{m}$  opening was placed at the bottom of the column. During sand packing, ultrapure water was introduced from the bottom of the column. The cleaned, dry sand was then wetted with ultrapure water, and gradually added to the column using a spoon and while gently stirring the column to prevent layering and air entrapment. The resulting sand bed porosity was 0.39, calculated based on the inserted sand mass, the packed column volume, and a sand density of 2.56 g/cm<sup>3</sup>. After packing, several pore volumes (PVs) of ultrapure water were injected to wash the sand in the columns. 10 mM NaCl was used as a tracer to assess the conservative transport properties of the packed columns, while measuring the electrical conductivity with a potable conductivity meter (HQ1140, HACH, USA) in the effluents of the column. As for all experiments, a constant flow of 1 mL/min (0.54 m/h) was applied in an upward direction, using a peristaltic pump (Longer BT100-3J).

For NP transport studies, the columns were pre-flushed with a particle-free background electrolyte (10 mM NaCl) for 10 PVs to establish stable baseline conditions. Following this, 25 or more PVs of NP suspension were injected, followed by 10 PVs of background electrolyte elution to allow the column effluent  $UV_{289}$  to return to baseline levels. Effluent samples were collected in glass tubes from the top of the column at equal time intervals to obtain BTCs. NP concentrations were measured using a UV spectrophotometer (G10S UV-Vis, Thermo Fisher Scientific) at a wavelength of 289 nm. Transport experiments for pristine NPs were conducted at concentrations of 2 mg/L ( $9.36 \times 10^{11}$  particles/L,  $UV_{289} = 0.211 \text{ cm}^{-1}$ ), 5 mg/L ( $2.34 \times 10^{12}$  particles/L,  $UV_{289} = 0.505 \text{ cm}^{-1}$ ), and 10 mg/L ( $4.68 \times 10^{12}$  particles/L,  $UV_{289} = 0.952 \text{ cm}^{-1}$ ) in 10

mM NaCl. For UV-weathered and NOM-weathered NPs' transport studies,  $4.68 \times 10^{12}$  particles/L in 10 mM NaCl was used. Both non-weathered and weathered NPs were pre-equilibrated for 24 h before injection. NP aggregation was not observed after the 24-h reaction period, as indicated by dynamic light scattering measurements. Either duplicate or triplicate experiments were conducted for each transport condition.

#### 4.2.4. Adsorption and Desorption Experiments

Batch adsorption experiments were conducted to study the adsorption of non-weathered and weathered NPs by the cleaned 0.425–0.600 mm vidaXL sand. A 100 mL suspension of  $4.68 \times 10^{12}$  particles/L ( $UV_{289} = 0.952 \text{ cm}^{-1}$ ) of either non-weathered or weathered NPs was mixed with 50 g of sand in 10 mM NaCl. The mixture was agitated at 160 rpm for 48 hours. The suspension was sampled at specific time intervals (0, 1, 2, 10 min and 0.5, 2.5, 20, 24 and 48 h) and tested for  $UV_{289}$ . After 48 hours, the suspension was replaced with 85 mL of particle-free 10 mM NaCl solution, and the desorption of NPs was tested at several time intervals (0, 1, 2, 10, and 30 minutes). Controls, without sand addition, showed no obvious  $UV_{289}$  reduction of NPs following agitation for 48 hours (*Figure S24*). Blanks indicated that agitation caused the fragmentation and release of suspended fine sands, which interfered with the UV absorbance of NPs (*Figure S25*). Detailed analysis results are presented in *Text S5*.

#### 4.2.5. Characterization

Detailed characterization and analysis regarding the physicochemical properties of non-weathered and weathered NPs, and NOM can be found in [Chapter 3](#).

The zeta potential of sands was characterized using a Zetasizer Nano ZS90. Prior to testing, the sands were ground into fine particles using a stainless steel rod to facilitate suspension and measurement [427]. The surface morphology of quartz sand and the deposited NPs was characterized using both an optical microscope and SEM. Energy-dispersive X-ray spectroscopy (EDX; EDX1800ROHS) was conducted to identify the major elemental components present on the sand surfaces. In addition, X-ray diffraction (XRD; PHILIPS PW 1710) was used to analyze the mineralogical composition of the sands.

#### 4.2.6. Modelling

In porous media, the transport and deposition of NPs are primarily controlled by three major processes: advection, dispersion, and attachment to collector surfaces. These processes are typically described by 1-D advection-dispersion-reaction (ADR) equation:

$$\frac{\partial C}{\partial t} = D \frac{\partial^2 C}{\partial z^2} - v \frac{\partial C}{\partial z} - \frac{\rho_b}{\theta} \frac{\partial S}{\partial t} \quad (4-1)$$

In this model,  $t$  represents time (min),  $z$  is the distance (m), and  $C$  denotes the concentration of NPs in solution (mg/L or particle/L).  $D$  is the hydrodynamic dispersion coefficient ( $\text{cm}^2/\text{min}$ ),  $v$  is the average pore water flow velocity (cm/min), and  $\rho_b$  is the sand bulk density ( $\text{mg}/\text{cm}^3$ ) and  $\theta$  is the porosity of the sand media (dimensionless).  $\frac{\partial S}{\partial t}$  denotes the change in concentration of NPs due to reactions such as deposition ( $S$  in the same units as  $C$ ). The mean pore-water flow velocity and the hydrodynamic dispersion coefficient used in NP simulations were obtained by fitting to NaCl tracer breakthrough curve. The first-order reversible kinetic model is expressed as follows [428]:

$$\frac{\rho_b}{\theta} \frac{\partial S}{\partial t} = k_{att} \psi C - \frac{\rho_b}{\theta} k_{det} S \quad (4-2)$$

Where  $k_{att}$  ( $\text{min}^{-1}$ ) is the first-order attachment coefficient,  $k_{det}$  ( $\text{min}^{-1}$ ) is the first-order detachment coefficient (equal to 0 for irreversible retention). The function  $\psi$  in the attachment term is a general term that varies according to the attachment mechanisms being modeled (e.g., clean bed, blocking, ripening, etc.). The following attachment mechanisms are considered in this study to simulate the experimental results [412].

(1) Clean bed filtration (CFT) model ( $\psi = 1$ ).

The rate of NPs attachment  $k_{att}$  can be expressed as below:

$$k_{att} = \frac{v}{L} \ln\left(\frac{C_0}{C}\right) \quad (4-3)$$

Where  $L$  is the column length (cm),  $C_0$  and  $C$  represent the influent and steady-state effluent NP concentrations (mg/L), respectively. The steady-state concentration  $C$  is used to evaluate the retention behavior of NPs in the column. The obtained first-order attachment rate coefficient  $k_{att}$  ( $\text{min}^{-1}$ ) can then be used to calculate the attachment efficiency  $\alpha$  (dimensionless) using the following equation [416]:

$$\alpha = \frac{2k_{att}d_c}{3(1-\theta)v\eta_0} \quad (4-4)$$

where  $d_c$  is the diameter of sand grain (cm),  $\alpha$  represents the attachment efficiency (the ratio of particle attached to the collector to all particles colliding with the collector), and  $\eta_0$  is the single collector efficiency (dimensionless), calculated using the Tufenkji-Elimelech equation [74].

(2) Site blocking. The clean bed with site-blocking model includes a maximum retention capacity,  $S_{max}$  ( $\mu\text{g}/\text{g}$ ), to limit NP deposition [412]. This is represented by the following equation:

$$\psi = 1 - \frac{S}{S_{max}} \quad (4-5)$$

In this model,  $\psi$  is a dimensionless Langmuirian blocking function. When the retention capacity  $S_{max}$  is much larger than  $S$ ,  $\psi$  approaches 1, and Equation (2) simplifies to the clean bed filtration model. Initially, there are no NPs associated with the solid phase, making the site-blocking term equal to unity. As NP attachment increases and  $S$  approaches  $S_{max}$ , the site-blocking term approaches zero.

To investigate the presence of multiple kinetic deposition sites, a two-site kinetic model was employed to fit the BTCs using HYDRUS 1-D. This model accounts for both reversible and irreversible kinetic attachment at two different sites, as described by the equation below [414]:

$$\frac{\rho_b}{\theta} \frac{\partial(S_1+S_2)}{\partial t} = k_{a1}\psi_1C + k_{a2}\psi_2C - \frac{\rho_b}{\theta} k_{d1}S_1 \quad (4-6)$$

where  $S_1$  and  $S_2$  are the solid phase NP concentration on site 1 and site 2, respectively.  $k_{a1}$  and  $k_{a2}$  are the attachment rate coefficient for site 1 and site 2, respectively.  $k_{d1}$  is the detachment rate at site 1 and the detachment at site 2 was negligible in this study [414].

(3) Equilibrium and kinetic model. A combined model containing a first-order kinetic component ( $S_k$ ) and an equilibrium component ( $S_e$ ), in accordance with a linear Freundlich isotherm, can be written:

$$\frac{\rho_b}{\theta} \frac{\partial(S_k+S_e)}{\partial t} = k_{att}C - \frac{\rho_b}{\theta} k_{det}S + K_d \frac{\rho_b}{\theta} \frac{\partial C}{\partial t} \quad (4-7)$$

When the kinetic detachment term ( $k_{det}$ ) is neglected, and first-order attachment was assumed to be irreversible, the equilibrium component could be incorporated into 1-D advection-dispersion-reaction (ADR) equation (1):

$$(1 + K_d \frac{\rho_b}{\theta}) \frac{\partial C}{\partial t} = D \frac{\partial^2 C}{\partial z^2} - v \frac{\partial C}{\partial z} - k_{att}C \quad (4-8)$$

$$R = 1 + K_d \frac{\rho_b}{\theta} \quad (4-9)$$

Where  $R$  is the retardation factor and  $K_d$  is the distribution coefficient. Introducing  $K_d$  in NP transport modeling simplifies the attachment/detachment process by reducing the parameters. However, conceptually, the equilibrium assumption is invalid because  $K_d$  is fundamentally based on Gibbs energy and the assumption of thermodynamic equilibrium, whereas NPs are inherently thermodynamically unstable [418]. On the other hand, several authors have successfully applied the concept of  $K_d$  in modeling NP transport [405, 429-431], aligning with other experimental studies that observe retarded BTCs [414, 432]. In this study, “equilibrium retention” of NPs was observed based on the adsorption and desorption experiments, along with obvious retardation in the BTCs of PS NPs. Therefore, the equilibrium-kinetic model

incorporating the distribution coefficient ( $K_d$ ) and retardation factor ( $R$ ) was also considered to fit the BTCs using STANMOD software.

#### 4.2.7. DLVO and XDLVO Interaction Energy

The classical DLVO theory, which accounts for van der Waals attraction and electrostatic double-layer repulsion, was applied to describe the interaction energies between NPs and sand [188, 370]. In the presence of NOM, the extended DLVO (XDLVO) theory was employed to incorporate steric repulsion when evaluating the interaction energies between NPs and sand surfaces. Surface physical heterogeneity or roughness (*Figure S26*), and chemical heterogeneity were also considered in the DLVO and XDLVO interaction calculation [433, 434]. Detailed calculations of DLVO and XDLVO interaction energies are provided in *Text S6*.

### 4.3. Results and Discussion

#### 4.3.1. Two-Stage Deposition of Nanoplastics

The BTCs of 2, 5 and 10 mg/L PS NPs, along with the corresponding total input mass and cumulative breakthrough mass profiles during a single pulse under 10 mM NaCl are depicted in *Figure 4.1a*. The BTC of the tracer (10 mM NaCl) in the column showed distinct single peaks (*Figure S27*), suggesting that NaCl behaved as a non-reactive tracer and confirming the sand-packed column was properly prepared. In contrast with most previous studies, where NP BTC was typically observed after only a few PVs [98, 129], NP suspensions in this study were injected for 25 PVs, to observe the full breakthrough. This study revealed an S-shaped breakthrough pattern: the BTCs of NPs in the first pulse exhibited an initial retardation, followed by a rapid increase, and then a gradual rise until eventually flattening at  $C/C_0 = 0.91$  (*Figure 4.1a*). Also, at lower NP concentrations, the initial NP breakthrough curve was S-shaped but the plateau of constant NP effluent concentration was reached later (*Figure 4.1b* and *Figure 4.1c*). Correspondingly, the cumulative breakthrough mass profiles showed a negligible NP breakthrough in the initial stage, followed by a gradual, linear increase at a near-constant rate until the start of the elution stage.

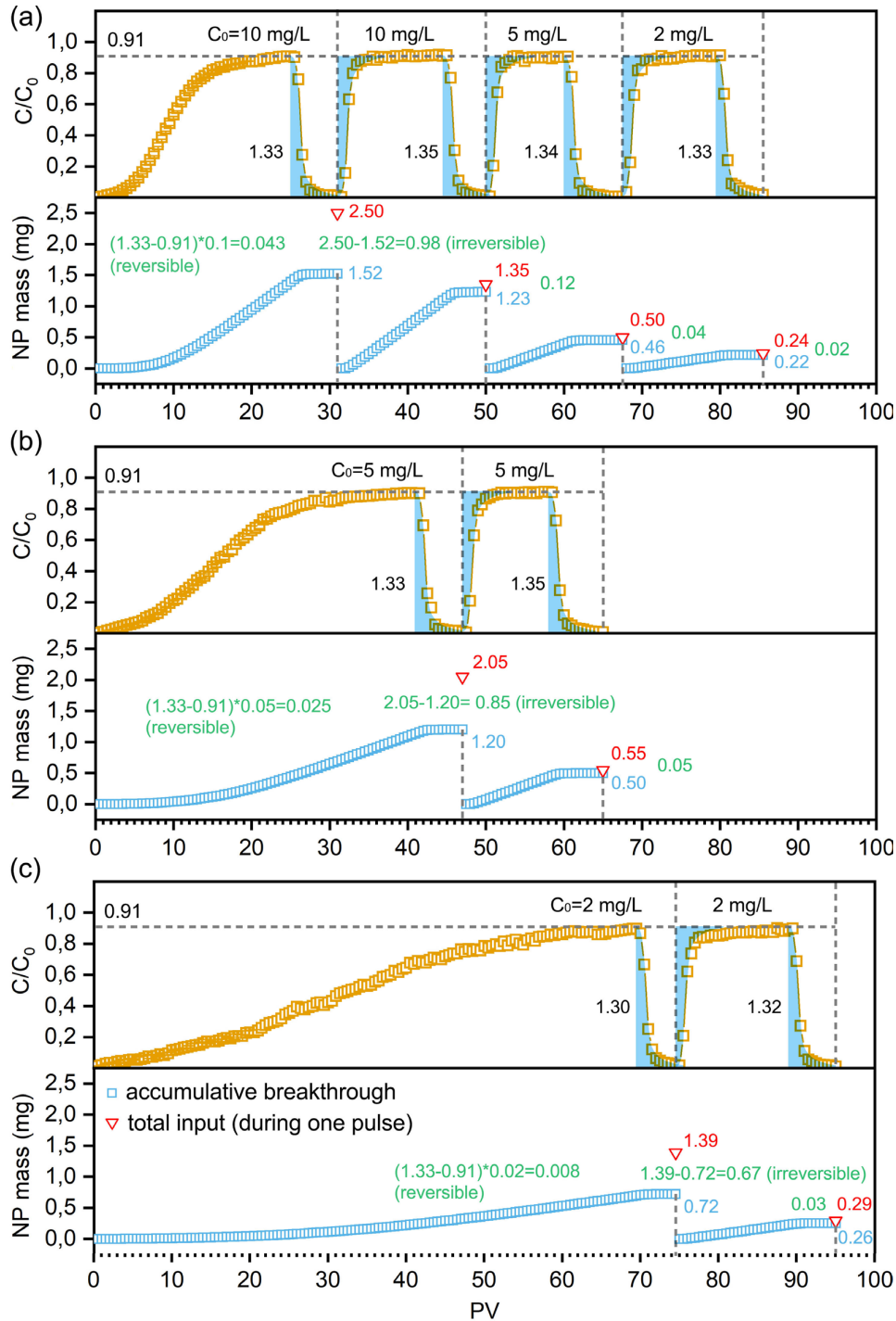


**Figure 4.1.** The BTCs (yellow dots), total input NP mass (red dots), and accumulative breakthrough mass profiles (blue dots) of 2, 5 and 10 mg/L non-weathered NPs during a single pulse in 10 mM NaCl. The red, blue, and green numbers indicate the total input NP mass (mg), total NP breakthrough (mg), and total retention (mg), respectively, during a single pulse. The shaded area under the tail of the curve represents the normalized NP concentration during the

*elution stage, which is symmetric to the shaded region during initial ascent stage. Error bars represent the mean  $\pm$  range (minimum to maximum) ( $n = 2$ ).*

The elution stage with NP-free solution should theoretically result in a washout of  $C/C_0 \cdot PV = 0.91$  (representing the mass of NPs in 1 PV of water) if no detachment occurs. However, the integrated areas under the elution curves during the first pulse were  $C/C_0 \cdot PV = 1.30$ – $1.33$  at different NP input concentrations, suggesting that only a small part of the NPs underwent reversible attachment. This observation is consistent with the results of the batch experiments, where NPs were detached upon replacement with NP-free solution ([Text S5](#) and [Figure S25](#)). By subtracting the total breakthrough (including the elution stage) from the total mass input, the retained NPs were attributed to irreversible attachment. The mass of irreversibly attached NPs was calculated to be in pulse 1 a ( $2.50 \text{ mg} - 1.52 \text{ mg} =$ )  $0.98 \text{ mg}$ , pulse 1 b ( $2.05 \text{ mg} - 1.20 \text{ mg} =$ )  $0.85 \text{ mg}$ , and pulse 1 c ( $1.39 \text{ mg} - 0.72 \text{ mg} =$ )  $0.67 \text{ mg}$  for input concentrations of  $10 \text{ mg/L}$ ,  $5 \text{ mg/L}$ , and  $2 \text{ mg/L}$ , respectively. These results demonstrate that both reversible and irreversible NP attachment are concentration-dependent processes, with irreversible attachment predominating during the first pulse.

Unlike the first pulse BTCs, all concentrations of NPs in the second and subsequent pulses exhibited approximately a normal breakthrough: no noticeable retardation (noticeably breaking through at the first PV) and quickly leveled off at the same plateau (i.e.,  $0.91$ ) ([Figure 4.1](#)). The shaded area under the tail of the curve in the elution stage mirrored that observed during the initial ascent, indicating symmetry between the initial injection and the final elution. This breakthrough pattern is consistent with the principles of traditional CFT that assumes a constant attachment rate under steady-state conditions [412]. Furthermore, the integrated areas under the elution curves during the second and subsequent pulses showed little change compared to the elution stage of the first pulse. This suggests that the amount of reversibly attached NPs remained relatively constant and low between pulses, indicating that NP attachment was predominantly irreversible, and reversible attachment mainly occurred during the initial stage of transport.

Physical straining and site blocking are commonly cited mechanisms explaining the deviation of colloid transport from CFT [405]. Straining refers to the trapping of relatively large particles, where the ratio of particle radius to the median collector radius exceeds  $0.0017$ , within pore throats [435]. As higher concentrations may lead to more colloid aggregation and increased particle size, straining typically results in decreased transport of colloids as the input concentration increases [436]. In this study, PS NPs had a size ratio to sand grains of about  $0.0003$ , showed no aggregation, and demonstrated an opposite concentration-dependent transport behavior, suggesting straining was not the deposition mechanism of PS NPs.

Therefore, to study site blocking, a modeling approach (Equation 4-5) was adopted where a maximum solid stage concentration ( $S_{max}$ ) was added to constrain the NP deposition. As NP attachment increases over time, the available sites on the collector surface are gradually covered by the deposited NPs (as  $S$  approaches  $S_{max}$ ), leaving fewer sites available for further deposition [412]. Typically, increasing the input concentration of particles facilitates their transport, as higher input concentrations lead to greater surface coverage and faster site saturation [437-439]. Therefore, in this study, site blocking might be responsible for the time-dependent and concentration-dependent deposition of PS NPs in the first pulse.

However, the one-site model, both with and without the Langmuirian blocking function, did not adequately fit the entire BTCs in the first pulse (*Figure S28*). On the other hand, the two-site kinetic model with a Langmuirian blocking function for each site provided a good fit for all the BTCs (*Figure S28*). The value of the attachment coefficient  $k_{a1}$  was approximately one order of magnitude larger than  $k_{a2}$  for PS NPs (*Table 4.1*), indicating that NP deposition was dominated by fast deposition at site 1. The time retardation of BTCs was predominantly determined by the values of  $k_{a1}$  and  $S_{max1}$ . A higher value of  $k_{a1}$  indicates a more favorable deposition, leading to complete retention until the solid stage concentration of NPs at site 1 approached  $S_{max1}$ . The above analysis indicates that some reversible attachment could occur during the initial stage of transport; therefore, the detachment rate constant  $k_{d1}$  was incorporated in the two-site blocking model. The fitted values showed that  $k_{d1}$  was approximately one order of magnitude lower than  $k_{a1}$  (*Table 4.1*), suggesting that the attachment process dominated over detachment at site 1 during NP filtration, until saturation. In the batch experiments, the rapid attachment of PS NPs by sand during the initial mixing stage (< 10 min), along with rapid detachment (*Figure S25*), was consistent with rapid attachment during the first NP injection and fast detachment during the initial elution stage in the transport experiments, suggesting that breakthrough curve can be approximated with a model that uses equilibrium processes [440, 441]. Additionally, the observed initial retardation followed by a breakthrough supports the use of an equilibrium-kinetic model, which also well described the BTCs (*Figure S28*). The initial retardation, as indicated by high  $R$  and  $K_r$ , reflected the rapid, instantaneous retention of NPs during the first stage. As particle accumulation continued, the sand surface reached its apparent equilibrium, leading to breakthrough. Subsequently, NP attachment during the plateau ( $k_{att}$ ) was primarily governed by slow kinetic irreversible attachment, consistent with  $k_{a2}$  in the two-site kinetic model. Overall, the modeling further supports a two-stage deposition process of NPs: an initial stage characterized by a low amount of fast, reversible or pseudo-equilibrium attachment until site saturation, followed by a subsequent stage dominated by slow, irreversible attachment.

### 4.3.2. Sand Surface Heterogeneity Creates Favorable Deposition Sites

Typically, primary and secondary energy minima can produce irreversible and reversible deposition sites, with primary-minimum deposition being much more stable than secondary-minimum deposition [407, 409]. Based on DLVO theory calculations (*Figure S29*), a relatively high energy barrier ( $220 k_B T$ ) was observed for NP-sand interactions, making it difficult for the NPs to diffuse over these barriers into the primary energy minimum [442]. The shallow secondary energy minimum of  $-0.145 k_B T$  suggests that only limited NP deposition might occur. Therefore, the visible retardation of BTC and site blocking of PS NPs could not be explained by the classical DLVO theory, although the interaction energy only represents the average value between NPs and sand surfaces. For a homogeneous surface, the attachment potential predicted by the interaction energy would result in a constant deposition rate. However, natural sands are typically physically and chemically heterogeneous, leading to variations in the interaction energies between particles and different locations on the heterogeneous surfaces [443], which might explain the deviation from the classical DLVO and CFT.

To elucidate the underlying mechanism behind the observed retardation phenomenon, the transport behavior of PS NPs in 10 mM NaCl was tested using sands from various sources, as shown in *Figure 4.2*. Site blocking was observed across all types of sands; however, differences in retardation were evident. Specifically, negligible retardation occurred in Sigma-1 sands with diameters of 0.425–0.6 mm and 0.2–0.425 mm, whereas considerable retardation was observed in the 0.210–0.297 mm Sigma-2 sand, similar to the behavior seen with vidaXL sand. SEM images exhibited that the surface of Sigma-1 sand was relatively smooth, with regular shallow scratches or grooves (*Figure 4.2b*). However, the surfaces of vidaXL sand and Sigma-2 sand exhibited numerous irregularities and pronounced unevenness. Most NPs tended to accumulate at these rough sites, suggesting that physical heterogeneity was likely responsible for the retardation of NPs in vidaXL and Sigma-2 sand (*Figure 4.2b*). In a previous study [444], we observed a similar phenomenon, where retardation of silver nanoparticles occurred in rough sand, while negligible retardation was noted in relatively smooth sand.

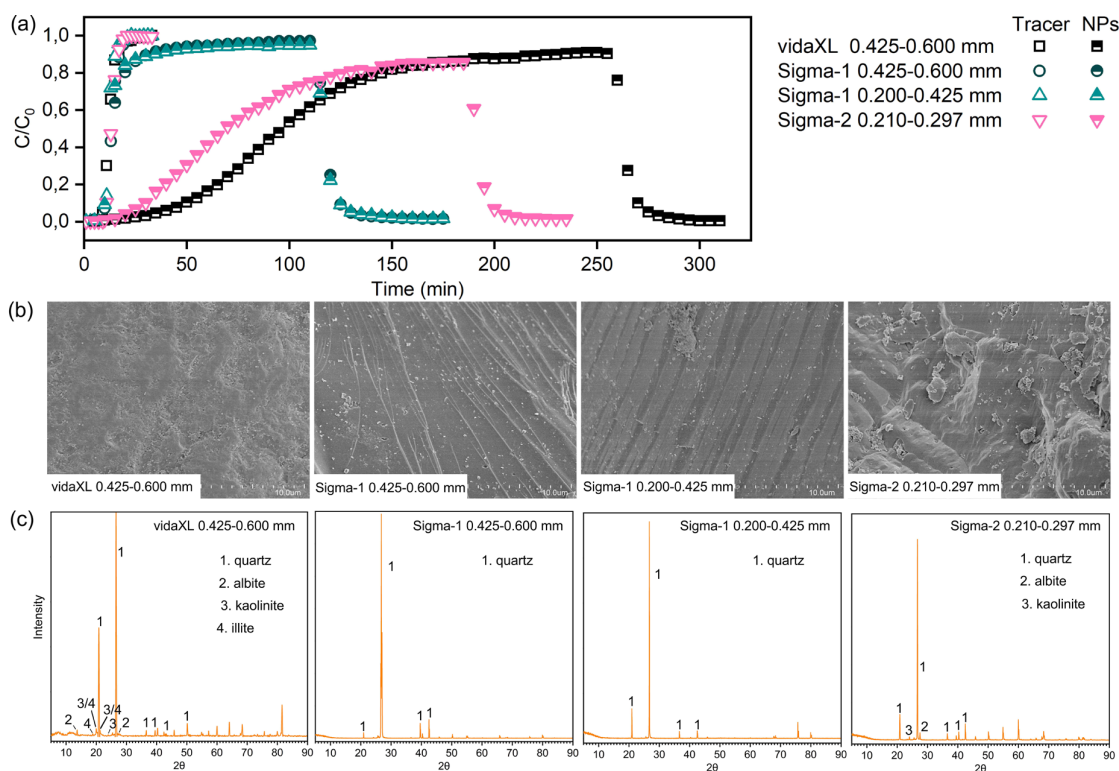


**Figure 4.2.** (a) the BTCs of tracer and NPs in different types of sand, (b) the SEM images showing sand morphology and NP deposition on sand surfaces, and (c) the XRD spectra of the various sand types.

The surface roughness of sand including protruding asperities and concave areas can create favorable sites for NP attachment under unfavorable conditions [413, 414]. As calculated, the energy barrier decreased from 220  $k_B T$  to 84.6  $k_B T$ , 44.1  $k_B T$ , and 33.5  $k_B T$  in the presence of 50 nm, 20 nm, and 10 nm convex asperities, respectively (Figure S29). Irreversible attachment at the primary energy minimum may be enhanced at the tops of nanoscale protruding asperities [443]. Studies further indicate that colloid immobilization under unfavorable conditions may arise from wedging within grain-grain junctions [445, 446]. Instead of overcoming the energy barrier, colloids may migrate along collector surfaces via secondary-minimum interactions until they become immobilized in regions with reduced hydrodynamic shear, such as interstitial spaces between grains [445, 446].

In addition, microscopic analyses showed that the 0.425–0.6 mm and 0.2–0.425 mm Sigma-1 sands were clean and transparent with no visible impurities, whereas the 0.210–0.297 mm Sigma-2 sand and vidaXL sand exhibited colored hues (Figure S30). Despite sequential treatments with HCl, NaOH, and thermal combustion to remove metal oxides and organic impurities, certain clay minerals might have remained due to their resistance to these treatments [447]. SEM-EDS and XRD analyses confirmed the potential presence of minerals

in vidaXL sand (albite, kaolinite, and illite) and in the 0.210–0.297 mm Sigma sand (albite and kaolinite) (*Figure S31* and *Figure 4.2c*) [448]. The presence of minerals was also associated with the less negative zeta potential of vidaXL sand ( $-41.7 \pm 0.8$  mV) and 0.210–0.297 mm Sigma-2 sand ( $-45.5 \pm 0.5$  mV) compared to the 0.425–0.6 mm ( $-46.8 \pm 1.3$  mV) and 0.2–0.425 mm ( $-40.4 \pm 0.7$  mV) Sigma-1 sands (*Figure S32*), likely due to positively charged edge positions such as  $\text{Al}^{3+}$  [449–451]. Considering the chemical heterogeneity, the energy barrier decreased from  $220 k_{\text{B}}T$  to  $163 k_{\text{B}}T$ ,  $119 k_{\text{B}}T$ , and  $34.1 k_{\text{B}}T$  in the presence of a positively charged area (e.g., + 40 mV) with size of 10 nm, 20 nm, and 50 nm, respectively (*Figure S29c1*), thereby promoting irreversible attachment at the primary energy minimum. Concurrently, the secondary energy minimum increased from  $0.145 k_{\text{B}}T$  to  $0.155 k_{\text{B}}T$ ,  $0.165 k_{\text{B}}T$ , and  $0.217 k_{\text{B}}T$  (*Figure S29c2*), enhancing the potential for irreversible attachment. Although previous studies did not explicitly mention retardation, the findings have suggested a potential link between the observed retardation of colloids and the presence of clay minerals [447, 451, 452]. For instance, increasing contents of clay minerals such as kaolinite, montmorillonite, and illite have appeared to cause more retardation of NPs [423, 451, 452]. Using the same 0.210–0.297 mm Sigma-2 sand, retardation has also been observed for PS NPs [67], and graphene oxide nanoparticles [453].

Consequently, the combined physical and chemical heterogeneity of sand surfaces in sand can lead to a wide distribution of primary and/or secondary minimum depths as well as attenuated hydrodynamic shear forces, which contribute to the observed breakthrough behavior of NPs. As reported, attachment to kinetically limited sites occurs in the primary energy minimum where overcoming an energy barrier is required, while attachment to fast equilibrium sites takes place in the secondary energy minimum [454]. In the initial stage, surface heterogeneity creates numerous favorable locations for both rapid reversible (less important) and irreversible (dominant process) NP attachment at these energy minima, leading to initial NP retardation. As these high-affinity sites become saturated, they are no longer available for further attachment, resulting in site blocking. Subsequently, during the second or third NP pulses, incoming NPs deposit predominantly onto relatively smooth surfaces, where irreversible attachment at the primary energy minimum dominates [409, 455].

#### 4.3.3. UV Weathering Reduces Surface Heterogeneity Effects

The BTCs for both pristine and UV-weathered NPs in sand columns are depicted in Figure 3. Compared to the pristine NPs, the UV-weathered NPs exhibited earlier breakthrough. The concentration plateau was reached faster as the aging time increased, indicating that photo-oxidation enhanced NP mobility (*Table 4.1*). The equilibrium-kinetic model and two-site kinetic model also accurately described the transport of UV-weathered NPs (*Figure S28*). The reduction in  $K_d$  from an initial value of 2.15 mL/g to 1.54 mL/g, 1.37 mL/g and 1.06 mL/g

indicates that the retention capacity of sand for PS NPs decreased with UV weathering. This trend was consistent with the batch experiments, where the removal of NPs after 48 h decreased from 82.0% for PS<sub>0</sub> to 58.0%, 49.9%, and 32.8% for PS<sub>2</sub>, PS<sub>4</sub>, and PS<sub>8</sub>, respectively (Figure S25). The initial  $k_{a1}$  value of 1.038 min<sup>-1</sup> for PS<sub>0</sub> reduced to 0.464 min<sup>-1</sup>, 0.328 min<sup>-1</sup>, and 0.300 min<sup>-1</sup> for PS<sub>2</sub>, PS<sub>4</sub>, and PS<sub>8</sub>, respectively. The same trend was observed for  $k_{a2}$  and  $k_{att}$ . Correspondingly,  $S_{max1}$  exhibited a decrease from 8.84 µg/g for PS<sub>0</sub> to 6.12 µg/g, 3.01 µg/g, and 2.96 µg/g for PS<sub>2</sub>, PS<sub>4</sub>, and PS<sub>8</sub>, respectively, while  $S_{max2}$  dropped from 0.632 µg/g for PS<sub>0</sub> to 0.391 µg/g, 0.310 µg/g, and 0.276 µg/g for PS<sub>2</sub>, PS<sub>4</sub>, and PS<sub>8</sub>, respectively. Similar to pristine NPs, multi-site deposition was observed for UV-weathered NPs; however, the number of available sites was lower compared to the pristine NPs. This reduction likely reflected changes in surface properties of the NPs, impacting their interaction dynamics with the collector surfaces.

Since the UV-weathered NPs carried a more negative charge compared to pristine ones (Figure S11), the increased electrostatic repulsion between the NPs and sand could be a contributing factor for the reduced retention [129]. Table S13 shows the energy barrier and secondary energy minimum between NPs and heterogeneous/homogeneous surfaces. Although surface roughness greatly reduced the energy barriers, the barriers between UV-weathered NPs and convex asperity (e.g., 10 nm) (46.1–52.4 k<sub>B</sub>T) remained higher than those for pristine NPs (33.5 k<sub>B</sub>T). Meanwhile, the secondary minimum between NPs and concave valley decreased (0.090–0.196 k<sub>B</sub>T vs. 0.507 k<sub>B</sub>T). Although the presence of positively charged areas may favor the attachment of more negatively charged UV-weathered NPs, DLVO calculations still predicted higher energy barriers (54.2–96.2 k<sub>B</sub>T vs. 34.1 k<sub>B</sub>T) and shallower secondary minima (0.038–0.079 k<sub>B</sub>T vs. 0.217 k<sub>B</sub>T) between UV-weathered NPs and a positively charged area (e.g., 50 nm, + 40 mV) (Table S13), due to the dominant influence of the surrounding negatively charged surface. It indicates that UV weathering reduced both irreversible deposition at the primary energy minimum and reversible deposition at the secondary energy minimum. Furthermore, UV weathering rendered these originally favorable heterogeneous sites for non-weathered NPs unfavorable, leading to the reduced retardation and the rapid reaching of the steady-state plateau observed in the BTCs of UV-weathered NPs. Although not emphasized by the respective authors, carboxyl group-functionalized NPs that mimic weathered NPs, exhibited negligible retardation compared to their non-functionalized counterparts when transported through Sigma sand with an average diameter of 0.260 µm [67]. Therefore, UV weathering can reshape NP surface properties, reducing the influence of sand surface heterogeneity and causing NPs to undergo distinct transport dynamics.

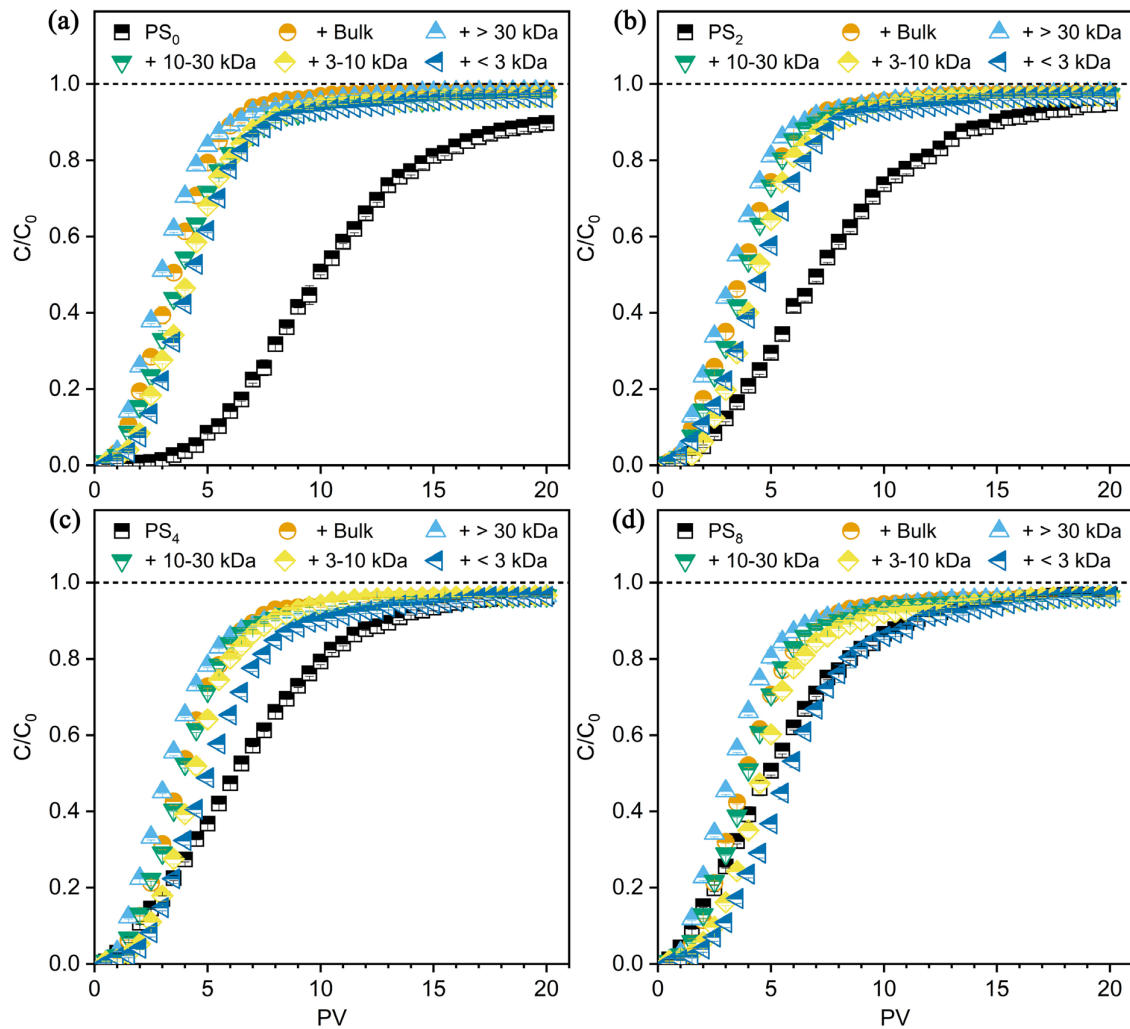


**Figure 4.3.** The BTCs of non-weathered and UV-weathered NPs in the absence and presence of bulk NOM and NOM fractions (2 mg C/L) in 10 mM NaCl. Subscripts 0, 2, 4 and 8 mean aging times of 0, 2, 4 and 8 d. Error bars represent the mean  $\pm$  range (minimum to maximum) ( $n = 2$ ).

**Table 4.1.** The average effluent concentration, attachment efficiency, and the fitted parameters using two-site kinetic model and equilibrium-kinetic model.  $C/C_0$  and  $C_2/C_0$  are the overall and steady-state plateau average effluent concentrations, respectively.  $\alpha$  and  $\alpha_2$  are the overall and steady-state attachment efficiency, respectively.  $\alpha_1$  ( $= \alpha - \alpha_2$ ) represents the attachment efficiency before steady-state plateau.

	$C/C_0$	$\alpha$	$C_2/C_0$	$\alpha_2$	$\alpha_1$	$S_{max1}$ ( $\mu\text{g/g}$ )	$k_{a1}$ ( $\text{min}^{-1}$ )	$k_{d1}$ ( $\text{min}^{-1}$ )	$S_{max2}$ ( $\mu\text{g/g}$ )	$k_{a2}$ ( $\text{min}^{-1}$ )	R	$K_r$ ( $\text{mL/g}$ )	$k_{att}$ ( $\text{min}^{-1}$ )
PS <sub>0</sub>	0.559	9.40E-02	0.912	1.49E-02	7.91E-02	8.84	1.038	0.104	0.632	2.15E-02	10.03	2.153	9.93E-03
PS <sub>0</sub> + bulk	0.814	3.29E-02	0.979	3.38E-03	2.95E-02	0.72	0.266	0.039	0.161	3.88E-03	3.64	0.629	2.41E-03
PS <sub>0</sub> + > 30 kDa	0.826	3.03E-02	0.974	4.11E-03	2.62E-02	0.97	0.267	0.097	0.185	9.57E-03	3.24	0.534	3.36E-03
PS <sub>0</sub> + 10-30 kDa	0.780	3.98E-02	0.964	5.93E-03	3.39E-02	1.07	0.315	0.062	0.256	9.99E-03	4.01	0.718	4.55E-03
PS <sub>0</sub> + 3-10 kDa	0.767	4.28E-02	0.964	5.97E-03	3.69E-02	1.32	0.426	0.083	0.276	7.94E-03	4.26	0.776	4.82E-03
PS <sub>0</sub> + < 3 kDa	0.752	4.62E-02	0.960	6.58E-03	3.97E-02	1.53	0.475	0.096	0.309	8.37E-03	4.49	0.832	5.34E-03
PS <sub>2</sub>	0.681	6.48E-02	0.958	7.29E-03	5.75E-02	6.12	0.464	0.017	0.391	1.85E-02	7.46	1.540	5.28E-03
PS <sub>2</sub> + bulk	0.798	3.76E-02	0.972	4.69E-03	3.29E-02	0.91	0.314	0.044	0.324	4.94E-03	3.82	0.672	4.34E-03
PS <sub>2</sub> + > 30 kDa	0.813	3.43E-02	0.971	4.80E-03	2.95E-02	0.92	0.292	0.062	0.340	6.83E-03	3.40	0.573	4.66E-03
PS <sub>2</sub> + 10-30 kDa	0.786	3.97E-02	0.970	5.11E-03	3.46E-02	0.81	0.331	0.032	0.337	7.58E-03	3.94	0.701	4.76E-03
PS <sub>2</sub> + 3-10 kDa	0.759	4.59E-02	0.966	5.73E-03	4.01E-02	1.11	0.509	0.063	0.303	9.85E-03	4.46	0.825	5.12E-03
PS <sub>2</sub> + < 3 kDa	0.748	4.86E-02	0.960	6.77E-03	4.18E-02	0.82	0.321	0.079	0.372	8.45E-03	4.66	0.874	4.93E-03
PS <sub>4</sub>	0.723	5.71E-02	0.961	7.09E-03	5.00E-02	3.01	0.328	0.024	0.310	4.85E-03	6.76	1.373	2.83E-03
PS <sub>4</sub> + bulk	0.781	4.26E-02	0.961	6.76E-03	3.58E-02	1.70	0.452	0.115	0.331	6.97E-03	3.99	0.712	4.13E-03
PS <sub>4</sub> + > 30 kDa	0.797	3.91E-02	0.961	6.78E-03	3.23E-02	1.16	0.322	0.098	0.332	1.32E-02	3.47	0.589	5.70E-03
PS <sub>4</sub> + 10-30 kDa	0.776	4.37E-02	0.962	6.62E-03	3.71E-02	0.79	0.342	0.035	0.308	1.14E-02	4.03	0.722	5.12E-03
PS <sub>4</sub> + 3-10 kDa	0.755	4.92E-02	0.963	6.56E-03	4.26E-02	1.25	0.580	0.084	0.269	1.08E-02	4.51	0.837	4.82E-03
PS <sub>4</sub> + < 3 kDa	0.715	5.92E-02	0.962	6.90E-03	5.22E-02	3.06	0.681	0.136	0.330	1.36E-02	5.22	1.006	5.82E-03
PS <sub>8</sub>	0.765	4.84E-02	0.966	6.26E-03	4.21E-02	2.96	0.300	0.058	0.276	1.31E-02	5.43	1.057	3.30E-03
PS <sub>8</sub> + bulk	0.771	4.67E-02	0.960	7.30E-03	3.94E-02	2.15	0.466	0.116	0.347	6.87E-03	4.09	0.736	3.85E-03
PS <sub>8</sub> + > 30 kDa	0.798	4.05E-02	0.960	7.37E-03	3.32E-02	1.31	0.334	0.106	0.329	1.05E-02	3.40	0.571	5.52E-03
PS <sub>8</sub> + 10-30 kDa	0.766	4.79E-02	0.961	7.19E-03	4.08E-02	0.84	0.353	0.039	0.338	1.13E-02	4.07	0.732	5.55E-03
PS <sub>8</sub> + 3-10 kDa	0.731	5.60E-02	0.962	6.99E-03	4.90E-02	2.31	0.587	0.073	0.342	1.44E-02	4.65	0.871	6.54E-03
PS <sub>8</sub> + < 3 kDa	0.728	5.67E-02	0.962	6.98E-03	4.97E-02	4.71	0.741	0.138	0.337	1.75E-02	6.01	1.194	5.78E-03

#### 4.3.4. NOM Reduces Surface Heterogeneity Effects

The retardation of pristine NPs decreased in the presence of NOM, as evidenced by the rapid breakthrough of NPs at first PV (*Figure 4.2*). After NOM addition, the attachment efficiencies  $\alpha_1$  and  $\alpha_2$  reduced from 0.079 and 0.015 to 0.030 and 0.003, respectively, corresponding to the reduction in  $K_d$  and  $k_{att}$  in the equilibrium-kinetic model. Based on the two-site model fitting, the parameters  $S_{max1}$  and  $S_{max2}$  decreased from 8.84  $\mu\text{g/g}$  and 0.632  $\mu\text{g/g}$  to 0.720  $\mu\text{g/g}$  and 0.161  $\mu\text{g/g}$  after the addition of NOM, indicating that NP deposition on both heterogeneous and homogeneous surfaces decreased. Batch adsorption experiments revealed that 9% of NOM adsorbed onto PS NPs (*Figure S13*). Additionally, the adsorption of NOM greatly increased the negative charge of the pristine NPs (*Figure S11*), probably due to the charge superposition of the adsorbed NOM [357, 380]. The increase in electrostatic repulsion likely explains the enhanced mobility of NPs in the presence of NOM [94]. Steric repulsion due to NOM adsorption is typically considered a key factor contributing to increased mobility of engineered colloids in porous media, such as graphene oxide [456], ZnO [457], and Ag [458], as well as PS NPs [67, 89]. In this study, steric repulsion likely played a critical role in increasing the mobility of PS NPs as well. According to XDLVO theory, NOM adsorption greatly increased the energy barrier between NPs and sand surfaces (*Table S13*), thereby reducing the irreversible deposition of NPs.

Similar to pristine NPs, the deposition of UV-weathered NPs on heterogeneous and homogeneous surfaces reduced in the presence of NOM, as indicated by reductions in the fitted parameters  $k_{a1}$ ,  $k_{a2}$ ,  $S_{max1}$  and  $S_{max2}$ , as well as  $K_d$  and  $k_{att}$ . In contrast to the pristine NPs, the zeta potential of UV-weathered NPs, especially PS<sub>4</sub> and PS<sub>8</sub>, became less negative in the presence of NOM (*Figure S11*). Limited studies have reported this phenomenon, but we propose that the reduction in negative charges may be attributed to the shielding of charges or oxygen-containing groups on UV-weathered NPs by NOM [425]. Furthermore, this effect was more pronounced as UV aging time increased, due to the generation of more surface oxygen-containing groups on the more weathered NPs (*Figure S11*). Although NOM could decrease the electrostatic repulsion between UV-weathered NPs and the sand, steric repulsion may outweigh the effects of reduced electrostatic interaction. XDLVO theory suggested that NOM-induced short-distance steric repulsion primarily affected the energy barriers between UV-weathered NPs and both heterogeneous and homogeneous surfaces, with minimal impact on the secondary energy minimum (*Table S13*). This led to a reduction in the irreversible deposition of UV-weathered NPs at the primary energy minimum.

Similar to UV weathering, the weathering of NPs by NOM also diminished the effect of sand surface heterogeneity on NP transport and greatly reduced retardation. Different effects of NOM on NP transport dynamics have been identified in previous studies, although not

explicitly highlighted. For instance, on standard quartz sand and glass beads, NPs have exhibited a steady-state breakthrough, and model NOM compounds such as humic acid, bovine serum albumin, and sodium alginate have been found to only enhance the height of the BTC plateau without altering the overall transport dynamics [88, 459]. However, in the study by Zhu et al., retardation of pristine NPs has been observed in Sigma sand (0.260 mm), while NOM components such as fulvic acid, humic acid, and macromolecular extracellular polymeric substances (EPS) have been found to reduce this retardation. In particular, EPS appeared to eliminate retardation entirely, resulting in a near steady-state breakthrough [67]. Similarly, low-molecular-weight organic acids have been observed to reduce the retardation of NPs in columns using sand sourced from Tianjin Guangfu Technology Development Co., Ltd. [460]. These findings highlight the complex interplay between NP weathering by NOM and sand surface heterogeneity in shaping NP transport.

#### 4.3.5. NOM Molecular Weight-Dependent Deposition of Nanoplastics

NOM is a heterogeneous group of compounds with varying MW and chemical properties [393]. The MW of NOM could determine its reactivity with NPs and control their mobility in porous media [67]. For pristine NPs in the presence of NOM fractions, the attachment efficiencies  $\alpha$ ,  $\alpha_1$  and  $\alpha_2$  generally decreased as the MW of NOM increased, indicating that mostly the higher-MW NOM increased NP mobility. In the equilibrium-kinetic model, the  $K_d$  value increased from 0.534 mL/g to 0.718 mL/g, 0.776 mL/g, and 0.832 mL/g, and  $k_{att}$  increased from 0.0034 min<sup>-1</sup>, 0.0034 min<sup>-1</sup>, 0.0046 min<sup>-1</sup>, 0.0048 min<sup>-1</sup> as NOM MW decreased. Similarly,  $k_{a1}$ ,  $S_{max1}$ ,  $S_{max2}$  decreased with increasing NOM MW, whereas  $k_{a2}$  showed no obvious correlation. This suggests that NOM with a higher MW had a stronger capacity to reduce the deposition of NPs. Higher-MW NOM with larger molecular size and greater aromaticity, could form a thicker adsorption layer via hydrophobic and  $\pi$ - $\pi$  interactions (Figure S14), enabling higher-MW NOM to induce stronger steric repulsion, thereby enhancing the mobility of pristine NPs. XDLVO theory revealed that the energy barriers between NPs and sand surfaces increased with higher NOM MW, while the secondary energy minima between NPs and sand surfaces remained nearly unchanged across different NOM MWs. Therefore, NOM MW primarily influenced the availability of irreversible deposition sites on heterogeneous and homogeneous surfaces.

For UV-weathered NPs, a similar trend was observed, with higher mobility in the presence of higher MW NOM. However, not all MW NOMs enhanced the mobility of UV-weathered NPs. As evidenced by the increase in attachment efficiencies  $\alpha$ , the presence of < 3 kDa and 3-10 kDa NOM reduced the mobility of PS<sub>4</sub> and PS<sub>8</sub>. Although all NOM fractions reduced the negative charges of UV-weathered NPs, the adsorption of lower MW NOM (e.g., < 3 kDa) on PS<sub>4</sub> and PS<sub>8</sub> was negligible (Figure S13). We propose that a competition between electrostatic

interaction and steric repulsion was at play. In the presence of higher MW NOM, the additional steric repulsion outweighed the reduced electrostatic repulsion, leading to enhanced mobility of UV-weathered NPs. Conversely, with lower MW NOM, the reduced electrostatic repulsion dominated, resulting in increased deposition of PS<sub>4</sub> and PS<sub>8</sub>. According to XDLVO predictions, the energy barrier between PS<sub>8</sub> and convex asperity increased from 52.4 k<sub>B</sub>T to 62.4 and 58.9 k<sub>B</sub>T in the presence of > 30 kDa and 10–30 kDa NOM, respectively, but decreased to 43.1 and 42.1 k<sub>B</sub>T in the presence of 3–10 kDa and < 3 kDa NOM, respectively (*Table S13*). On smooth surfaces, the energy barriers remained high (> 260 k<sub>B</sub>T) both in the absence and presence of NOM fractions. Therefore, the influence of NOM and its fractions on the irreversible deposition of UV-weathered NPs primarily occurred on these heterogeneous surfaces.

#### 4.4. Environmental Implications

This study focused on the deposition mechanisms of non-weathered and weathered PS NPs in saturated porous media under typically low ionic strength conditions. Our findings reveal that the transport dynamic of NPs deviated from traditional CFT and DLVO theory. Instead, a two-stage transport with mostly irreversible and to a lesser degree also reversible attachment was observed, particularly for non-weathered NPs during the first filtration pulse. This retardation behavior is often overlooked in other studies [94, 97, 447], as it can resemble steady-state transport with a very low breakthrough when breakthrough curves are measured over short timeframes and/or at low concentrations of NPs. These results highlight the importance of considering the full breakthrough curve, especially during the first filtration pulse.

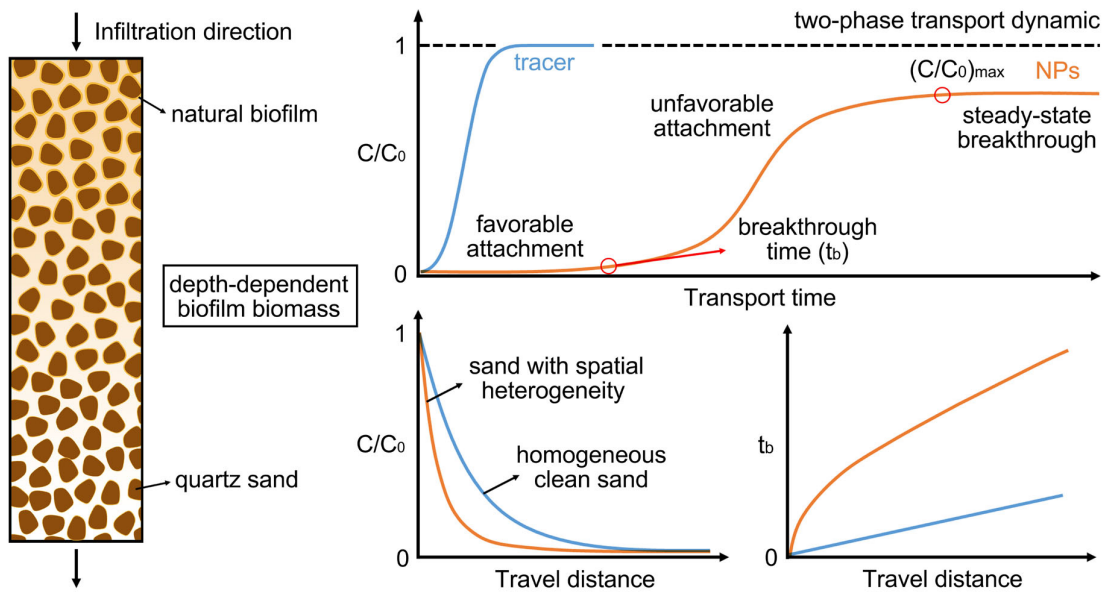
The study also reveals the critical role of sand grain physical and chemical heterogeneity in this two-stage transport of NPs. It can explain deviations in transport behaviors observed across previous studies [67, 410, 414, 422, 451], as traditional cleaning methods, such as acid treatment, cannot fully eliminate chemical heterogeneity in certain sand sources. Moreover, it suggests that clean, ideal quartz sands or glass beads are inadequate representations of natural sands in transport studies, as impurities in natural sands, such as minerals and organic matter, can make NP undergo distinct transport dynamics. Although weathering of NPs may diminish this effect, it nonetheless challenges the applicability of CFT and steady-state transport assumptions for predicting NP behavior in natural sand systems.

Additionally, this study underscores the role of natural weathering in reshaping the transport behaviors of NPs, particularly in masking the influence of sand surface heterogeneity on retardation. This phenomenon also helps explain the distinct transport behaviors reported in literature, where different studies often employ commercial NPs with diverse surface functionalities and stabilizing coatings. For instance, carboxyl-functionalized NPs have exhibited steady-state breakthrough behavior, in contrast to non-functionalized NPs [67].

Many commercial NPs are stabilized with surfactants such as sodium dodecyl sulfate, which can mask surface charge heterogeneities and reduce deviations from CFT [410, 461]. These commercial carboxyl-functionalized and coating-modified NPs may partially resemble the transport dynamics of weathered NPs. However, they may not adequately represent the physicochemical properties or dynamic interactions of real-world NPs in natural environments. To better reflect real-world scenarios, future studies should prioritize the use of weathered NPs in natural waters, whose surfaces can vary depending on water matrices, such as the composition and concentration of NOM.

# Chapter 5

## Beyond Classic Colloid Filtration: the Role of Natural Weathering and Biofilm Spatial Heterogeneity in Nanoplastic Transport and Predictive Modeling During Riverbank Filtration



## Abstract

Riverbank filtration (RBF) is a widely used natural treatment process to remove contaminants for drinking water production via biodegradation and filtration. Its potential to remove also nanoplastics (NPs), a new pollutant of concern for human health, is still unclear. Predicting NP transport during RBF remains challenging, particularly with spatially heterogeneous biofilms, driven by oxygen and nutrient gradients during infiltration, adding to the complexity. We constructed a simulated RBF to cultivate natural biofilms and study how spatially heterogeneous biofilm distributions influence NP transport. Distinct from traditional clean bed filtration theory (CFT), we identified a two-stage transport dynamic of NPs: an initial retardation dominated by favorable attachment until breakthrough, followed by unfavorable attachment until an approximate steady-state breakthrough was reached. Biofilms, particularly in the upper layer of the sand column, enhanced both favorable and unfavorable NP attachment, with both attachment stages decreasing with depth and positively correlating with biofilm biomass. Moreover, weathering of NPs in river water through eco-corona formation inhibited initial favorable deposition while promoting unfavorable deposition, ultimately reducing NP transport potential. Leveraging the two stage transport, we predicted NP travel distance and breakthrough time in spatially heterogeneous natural sand. These findings provide valuable insights for refining predictive models and guiding the design of engineered filtration systems to mitigate NP contamination.

## 5.1. Introduction

Nanoplastics (NPs), defined as plastic particles smaller than 1  $\mu\text{m}$ , are increasingly recognized as ubiquitous contaminants in the environment [401]. Due to their small size and large surface area, NPs exhibit a high mobility, raising concerns about their potential ecological and human health impacts [401]. NPs can originate from primary sources, such as engineered NPs, used in industrial applications [402], or as secondary products from the fragmentation and degradation of larger plastic debris, including microplastics, under environmental stressors like UV radiation, mechanical abrasion, and chemical oxidation [403]. NPs have been detected in various freshwater bodies, including surface water [10, 15], groundwater [10], and even treated drinking water [462]. As plastics continue to accumulate in fresh water, the level of NPs is expected to rise, raising concerns about the safety of e.g. drinking water. Riverbank filtration (RBF) is a widely implemented natural water treatment process, particularly in Europe, where it contributes to drinking water production [101]. In this process, river water infiltrates through bank sediments toward abstraction wells, undergoing a combination of physical filtration, biological degradation, and geochemical transformation [105, 106].

Given the widespread use of RBF for drinking water production, it is essential to also understand NP transport and retention in RBF, in order to assess potential risks to drinking water quality. Numerous experimental and mathematical modeling studies have been performed to understand NP transport and deposition in porous media. Among the most commonly used theoretical frameworks for describing NP transport are the clean bed filtration (CFT) and the classical and modified Derjaguin–Landau–Verwey–Overbeek (DLVO) theories [74, 408]. NP transport has extensively been evaluated using model polystyrene (PS) NPs in small-scale columns, packed with clean quartz sand, under varying conditions, including flow rate, flow orientation, water saturation [87], solution chemistry (e.g., pH, ionic strength, and ion valence)[88], and the presence of coexisting environmental colloids and molecules, particularly natural organic matter (NOM) [88, 89]. Adsorption of NOM onto NPs can lead to the formation of an eco-corona, representing environmentally relevant forms of weathered NPs. Studies using model NOM have shown that the eco-corona typically enhances NP mobility in porous media by increasing electrostatic repulsion [88, 94], or introducing additional steric hindrance (elastic and osmotic interaction) [67, 89]. However, the influence of eco-coronas formed under environmentally relevant conditions, such as in natural waters with complex NOM composition and variable aqueous chemistry, remains poorly understood.

Unlike laboratory conditions that often use clean quartz sand, natural sand grains in the subsurface are typically coated with organic and biological materials [463]. In these settings, microorganisms preferentially attach to grain surfaces and develop thin, patchy biofilms [464]. Biofilms are structured communities of sessile microorganisms embedded within a self-produced matrix of extracellular polymeric substances (EPS), and they can constitute the majority of bacterial biomass in natural porous media [463, 465]. Especially during RBF, a condensed biologically active surface sediment layer, commonly referred to as the colmation layer or *Schmutzdecke*, plays an important role in effectively removing suspended solids, pathogens, and other contaminants [101]. The role of biofilms in NP deposition has primarily been studied using biofilms derived from single-species bacterial models, such as *Pseudomonas aeruginosa* and *Escherichia coli* [97, 98]. For example, He et al. have reported that biofilms formed by *E. coli* enhance PS NP retention in porous media by increasing surface roughness, restricting flow paths, and facilitating hydrogen bonding between EPS and the NPs [97]. Although these studies provide mechanistic insights into the potential role of biofilms in NP transport, they do not fully reflect real-world conditions, where natural biofilms are typically heterogeneous and composed of diverse microbial communities.

In natural RBF systems, biofilms also exhibit pronounced spatial heterogeneity along infiltration gradients due to progressive oxygen and nutrient depletion [101]. This ecological zonation gives rise to stratified microbial communities and results in variability in biofilm

biomass, composition, and physicochemical properties (e.g., surface charge, hydrophobicity, and EPS content) [466, 467], all of which can influence NP interactions with porous media. However, the influence of spatially heterogeneous biofilms on NP transport and removal in RBF remains poorly understood. In addition, traditional models for predicting long-distance NP transport in the field are largely based on small-scale laboratory experiments conducted under simplified conditions, which fail to capture the complexity of natural systems. To improve the accuracy and applicability of these models, it is essential to incorporate the spatial variability of natural biofilms under environmentally relevant conditions. Addressing this knowledge gap will be critical for developing more realistic and predictive frameworks for assessing NP fate and transport in RBF systems.

Therefore, the main objective of this study is to elucidate how the spatial heterogeneity of biofilms influences the transport and removal of NPs, thereby improving predictive models for RBF systems. We address three key questions grounded in identified research gaps: (1) How does biofilm-induced weathering (spatially heterogeneous biofilms) of sand surfaces influence NP migration? (2) How does the weathering of NPs in natural waters affect their transport? and (3) How can incorporating natural weathering and biofilm spatial heterogeneity improve the predictive accuracy of NP transport models? To investigate these questions, we constructed long (90 cm), segmented columns, packed with clean sand, that were continuously fed with river water from an RBF site in the Netherlands to allow biofilm development over periods of 1, 3, and 6 months. Following biofilm growth, the column segments were separated into 10-cm short, undisturbed sections, representing different filter depths, which were then used for NP transport experiments. First, we explored the transport mechanisms of NPs in columns with and without biofilm. We then examined how spatially heterogeneous biofilms at different filter depths affected the transport and retention capacity of NPs. Additionally, we conducted transport experiments in the column segments to compare the transport of non-weathered NPs in synthetic water with that of environmentally weathered NPs in river water to evaluate the role of naturally formed eco-coronas on NP mobility. Finally, we developed several modeling approaches that incorporate spatial biofilm heterogeneity to predict NP retention and transport in RBF systems.

## 5.2. Materials and Methods

### 5.2.1. Biofilm Inoculation and Development in Laboratory

Seven long, segmented acrylic glass columns, each 90 cm in length, were assembled by connecting ten short segments (9 cm in length, 2 cm in diameter) via threaded joints (see [Figure S33](#) for the experimental setup). Each segment was packed with clean quartz sand

(particle diameter: 0.425–0.6 mm). The sand was purchased from vidaXL and cleaned sequentially by soaking it in concentrated 5.0 M NaOH for 24 hours, followed by treatment with 12 M concentrated HCl for another 24 hours to remove organics and metals following previously published protocols [197]. After chemical treatment, it was thoroughly rinsed with ultrapure water until the pH stabilized, then dried and heated at 550 °C for 5 hours to remove residual organic matter. During column packing, ultrapure water was introduced from the bottom to ensure full saturation. The cleaned sand was rewetted with ultrapure water, and then gradually added with a spoon and gently mixed to prevent layering and air entrapment. A stainless steel mesh with 200 µm openings was installed at the base of each short column to prevent sand loss and ensure uniform flow distribution. The final porosity of the packed bed was calculated to be 0.39, based on the sand mass, column volume, and a particle density of 2.56 g/cm<sup>3</sup>.

River water was collected twice from an RBF site in the Netherlands in September and December 2024. A portion of the water was microfiltered (MF-Water) through a 2 µm Whatman membrane to remove large particles and algae, preventing clogging and algal growth in the columns. Another portion was ultrafiltered (UF-Water) using a 100 kDa cut-off device to remove microorganisms while retaining native dissolved organic carbon (DOC) and ions. The filtered waters were stored at 4 °C in a refrigerator and brought to room temperature prior to the column experiments.

The MF-Water was pumped upflow through the seven columns using peristaltic pumps at 0.1 mL/min (1.3 m/d) for two weeks to inoculate native bacteria onto the sand grains. Subsequently, the columns were supplied with UF-Water at 0.1 mL/min from bottom to top to support biofilm development for 1, 3, or 6 months. Two dual-channel peristaltic pumps supplied four of the seven columns (two each for 1 and 3 months, respectively), and a three-channel pump supplied three of the seven columns for 6 months. For 1-month and 3-month sets, one was used for biofilm characterization and the other for NP transport experiments in synthetic water (without DOC), replicating the ion composition of the river water (see [Table S14](#) for detailed water quality parameters). For the 6-month set, one column was used for biofilm analysis, one for NP transport in synthetic water, and one for NP transport in river water (< 100 kDa). The columns were operated at room temperature and covered by a black film to prevent light exposure and inhibit algal growth.

### 5.2.2. Biofilm Characterization

**Biomass quantification.** After biofilm formation, the long columns designed for biofilm characterization were disassembled into ten short segments each to assess biofilm biomass and surface characteristics at different depths (0–9 cm, 9–18 cm, ..., 81–90 cm). Each short

segment was further divided into three 3 cm layers, which were thoroughly mixed using a spoon. Biofilm biomass was quantified by measuring total carbon and nitrogen content using an Elemental Analyzer (vario EL cube). For segments C1 and C2 (0–9 cm and 9–18 cm), all three sublayers (upper, middle, and lower 3 cm) were analyzed. For segments C3 to C10, only the middle layer was selected for total carbon and nitrogen analysis. Prior to measurement, the sand samples were ground into fine powder using a mortar. Approximately 50 mg of each sample, as well as blank clean sand, was used for analysis, with measurements conducted in duplicate.

**Adenosine triphosphate detection.** Active biofilm biomass was assessed by adenosine triphosphate (ATP) using a commercial ATP assay kit (Beyotime) and quantified with a fluorescence luminometer. Following the manufacturer's protocol, approximately 0.5 g of sample was used for each ATP measurement. For segments C1 and C2 (0–9 cm and 9–18 cm), all three 3 cm layers were analyzed. For segments C3 to C10, only the middle layer was selected. Clean sand was also tested as a control. Each sample was measured in duplicate to ensure reproducibility.

**Extracellular polymeric substances extraction and quantification.** EPS from biofilms were quantified by measuring protein and polysaccharide contents. For each segment, the top 3 cm layer was used for analysis. Approximately 5 g of sand was transferred into a 10 mL glass vial, and 5 mL of synthetic water was added. The mixture was sonicated at 40 Hz for 1 minute, shaken for 30 seconds, and sonicated again for 1 minute to detach biofilm material from the sand grains [468]. A 3.5 mL aliquot of the resulting suspension was transferred to a new glass vial. Cation exchange resin (CER; Dowex Marathon C, 20–50 mesh, sodium form, Fluka 91973), pre-soaked overnight in ultrapure water, was added to the suspension at a dosage of 0.1 g. The biofilm-CER suspension was stirred at 600 rpm for 2.5 hours at 4 °C, then allowed to settle for 3 minutes to separate the resin. The supernatant was collected and centrifuged at 8,000 rpm for 20 minutes at 4 °C to obtain the extracted EPS [469]. Protein content in the EPS (expressed as  $\mu\text{g/g}$  sand) was determined using the bicinchoninic acid (BCA) assay with a BCA Protein Assay Kit (Thermo Fisher Scientific, Waltham, MA), using bovine serum albumin as a standard. Polysaccharide content ( $\mu\text{g/g}$  sand) was quantified by the phenol–sulfuric acid method, using glucose as the calibration standard [469]. Each sample was measured in duplicate.

**Zeta potential measurement.** The zeta potential of clean sand and biofilms was measured using a Litesizer DLS 700 instrument (Anton Paar, Austria). To facilitate suspension and accurate measurement in synthetic water, clean sand was first ground into fine particles using a stainless steel rod [427]. For the zeta potential of biofilms, the middle 3 cm layer from each

segment was selected. Biofilms were extracted using the sonication protocol described previously. The resulting suspension was allowed to settle for 1 minute to remove the larger sand particles. The supernatant water, containing detached biofilm, was collected and analyzed using the Litesizer DLS 700 instrument. Each sample was measured ten times to ensure accuracy and reproducibility.

**Scanning electron microscopy.** The surface morphology of bare and biofilm-coated sand was characterized using scanning electron microscopy (SEM; Quattro, FEI). Sand samples were collected from the top layer (C1, 0–9 cm) and middle layer (C5, 36–45 cm) of the column after 6 months of biofilm development. The samples were gently dried at 40 °C, mounted on glass slides, and coated with a thin layer of gold prior to imaging to enhance conductivity and image quality.

### 5.2.3. Nanoplastic Transport Experiments

Commercial PS NPs (nominal size: 100 nm) were purchased from Zhichuan Intelligent Technology (Suzhou, China) Co., Ltd and used as model NPs. The PS stock solution was diluted in synthetic water and UF-Water to prepare two types of suspensions: pristine NPs and weathered NPs, respectively, at a final concentration of 30 mg/L. The weathered NPs were incubated in UF-Water for two days to form a stable eco-corona (*Figure S34*). A relatively high NP concentration was selected to enable observation of full transport dynamics within a daytime.

After biofilm development, the long columns were carefully disassembled into ten short segments (C1–C10), each representing a depth interval of 0–9 cm, 9–18 cm, etc., down to 81–90 cm, for NP transport experiments. Before removing a segment from the top, the pump and the effluent outlet were shut off. The segment was then carefully unscrewed from the long column. It was immediately inverted, filled with background water to maintain saturation, and sealed with a cap to remove excess water. This procedure was done such that the formation of air bubbles or sand loss were prevented. Finally, the segment was returned to its original orientation, becoming a self-contained short column ready for transport experiments.

Prior to NP injection, approximately 8 pore volumes (PVs, 53.3 min) of particle-free background electrolyte (synthetic or river water) were injected at a constant upward flow rate of 0.75 mL/min (9.75 m/d) to flush the columns and remove loosely attached biofilms. Subsequently, 35 PVs (466.7 min) of NP suspension were injected, followed by 8 PVs of background electrolyte for elution, both at 0.75 mL/min. The total transport experiment duration was 9.6 hours. The higher flow velocity used during transport experiments compared to biofilm development was intended to facilitate the full observation of transport dynamics

within a single day. Transport experiments were conducted on four segments per day, so completing all transport experiments for a single long column took three days.

Effluents were collected from the column outlet at regular time intervals (0.5 PVs) in glass tubes using an autosampler to generate breakthrough curves (BTCs). NP concentrations in the effluent were quantified using a UV-Vis spectrophotometer (G10S, Thermo Fisher Scientific) at a wavelength of 270 nm. The UV absorbance at 270 nm ( $UV_{270}$ ) for 30 mg/L PS NPs in synthetic water was  $0.965 \text{ cm}^{-1}$ . For comparison, the  $UV_{270}$  of background UF-Water was only  $0.067 \text{ cm}^{-1}$ . Adsorption tests showed that the  $UV_{270}$  of DOC remained unchanged before and after adsorption by NPs (*Text S7* and *Table S15*). Therefore, for NP transport experiments in river water, the measured  $UV_{270}$  values were corrected by subtracting the background absorbance of 0.067 to determine NP concentrations.

To validate the applicability of the observed transport dynamics and mechanisms in natural systems, we also collected surface-layer river sand from a RBF site in the Netherlands and conducted NP transport experiments. Untreated wet river sand was packed into a 9 cm column, and NP transport experiments were carried out using both synthetic water and UF-Water, following the same procedure as described above. Due to the substantial retention of NPs in river sand, long-term transport (40–45 h) was monitored to capture the complete transport dynamics.

#### 5.2.4. Nanoplastic Characterization

The hydrodynamic size and zeta potential of PS NPs in synthetic water and river water were measured using the Litesizer DLS 700 instrument (Anton Paar, Austria), with ten replicate measurements conducted for each sample. To examine NP deposition, sand samples were collected from the top segment (C1, 0–9 cm) and middle segment (C5, 36–45 cm) of the column after 6 months of biofilm development. The deposited NPs on clean sand and biofilm-coated sand were visualized using SEM.

#### 5.2.5. Modelling

**Two-site blocking model.** NP transport in porous media is influenced by three fundamental mechanisms: advection, dispersion, and attachment to solid surfaces. It is often captured using the one-dimensional advection-dispersion-reaction (ADR) model:

$$\frac{\partial C}{\partial t} = D \frac{\partial^2 C}{\partial z^2} - v \frac{\partial C}{\partial z} - \frac{\rho_b}{\theta} \frac{\partial S}{\partial t} \quad (5-1)$$

In this model,  $t$  represents time (min),  $z$  is the distance along the column (m), and  $C$  denotes the NP concentration in the aqueous phase (mg/L). The hydrodynamic dispersion coefficient is represented by  $D$  ( $\text{cm}^2/\text{min}$ ), while  $v$  is the average pore-water velocity ( $\text{cm}/\text{min}$ ). The bulk

density of the porous medium is  $\rho_b$  (mg/cm<sup>3</sup>), and  $\theta$  denotes the porosity of the sand bed. The term  $\frac{\partial S}{\partial t}$  captures changes in solid-phase NP concentration  $S$  (same units as  $C$ ) due to attachment or detachment. The key transport parameters, mean pore-water velocity and dispersion coefficient, were obtained by fitting experimental NaCl tracer breakthrough curves. The NP deposition and release processes were described using a first-order reversible kinetic model, given as [428]:

$$\frac{\rho_b}{\theta} \frac{\partial S}{\partial t} = k_{att} \psi C - \frac{\rho_b}{\theta} k_{det} S \quad (5-2)$$

Here,  $k_{att}$  (min<sup>-1</sup>) is the first-order attachment coefficient, and  $k_{det}$  (min<sup>-1</sup>) is the first-order detachment coefficient, which is set to zero when assuming irreversible retention. The term  $\psi$  in the attachment expression serves as a generalized factor that reflects the specific attachment mechanism being modeled, such as clean-bed filtration, blocking, or ripening [412].

In CFT ( $\psi = 1$ ), the rate of NPs attachment  $k_{att}$  can be expressed as below:

$$k_{att} = \frac{v}{L} \ln\left(\frac{C_0}{C}\right) \quad (5-3)$$

Where  $L$  is the column length (cm),  $C_0$  and  $C$  represent the influent and steady-state effluent NP concentrations (mg/L), respectively. The steady-state concentration  $C$  is used to evaluate the retention behavior of NPs in the column [416].

The clean-bed filtration model with site-blocking incorporates a maximum retention capacity ( $S_{max}$ ) to account for the finite availability of attachment sites on the collector surface. This model describes NP deposition with the following equation [412]:

$$\psi = 1 - \frac{S}{S_{max}} \quad (5-4)$$

In this model,  $\psi$  represents a dimensionless Langmuirian blocking function. When the deposited NP concentration  $S$  is much smaller than the maximum retention capacity  $S_{max}$ ,  $\psi$  approaches 1, and the equation simplifies to the clean-bed filtration model. Initially, when no NPs are associated with the solid phase, the blocking effect is negligible. However, as more NPs attach and  $S$  approaches  $S_{max}$ ,  $\psi$  decreases, indicating reduced availability of attachment sites due to site saturation.

In this study, as NPs were deposited at multiple kinetic deposition sites, a two-site kinetic model was employed to fit the BTCs using HYDRUS-1D. This model accounts for NP attachment at two distinct sites and is described by the following equation:

$$\frac{\rho_b}{\theta} \frac{\partial (S_1 + S_2)}{\partial t} = k_{a1} \psi_1 C + k_{a2} \psi_2 C \quad (5-5)$$

Where  $S_1$  and  $S_2$  represent the solid phase NP concentration at site 1 and site 2, respectively.  $k_{a1}$  and  $k_{a2}$  are the attachment rate coefficients for site 1 and site 2, respectively. The detachment rates at both sites were considered negligible, as no obvious NP tailing was observed in the BTCs [414].

**Logistic model.** The two-site blocking model sometimes fails to fit the BTCs of weathered NPs or produces fitted parameters that cannot be directly compared with those of non-weathered NPs. Therefore, the logistic model was further employed to fit the BTCs of both non-weathered and weathered NPs. The logistic model is commonly employed to describe the S-shaped adsorption behavior of organic chemicals in column systems [470, 471]. In this study, the attachment of NPs resembled an adsorption-like process of chemicals, prompting the use of a modified logistic model to fit the BTCs of NPs, as shown below:

$$\frac{C_t}{C_0} = \frac{\left(\frac{C}{C_0}\right)_{max}}{1 + e^{-k(t-t_0)}} \quad (5-6)$$

Where  $(C/C_0)_{max}$  represents the predicted maximum steady-state plateau of the breakthrough curve. The logistic curve typically exhibits an S-shape, with its first derivative (the differential coefficient) displaying a symmetrical pattern, initially increasing to a peak and then decreasing. The parameter  $t_0$  denotes the time at which the rate of change is highest, i.e., the breakthrough occurs most rapidly. Beyond estimating  $(C/C_0)_{max}$ , this model is also used to derive the favorable retention ( $S_f$ ), unfavorable retention ( $S_{uf}$ ), and the retardation factor ( $R$ ) as follows:

$$S_f = \int_0^{t_b} \left(1 - \frac{C_t}{C_0}\right) dt \quad (5-7)$$

$$S_{uf} = \int_{t_b}^{t_{end}} \left(1 - \frac{C_t}{C_0}\right) dt \quad (5-8)$$

$$R = \frac{t_b}{t_{b,tracer}} \quad (5-9)$$

$$t_b = t_{\frac{C_t}{C_0}=0.1} \quad (5-10)$$

The breakthrough time ( $t_b$ , min) is defined as the time when the normalized effluent concentration ( $C/C_0$ ) reaches 0.1. The retardation factor ( $R$ ) is calculated as the ratio of the breakthrough time of NPs ( $t_b$ ) to that of the conservative tracer ( $t_{b,tracer}$ ). The favorable retention ( $S_f$ ) represents the mass of NPs retained on the sand up to  $t_b$ , and is expressed in  $\mu\text{g/g}$  sand. The unfavorable retention is defined as the additional NP retention occurring after  $t_b$  until the end of the transport experiment (i.e., the given maximum transport time).

### 5.2.6. Interaction Energy Calculation

The classical Derjaguin–Landau–Verwey–Overbeek (DLVO) theory accounts for van der Waals and electrostatic double layer interactions [188, 370]. To incorporate the influence of hydrophobic interactions, the extended DLVO (XDLVO) framework was applied by including Lewis acid–base interactions [472]. Surface heterogeneity, such as surface roughness, charge, and hydrophobicity variations, was also considered. The details are provided in [Text S8](#).

## 5.3. Results and Discussions

### 5.3.1. Surface Heterogeneity Drives Two-Stage Transport Dynamics of NPs

According to the CFT, colloids typically exhibit rapid breakthrough within the first PV under unfavorable conditions (both colloids and sand are negatively charged), followed by a rapid stabilization of the BTC to a steady plateau, reflecting a constant attachment rate [88, 97, 129]. CFT is consistent with predictions from classic DLVO theory. On an even and homogeneous sand surface, the uniform energy barrier and secondary minimum result in a steady, consistent deposition rate. However, this study revealed an S-shaped, BTC during the initial pulse ([Figure 5. 1a](#)): characterized by early-stage retardation, followed by a rapid increase in breakthrough, and then a gradual approach to a plateau at  $C/C_0 = 0.92$ . In theory, when detachment is neglected, flushing with NP-free solution should produce a washout equivalent to one PV of NPs. In practice, however, the integrated area under the elution curves during the first pulse (8 PVs) was  $C/C_0=1.22$ , suggesting that a fraction of previously deposited NPs was released. By subtracting one PV of breakthrough (0.92), the detached NPs, representing reversible attachment, were estimated as 0.09 mg. In contrast, the irreversibly retained fraction was substantially higher, amounting to 2.94 mg as determined from mass balance analysis. These results indicate that irreversible attachment dominated attachment during the first pulse. During the second pulse, NPs exhibited an approximately normal breakthrough, as defined by the CFT, reaching the same plateau value (0.92) as observed in the later stage of the first pulse. The integrated area under the elution curve during the second pulse showed little change compared to that of the first pulse, indicating that the same reversible attachment occurred during the first and second pulse. These observations suggests that NP transport in the later stage of the first pulse and the second pulse followed the traditional CFT that assumes irreversible attachment at a constant attachment rate [412].

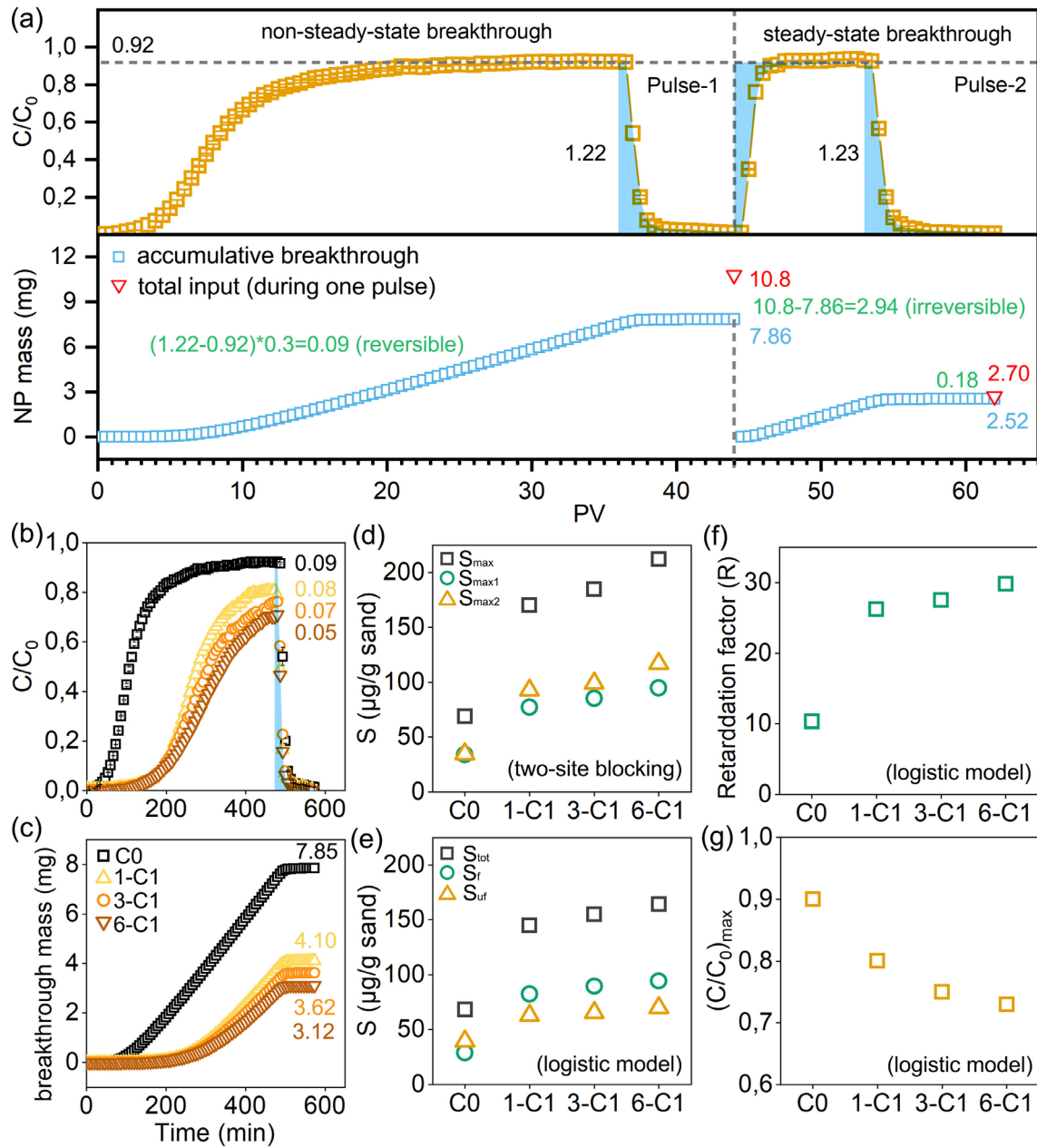


**Figure 5. 1.** (a). The BTCs (yellow dots), total input NP mass (red dots), and accumulative breakthrough mass profiles (blue dots) of NPs in clean sand during pulse 1 and 2 (a). The red, blue, and green numbers indicate the total input NP mass (mg), total NP breakthrough (mg), and total retention (mg), respectively, during a single pulse. The shaded area under the tail of the curve represents the normalized NP concentration during the elution stage, which is symmetric to the shaded region during initial ascent stage. Error bars represent the mean  $\pm$  range (minimum to maximum) ( $n = 2$ ). Comparison of BTCs (b) and breakthrough mass profiles (c) of NPs in clean sand (C0) and biofilm-coated sand segments (0–9 cm) cultivated for 1, 3, and 6 months (1-C1, 3-C1, and 6-C1); Fitted parameters  $S_{max}$ ,  $S_{max1}$  and  $S_{max2}$  using

the two-site blocking model (d); and the fitted  $S_{tot}$ ,  $S_f$ ,  $S_{uf}$  (e),  $R$  (f), and  $(C/C_0)_{max}$  (g) using the logistic model.

Both DLVO and XDLVO calculations revealed a high energy barrier and a shallow secondary minimum between NPs and sand (*Figure S35*), indicating limited deposition under this energetically unfavorable condition. However, the physical and chemical heterogeneity of natural sand might introduce a distribution of interaction energies, leading to variability in NP attachment rates [443]. The sand surface roughness (physical heterogeneity) can enhance both irreversible and reversible attachment of NPs by lowering energy barriers at asperities (*Figure S36*) [443], and by deepening secondary minima while reducing hydrodynamic drag in concave areas [407, 434]. SEM images revealed that NPs were predominantly deposited on these rough surface areas (*Figure 5.2h*). Additionally, the presence of trace amounts of clay minerals (as shown in the XRD and EDS results, *Figure S31* and *Figure 4.2c*) may further enhance irreversible and reversible attachment by offering positively charged edge sites (*Figure S37*) [449-451]. This physical and chemical heterogeneity was probably responsible for the observed non-steady-state breakthrough. During the initial stage, PS NPs preferentially occupied these energetically favorable heterogeneous sites (including both irreversible and reversible sites), resulting in transport retardation. Once these limited sites were saturated, they became unavailable for further attachment, leading to site blocking. In the subsequent transport stage, incoming NPs deposited slowly and predominantly irreversibly onto less favorable, relatively homogeneous surfaces. During the elution stage, a small fraction of attached NPs was released; however, these particles rapidly reattached during the initial injection of the second pulse. In contrast, the irreversible attachment sites on heterogeneous areas remained occupied and thus unavailable for new NP attachment. As a result, during the second pulse, irreversible attachment on relatively homogeneous surfaces dominated the retention process.

The two-site blocking model, which assumes that NPs attach to two distinct types of sites (Site 1 and Site 2), provided a good fit to the BTCs in the first pulse. The attachment rate constant  $k_{a1}$  for NPs was an order of magnitude higher than  $k_{a2}$ , indicating that Site 1 represented more favorable deposition sites compared to Site 2. In this study, Site 1 is interpreted as the energetically favorable, heterogeneous areas of the sand surface, while Site 2 corresponds to the relatively homogeneous, less favorable areas. BTC retardation was governed by  $k_{a1}$  and  $S_{max1}$ , enabling near-complete retention of NPs until Site 1 reached  $S_{max1}$ . After Site 1 became saturated, the BTCs plateaued as further, irreversible deposition occurred only at the energetically unfavorable Site 2. Here,  $S_{max1}$  and  $S_{max2}$  represent the maximum retention capacity of the favorable and unfavorable sites, respectively. However,  $S_{max2}$  in two-site modeling reflects only the amount of NPs retained on unfavorable sites within the experimental

duration. Under steady-state conditions, this value may continue to increase over time, as it corresponds to slow, irreversible attachment onto a large and relatively homogeneous surface area that can act as an effectively infinite sink. To better describe the steady-state transport, the logistic model was also used to fit the BTCs (*Figure S38*), where  $S_f$  represents the maximum capacity for favorable retention, analogous to  $S_{max1}$  in the two-site model, and  $(C/C_0)_{max}$  denotes the ideal plateau during the steady-state transport stage. Distinct from CFT, which uses the steady-state  $C/C_0$  to evaluate colloid transport and travel distance, the two-stage transport of NPs in this study can be described by energetically favorable attachment at limited heterogeneous sites quantified by  $S_{max1}$  and  $S_f$ , and energetically unfavorable attachment at unlimited homogeneous sites, represented by  $(C/C_0)_{max}$ .

### 5.3.2. Biofilm Facilitates Both Favorable and Unfavorable Attachment of NPs

PS NPs in biofilm-coated sand columns (0–9 cm) cultivated for 1, 3, and 6 months also exhibited two-stage transport dynamics (*Figure 5. 1b* and *Figure S39*). The presence of biofilm increased NP attachment, with cumulative breakthrough masses decreasing from 7.85 mg in clean sand to 4.10 mg, 3.62 mg, and 3.12 mg for biofilms grown over 1, 3 and 6 months, respectively (*Figure 5. 1b*). Correspondingly, the mass of irreversibly attached NPs increased from 2.95 mg in clean sand to 6.70 mg, 7.18 mg, and 7.68 mg with increasing biofilm age. In contrast, reversibly attached NPs decreased from 0.09 mg to 0.08 mg, 0.07 mg, and 0.05 mg, respectively, over the same period. These findings demonstrate that biofilm formation could increase irreversible attachment and reduce NP detachment. Based on the two-site blocking model, the total retention capacity ( $S_{max}$ ; the sum of  $S_{max1}$  and  $S_{max2}$ ) of NPs increased from 68.9  $\mu\text{g/g}$  in bare sand to 170.1  $\mu\text{g/g}$ , 184.7  $\mu\text{g/g}$ , and 212.3  $\mu\text{g/g}$  in sand coated with biofilm cultivated for 1, 3, and 6 months, respectively. A similar trend was observed for the retention capacities at Site 1 ( $S_{max1}$ ) and Site 2 ( $S_{max2}$ ), indicating that biofilm formation enhanced both favorable and unfavorable attachment. Consistent with the increase in  $S_{max1}$ , the retention capacity at favorable sites ( $S_f$ ) in the logistic model also increased from 28.8  $\mu\text{g/g}$  in bare sand to 80.2  $\mu\text{g/g}$ , 89.6  $\mu\text{g/g}$ , 94.4  $\mu\text{g/g}$  in sand coated with biofilm cultivated for 1, 3, and 6 months, respectively. This biofilm-enhanced retention at favorable sites was responsible for the observed increase in NP transport retardation ( $R$ ). Additionally, the predicted  $(C/C_0)_{max}$  were 0.90, 0.80, 0.75, and 0.72 for bare sand and sand coated with biofilm cultivated for 1, 3, and 6 months, respectively, indicating that biofilm reduced steady-state transport at unfavorable sites. Collectively, these findings demonstrated that biofilms greatly increased both favorable and unfavorable attachment of NPs.

As biofilms carried less negative charges compared to sand surfaces (*Figure 5.2a*), the reduced electrostatic repulsion between NPs and biofilms explained the enhanced attachment of NPs in biofilm-coated sand [473]. The more hydrophobic nature of biofilms (*Figure S40*),

compared to the silica surface, also facilitated NP attachment through hydrophobic interactions [474, 475]. XDLVO calculations revealed that the energy barrier for NPs interacting with biofilms was lower than that for interactions with sand (*Figure S35*), facilitating irreversible deposition. Additionally, depth of the secondary energy minimum for NPs and biofilms exceeded that for NPs and sand (*Figure S35*), suggesting an increased likelihood of irreversible or reversible attachment at secondary energy minimum. Thus, biofilm surfaces were more favorable deposition sites compared to clean sand. However, similar to clean sand, XDLVO theory only accounts for interactions with homogeneous surfaces and cannot fully explain the observed non-steady-state transport.

SEM images indeed revealed that biofilm-coated sand grains exhibited more pronounced convex asperities and concave valleys compared to the clean sand (*Figure 5.2g*). Moreover, NPs were visibly deposited and accumulated at these heterogeneous sites on biofilms (*Figure 5.2h* and *Figure S41*). These convex asperities of biofilms probably further promoted irreversible attachment by lowering energy barriers. Moreover, the deeper secondary energy minimum and reduced hydrodynamic drag in concave areas (*Figure S36*) may promote the conversion of reversible attachment into irreversible retention, potentially explaining the reduced detachment on biofilm-coated sand. The enhanced deposition of PS NPs [97], along with other nanoparticles such as nano Fe (0) [476], and ZnO [477], due to biofilm-induced surface roughness has also been reported in previous studies.

In addition to surface physical heterogeneity, biofilms probably also contributed to the complete deposition of NPs on biofilm surfaces via providing chemically heterogeneous sites. EPS, primarily consisting of proteins and polysaccharides, are key components of biofilms [478]. Biofilm-coated sand contained abundant active biofilms (*Figure 5.2d*) rich in proteins and polysaccharides (*Figure 5.2b* and *Figure 5.2c*), accompanied by increased carbon and nitrogen content (*Figure 5.2e* and *Figure 5.2f*). Proteins within EPS are strongly linked to the hydrophobic character of biofilms [479], which might promote NP deposition through hydrophobic interactions in specific regions of the biofilm matrix (*Figure S42*) [478-480]. Furthermore, the presence of positively charged amine groups in the protein structure of EPS may enhance NP binding via electrostatic attraction (*Figure S37*) [83, 480]. Beyond these interactions, polymer bridging between NPs and EPS molecules, such as polysaccharides, may occur in the presence of divalent ions [477, 479], further strengthening NP-EPS associations [188, 476]. SEM images also revealed that NPs were trapped by the EPS, showing high surface coverage on the biofilm (*Figure 5.2h* and *Figure S41*). Particularly, some NPs penetrated into and became embedded within the EPS or biofilm matrix, highlighting the role of EPS network in physically entrapping NPs [478]. During the growth and maturation of biofilms from 1 to 6 months, the zeta potential of the biofilms showed little change (*Figure*

5.2a), suggesting that their surface properties remained relatively constant. The increased retention capacity with biofilm growth was thus probably due to the enhanced biomass and EPS content (Figure 5.2b–Figure 5.2f), which provided more available sites to capture NPs.

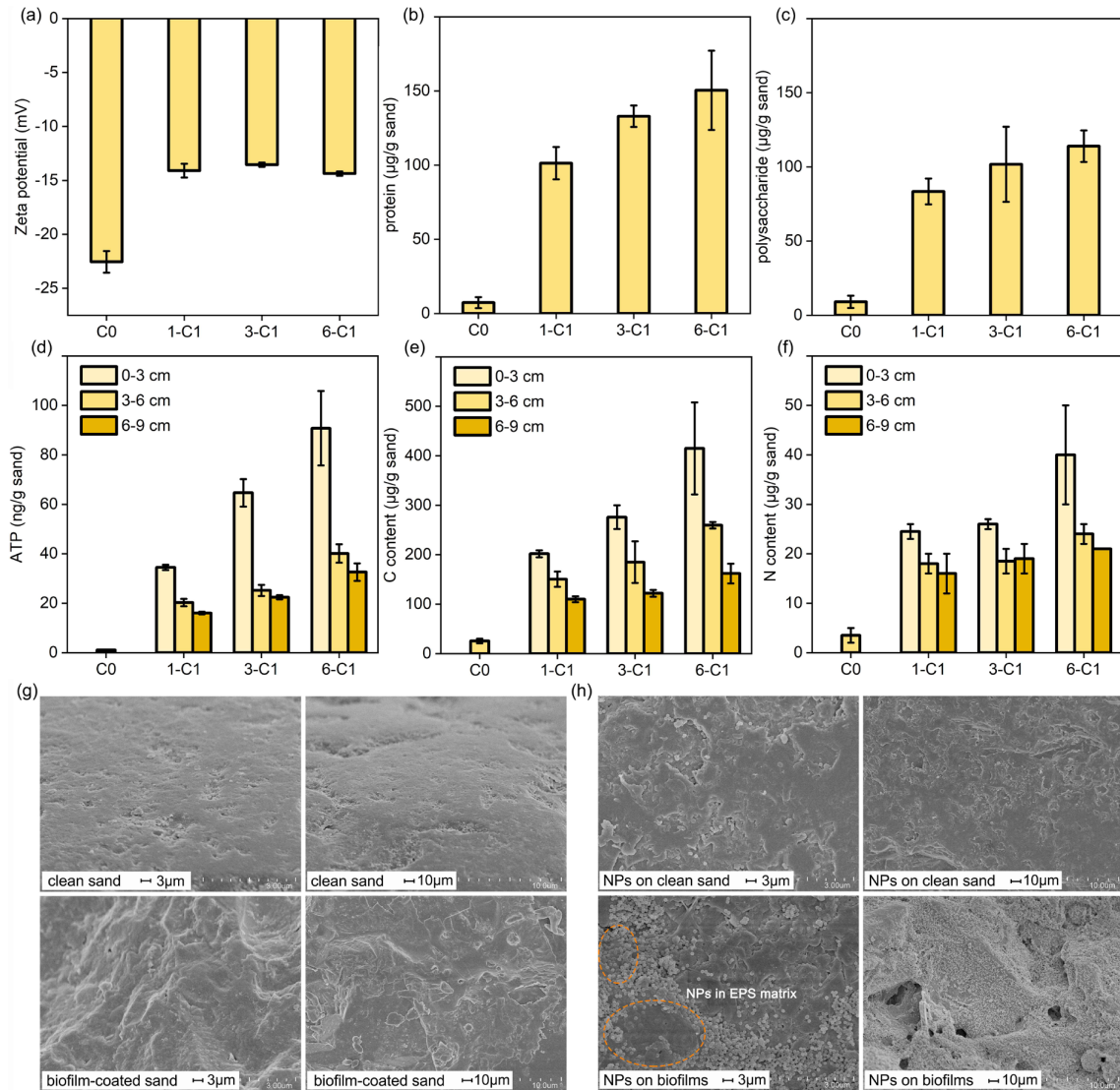
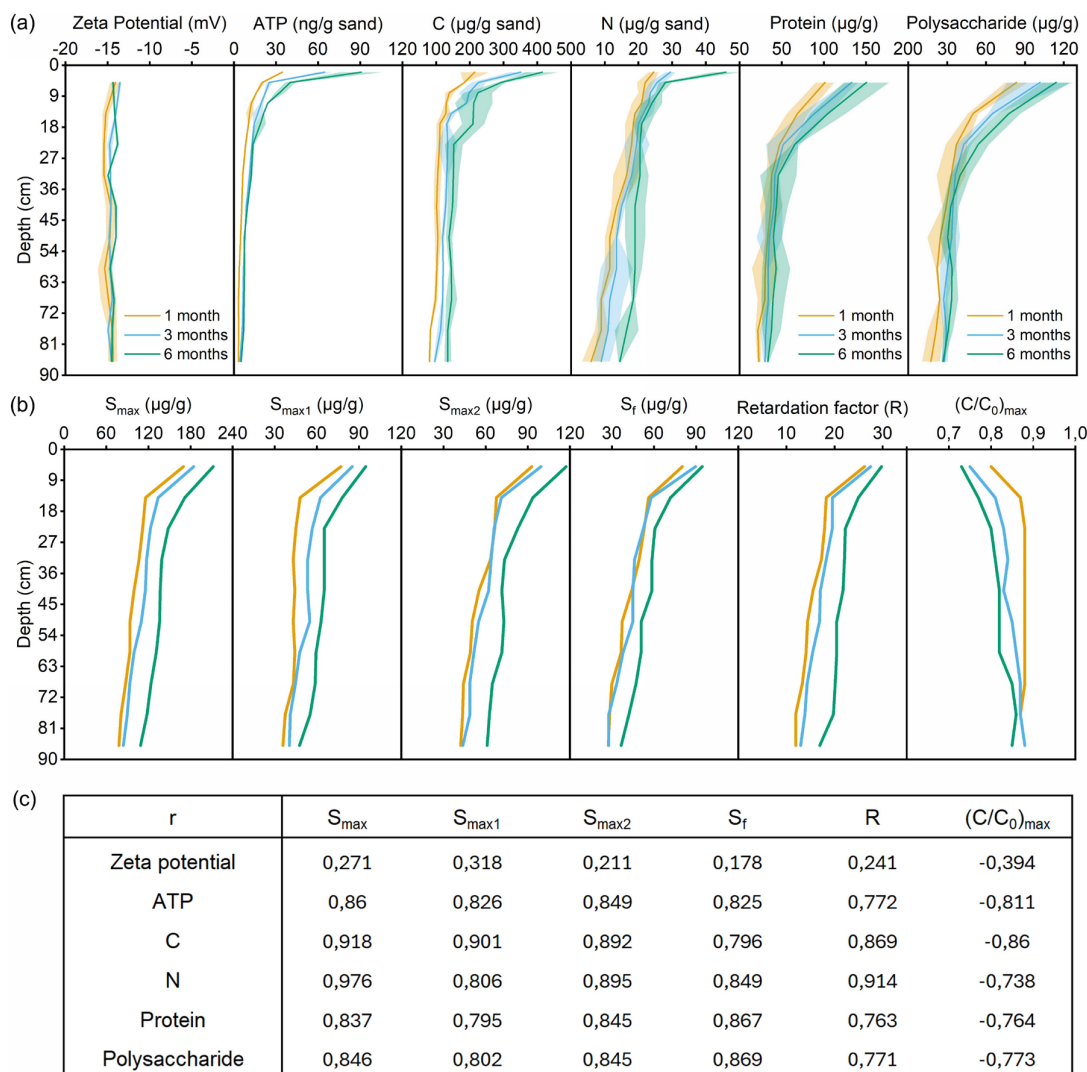


Figure 5.2. zeta potential (a), protein (b), polysaccharide (c), ATP (d), C content (e) and N content (f) of bare and biofilm-coated sand (0-9 cm); the SEM images of bare and biofilm-coated sand (g), as well as deposited NPs (h). Error bars represent the mean  $\pm$  SD ( $n = 10$ ) in (a) and mean  $\pm$  range (minimum to maximum) in (b)-(f) ( $n = 2$ ).

### 5.3.3. Spatial Heterogeneity of Biofilms Determines NP Retention

During RBF, microbial activity within biofilms rapidly depletes oxygen through the degradation of organic matter and nutrients, leading to the formation of spatially heterogeneous zones. In our study, as the infiltration depth increased to 90 cm, reductions in ATP, EPS, and carbon and nitrogen contents were observed, indicating indeed a progressive decline in biofilm biomass with depth (*Figure 5.3a*). This decline was closely associated with a reduction in the total NP retention capacity ( $S_{max}$ ) (*Figure 5.3b*). Specifically, decreases in  $S_{max1}$ ,  $S_r$ , and the retardation factor ( $R$ ) suggest that favorable attachment processes became less dominant with depth. Similarly, the decline in  $S_{max2}$ , accompanied by an increase in the predicted  $(C/C_0)_{max}$ , reflected a weakening of unfavorable attachment at deeper layers (*Figure 5.3b*). Linear correlation analyses further demonstrated strong associations between biofilm biomass indicators and both total and site-specific retention parameters (*Figure 5.3c*), highlighting the critical role of spatial heterogeneity in biofilm development and subsequent NP retention within the subsurface porous media.

The first 9 cm on the inflow-side of the column exhibited the highest NP retention capacity (*Figure 5.3-Figure 5.3g*), corresponding to the biologically active surface sediment layer commonly referred to as the colmation layer in rivers or *Schmutzdecke* in slow sand filters [101]. It is known to act as a natural filtration barrier, effectively removing suspended solids, pathogens, and organic contaminants through a combination of adsorption, biodegradation, and physical straining [51, 481, 482]. The favored retention capacity observed in the *Schmutzdecke* can be attributed to its dense microbial colonization and elevated EPS production, which together foster a complex surface topography and abundant interaction sites for NP attachment.



**Figure 5.3.** Variation in zeta potential, ATP content, total carbon (C), nitrogen (N), protein, and polysaccharide concentrations with increasing depth (a); Depth profiles of fitted transport parameters:  $S_{max}$ ,  $S_{max1}$  and  $S_{max2}$ ,  $S_f$ , R, and  $(C/C_0)_{max}$  (b); Correlations between biofilm biomass indicators (zeta potential, ATP, C, N, protein, and polysaccharide) and the fitted transport parameters ( $S_{max}$ ,  $S_{max1}$  and  $S_{max2}$ ,  $S_f$ , R, and  $(C/C_0)_{max}$ ) (c).

#### 5.3.4. Eco-Corona Reduces Favorable but Enhances Unfavorable Attachment

The formation of eco-corona due to DOM adsorption was an important weathering pattern of NPs in natural waters. In this study, NPs in river water ( $< 100$  kDa) had larger hydrodynamic size compared to that in synthetic water ( $233.2 \pm 2.8$  nm vs.  $118.2 \pm 1.3$  nm) (Table S15). The formation of a thick eco-corona ( $\sim 57.5$  nm) indicated the strong interaction between DOM and NPs. Especially, eco-corona induced a less negative charge on NPs ( $20.0 \pm 0.1$  mV in river water vs.  $29.0 \pm 0.6$  mV in synthetic water), and reduced their hydrophobicity, as indicated by

a decrease in water contact angle from 101.6° to 47.8° (Table S15). These results suggest that eco-corona formation during NP weathering can effectively mask and alter the original surface properties of pristine NPs.

Figure 5.4a-Figure 5.4f illustrate the BTCs of NPs in synthetic water and river water through columns packed with bare and biofilm-coated sand. In bare sand, NPs in river water displayed distinct transport behavior compared to those in synthetic water (Figure 5.4f). The weathered NPs exhibited minimal retardation, breaking through rapidly and reaching a relatively stable plateau that was slightly lower than that for NPs in synthetic water. The total retention capacity and the retention capacity at favorable sites ( $S_f$ ) decreased from 67.2  $\mu\text{g/g}$  and 22.3  $\mu\text{g/g}$  in synthetic water to 54.0  $\mu\text{g/g}$  and 7.0  $\mu\text{g/g}$  in river water, respectively. In contrast, the retention at unfavorable sites ( $S_{uf}$ ) for weathered NPs was slightly higher than that for NPs in synthetic water (47.0  $\mu\text{g/g}$  vs. 44.9  $\mu\text{g/g}$ ). Meanwhile, the predicted steady-state plateau  $(C/C_0)_{max}$  decreased from 0.90 to 0.87. These results suggest that eco-corona formation primarily inhibited favorable deposition onto heterogeneous sites in bare sand, while slightly promoting unfavorable deposition onto relatively homogeneous surfaces. In biofilm-coated sand, the eco-corona also inhibited favorable attachment while enhancing unfavorable attachment. Nevertheless, the overall retention of NPs increased, primarily due to the enhanced unfavorable deposition. This effect was more evident in the shallower layers, where higher biofilm biomass led to greater unfavorable retention (Figure 5.4g). For instance, in the 0–9 cm segment, the predicted  $(C/C_0)_{max}$  decreased from 0.73 in synthetic water to 0.62 in UF-water (Figure 5.4g).

Although the reduced hydrophobicity of eco-corona-coated NPs was generally unfavorable for their attachment, the concurrent decrease in electrostatic repulsion lowered the overall interaction energy barrier on homogeneous surfaces (Figure S43). This probably explains the enhanced unfavorable attachment observed for eco-corona-coated NPs; however, it does not account for the observed reduction in favorable attachment. We propose several possible mechanisms by which the eco-corona may suppress favorable attachment on heterogeneous areas. First, the eco-corona reduced the depth of the secondary energy minimum within concave valleys (Figure S44) and increased the hydrodynamic diameter of the NPs, potentially limiting their access to small concave features that promote physical entrapment. Second, positively charged surface heterogeneities were less favorable for eco-corona-coated NPs compared to the more negatively charged, non-weathered NPs (Figure S45). Third, hydrophobic surface domains were also less favorable for eco-corona-coated NPs, which exhibited reduced hydrophobicity compared to the non-weathered NPs (Figure S46).

Previous studies have often used model NOM to simulate eco-corona formation on NPs and conducted transport experiments in clean sand [67, 88, 89]. These studies typically report that the eco-corona enhances NP transport. However, such simplified systems do not fully capture natural conditions, where the eco-corona exhibits a complex and variable composition, and sand grains present important surface heterogeneity. In this study, we demonstrate that eco-coronas formed in natural river water enhance the initial transport of NPs but reduce their subsequent transport in biofilm-coated sand. This means that although weathered NPs may break through earlier than non-weathered NPs, their lower final effluent concentration indicates reduced long-term leaching potential and a lower risk of groundwater contamination.

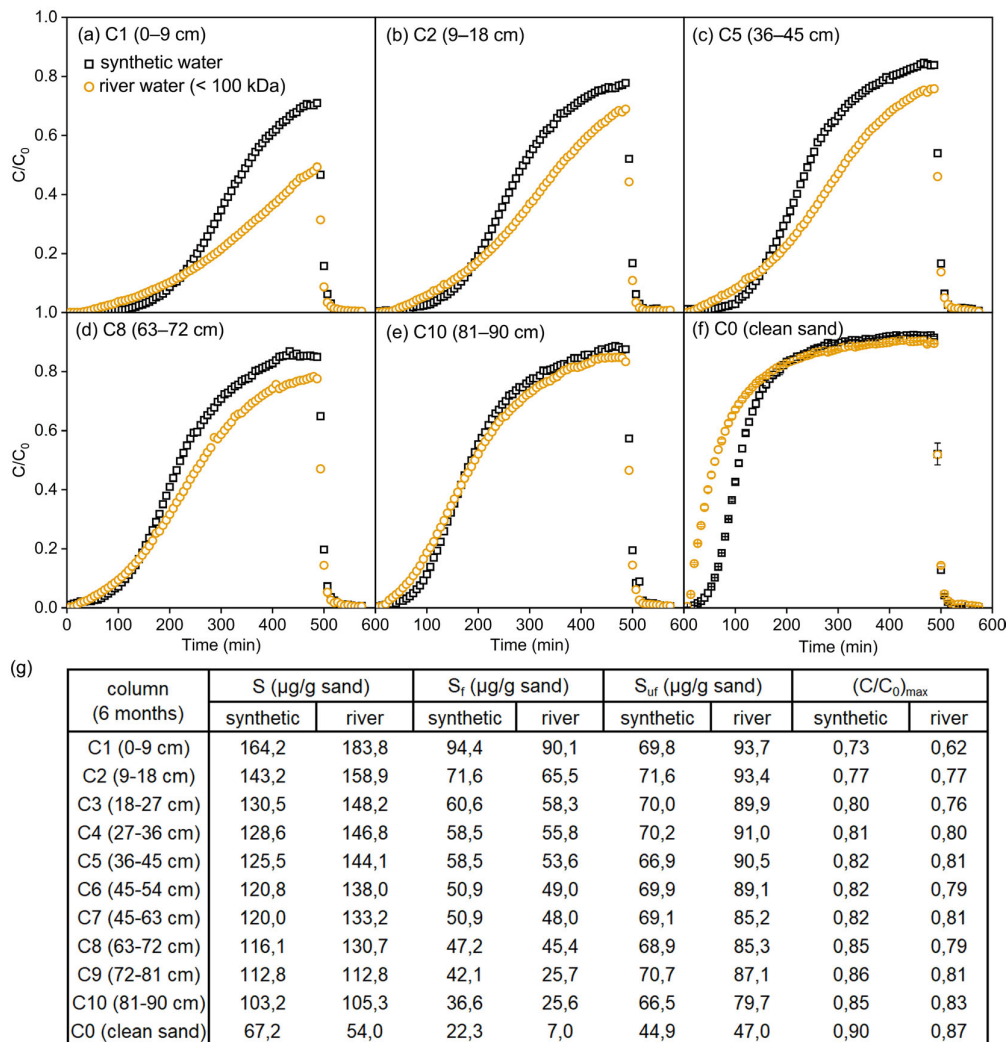
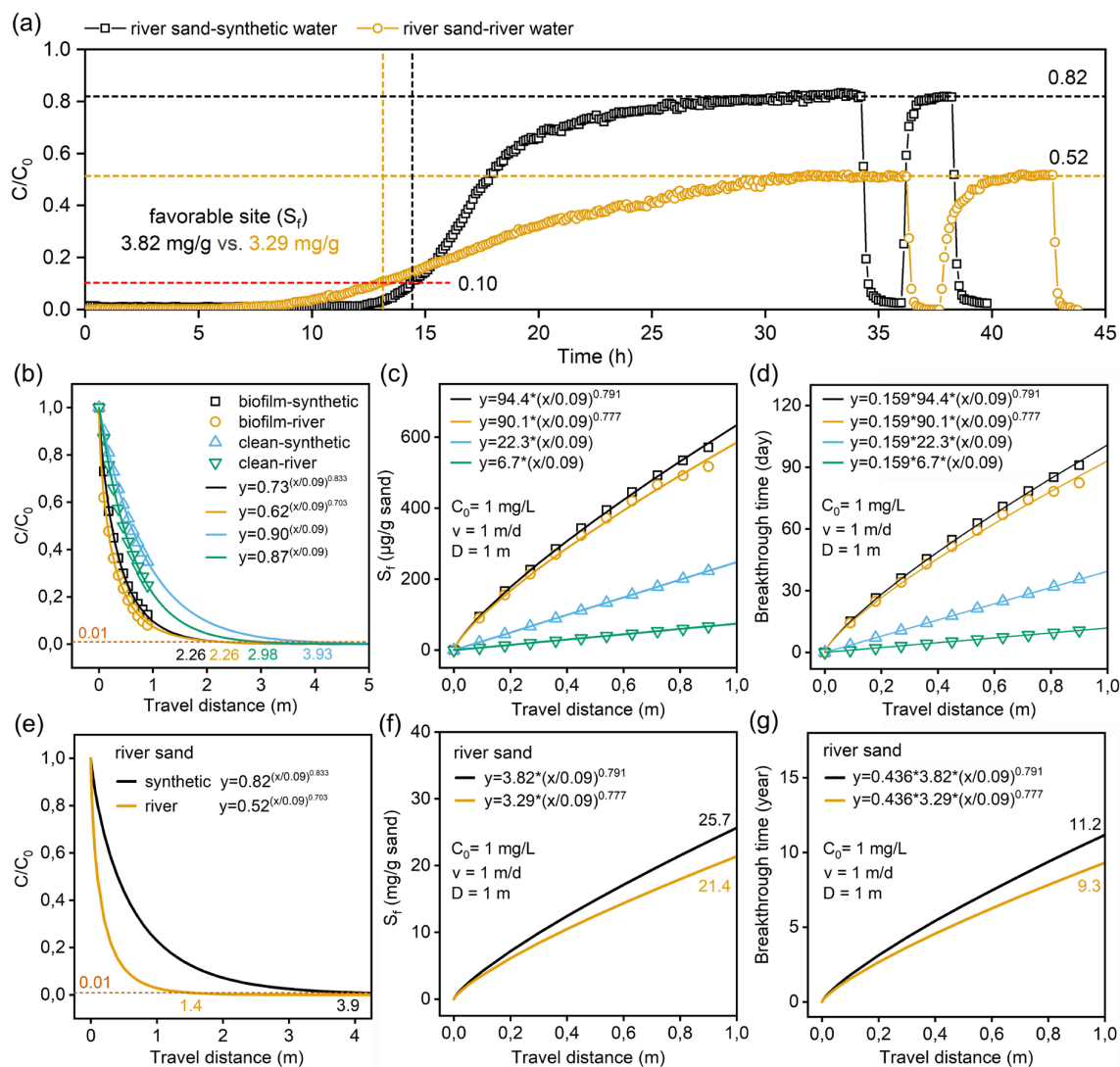


Figure 5.4. BTCs of NPs in synthetic water and UF-water for segments: C1 (a), C2 (b), C5 (c), C8 (d), C10 (e) and C0; Corresponding fitted transport parameters derived from BTCs (g).

### 5.3.5. Refinement of NP Transport Prediction in Filtration-Based Processes

To validate the applicability of the observed transport mechanisms in natural systems, we collected surface-layer river sand and conducted long-term NP transport experiments (*Figure 5.5a*). The results revealed a similar two-stage transport dynamic as observed in laboratory settings. However, compared to controlled column experiments using artificial media, NP transport in natural river sand exhibited extreme retardation. In this real-world setting, NPs took 14 hours in synthetic water and 10 hours in UF-Water to achieve visible breakthrough. This is likely because the river sand was highly weathered by biofilms and other impurities, which provided abundant favorable heterogeneous sites for NP attachment. The calculated mass of NPs retained under favorable conditions reached 3.82 mg/g in synthetic water and 3.29 mg/g in UF-Water. Following the saturation of these energetically favorable sites, NPs transitioned to attachment under energetically unfavorable conditions. The final transport stage approached a near steady-state breakthrough, with relative concentrations ( $C/C_0$ ) of 0.82 in synthetic water and 0.52 in UF-Water, respectively. These findings suggest that NP weathering enhanced unfavorable deposition, consistent with our earlier observations under controlled laboratory conditions. Previous studies have rarely examined NP transport over the extended timeframes as executed in our study [75, 97, 98, 459]. Then particles have been assumed to be completely immobilized if breakthrough was not observed within the relatively short experimental durations. This highlights the importance of monitoring full transport dynamics for the prediction of NP mobility in natural porous media, particularly in environmentally relevant scenarios such as RBF systems.



**Figure 5.5.** BTCs of NPs in synthetic and UF-Water using river sand collected from an RBF site (a); Simulated relationships between travel distance and  $C/C_0$  (b),  $S_r$  (c), and breakthrough time (d) under laboratory conditions; and predicted relationships between travel distance and  $C/C_0$  (e),  $S_r$  (f), and breakthrough time (g) in river sand based on laboratory-derived models.

Traditional NP transport models often rely on idealized conditions and CFT to predict NP transport distance. Here, we used the estimated maximum steady-state plateau ( $(C/C_0)_{\max}$ ) under unfavorable conditions for this prediction. As shown in Figure 5.5a, the travel distance required for NP concentration to decline to 1% ( $C/C_0 = 0.01$ ) was 3.93 m in synthetic water with bare sand, decreasing to 2.98 m in UF-Water due to eco-corona effects. Accounting for spatial heterogeneity from biofilms further reduced these distances to 2.26 m, highlighting the need to incorporate natural variability into predictive models. This study also emphasized the role of favorable retention in delaying NP breakthrough. Assuming a 1 m column diameter,

1 m/day flow velocity, and 1 mg/L influent NP concentration in a 1 m-long column, favorable attachment resulted in retention capacities of 247.8  $\mu\text{g/g}$  (synthetic water) and 74.4  $\mu\text{g/g}$  (UF-Water) with clean sand, increasing substantially to 634  $\mu\text{g/g}$  and 585  $\mu\text{g/g}$ , respectively, when biofilms were present (*Figure 5.5b*). Considering biofilm heterogeneity, breakthrough times after a 1 m length extended from 12 to 101 days in synthetic water and from 39 to 93 days in ultrafiltered river water (*Figure 5.5c*).

Applying the same transport equations used in laboratory settings, we extended our analysis to natural river sand to predict long-term NP mobility in environmentally relevant settings. Model simulations revealed that, in river water, it would take approximately 9.4 years for NPs to traverse a 1-meter column of river sand (*Figure 5.5g*). This indicates that, in real-world scenarios, NPs are highly unlikely to migrate into deeper subsurface layers over time scales of several years. While eventual breakthrough and attachment under energetically unfavorable conditions may occur over extended periods, the total predicted travel distance remained limited to approximately 1.40 meters in river water (*Figure 5.5f*). These findings reveal the low potential of NP migration to groundwater or drinking water sources in such sedimentary environments.

#### 5.4. Summary

We designed and tested a column system to cultivate natural biofilms on sand grains under simulated RBF conditions and studied how spatially heterogeneous biofilms regulate NP transport. We found that NP transport deviated from conventional clean-bed filtration theory, instead following a two-stage dynamic: an initial stage of favorable deposition followed by a steady-state stage of unfavorable deposition. Weathering of sand grains by natural biofilms enhanced both favorable and unfavorable NP retention, both of which were strongly correlated with biofilm biomass across different depths. In addition, we weathered NPs in river water to develop a natural eco-corona that reshaped their surface identity. This eco-corona inhibited favorable deposition and promoted unfavorable deposition, and together reduced their transport potential. These insights provide a mechanistic understanding of NP mobility under environmentally realistic conditions and underscore the importance of considering natural weathering processes of both NPs and filter media when evaluating transport dynamics.

Building upon these findings, we aimed to refine predictive models for NP transport in filtration-based systems. By incorporating spatial heterogeneity into the model, we achieved more accurate predictions of NP travel distance, based on the steady-state breakthrough stage under unfavorable deposition conditions. Beyond focusing solely on the unfavorable stage, we also highlighted the importance of accounting for the favorable retention stage, which is

critical for predicting NP breakthrough times. The proposed two-stage transport behavior provides valuable insights for optimizing engineered filtration systems such as RBF.

# Chapter 6

## Conclusion and Perspectives

This chapter comprises the main conclusions of the dissertation and the perspectives for future research

## 6.1. Conclusion and Implications for Environmental Science and Engineering

In this thesis, the influence of natural weathering processes on the transport of nanoplastics (NPs) through porous media were elucidated, including UV-induced weathering, eco-corona formation, and the development of spatially heterogeneous biofilms on sand grains. Overall it was concluded that weathered NPs display fundamentally altered surface properties and interfacial interactions, leading to distinct aggregation and deposition behavior compared to non-weathered NPs. Furthermore, weathered sand largely increases NP retention, thereby reducing their subsurface transport potential. These insights supported the refinement of predictive models for NP transport in riverbank filtration (RBF) systems, and can guide the design of engineered filtration strategies for NP removal.

In the following the conclusions from the various chapters are presented.

In [Chapter 2](#), the effects of photo-oxidation on the physical, chemical, and biological behavior of MNPs in both aquatic and terrestrial environments were reviewed. Physically, photo-oxidation increases surface O-containing functional groups and negative charges, and hydrophilicity, thus increasing the stability and mobility of NPs in water and porous media. Moreover, photo-oxidation changes the interactions (e.g., electrostatic interaction, hydrophobic and hydrophilic interactions) between MNPs and co-existing contaminants such as polar or hydrophobic organic compounds and heavy metals, either increasing or reducing their ability to adsorb, transport, and release various contaminants in natural environments.

MNPs do not undergo photo-oxidation in isolation but rather in the presence of various environmental components such as inorganic ions, natural colloids, and natural organic matter (NOM). Some constituents act as inhibitors by scavenging reactive species or competing for photons, thereby reducing the extent of photo-oxidation of micro- and nanoplastics (MNPs). Conversely, others function as photosensitizers, accelerating photo-oxidation by actively facilitating the generation of reactive oxygen species. MNPs also affect the photo-transformation of co-existing contaminants: they may inhibit direct photolysis by competing for light but can facilitate indirect photo-transformation by generating free radicals and providing surfaces for pollutant adsorption and reactions.

Photoaged MNPs are usually more toxic to organisms due to reduced particle size, increased surface reactivity, enhanced affinity for biological membranes, elevated oxidative stress, and the release of toxic leachates. Photo-oxidation also facilitates biofilm formation on MPs by increasing surface roughness, introducing oxygenated functional groups, and releasing more bioavailable carbon that supports microbial colonization. In aquatic systems, planktonic microbial responses to leachates from aged MNPs depend on the leachates' bioavailability or biotoxicity and the metabolic adaptability of the local microbial communities. Photoaged MNPs

further impacts microbial communities and functions, such as carbon and nitrogen cycling, particularly in soil and sediment systems.

Overall, the review reveals the diverse physical, chemical, and biological effects of MNPs in environments induced by UV weathering. It underscores the importance of using environmentally weathered MNPs in experimental designs to more accurately reflect their behavior and impacts under real-world environmental conditions.

In [Chapter 3](#), the change in adsorption behavior of NOM and the conformation of the eco-corona by UV weathering were identified, thereby influencing NP aggregation. The results revealed that UV weathering altered the eco-corona structure, which controls NP stability in the presence of NOM. For non-weathered NPs, hydrophobic NOM components primarily bound via hydrophobic and  $\pi$ - $\pi$  interactions, while extended hydrophilic NOM segments provided steric repulsion, inhibiting aggregation. In contrast, for UV-weathered NPs, hydrogen bonding promoted binding of hydrophilic NOM segments to multiple particles, leading to destabilization through polymer bridging. Moreover, both the stabilizing and destabilizing effects of NOM increased with its concentration and molecular weight. Using a combined DLVO and steric interaction model, including steric repulsion and polymer bridging, NOM's role in the stability of non-weathered and UV-weathered NPs could be predicted.

This chapter also reveals a contrasting role of the eco-corona in influencing the aggregation behavior of non-weathered versus UV-weathered NPs, highlighting the complexity of NP fate in natural aquatic environments. These findings demonstrate that the aggregation process is highly dependent on both the physicochemical state of the NPs and the composition of the surrounding NOM, underscoring the need to consider natural weathering when assessing NP stability. Traditionally, NOM has been understood to stabilize NPs or engineered nanomaterials in monovalent electrolyte solutions through steric repulsion. The destabilization effects of NOM are usually attributed to the presence of multivalent cations (e.g., calcium ion), which promote cation bridging. However, this study challenges the prevailing paradigm by demonstrating that NOM can induce destabilization even in the absence of multivalent ions, revealing a previously underrecognized mechanism of NP aggregation in environmentally relevant conditions. This advances current understanding in environmental colloid chemistry.

In [Chapter 4](#), NP weathering, induced by UV exposure and NOM adsorption, is reported, affecting their transport behavior and deposition mechanisms in porous media. Our findings revealed key deviations from the classical clean bed filtration theory (CFT), highlighting the critical role of physical and chemical heterogeneity of sand surfaces in governing NP retention. It was observed that surface heterogeneity led to distinct site-blocking and retardation, with NP deposition following a two-stage attachment process: an initial stage characterized by both

rapid, irreversible and reversible attachment onto heterogeneous surface domains until site saturation was reached, followed by a slower, predominantly irreversible attachment onto more homogeneous regions of the grain surfaces.

Both UV-induced aging and NOM coating altered the surface charge of NPs, making them more negatively charged. This modification reduced the extent of both irreversible and reversible deposition compared to non-weathered NPs. As a result, these weathering processes reshaped NP transport dynamics and screened the retardation effects imposed by surface heterogeneity. These findings reinforce the importance of incorporating environmentally realistic NPs into predictive models of NP transport and fate in porous media.

The two-stage transport behavior has often been overlooked in previous studies, particularly when breakthrough curves are measured over short timeframes, leading to misinterpretations of NP transport as steady-state with very low breakthrough. These results underscore the necessity of analyzing the full temporal evolution of transport profiles to accurately capture NP dynamics and avoid inaccurate conclusions. This challenges the general applicability of CFT and steady-state assumptions in predicting NP fate in natural porous media. It highlights the significance of surface heterogeneity-induced retardation in determining NP removal efficiency in natural sands. In this chapter, also a low removal efficiency was observed for both non-weathered and weathered NPs in clean quartz sand under controlled conditions, suggesting that clean sand is not suitable for effective NP removal. However, under real-world conditions, the abundance of various surface impurities and organic coatings on natural sands, likely enhance NP retention and limit deep NP penetration during long-distance migration.

In [Chapter 5](#), the spatial heterogeneity of biofilms was examined, influencing NP transport during RBF and how incorporating this complexity can improve model predictions. NP transport was characterized by a two-stage dynamic: an initial stage dominated by favorable attachment, leading to strong retention and delayed breakthrough, followed by a later stage characterized by unfavorable attachment. Biofilms, particularly the top layer, played a critical role in enhancing both favorable and unfavorable retention of NPs. However, the extent of retention decreased with depth, showing a clear correlation with declining biofilm biomass. To better reflect real-world conditions, environmentally relevant NPs were used that were pre-incubated in river water to allow for the formation of an eco-corona. Our results indicate that eco-corona formation suppressed initial favorable deposition while enhancing unfavorable deposition, ultimately reducing the overall transport potential of NPs through porous media.

Building on the mechanistic understanding of NP transport dynamics, predictive models were refined to better capture NP behavior in natural and engineered filtration systems. A major advancement was the explicit incorporation of spatial heterogeneity in predictive modelling in

natural porous media. Traditional modeling approaches often assume uniform deposition conditions, which can lead to inaccurate estimations of NP mobility and retention. By integrating spatial variability into the model framework, the accuracy of predictions regarding NP travel distance was improved, especially under environmentally relevant conditions such as those found in RBF and slow sand filtration systems.

One of the key findings further is the recognition of the initial favorable retention stage as a critical factor for estimating NP breakthrough time. While most previous studies have predominantly used the unfavorable attachment stage, typically associated with steady-state transport to predict NP transport distance, the results demonstrated that the favorable retention stage plays an equally important role in accurately predicting breakthrough timing.

Using these two approaches, the transport distance and breakthrough time of NPs at a RBF site could be predicted. The results indicate that NPs require a long time—several years—to travel even short distances (e.g., 1 meter) through the RBF system. Moreover, even when breakthrough eventually occurs, the resulting effluent concentrations are negligible. These findings suggest that RBF, particularly upper layers with highly weathered sand grains, can serve as an effective natural barrier for NP attenuation in drinking water treatment.

## 6.2. Limitations and Future Perspectives

This thesis has advanced the understanding of how natural weathering processes reshape the transport and fate of NPs in environmental and engineered systems. Despite these advancements, replicating truly realistic environmental conditions remains inherently challenging due to numerous sources of uncertainty and obstacles.

PS NPs were selected as model non-weathered NPs due to their ease of preparation and characterization. However, in real-world scenarios, other polymer types, such as PE, PP and PET, may be more prevalent. Future research should therefore broaden its scope to include a wider range of environmentally relevant plastic types to improve generalizability. The concentrations of NPs used in this thesis were relatively high, enabling robust detection and mechanistic interpretation. However, actual environmental concentrations of NPs are typically several orders of magnitude lower, presenting serious analytical challenges. Although techniques such as metal doping followed by ICP-MS analysis or the use of stable isotopes like  $^{13}\text{C}$ -labeled NPs offer promising alternatives for trace-level detection, they are still constrained to specific polymer types like PS, relatively high detection thresholds and potential interference from environmental impurities.

While this work has focused on the homoaggregation behavior of NPs, it is increasingly evident that heteroaggregation, or the interaction of NPs with naturally occurring colloids such as clay minerals and microbial particles, may be even more influential in determining their environmental fate [352]. A key area for further investigation is how environmental weathering processes, particularly eco-corona formation, affect heteroaggregation dynamics and the subsequent settling behavior of NPs in natural waters. To advance this understanding, the development of in situ microscopic and characterization techniques is essential for capturing these complex and dynamic interactions under environmentally relevant conditions. Furthermore, given the high heterogeneity and complexity of natural colloids, AI-based analytical approaches offer promising pathways for predicting NP fate by integrating diverse datasets and identifying patterns that may not be apparent through conventional methods [483].

The findings presented in the chapters 4 and 5 highlight the critical importance of considering natural weathering processes of sand grains, particularly the development of heterogeneous biofilms, when assessing NP transport and retention in subsurface environments. By using natural river sand, valuable insights into the capacity of real-world porous media were gained, to attenuate NPs through both favorable and unfavorable retention mechanisms. One of the key observations was the prolonged transport time of NPs through natural media, which suggests that factors beyond biofilms, such as mineral particles and naturally occurring colloids may make a difference.

The top layer with dense biofilms at the entrance of the RBF system markedly enhanced NP removal, highlighting its potential value in engineered filtration systems. This finding suggests promising opportunities to optimize NP retention by leveraging or mimicking biofilm formation. Since biofilm formation is driven by the availability of oxygen and nutrients, engineered systems may be optimized through strategies such as increasing aeration and supplementing with nutrient-rich influents.

## Supplementary Materials

Table S1. The adsorption capacity and adsorption mechanism of photo-aged MNPs towards OPs.

Contaminants	Log Kow	Functional groups	MNPs	Radiation conditions	Adsorption mechanisms	Adsorption capacity	Ref.
Benzene	2.13	Benzene (1)	PP,	UV <sub>340</sub> ;	π-π bond; Hydrophobic	Log K <sub>D</sub> : Benzene: 1.01→0.68 (PS); 1.43→1.56 (PP);	[174]
Toluene	2.73		PS	6.27 kJ/cm <sup>2</sup> ;	interaction	Toluene: 1.37→1.14 (PS); 1.92→1.95 (PP);	
Ethyl benzene	3.15			4 weeks		Ethyl benzene: 1.60→1.40 (PS); 2.30→2.28 (PP);	
m-Xylene	3.20					m-Xylene: 1.57→1.32 (PS); 2.34→2.29 (PP);	
o-Xylene	3.12					o-Xylene: 1.26→1.02 (PS); 2.16→2.17 (PP)	
Benzene	2.13	Benzene (1)	PS, PE, PET, PVC	UV/VUV; 180–1080 mJ/cm <sup>2</sup>	π-π bond;	K <sub>F</sub> (L/g): 0.653→0.612→0.459 (UV, PS); →0.361→0.105 (VUV, PS); 0.086→0.082→0.080 (UV, PE); →0.079→0.076 (VUV, PE); 0.267→0.215→0.168 (UV, PVC); →0.186→0.110 (VUV, PVC); 0.592→0.461→0.344 (UV, PET); →0.326→0.156 (VUV, PET);	[166]
Ciprofloxacin	1.81	Benzene (1) Amino (1) Carboxyl (1)			H bond; π-π bond	K <sub>F</sub> (L/g): 0.208→0.183→0.119 (UV, PS); →0.151→0.072 (VUV, PS); 0.141→0.121→0.112 (UV, PE); →0.116→0.108 (VUV, PE); 0.069→0.057→0.046 (UV, PVC); →0.071→0.088 (VUV, PVC); 0.219→0.181→0.111 (UV, PET); →0.192→0.171 (VUV, PET);	
Ciprofloxacin	1.81	Benzene (1) Amino (1) Carboxyl (1)	PS, PVC	UV <sub>254</sub> ; 96 h	Electrostatic interaction; H bond	K <sub>F</sub> : 0.58→0.54 (PS); 0.55→0.74 (PVC); K <sub>L</sub> : 0.959→0.993 (PS); 0.966→0.969 (PVC); K <sub>d</sub> : 0.210→0.318 (PS); 0.215→0.251 (PVC)	[170]
Ciprofloxacin	1.81	Benzene (1) Amino (1) Carboxyl (1)	PVC, PLA	UV <sub>313</sub> ; 0.05–1.29 kJ/cm <sup>2</sup>	Electrostatic interaction; H bond	Q <sub>e,1</sub> (mg/g): 0.39→0.69 (PLA); 0.34→0.44 (PVC); Q <sub>e,2</sub> (mg/g): 0.91→1.19 (PLA); 0.61→0.77 (PVC); K <sub>F</sub> (mg/g(L/mg) <sup>1/n</sup> ): 0.211→0.282 (PLA); 0.457→0.544 (PVC);	[177]
Tetracycline	-0.07	Benzene (1) Amino (1) Hydroxyl (5)			Electrostatic interaction; H bond	K <sub>L</sub> (L/mg): 0.071→0.073 (PLA); 1.580→1.319 (PVC); Q <sub>max</sub> (mg/g): 3.19→3.77 (PLA); 0.67→0.85 (PVC); Q <sub>e,1</sub> (mg/g): 0.46→1.28 (PLA); 0.43→0.87 (PVC); Q <sub>e,2</sub> (mg/g): 0.90→1.97 (PLA); 0.75→1.36 (PVC); K <sub>F</sub> (mg <sup>1-n</sup> ·L <sup>n</sup> /g): 0.182→0.286 (PLA); 0.600→0.867 (PVC); K <sub>L</sub> (L/mg): 0.079→0.056 (PLA); 1.404→1.338 (PVC); Q <sub>max</sub> (mg/g): 2.51→5.49 (PLA); 0.96→1.57 (PVC);	

Contaminants	Log K <sub>ow</sub>	Functional groups	MNPs	Radiation conditions	Adsorption mechanisms	Adsorption capacity	Ref.
Pyrene	4.88	Fused Ring	PS	mercury lamp; 6–12 h	–	K <sub>F</sub> (mg <sup>-1</sup> ·L <sup>n</sup> /kg): 177000→279000→82700; n: 0.95→1.07→0.78	[136]
4-nonylphenol	4.28	Benzene (1) Hydroxyl (1)			H bond	K <sub>F</sub> : 19600→14500→31000; n: 1.03→0.93→0.78	
Sulfadiazine	-1.47	Benzene (1) Amino (2)	TPU, PA	mercury lamp; 96 h	H bond;	Q <sub>e,1</sub> (μmol/g): 0.676→0.499 (PA); 0.084→0.095 (TPU); Q <sub>e,2</sub> (μmol/g): 0.727→0.536 (PA); 0.087→0.099 (TPU); K <sub>F</sub> (L/g): 0.025→0.030 (PA); 0.0021→0.0019 (TPU); n: 1.07→0.922 (PA); 1.11→1.18 (TPU); K <sub>d</sub> (L/g): 0.0309→0.0226 (PA); 0.0032→0.0036 (TPU); Q <sub>e,1</sub> (mg/g): 2.12→1.81 (PA); 0.293→0.324 (TPU); Q <sub>e,2</sub> (mg/g): 2.24→1.92 (PA); 0.087→0.099 (TPU); K <sub>F</sub> (L/g): 0.688→0.256 (PA); 0.298→0.331 (TPU); n: 0.858→0.907 (PA); 1.41→1.44 (TPU); K <sub>d</sub> (L/g): 0.529→0.201 (PA); 0.012→0.014 (TPU);	[151]
Sulfachloropyridazine	0.90	Benzene (1) Amino (2)			Electrostatic interaction		
Benzalkonium chlorides		Benzene (1) Long-chain alkane	PE	UVC; 120 h	Hydrophobic interaction; H bond	K <sub>F</sub> (L/mg): 3.337→4.052 (BAC <sub>12</sub> ); 6.543→7.052 (BAC <sub>14</sub> ); 5.570→6.280 (BAC <sub>16</sub> ); 1/n: 0.2177→0.2147 (BAC <sub>12</sub> ); 0.2064→0.1533 (BAC <sub>14</sub> ); 0.2696→0.2058 (BAC <sub>16</sub> ); K <sub>L</sub> (L/mg): 0.0319→0.0373 (BAC <sub>12</sub> ); 0.0474→0.0744 (BAC <sub>14</sub> ); 0.0354→0.0526 (BAC <sub>16</sub> ); Q <sub>max</sub> (mg/g): 12.6699→14.7535 (BAC <sub>12</sub> ); 22.0704→17.1392 (BAC <sub>14</sub> ); 26.9646→20.7013 (BAC <sub>16</sub> );	[135]
Benzalkonium (C21H38NCl)	2.93						
BAC <sub>14</sub> (C23H42NCl)	3.91						
BAC <sub>16</sub> (C25H46NCl)	4.89						
Atorvastatin	3.44	Benzene (3) Carboxyl (1) Hydroxyl (2)	PS	mercury lamp; 0.05–0.81 kJ/cm <sup>2</sup> ;	Hydrophobic interaction; π–π bond;	Q <sub>e,2</sub> (mg/g): 1.24→0.59→1.33; K <sub>d</sub> (L/g): 0.39→0.09→0.50; K <sub>d-SSA</sub> (L/m <sup>2</sup> ): 1.21→0.08→0.24; K <sub>d-o/c</sub> (L/g): 52.91→2.07→4.25;	[167] [82]
Amlodipine	2.08	Benzene (1) Amino (2)			Electrostatic interaction; H bond	K <sub>L</sub> (L/mg): 0.58→0.29; Q <sub>max</sub> : 1.61→0.85→2.52; K <sub>F</sub> : 0.63→0.31→0.66; n: 0.28→0.28→0.40; Q <sub>e,2</sub> (mg/g): 0.22→1.10; K <sub>d</sub> (L/g): 0.03→0.28; K <sub>d-SSA</sub> (L/m <sup>2</sup> ): 0.08→0.05→0.14; K <sub>d-o/c</sub> (L/g): 3.40→1.18→2.39; K <sub>L</sub> (L/mg): 0.16→0.57; Q <sub>max</sub> : 0.46→1.51; K <sub>F</sub> : 0.13→0.65; n: 0.31→0.25→0.25;	

Contaminants	Log K <sub>ow</sub>	Functional groups	MNPs	Radiation conditions	Adsorption mechanisms	Adsorption capacity	Ref.
Bisphenol A	3.03	Benzene (2) Hydroxyl (2)	PS	UV <sub>365</sub> ; 96 h	$\pi$ - $\pi$ bond; Hydrophobic interaction	$K_d$ (L/kg): 18.8→1.4; $K_{d-cl}$ (L/kg): 348→6.0; $Q_{e,1}$ ( $\mu$ g/g): 2.25→0.697; $Q_{e,2}$ ( $\mu$ g/g): 2.51→0.726	[152]
Atrazine	2.70	Amino (3)	PP, PE, PS	UV <sub>254</sub> ; 96 h	Electrostatic attraction; H bond	$Q_{e,1}$ (mg/g): 0.569→0.661 (PS); 0.519→0.935 (PE); 0.394→0.663 (PP); $Q_{e,2}$ : 0.644→0.760 (PS); 0.598→1.104 (PE); 0.456→0.790 (PP); $K_L$ : 0.088→0.278 (PS); 0.038→0.227 (PE); 0.109→0.416 (PP); $Q_{max}$ (mg/g): 1.349→2.483 (PS); 1.992→3.539 (PE); 1.148→2.242 (PP); $K_F$ : 0.277→0.360 (PS); 0.249→0.446 (PE); 0.228→0.386 (PP); n: 0.429→0.399 (PS); 0.491→0.426 (PE); 0.424→0.369 (PP);	[172]
2,2',4,4'- tetrabromodip henyl ether	-	Benzene (2)	PS	UV <sub>254</sub> ; 0.34 kJ/cm <sup>2</sup>	$\pi$ - $\pi$ bond; Hydrophobic interaction	$Q_{e,2}$ (ng/L): 6.105→3.755; $K_L$ (mL/ng): 0.107→0.136; $Q_{max}$ : 50.761→7.342; $K_F$ (ng/g) (dm <sup>3</sup> /g): 11.92→5.33; n: 0.942→0.544	[484]
Sulfanilamide	-1.26	Benzene (1) Amino (2)	PA, PVC, PET	-	Hydrophobic interaction; Electrostatic interaction	$Q_{e,1}$ ( $\mu$ g/g): 17.178 (PVC); 13.977 (PA); 7.142 (PET); $Q_{e,2}$ ( $\mu$ g/g): 17.238 (PVC); 14.278 (PA); 7.249 (PET); $K_L$ (L/mg): 0.05 (PVC); 0.039 (PA); 0.018 (PET); $Q_{max}$ (mg/g): 24.27 (PVC); 19.70 (PA); 12.45 (PET);	[485]
Oxytetracyclin e	-0.90	Benzene (1) Amino (1) Hydroxyl (6)	TPU	UV <sub>254</sub> ; 44.30 kJ/cm <sup>2</sup>	H bond; Cation bridging	$Q_{e,1}$ (mg/g): 0.280→0.372; 0.692→0.981 (with Cu <sup>2+</sup> ); $Q_{e,2}$ (mg/g): 0.318→0.398; 0.817→1.086 (with Cu <sup>2+</sup> ); $K_L$ (L/mg): 0.137→0.070; 0.325→0.640 (with Cu <sup>2+</sup> ); $Q_{max}$ (mg/g): 0.582→1.113; 0.980→1.506 (with Cu <sup>2+</sup> ); $F_L$ (mg <sup>1-n</sup> L <sup>n</sup> /g): 0.141→0.137; 0.390→0.706 (with Cu <sup>2+</sup> ); n: 2.898→2.035; 4.062→4.319 (with Cu <sup>2+</sup> );	[182]

Note.  $Q_{e,1}$  and  $Q_{e,2}$  represent the amount of adsorption at equilibrium of the pseudo-first-order and pseudo-second-order model, respectively;  $Q_m$  and  $K_L$  are the theoretical maximum adsorption capacity and an equilibrium constant reflecting the adsorption energy of Langmuir model;  $K_F$  and  $n$  are the parameters reflecting adsorption capacity and the parameter reflecting adsorption strength of Freundlich model.

Table S2. The influence of photo-oxidation on the colloidal stability of NPs under different conditions.

Material information	Radiation condition	Surface properties	Critical results and CCC (mM) under different conditions	Ref.
PS; 100 nm	UV <sub>365</sub> ; 0.0006–0.147 kJ/cm <sup>2</sup> ; 1, 3, 5, 9, 12, 24 h	Size (nm): 120.1→80.2 (24 h); ZP (mV): -43.03→-34.5→-44.1 (24 h); WA (°): 108.2→90.7→73.7	NaCl (pH=6): 450→458→480→530→550→630→760; CaCl <sub>2</sub> : 33→27→21→18→16→12→8	[128]
PS; 100 nm	UV <sub>254</sub> + H <sub>2</sub> O <sub>2</sub> ; 60 and 120 h	CI: 0.05→0.41→0.75; PI: 0.05→0.08→0.09	NaCl (pH=7.5): 591→957→1108	[130]
PS; 100 nm	mercury lamp; 12 and 24 h	WCA (°): 119.7→82.9→66.0; PI: 0.02→0.05→0.17	NaCl (pH=5): 198→293→411; CaCl <sub>2</sub> : 21.2→20.5→9.67; NaCl (HA): 705→480→ND; CaCl <sub>2</sub> (HA): 12.3→14.1→ND; NaCl (lysozyme): 169→73.9→ND; CaCl <sub>2</sub> (lysozyme): 10.2→12.7→ND; NaCl (sodium alginate): 494→200→ND; CaCl <sub>2</sub> (sodium alginate): 23→17.7→ND	[133]
PS; 100 nm	UV <sub>254</sub> ; 12 and 24 h	ZP (mV): -44.4→-41.4→-43.3; Size (nm): 117.8→98.1→70.9; PI: 0.07→0.11→0.18	NaCl (pH=7): 585→700→ND; NaCl (HA): 1200→1100→ND; NaCl (DBC): 500→550→635→680→ND	[175]
PS; 100 nm	0.086–0.172 kJ/cm <sup>2</sup> ; 6, 12 and 24 h	ZP (mV): -40.1→-38.4; Size (nm): 117.8→98.1→70.9; PI: 0.16→0.18→0.21	NaCl (pH=6.5): 400→500→650→800; CaCl <sub>2</sub> : 38→30→25→18; NaCl (HA): ND; CaCl <sub>2</sub> (HA): 8→10→12→13; UV reduced and enhanced NP stability with HA in NaCl and CaCl <sub>2</sub> , respectively; UV induced-flocculation of BSA molecules wrapped and destabilized NPs.	[83]
PS; 50, 200 and 1000 nm	mercury lamp; 10–120 min	no obvious change in the particle size distribution, and O/C	The effect of direct light irradiation on the aggregation of PS is negligible in PBS solution (1.0 mM, pH = 7.0).	[184]
PS, PS-NH <sub>2</sub> , PS-COOH; 100 nm	UV <sub>365</sub> ; 0.0007 kJ/cm <sup>2</sup> 0.5 h	ZP (mV): -59.9→-57.5 (PS); -41.5→-38.6 (PS-NH <sub>2</sub> ); -39.7→-40.6 (PS-COOH) WCA (°): 65.4→66.7 (PS); 45.1→44.6 (PS-NH <sub>2</sub> ); 40.2→40.1 (PS-COOH)	UV irradiation reduced the stability of PS NPs in 200 mM NaCl, that of PS-COOH NPs in 20–50 mM CaCl <sub>2</sub> , and that of PS-NH <sub>2</sub> NPs in 100–200 mM NaCl/Na <sub>2</sub> SO <sub>4</sub> solutions.	[132]
PS, PS-COOH; 50 nm	No aging	Size (nm): 49 (PS); 47 (PS-COOH); ZP (mV): -34 (PS); -40 (PS-COOH)	NaCl (pH=5): 264 (PS); 191 (PS-COOH); 478 (PS+BSA); 628 (PS-COOH+BSA); CaCl <sub>2</sub> : 29.1 (PS); 16 (PS-COOH); 42.2 (PS+BSA); 97.4 (PS-COOH+BSA); Na <sub>2</sub> SO <sub>4</sub> : 200 (PS); 540 (PS-COOH); 267 (PS+BSA); 611 (PS-COOH+BSA);	[183]

---

PS, PS-COOH; 100 nm	No aging	Size (nm): 92.8 (PS); 97.3 (PS-COOH); ZP (mV): -35.5 (PS); -34.7 (PS-COOH)	NaCl (pH=7.4): 310 (PS); 308 (PS-COOH); 410 (PS+1 mg/L HA); 393 (PS COOH+1 mg/L HA); 1138(PS+5 mg/L HA); 999 (PS-COOH+5 mg/L HA); CaCl <sub>2</sub> : 28.9 (PS); 28.0 (PS-COOH); 31.8 (PS+1 mg/L HA); 39.7 (PS-COOH+1 mg/L HA); 27.0 (PS+5 mg/L HA); 27.0 (PS-COOH+5 mg/L HA);	[77]
---------------------------	----------	---	---	------

---

Table S3. Critical factors influencing the photo-oxidation of MNPs.

Factors	MNPs	Radiation condition	Influence	Mechanism	Critical results	Ref.
HA; FA	PP	mercury lamp; 1.72–8.61 kJ/cm <sup>2</sup>	inhibit	ROS scavengers and optical light filters	size change: 0.14 ± 0.03 vs 0.28 ± 0.02 (HA) vs 0.28 ± 0.01 (FA); T <sub>m</sub> (°C): 148.1 ± 0.47 vs 150.4 ± 0.53 (HA) vs 153.8 ± 3.06 (FA); ZP (mV): -8.8 ± 0.64 vs -0.94 ± 2.13 (HA) vs -6.75 ± 3.73 (FA);	[126]
HA; halide ions	PVC	UV <sub>365</sub> ; 0.5–56 h	promote/ inhibit	produce <sup>3</sup> DOM*; sequester •OH	promote and inhibit organotin compounds release	[121]
HA; FA	PS	mercury lamp; 4.30–34.4 kJ/cm <sup>2</sup>	promote	produce •OH and <sup>1</sup> O <sub>2</sub>	Cl: 0.026 (pristine), 0.15–0.18 (HA) vs 0.22 (FA)	[215]
FA	PS	mercury lamp; 10–120 min	promote	produce <sup>3</sup> FA*, •OH, and <sup>1</sup> O <sub>2</sub>	O/C: 0.03 (200 nm) vs 0.56 (200 nm, FA); 0.04 (1000 nm) vs 0.48 (1000 nm, FA)	[184]
pyrite	PS	xenon lamp; 3–30 d	promote	produce O <sub>2</sub> <sup>•-</sup> , •OH and <sup>1</sup> O <sub>2</sub>	Cl: 0.68 vs 0.86 (pyrite); PO/C 0.13 vs 0.40 (pyrite)	[212]
clay minerals	PVC, PET	mercury lamp; 8.61–60.26 kJ/cm <sup>2</sup>	promote	produce •OH	weight loss (%): 19.78 (PVC) vs 39.68 (PVC, kaolinite) vs 31.94 (PVC, montmorillonite); 20.22 (PET) vs 44.25 (PET, kaolinite) vs 36.99 (PET, montmorillonite) O/C: 0.12 (PVC) vs 0.38 (PVC, kaolinite) vs 0.2 (PVC, montmorillonite); 0.15 (PET) vs 0.47 (PET, kaolinite) vs 0.24 (PET, montmorillonite); Cl: 0.15 (PVC) vs 0.33 (PVC, kaolinite) vs 0.26 (PVC, montmorillonite); 0.2 (PET) vs 0.35 (PET, kaolinite) vs 0.29 (PET, montmorillonite)	[122]
goethite; hematite	PP, PE	xenon lamp; 10.62–42.47 kJ/cm <sup>2</sup>	promote	light-driven Fenton reaction and •OH	TOC (mg/L): 2.7 vs 4.2 (hematite) vs 7.2 (goethite); Cl: 0.49 (PP) vs 0.59 (PP, hematite) vs 0.64 (PP, goethite); 0.39 (PE) vs 0.49 (PE, hematite) vs 0.54 (PE, goethite); weight loss (%): 36 (PP) vs 44 (PP, hematite) vs 58 (PP, goethite); 27 (PE) vs 36 (PE, hematite) vs 48 (PE, goethite) O/C: 0.33 (PP); 0.24 (PE)	[150]
soil component	PET	xenon lamp; 10.62–42.47 kJ/cm <sup>2</sup>	promote/ inhibit	electrostatic interaction	weight loss (%): 11 vs 28 (MnO <sub>2</sub> ) vs 21 (SiO <sub>2</sub> ) vs 16 (Al <sub>2</sub> O <sub>3</sub> ) vs 26 (goethite) vs 27 (hematite) vs 31 (kaolinite) vs 29 (montmorillonite) vs 5 (DOM) vs 5 (FA)	[486]

Factors	MNPs	Radiation condition	Influence	Mechanism	Critical results	Ref.
organic acids; Fe (III)	PVC	xenon lamp; 13.77 kJ/cm <sup>2</sup>	promote	produce •OH	[Cl <sup>-</sup> ] (μM): 21.4 (2 μm) vs 24 (2 μm, oxalate) vs 31.6 (2 μm, oxalate-Fe(III)); 13.2 (10 μm) vs 17.2 (10 μm, oxalate) vs 23.8 (10 μm, oxalate-Fe(III)); 10.6 (25 μm) vs 16.4 (25 μm, oxalate) vs 22.2 (25 μm, oxalate-Fe(III)); 7.2 (150 μm) vs 9.9 (150 μm, oxalate) vs 12.4 (150 μm, oxalate-Fe(III)); SSA (m <sup>2</sup> /g): 70.25 (2 μm) vs 74.27 (2 μm, oxalate) vs 81.87 (2 μm, oxalate-Fe(III)); 13.29 (10 μm) vs 13.91 (10 μm, oxalate) vs 15.35 (10 μm, oxalate-Fe(III)); 5.58 (25 μm) vs 5.7 (25 μm, oxalate) vs 6.36 (25 μm, oxalate-Fe(III)); 0.85 (150 μm) vs 0.88 (150 μm, oxalate) vs 0.97 (150 μm, oxalate-Fe(III)); WCA (°): 102.9 (150 μm) vs 69.2 (150 μm, oxalate) vs 35.4 (150 μm, oxalate-Fe(III)) vs 99.7 (150 μm, citrate) vs 52 (150 μm, citrate-Fe(III))	[487]
brominated flame retardants	PS	xenon lamp; 0.13–353.21 kJ/cm <sup>2</sup>	promote	produce radicals	M <sub>w</sub> (kDa): 0.18*10 <sup>5</sup> vs 0.012*10 <sup>5</sup> (BDE-209); BFRs enhanced photo-oxidation rate of PS by 7 for TBBPA-DBPE and TBBPA, and 10 for BDE-209.	[488]
PS and its released DOM	PS, PP	mercury lamp; 3–25 d	promote	produce •OH and <sup>1</sup> O <sub>2</sub>	size distribution (%): 76.9 (> 100 μm) vs 62.5 (> 100 μm, virgin PS) and 66.2 (> 100 μm, aged PS); 0 (< 10 μm) vs 85.2 (< 10 μm, virgin PS) and 96.3 (< 10 μm, aged PS); 1.98 (< 1 μm) vs 24.5 (< 1 μm, virgin PS) and 20.6 (< 1 μm, aged PS); Cl: 0.32 vs 0.41 (PS-DOM); average size (μm): 3 vs 1.5 (PS-DOM)	[153]
iron red pigment	PP	xenon lamp; 1.8 mW/cm <sup>2</sup> ; 10–120 d	inhibit	light shielding and compete for electrons and ROS	T <sub>m</sub> (°C): 132.8 vs 147.2 (Fe <sub>2</sub> O <sub>3</sub> ); X <sub>c</sub> : 0.48 vs 0.71 (Fe <sub>2</sub> O <sub>3</sub> ); WCA (°): 108.3→91.7 vs 102.8→92.3 (Fe <sub>2</sub> O <sub>3</sub> ); O/C: 0.009→0.081 vs 0.012→0.079 ((Fe <sub>2</sub> O <sub>3</sub> );	[125]
antioxidant	PP	mercury lamp; 1.55–9.30 kJ/cm <sup>2</sup>	inhibit	sequester •OH	Cl: 0.12→0.5 (pure PP) vs 0.01→0.16 (meal box PP) vs 0.05→0.19 (tea cup PP); O/C: 0.02→0.14 (pure PP) vs 0.02→0.05 (meal box) vs 0.02→0.05 (tea cup); X <sub>c</sub> : 0.62→0.564 (pure PP) vs 0.613→0.612 (meal box) vs 0.612→0.607 (tea cup); T <sub>m</sub> (°C): 166→159 (pure PP) vs 156→149 (meal box) vs 167→149 (tea cup); ZP (mV): -1.37→-6.12 (pure PP) vs 2.5→-2.5 (meal box) vs 0→-2 (tea cup); size (μm): 444→34 (pure PP) vs 443→60 (meal box) vs 443→200 (tea cup)	[489]
NO <sub>3</sub> <sup>-</sup> , Br <sup>-</sup> , Cl <sup>-</sup> , HCO <sub>3</sub> <sup>-</sup>	PS	xenon lamp; 5–40 d	promote/ inhibit	NO <sub>3</sub> <sup>-</sup> , Br <sup>-</sup> and Cl <sup>-</sup> produce ROS;	size (μm): 27 (UP) vs 26 (HCO <sub>3</sub> <sup>-</sup> ) vs 20 (NO <sub>3</sub> <sup>-</sup> ) vs 23 (Cl <sup>-</sup> ) vs 22 (Br <sup>-</sup> ); O/C: 0.203 (UP) vs 0.215 (HCO <sub>3</sub> <sup>-</sup> ) vs 0.246 (NO <sub>3</sub> <sup>-</sup> ) vs 0.221 (Cl <sup>-</sup> ) vs 0.242 (Br <sup>-</sup> ); M <sub>w</sub> (kDa): 229.8 (UP) vs 230.9 (HCO <sub>3</sub> <sup>-</sup> ) vs 179.5 (NO <sub>3</sub> <sup>-</sup> ) vs 188.1 (Cl <sup>-</sup> ) vs 184.7 (Br <sup>-</sup> );	[124]

Factors	MNPs	Radiation condition	Influence	Mechanism	Critical results	Ref.
Cl <sup>-</sup>	PP	mercury lamp; 1.72–17.22 kJ/cm <sup>2</sup>	inhibit	HCO <sub>3</sub> <sup>-</sup> sequester in seawater could react with HO <sub>2</sub> <sup>•</sup> and prevent the formation O <sub>2</sub> <sup>•-</sup>	M <sub>n</sub> (KDa): 77.1 (UP) vs 76.0 (HCO <sub>3</sub> <sup>-</sup> ) vs 45.1 (NO <sub>3</sub> <sup>-</sup> ) vs 51.4 (Cl <sup>-</sup> ) vs 48.0 (Br <sup>-</sup> ); M <sub>p</sub> (KDa): 151.4 (UP) vs 149.8 (HCO <sub>3</sub> <sup>-</sup> ) vs 127.1 (NO <sub>3</sub> <sup>-</sup> ) vs 133.0 (Cl <sup>-</sup> ) vs 120.9 (Br <sup>-</sup> ); PDI: 2.98 (UP) vs 3.04 (HCO <sub>3</sub> <sup>-</sup> ) vs 3.98 (NO <sub>3</sub> <sup>-</sup> ) vs 3.66 (Cl <sup>-</sup> ) vs 3.85 (Br <sup>-</sup> ); CI: 1.609 (UP) vs 1.643 (HCO <sub>3</sub> <sup>-</sup> ) vs 1.762 (NO <sub>3</sub> <sup>-</sup> ) vs 1.671 (Cl <sup>-</sup> ) vs 1.706 (Br <sup>-</sup> ); O content (%): 0.50 ± 0.14 (pristine); 2.95 ± 0.63 (UP) vs 1.35 ± 0.07 (estuary) vs 1.30 ± 0.28 (seawater); ZP (mV): 1.94 ± 0.64 (pristine); -10.4 ± 4.71 (UP) vs -7.37 ± 1.76 (estuary) vs -7.07 ± 1.18 (seawater); WCA (°): 103 (pristine); 89.8 (UP) vs 97.9 (estuary) vs 98.2 (seawater); T <sub>m</sub> (°C): 166.2 (pristine); 147.3 (UP) vs 147.4 (estuary) vs 156.3 (seawater); X <sub>c</sub> (%): 98.56 ± 0.98 (pristine); 91.75 ± 0.46 (UP) vs 95.53 ± 0.65 (estuary) vs 98.16 ± 4.15 (seawater)	[127]
Cu <sup>2+</sup> , Pb <sup>2+</sup>	PS	xenon lamp; 1–7 d	promote	produce ROS	CI: 0.03 (pristine); 0.034 (UP) vs 0.048 (Cu <sup>2+</sup> ) vs 0.086 (Pb <sup>2+</sup> ); O/C: 0.013 (pristine); 0.022 (UP) vs 0.029 (Cu <sup>2+</sup> ) vs 0.035 (Pb <sup>2+</sup> );	[123]
nano-ZnO	PS	xenon lamp; 4.73–18.94 kJ/cm <sup>2</sup>	promote	produce •OH, <sup>1</sup> O <sub>2</sub>	PS NPs were almost photodegraded with ZnO NPs after 96 h irradiation.	[140]

Notes. T<sub>m</sub>: melting temperature; ZP: zeta potential; CI: carboxyl index; O/C: ratio of O content to C content; X<sub>c</sub>: the degree of crystallinity; WCA: water contact angle. SSA: specific surface area; M<sub>w</sub>: weight-average molecular weight; M<sub>n</sub>: number-average molecular weight; M<sub>p</sub>: peak molecular weight; PDI: polydispersity index. μm: micrometer (particle size unit of MNPs). DBE-209: decabromodiphenylether; TBBPA: tetrabromobisphenol A; TBBPA-DBPE: tetrabromobisphenol A-bis (2,3-dibromopropylether).

Table S4. The effect of MNPs on the photo-transformation of pollutants.

Contaminants	MNPs	radiation condition	Influence	Mechanism	Critical results	Ref.
Sulfamethoxazole	pristine and aged PS, 100 mg/L	mercury lamp; 68.5 mW/cm <sup>2</sup> ; 2 h	inhibit oxidation	light screening	$k_{obs}$ (min <sup>-1</sup> ): 0.0025 vs 0.0024 (PS <sub>0</sub> ) vs 0.0023 (PS <sub>36</sub> ) vs 0.0017 (PS <sub>72</sub> ) vs 0.0014 (PS <sub>120</sub> ); degradation rate (%): 25.9 vs 24 (PS <sub>0</sub> ) vs 24 (PS <sub>36</sub> ) vs 18.3 (PS <sub>72</sub> ) vs 15.6 (PS <sub>120</sub> ); $t_{1/2}$ (min): 277 vs 289 (PS <sub>0</sub> ) vs 301 (PS <sub>36</sub> ) vs 408 (PS <sub>72</sub> ) vs 495 (PS <sub>120</sub> );	[137]
Sulfamethoxazole	PS- and PE-DOM; 5–30 mg/L	xenon lamp; 2 h	inhibit oxidation	light screening	degradation rate (%): 28.1 vs 19.5 (5 mg/L PS-DOM) vs 17.7 (10 mg/L PS-DOM) vs 14 (20 mg/L PS-DOM) vs 8.16 (30 mg/L PS-DOM) vs 33.4 (10 mg/L SRNOM); $k_{obs}$ (10 <sup>-5</sup> s <sup>-1</sup> ): 3.75 vs 2.48 (10 mg/L PS-DOM) vs 4.38 (10 mg/L SRNOM)	[138]
Pyrene	pristine PS; 1–20 mg/L	xenon lamp and UV <sub>315</sub> light; 3 h	inhibit oxidation	light screening;	$k_{obs}$ (10 <sup>-2</sup> min <sup>-1</sup> ): 0.54 vs 0.47 (1 mg/L 0.1 μm PS) vs 0.43 (20 mg/L 0.1 μm PS) vs 0.35 (1 mg/L 1 μm PS) vs 0.35 (20 mg/L 1 μm PS);	[222]
Anthracene			promote oxidation	quenching <sup>1</sup> O <sub>2</sub> , O <sub>2</sub> <sup>•-</sup> and •OH	$k_{obs}$ (10 <sup>-2</sup> min <sup>-1</sup> ): 0.82 vs 1.03 (1 mg/L 0.1 μm PS) vs 1.11 (20 mg/L 0.1 μm PS) vs 0.94 (1 mg/L 1 μm PS) vs 1.01 (20 mg/L 1 μm PS)	
Tetrabromodiphenyl ether	aged PS, PE and PP	xenon lamp; 860 mW/cm <sup>2</sup> ; 24 h	inhibit/promote oxidation	light shielding	degradation rate (%): 96.2 (PS <sub>0</sub> ) vs 50 (PS <sub>48</sub> ); 90.1 (PP <sub>0</sub> ) vs 96.8 (PP <sub>48</sub> ); $k_{obs}$ (min <sup>-1</sup> ): 0.095 (PP <sub>0</sub> ) vs 0.148 (PP <sub>48</sub> ); 0.123 (PE <sub>0</sub> ) vs 0.174 (PE <sub>48</sub> )	[154]
Cimetidine	pristine and aged PS; 0.4 g/L	xenon lamp; 70 mW/cm <sup>2</sup> ; 2 h	promote oxidation	<sup>1</sup> O <sub>2</sub> and <sup>3</sup> PS*	degradation rate (%): < 8 (PS <sub>0</sub> ) vs 93 (PS <sub>3d</sub> ); > 99 (PS <sub>5d</sub> ) vs 99 (PS <sub>7d</sub> ); $k_{obs}$ (h <sup>-1</sup> ): 0 (PS <sub>0</sub> ) vs 1.16 (PS <sub>3d</sub> ); 3.37 (PS <sub>5d</sub> ) vs 2.27 (PS <sub>7d</sub> )	[224]
Atorvastatin	pristine and aged PS; 0–0.5 g/L	xenon lamp; 1.65 mW/cm <sup>2</sup> ; 3 h	promote oxidation	<sup>1</sup> O <sub>2</sub> and <sup>3</sup> PS*	$k_{obs}$ (h <sup>-1</sup> ): 0.090 vs 0.100 (0.001 g/L) vs 0.103 (0.01 g/L) vs 0.170 (0.1 g/L) vs 0.250 (0.5 g/L); $t_{1/2}$ (h): 7.69 vs 6.90 (0.001 g/L) vs 6.71 (0.01 g/L) vs 4.07 (0.1 g/L) vs 2.78 (0.5 g/L); degradation rate (%): 19.82 vs 21.02 (0.001 g/L) vs 22.57 (0.01 g/L) vs 32.86 (0.1 g/L) vs 50.27 (0.5 g/L); $k_{obs}$ = 0.285Cl + 0.158 (0.1 g/L; R <sup>2</sup> =0.933)	[226]

Contaminants	MNPs	radiation condition	Influence	Mechanism	Critical results	Ref.
Cefazolin	pristine and aged PVC; 1g/L	mercury lamp; 7 d	promote oxidation no effect	H bonds	$k_{obs}$ ( $10^{-3} h^{-1}$ ): 1.1±0.09 vs 1.0±0.02 (pristine PVC) vs 3.4±0.04 (aged PVC); $k_{obs}$ ( $10^{-3} h^{-1}$ ): 1.5±0.05 vs 1.3±0.06 (pristine PVC) vs 1.4±0.08 (aged PVC);	[227]
Cephalexin						
Tetracycline	PS; 1.25–6.25 g/L	xenon lamp; 5 h	promote oxidation	$^1O_2$ , $O_2^{\bullet-}$ and $\bullet OH$	$k_{obs}$ ( $h^{-1}$ ): 0.066 vs 0.078 (PS); $t_{1/2}$ (h): 10.45 vs 8.92 (PS); degradation rate (%): 27.65 vs 39.47 (PS)	[225]
Organotin	PP, PE, PS, PMMA; 1 g/L	UV <sub>365</sub> lamp; 2.3 mW/cm <sup>2</sup> ; 8 h	inhibit oxidation	light screening	degradation rate: control (without MNPs) > PMMA > PS > PE > PP	[223]
PP MNPs	pristine and aged PS; 0.4–1 g/L	UV lamp; 0–25 d	promote oxidation	$\bullet OH$	$\ln(d/d_0)$ ( $d^{-1}$ ): 0.22 (PP) vs 0.25 (PP + pristine PS) vs 0.26 (PP + aged PS); size percent (<1 $\mu m$ ) (%): 1.98 (PP) vs 24.5 (PP + pristine PS) vs 20.6 (PP + aged PS); CI: 0.32 (PP) vs 0.35 (PP + 0.4 g/L pristine PS) vs 0.41 (PP + 1 g/L pristine PS) vs 0.41 (PP + 0.4 g/L aged PS) vs 0.43 (PP + 1 g/L aged PS) vs 0.41 (PP + 50 mg/L PS-DOM)	[153]
PS MNPs	aged BMP-DOM;	UV lamp; 0–5 d	promote oxidation	$^1O_2$ and $O_2^{\bullet-}$	size ( $\mu m$ ): 206 ± 24 (pristine); 175 ± 46 vs 116 ± 25 (PBOM) vs 131 ± 25 (PLOM); size percent (100–180 $\mu m$ ) (%): < 10 (pristine); 52.9 vs 94.1 (PBOM) vs 86.7 (PLOM); O/C: 0.034 (pristine); 0.112 vs 0.176 (PBOM) vs 0.125 (PLOM);	[490]
Cr(VI)	pristine and aged PS; 10 mg/L	xenon lamp; 55 mW/cm <sup>2</sup> ; 90 h	promote/inhibit reduction	$O_2^{\bullet-}$	Cr(VI) removal (%): 0.65 (dark, PS) vs 23.78 (light, PS); Cr(VI) reduction rate ( $h^{-1}$ ): 0.0029 (PS-0) vs 0.0023 (PS-200) vs 0.0019 (PS-500) vs 0.0017 (PS-800)	[139]
Cr(III)	PS, PA, PVC, PP	UV <sub>254</sub> ; 1 mW/cm <sup>2</sup> ; 120 h	inhibit oxidation	compete ROS	photo-oxidation rate: PS > PA > PVC > PP > control	[491]
Ag <sup>+</sup>	pristine and aged PS; 20 mg/L	xenon lamp; 55 mW/cm <sup>2</sup> ; 24 h	promote reduction	$^1O_2$ and $\bullet OH$	[Ag <sup>+</sup> ] (mg/L): 8.5→7.35(dark) vs 7.93 (dark, PS) vs 7.19 (light) vs 6.73 (light, PS); Ag <sup>+</sup> reduction rate ( $h^{-1}$ ): 0.054 (pristine PS) vs 0.117 (aged PS) vs	[228]

Contaminants	MNPs	radiation condition	Influence	Mechanism	Critical results	Ref.
Ag <sup>+</sup>	PS; 500 mg/L	xenon lamp; 50 mW/cm <sup>2</sup> ; 24 h	promote reduction	electron shuttling	0.086 (PS-NH <sub>2</sub> ) vs 0.048 (PS-COOH) [Ag <sup>+</sup> ] (mg/L): 48.3 ± 1.8 (light, PS) vs 43.9 ± 2.7 (light, PS)	[229]
Mn <sup>2+</sup>	PS; 10 mg/L	xenon lamp; 6 h	promote oxidation	ROO• and O <sub>2</sub> <sup>•-</sup>	[MnO <sub>2</sub> ] (μM): 3 (30 nm PS-COOH, without buffer) vs 47 (30 nm PS-COOH) vs 6 (100 nm PS-bare) vs 14 (100 nm PS-COOH) vs 17 (100 nm PS-NH <sub>2</sub> )	[230]
Nano-Ag	PS; 20 mg/L	xenon lamp; 55 mW/cm <sup>2</sup> ; 96 h	promote oxidation	<sup>1</sup> O <sub>2</sub> , •OH and acid release	[Ag <sup>+</sup> ] (mg/L): 0.64 vs 0.97 (PS)	[141]
Nano-ZnO	PS; 20 mg/L	xenon lamp; 55 mW/cm <sup>2</sup> ; 96 h	promote dissolution	<sup>1</sup> O <sub>2</sub> , •OH and acid release	[Zn <sup>2+</sup> ] (mg/L): 3 vs 11 (PS)	[140]

Table S5. The biological effects of photo-oxidized MNPs on organisms and microbes.

Objects	Dose condition	Properties of MNPs (pristine vs aged)	Effect	Description	Ref.
Zebrafish	PA (5, 20, and 50 mg/L)	WCA (°): 90.6 vs 83.3 (UV) vs 57.3 (UV, H <sub>2</sub> O <sub>2</sub> ); O/C: 0.43 vs 0.6 (UV, H <sub>2</sub> O <sub>2</sub> ); N/C: 0.27 vs 0.23 (UV, H <sub>2</sub> O <sub>2</sub> ); EPFRs: -CH <sub>2</sub> •, -CH•, O=C• (UV, H <sub>2</sub> O <sub>2</sub> ); size (µm): 8.13 vs 6.73 (UV, H <sub>2</sub> O <sub>2</sub> ); size after 12 h (µm): 17.2 vs 16.3 (UV) vs 10.2 (UV, H <sub>2</sub> O <sub>2</sub> );	reduced toxicity	malformation rate (%): 3.6 (blank) vs 11.5 vs 5.1 (UV, H <sub>2</sub> O <sub>2</sub> ); ROS level (%): 204.3 vs 162.7 (UV) vs 119.3 (UV, H <sub>2</sub> O <sub>2</sub> ); tumor necrosis factor $\alpha$ level (%): 61.6 vs 10.9 (UV, H <sub>2</sub> O <sub>2</sub> ); interleukin 6 level (%): 62.3 vs 16.2 (UV, H <sub>2</sub> O <sub>2</sub> ); body burden (mg/g): 1.28 vs 1.24 (UV) vs 0.92 (UV, H <sub>2</sub> O <sub>2</sub> ); gene number upregulated: 131 vs 69 (UV, H <sub>2</sub> O <sub>2</sub> ); gene number downregulated: 244 vs 126 (UV, H <sub>2</sub> O <sub>2</sub> );	[235]
Zebrafish	PA (100 µg/L); tris(1,3-dichloro-2-propyl) phosphate (TDCIPP) (0.4, 2, and 10 µg/L)	SSA (m <sup>2</sup> /g): 3.8 vs 1.4; O/C: 0.43 vs 0.6; N/C: 0.27 vs 0.23; WCA (°): 94.8 vs 52.6; size (µm): 17.4±7.2 vs 9.2±3.7; TDCIPP Q <sub>e</sub> (mg/g): 0.363 vs 0.789	reduced toxicity	[TDCIPP] (µg/kg) in adult zebrafish: 74.3, 223.1, and 735.9 vs 99.3, 359.3, and 1053.3 (pristine PA) vs 81.9, 269.3, and 832.5 (aged PA); F0 zebrafish intestine: aged PA + TDCIPP > TDCIPP > aged PA; F0 zebrafish gonad: aged PA + TDCIPP < pristine PA + TDCIPP; F1 larval: aged PA + TDCIPP > TDCIPP > aged PA + TDCIPP; [MPs] (particle/g) in adult zebrafish: 243.3–266.5 vs 239.5–251.5; F0 gonad: 3.51–3.71 vs 3.09–3.55; F1 larvae: 0 vs 0	[248]
Zebrafish	PLA; 0.1–25 mg/L	size (µm): 25.56 vs 11.22; WCA (°): 74.2 vs 47.1; ZP (mV): -16.6 vs -27.9; EPFRs: C-centred	enhanced toxicity	body length (mm): 4.5 vs 4.1; cellular content (mg/g): 0.28 and 0.56 vs 0.4 and 0.78; caspase activity (%): 114 and 153 vs 176 and 208; gene number upregulated: 192 vs 242; gene number downregulated: 88 vs 170;	[232]
Zebrafish	PA; 32.50 µm; 1, 10, and 20 mg/L; HA and FA	size (µm): 32.5 vs 24.3 (HA) vs 19.8 (FA); O/C: 0.45 vs 0.46–0.50 (HA) vs 0.51–0.63 (FA); EPFRs: O-centred (HA, FA); WCA (°): 80.6 vs 58.8 vs 52.1; ZP (mV): -10 vs -25 (HA) vs -28 (FA);	enhanced toxicity	hatching rate (%): 90.7 (blank) vs 88.9 vs 84.1 (HA) vs 79.7 (FA); body weight decrease (%): 12.8 vs 22.2 (HA) vs 29.8 (FA); ROS level (%): 146.7 vs 191.3 (HA) vs 268.4 (FA); MP content (mg/g): 0.66 and 0.95 vs 0.81 and 1.17 (HA) vs 0.93 and 1.37 (FA);	[231]

Objects	Dose condition	Properties of MNPs (pristine vs aged)	Effect	Description	Ref.
<i>Carassius auratus</i>	PS (100 µg/L); roxithromycin (ROX)	O-containing groups occurred	enhanced toxicity	ROX in intestine (ng/g): 460 (ROX) vs 660 (ROX, pristine PS) vs 770 (ROX, aged PS)	[246]
Groupers	PS (0.01–130 mg/g)	size (µm): 55.9±25.5 vs 38.6±24.6; O/C: 0.04 vs 0.22; O-containing groups (%): 42.8 vs 52.1; EPFRs: O-centred (aged);	enhanced toxicity	MP content (mg/g): 6.01±0.17 vs 8.21±0.30 ; Additives in liver (µg/kg): 0 (pristine) vs dibutyl phthalate (9.60±0.47), di-isobutyl phthalate (1.54±0.09), acetophenone (0.54±0.05), and benzaldehyde (0.37±0.03) (aged). growth inhibition extent: aged > pristine; hepatomegaly extent: aged > pristine	[236]
Tilapia	PS (10 µg/L); sulfamethoxazole (SMX) and propranolol (PRP) (50 µg/L)	size (µm): 5.1±0.36 vs 5.0±0.35; SSA (m <sup>2</sup> /g): 5.47 v 6.92; average pore diameter (nm): 4.56 vs 4.13; SMX Q <sub>e</sub> (µg/g): 1882 vs 2024; PRP Q <sub>e</sub> (µg/g): 1885 vs 1928;	enhanced/reduced toxicity	[PRP] (µg/kg) in liver: 2500 (control) vs 4750 vs 3500; gut: 590 vs 16500 vs 7500; brain: 1400 vs 18000 vs 33000; gill: 1700 vs 3300 vs 2200; [SMX] (µg/kg) in gut: 450 vs 500 vs 480; gill: 48 vs 138 vs 78	[247]
<i>Daphnia magna</i>	PE (14–71 mg/L); benzalkonium chlorides (BAC) (0.5 mg/L)	SSA (m <sup>2</sup> /g): 0.06 vs 0.78; ZP (mV): -11.7 vs -53.3; CI: 0.035 vs 0.044; BAC <sub>12</sub> Q <sub>e</sub> (mg/g): 12.7 vs 14.8; BAC <sub>14</sub> Q <sub>e</sub> (mg/g): 22.1 vs 17.1; BAC <sub>16</sub> Q <sub>e</sub> (mg/g): 27.0 vs 20.7;	enhanced/reduced toxicity	survival rate (%): 30 (BAC <sub>12</sub> ) vs 74 (BAC <sub>12</sub> , PE) vs 100 (BAC <sub>12</sub> , aged PE); 0 (BAC <sub>16</sub> ) vs 64 (BAC <sub>16</sub> , PE) vs 50 (BAC <sub>16</sub> , aged PE)	[135]
<i>Daphnia magna</i>	PS (1 mg/L); nano-ZnO (5 mg/L)	[Zn <sup>2+</sup> ] (mg/L): 0.17 (ZnO, dark) vs 0.17 (ZnO, PS, dark) vs 0.76 (ZnO, UV) vs 2.93 (ZnO, PS, UV);	enhanced toxicity	mortality (%): 20 (ZnO, dark) vs 16 (ZnO, PS, dark) vs 50 (ZnO, UV) vs 88.5 (ZnO, PS, UV); proportion of ion-related toxicity (%): 2.68 (ZnO, dark) vs 36.15 (ZnO, UV) vs 92 (ZnO, PS, UV)	[140]

Objects	Dose condition	Properties of MNPs (pristine vs aged)	Effect	Description	Ref.
<i>Daphnia magna</i>	PS (1 mg/L); nano-Ag (50 µg/L)	[Ag <sup>+</sup> ] (mg/L): 0.41 (Ag, dark) vs 0.41 (Ag, PS, dark) vs 1.3 (Ag, UV) vs 2.7 (Ag, PS, UV);	enhanced toxicity	mortality (%): 8.5 (Ag, dark) vs 10.4 (Ag, PS, dark) vs 49.6 (Ag, UV) vs 95.2 (Ag, PS, UV); proportion of ion-related toxicity (%): 1.58 (Ag, dark) vs 29.11 (Ag, UV) vs 42.5 (Ag, PS, UV)	[141]
<i>Chlorella vulgaris</i>	PS and PVC (10–1000 mg/L); Cu <sup>2+</sup> and Cd <sup>2+</sup>	ZP (mV): -30 vs -26 (PS); -22 vs -19 (PVC)	enhanced/reduced toxicity	growth inhibition rate (%): 11.46–29.1 vs 17.65–36.84 (PS); 5.27–14.55 vs 11.15–30.03 (PVC); growth inhibition rate (%): 25.7 (aged PS) vs 17.34 (aged PVC) vs 19.5 (Cu <sup>2+</sup> ) vs 85.14 (Cd <sup>2+</sup> ) vs 10.22 (aged PS, Cu <sup>2+</sup> ) vs 27.55 (aged PS, Cd <sup>2+</sup> ) vs 18.89 (aged PVC, Cu <sup>2+</sup> ) vs 32.51 (aged PVC, Cu <sup>2+</sup> )	[244]
<i>Chlamydomonas reinhardtii</i>	PVC (10–200 mg/L)	SSA (m <sup>2</sup> /g): 0.49 vs 1.02; ZP (mV): -30.3 vs -12.7	enhanced toxicity	EC <sub>50</sub> (mg/L): 104.93 vs 63.66; chlorophyll a content (µg/L): 3152 (control) vs 2667 vs 2571	[233]
<i>Caenorhabditis elegans</i>	PS (0.1–100 µg/L)	size (µm): 1.005±0.009 vs 1.014±0.130; Ci: 0.085 vs 0.442; O/C: 0.031 vs 0.147	enhanced toxicity	head thrashes (%): 83.2 vs 68.8; body bends (%): 80.08 vs 76.0	[223]
<i>Caenorhabditis elegans</i>	PS (0.1–100 µg/L)	size (µm): 1.010±0.037 vs 0.996±0.012; Ci: 0.14 vs 0.388; O/C: 0.062 vs 0.157	enhanced toxicity	brood size (%): 76.5 vs 68; number of egg ejection (%): 83.4 vs 77.7; number of foci (%): 100 (control) vs 217 (aged PS)	[492]
<i>Scenedesmus obliquus</i>	PS (1 mg/L); EPS	ZP (mV): -17.0 (PS) vs -14.9 (PS, EPS) vs -14.3 (PS, UV) vs -13.2 (PS, EPS, UV); size (nm): 238 (PS) vs 238 (PS, EPS) vs 925 (PS, UV) vs 1071 (PS, EPS, UV);	reduced toxicity	cell viability (%): 68.6 (PS, EPS) vs 91.5 (PS, PES, UV); superoxide dismutase activity (%): 153.8 (PS, EPS) vs 120.5 (PS, PES, UV); catalase activity (%): 648.6 (PS, EPS) vs 162.2 (PS, PES, UV); cell permeability (%): 123.3 (PS, EPS) vs 216.7 (PS, PES, UV);	[189]
Fungi	PE, PP, PET; methylene blue	TOC (mg/L): 4 vs 17 (PE); 2.3 vs 15 (PVC); 0.2 vs 17 (PP)	–	decolourization rate (%): 5.75 (control) vs 28.56 (PE leachate); 53.57 (control) vs 50.9 (PP leachate) vs 40.6 (PET leachate)	[493]
Bacteria	mSBR	size (µm): 3.074 vs 2.297;	enhanced	OD600 (A/A <sub>0</sub> ): 0.93 vs 0.88;	[494]

Objects	Dose condition	Properties of MNPs (pristine vs aged)	Effect	Description	Ref.
	(100–1000 mg/L)	WCA (°): 147.6→151.3→145; ZP (mV): -25.1→-27.2→-32.2→-33.1	toxicity	protein (A/A <sub>0</sub> ): 0.71 vs 0.63	
Biofilm	PBAT and PVC (1.2–1.7 items/mL)	MP generation (items/g): 428.67±300.46 -1473.27±143.67 (PBAT); 185.53±85.73–584±506.12 (PVC)	enhanced growth	OUT number: 104 vs 190–314 (PBAT); 54 vs 172–214 (PVC); Shannon index: 1.15 vs 3.22–3.59 (PBAT); 0.44 vs 3.13–3.62 (PVC); Chao 1 index: 111 vs 240–319 (PBAT); 63 vs 214–341 (PVC)	[255]
Biofilm	PE (5 g/L)	WCA (°): 122 vs 98 (5 mm); formation of carbonyl and vinyl groups	enhanced growth	protein content (µg/g): 498 vs 917 (1 mm); 895 vs 1504 (5 mm); OUT number: 391 vs 295 (1 mm); 371 vs 213 (5 mm); Shannon index: 5.1 vs 3.6 (1 mm); 5.8 vs 2.5 (5 mm); Chao 1 index: 395 vs 296 (1 mm); 273 vs 219 (5 mm)	[256]
Biofilm	PE	surface generated pores and became rough; O/C: 0.119–0.129 vs 0.154–0.183	–	OD595: 0.073–0.281 vs 0.263–0.414 (2 weeks); OUT number: 237–306 vs 251–907; Shannon index: 7.07 vs 7.59; Chao 1 index: 1946 vs 2161	[254]
Sediment microorganisms	PS (0.5 %)	CI: 0.028 vs 0.069;	reduced negative effect	DOM humification index: 0.39–2.31 (control) vs 0.60–2.83 vs 0.42–2.52; DOM biological index: 0.73–1.21 (control) vs 0.69–0.98 vs 0.60–0.99; DOM bioavailability: 0.92 (control) vs 0.78 vs 0.71	[145]
Sediment microorganisms	TW (0.3 g/L)	SSA (m <sup>2</sup> /g): 0.098 vs 0.139; ZP (mV): 1.78 vs -0.72	enhanced toxicity	B. subtilis viability (%): 35 vs 32 (12 h); 73 vs 64 (48 h); H. lutimaris viability (%): 89 vs 81 (12 h); 48 vs 35 (48h)	[287]
Soil microorganisms	PE (1 %)	CI: 0.28 vs 0.42	–	pristine and aged MNPs increased total CO <sub>2</sub> emissions by 15.8–36.1 and 10.0–14.4 for two types of soils; pristine and aged MNPs increased total N <sub>2</sub> O emissions by 13.6–41.9, 3.5–9.5 and 8.9–16.8 folds for three types of soils.	[295]
Soil microorganisms	PE (0.01–1 %)	–	–	microbial biomass carbon (MBC) (mg C/kg): 213.3 (control) vs 206.7–210.9 vs 217.2–238.3; metabolic quotient (mg CO <sub>2</sub> -C/mg MBC): 0.59–0.72 vs 0.54–0.64;	[296]

Objects	Dose condition	Properties of MNPs (pristine vs aged)	Effect	Description	Ref.
Soil microorganisms	PP and PS (5%)	formation of O-containing groups	enhanced negative effect	soil DOC (mg C/kg): 50.8–55.9 vs 55.5–65.8; soil NO <sub>3</sub> <sup>-</sup> (mg N/kg): 11.3–14.2 vs 12.4–14.6	[146]
Planktonic microorganisms	PE, PP and PS	DOC (mg/g): 68.2 ± 0.9 (ePS); 39.1 ± 0.3 (PP); 4.8 ± 0.1 (PEstd); 1.1 ± 0.2 (PE)	enhanced/reduced growth	DOC bioavailability (%): 76 ± 8 (ePS); 59 ± 8 (PP); 46 ± 8 (PE); 22 ± 4 (PEstd)	[262]
Planktonic microorganisms	PE	18.6% labile (DOC)	enhanced growth	bacteria protein production (µgC/L/hr): 0.058–0.105 (control) vs 0.132–0.240 bacterial growth efficiency (%): 5.8–11.5 (control) vs 10.0–19.5	[144]
Planktonic microorganisms	PE, PP	DOC (µg/cm <sup>2</sup> ): 8.92 vs 6.67 (LDPE); 2.79 vs 6.28 (HDPE); 0.26 vs 0.31 (PE packaging); 1.61 vs 2.17 (PP packaging)	enhanced growth	DOC consumption (µM/L): 150.4 vs 92.1 (LDPE); 69.6 vs 136.3 (HDPE); 30.9 vs 27.2 (PE packaging); 52.5 vs 55 (PP packaging); Leucine incorporation (nM/L/h): 0.9 vs 2.5 (LDPE); 0.4 vs 2.5 (HDPE); 1.6 vs 3.3 (PE packaging); 1.3 vs 2.6 (PP packaging);	[143]

Note. F0 and F1 mean the parent generation and the first generation of offspring; OD600 and OD595 mean optical density at 600 and 595 nm representing cell concentration; OUT number represents the abundance of species; Shannon index represents the diversity of species; Chao 1 index represents species richness.

*Text S1. Evaluation of the Accelerating Factor*

A mercury lamp (500 W) emitting UV light with an intensity of approximately 35 mW/cm<sup>2</sup> was employed to age PS NPs. The spectrum of the mercury lamp is shown in [Figure S1](#), and was evaluated by comparing the photoaging of PS NPs under actual sunlight exposure in the Netherlands. PS NPs at a concentration of 20 mg/L were initially photoaged for durations of 3, 6, 12, and 24 hours using a mercury lamp. The extent of aging was determined by measuring the UV absorbance at 289 nm with UV-vis absorbance spectroscopy. As depicted in [Figure S2](#), the UV289 initially increased slightly and then decreased with prolonged photoaging. Real sunlight exposure was conducted on a house roof for five days in the Netherlands during the summer of 2023. Based on calculations, five days of sunlight exposure equated to six hours of mercury lamp aging. Thus, one day of mercury lamp aging corresponded approximately to 20 days of sunlight exposure in the Netherlands.

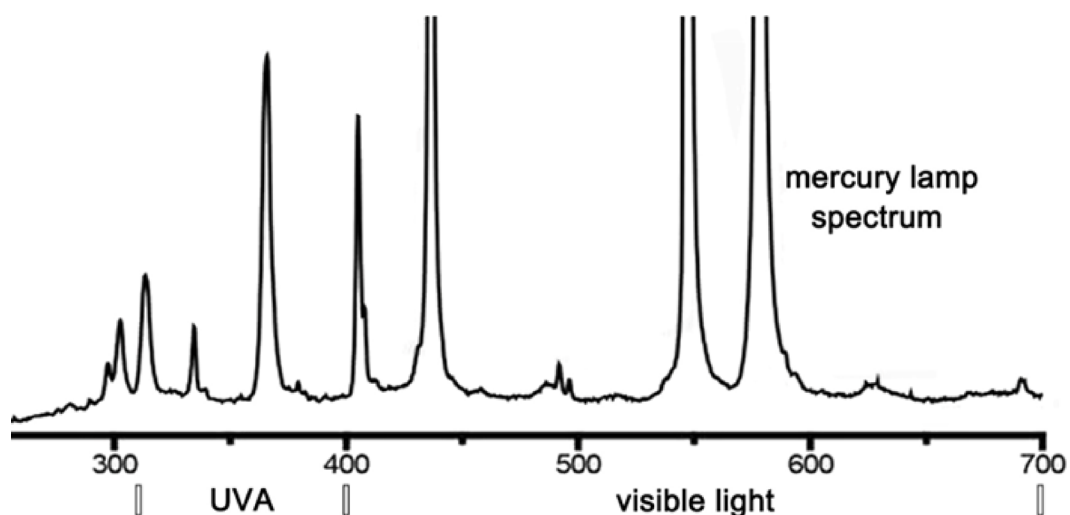


*Figure S1. The spectrum of the mercury lamp for accelerated photoaging.*

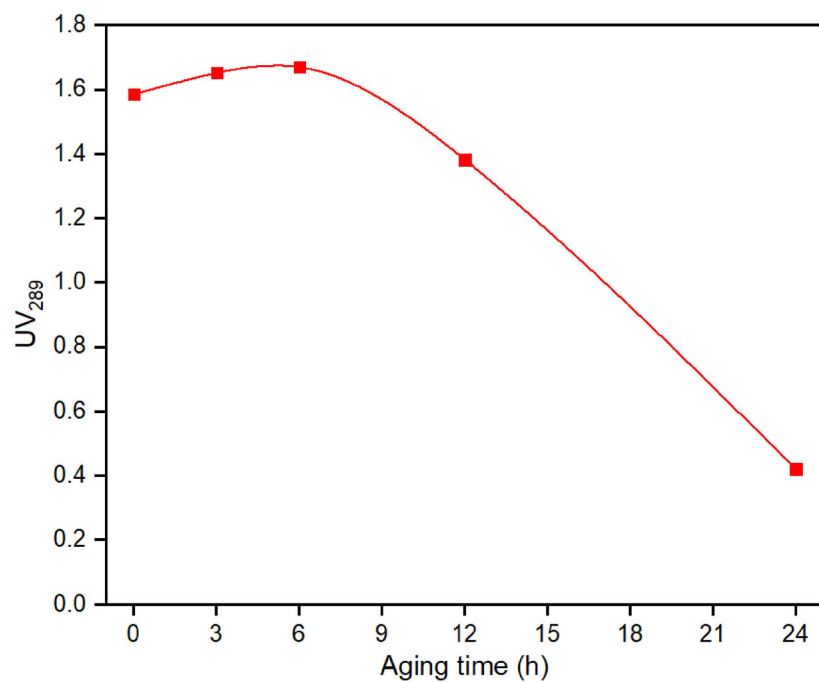


*Figure S2.* The change in UV absorbance at wavelength 289 nm of PS NPs (20 mg/L) under mercury lamp exposure.

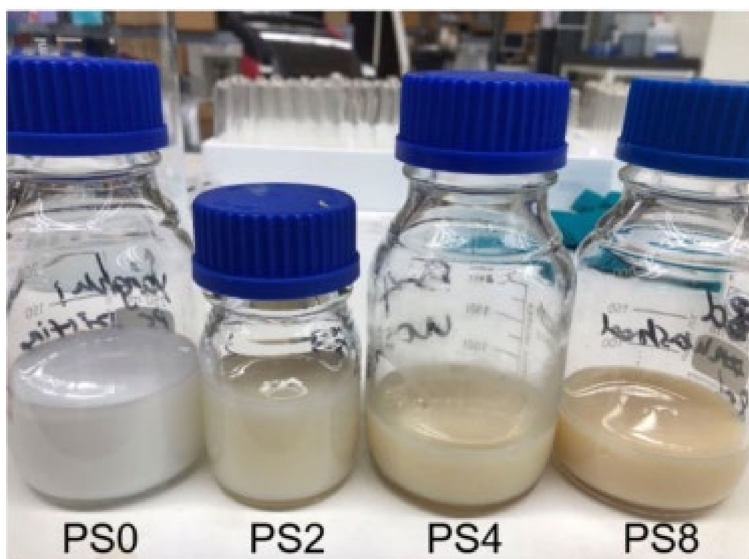


*Figure S3.* Pictures showing the color change of NPs after photoaging

**Table S6.** The UV289 (measured at approximately  $4.68 \times 10^{12}$  particles/L), TOC (measured at approximately  $4.68 \times 10^{12}$  particles/L) and size (measured with TEM) of PS<sub>0</sub>, PS<sub>2</sub>, PS<sub>4</sub> and PS<sub>8</sub>.

	PS <sub>0</sub>	PS <sub>2</sub>	PS <sub>4</sub>	PS <sub>8</sub>
UV289	0.967	0.927	0.916	0.902
TOC (mg C/L)	29.2 ± 0.1	27.8 ± 0.2	24.7 ± 0.1	23.6 ± 0.3
Size (nm)	159.2 ± 3.0	155.7 ± 4.2	152.7 ± 4.5	150.4 ± 4.9

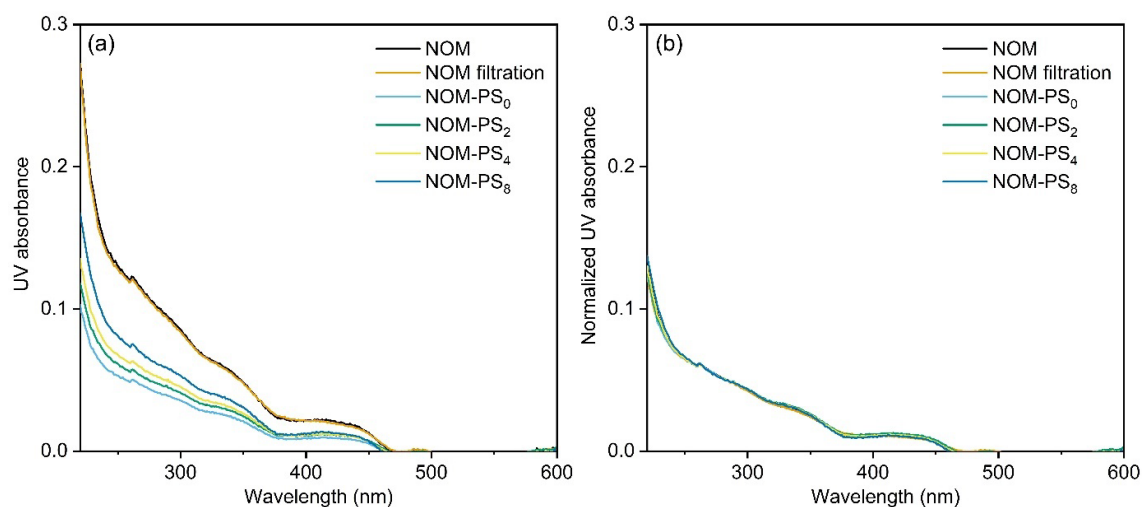


**Figure S4.** (a) UV absorbance of bulk NOM (2 mg C/L) before and after adsorption by pristine and photoaged NPs at 100 mM NaCl. (b) corresponding normalized UV absorbance (SUVA) to NOM mass that was estimated using UV<sub>280</sub>.

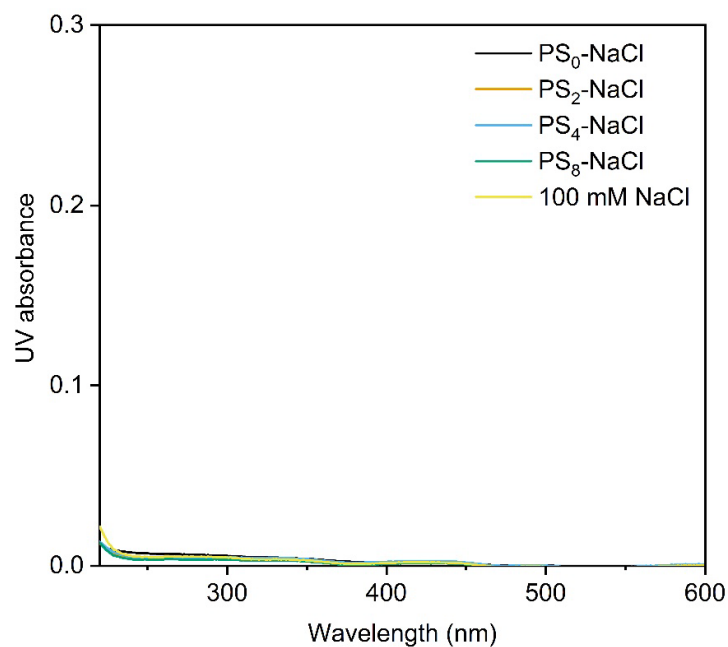


*Figure S5. UV absorbance of the filtrates of washed pristine and photoaged NPs (10 mg/L in 100 mM NaCl) after 0.1  $\mu\text{m}$  filtration, as well as 100 mM NaCl (blank).*

---

### Text S2. Aggregation Kinetics Measurements.

Time-resolved dynamic light scattering (DLS) technique was used to examine the aggregation kinetics of NPs in NaCl solutions utilizing a Malvern Zetasizer instrument (Nano ZS, Malvern, UK). The instrument featured a He–Ne laser operating at a wavelength of 633 nm and maintained a fixed scattering angle of 173° [370]. The NOM and NP samples were pre-mixed in ultrapure water, and the pH was adjusted to  $6.0 \pm 0.1$  using 0.1 M HCl and NaOH. The concentration of NPs was 10 mg/L, a common concentration for aggregation kinetic studies [76, 77, 82, 128]. Bulk NOM was adjusted to concentrations ranging from 1 to 10 mg C/L and NOM fractions to 2 mg C/L, falling within the typical range of NOM concentrations found in natural waters [81, 82, 369]. Before measurement, 0.5 mL of NPs or NPs/NOM were added to a 1-cm quartz cuvette, followed by the addition of 0.5 mL of NaCl solution with the desired concentration (ranging from 200 mM to 2000 mM). The mixture was immediately measured, and the aggregation kinetic was determined by continuously monitoring the hydrodynamic size change of samples every 30 seconds over a 15-minute period [495]. Duplicates or triplicates were conducted for each sample.

The aggregation kinetics of PS NPs in the early stages were assessed by measuring the initial rate of hydrodynamic size ( $D_h$ ) change over time ( $t$ ). The initial aggregation rate constant ( $k$ ) was directly proportional to the initial rate of  $D_h$  increase and was normalized to the initial concentration of PS NPs in the suspension ( $M_0$ ) (Equation (S1)) [81].

$$k \propto \frac{\left(\frac{dD_h(t)}{dt}\right)_{t \rightarrow 0}}{M_0} \quad (\text{S1})$$

The initial rate of the linear increase in  $D_h$  for PS NPs with time ( $dD_h(t)/dt$ ) was determined from  $t = 0$  until  $D_h$  reached  $1.5D_{h0}$ . This value was calculated using linear least squares regression analysis. The attachment efficiency ( $\alpha$ ), used to characterize the stability of PS NPs, was calculated by normalizing  $k$  under various solution conditions to  $k_f$  under rapid aggregation conditions [130, 496].

$$\alpha = \frac{k}{k_f} = \frac{\left(\frac{dD_h(t)}{dt}\right)_{t \rightarrow 0}}{\left(\frac{dD_h(t)}{dt}\right)_{t \rightarrow 0, fast}} \quad (\text{S2})$$

Two distinct regimes, termed reaction-limited and diffusion-limited aggregation, can be clearly identified. In the initial reaction-limited stage ( $\alpha < 1$ ), the aggregation efficiency of PS NPs increased with increasing salt concentration, consistent with DLVO theory [130, 175]. The salt concentration at which attachment efficiency ( $\alpha$ ) reaches its maximum value 1 was termed the critical coagulation concentration (CCC), serving as an indicator of the aggregation potential

of PS NPs [130, 372]. In this study, the CCC values of most samples, such as pristine and photoaged NPs in the presence of NOM, were not determined due to their strong stability.

The Zetasizer typically reports the intensity-weighted hydrodynamic size of nanoparticles, which may overestimate larger particles due to their stronger light scattering [497]. To ensure that the observed aggregation of NPs analyzed using the Zetasizer was not biased by a few larger aggregates, the additional aggregation measurements using the Litesizer DLS 700 (Anton Paar, Austria) were conducted to detect the changes in the intensity, volume, and number-weighted hydrodynamic sizes. The aggregation processes of pristine (PS<sub>0</sub>) and photoaged (PS<sub>4</sub>) NPs (10 mg/L) in the absence and presence of bulk NOM (10 mg/L) in 500 mM NaCl were studied.

*Text S3. Characterization methods of NPs*

The UV-vis spectroscopy (G10S UV-Vis, Thermo Fisher Scientific) and three-dimensional excitation-emission matrix (3D-EEM) fluorescence spectroscopy (Horiba Scientific) were employed to characterize the chemical properties of bulk NOM and NOM fractions. The hydrodynamic size and zeta potential of NPs in the absence and presence of NOM were measured using the Zetasizer Nano ZS90 (Malvern Instruments, UK). Before measurement, pristine or photoaged NPs (10 mg/L) and NOM or NOM fractions (2 mg C/L) were mixed in 10 and 100 mM NaCl for 24 h (preliminary tests indicated that no aggregation of NPs or NOM occurred at these conditions). The average adsorption layer thickness of NOM on the NPs was calculated based on the differences in the hydrodynamic size of NPs before and after interaction with NOM.

The size and morphology of pristine/photoaged NPs in ultrapure water were examined using a scanning electron microscope (SEM, Quattro, FEI) and a transmission electron microscope (TEM, Tecnai G20, FEI Corp, USA). For SEM measurement, NPs were pre-filtered onto 0.1  $\mu\text{m}$  PES membranes, dried at 40 °C and then coated with gold. Prior to TEM analysis, the samples were dropped onto 200 mesh carbon-coated copper grids and dried at 40 °C.

Attenuated total reflectance Fourier transform infrared spectroscopy (ATR-FTIR, Nicolet iN10, Thermo Fisher Scientific) was used to detect the surface functional groups of NPs and NOM, as well as their interactions utilizing wavenumbers ranging from 400 to 4000  $\text{cm}^{-1}$  [130]. The NP samples were prepared by drying concentrated NPs on a glass slide at 40 °C to avoid changes of NPs, while NOM samples were freeze-dried using a freeze-dry instrument (BK-FD12PT, Vertical Freeze Dryer, BIOBASE BIODUSTRY) before FTIR analysis. To detect the interactions between NPs and NOM, 100 mL reaction solutions containing 10 mg/L pristine or photoaged NPs and 2 mg/L bulk NOM or NOM fractions were prepared and incubated for 24 h in 100 mM NaCl. The mixture was then filtered using 0.1  $\mu\text{m}$  PES membranes, and the samples on the membranes were dried at 40 °C before being analyzed using FTIR. Twenty discrete spectral measurements were conducted linearly and subsequently integrated to synthesize a composite spectrum.

### Text S4. DLVO and Steric Model

The classical Derjaguin-Landau-Verwey-Overbeek (DLVO) theory includes van der Waals and electrostatic double layer interactions [188, 370]. The total interaction energy ( $E_{DLVO}$ ) defined as the sum of the van der Waals interaction energy ( $E_{vdW}$ ) and electric double layer interaction energy ( $E_{EDL}$ ). In the presence of NOM, the extend DLVO (XDLVO) considering a steric (polymer-mediated) model was used to investigate interaction energies between NPs based on repulsive steric interaction and attractive polymer bridging interaction.

**DLVO.** The equations of  $E_{DLVO}$ ,  $E_{vdW}$  and  $E_{EDL}$  are given as follows:

$$E_{DLVO} = E_{vdW} + E_{EDL} \quad (S3)$$

$$E_{vdW} = -\frac{A_{121}R}{12h(1+\frac{14h}{\lambda_0})} \quad (S4)$$

$$E_{EDL} = 32\pi\epsilon_0\epsilon_r R(k_B T/ze)^2 \tanh\left(\frac{\psi}{4k_B T/ze}\right)^2 \exp(-\kappa h) \quad (S5)$$

where  $A_{121}$  (J) is the Hamaker constant of NP-water-NP system.  $A_{121} \approx ((A_{11})^{1/2} - (A_{22})^{1/2})^2$ , where  $A_{11}$  and  $A_{22}$  denote the Hamaker constants of NPs and water ( $A_{22} \approx 3.7 \times 10^{-20}$  J) in a vacuum. The Hamaker constants of PS<sub>0</sub>, PS<sub>2</sub>, PS<sub>4</sub>, and PS<sub>8</sub> were estimated to be  $5.1 \times 10^{-21}$  J,  $1.2 \times 10^{-21}$  J,  $5.0 \times 10^{-22}$  J, and  $3.5 \times 10^{-22}$  J based on fitting results [128, 498].  $R$  (nm) is the particle radius.  $h$  (nm) is the separation distance.  $\epsilon_0$  and  $\epsilon_r$  are the permittivity of the vacuum ( $8.854 \times 10^{-12}$  C/(V·m)) and the relative dielectric constant of the liquid (78.5), respectively.  $k_B$  is the Boltzman constant ( $1.381 \times 10^{-23}$  J/K).  $T$  is absolute temperature (298 K),  $z$  is the valence state of ion.  $e$  is the electron charge ( $1.602 \times 10^{-19}$  C).  $\psi$  (V) is the potential of NPs.  $\kappa$  is the inverse Debye length (Eq. 6).

$$\kappa^{-1} = \sqrt{\frac{\epsilon_r \epsilon_0 k_B T}{2NAIe^2}} \quad (S6)$$

where  $NA$  is the Avogadro constant ( $6.02 \times 10^{23}$  mol<sup>-1</sup>), and  $I$  is the ionic strength of the solutions,  $I = 0.5 \sum c_i z_i^2$ ,  $c_i$  is the molarity of ion. The Debye length or ionic diffuse layer is a measure of the range of electrostatic interactions.  $\kappa^{-1}$  is calculated as 0.96 nm and 0.43 nm in 100 mM and 500 mM NaCl, respectively.

**Steric Repulsion.** The adsorbed polymer layer on NPs can lead to an increase in osmotic pressure and elastic repulsion. The repulsive steric interaction energy ( $E_s$ ) is defined as the sum of osmotic ( $E_{osm}$ ) and elastic repulsive energies ( $E_{elas}$ ). The equation of  $E_{osm}$  could be expressed as follows [499, 500]:

$$\frac{E_{osm}}{k_B T} = 0, \quad 2d \leq h \quad (S7)$$

$$\frac{E_{osm}}{k_B T} = \frac{4\pi R}{v_1} \Phi_{NOM}^2 \left(\frac{1}{2} - \chi\right) \left(d - \frac{h}{2}\right)^2, d \leq h \leq 2d \quad (S8)$$

$$\frac{V_{osm}}{k_B T} = \frac{4\pi R}{v_1} \Phi_{NOM}^2 \left(\frac{1}{2} - \chi\right) d^2 \left(\frac{h}{2d} - \frac{1}{4} - \ln\left(\frac{h}{d}\right)\right), h < d \quad (S9)$$

where  $v_1$  is the volume of one solvent molecule (0.03 nm<sup>3</sup>),  $\chi$  is the Flory-Huggins solvency parameter (0.45),  $d$  (nm) is the thickness of adsorbed NOM, estimated as half of the difference in the hydrodynamic size of NPs before and after NOM adsorption in 100 mM NaCl ([Table S7](#)) [501],  $\phi_{NOM}$  is the effective volume fraction of the adsorbed NOM layer and can be expressed as follows:

$$\Phi_{NOM} = 3 \frac{QR^2}{\rho_{NOM}[(d+R)^3 - R^3]} \quad (S10)$$

where  $Q$  (mg/m<sup>2</sup>) is the maximum adsorbed amount of NOM on NP surface ([Table S9](#)).  $\rho_{NOM}$  is the density of NOM (assumed to be 1.5 g/cm<sup>3</sup>) [502].

The equation of  $E_{elas}$  could be expressed as follows [503]:

$$\frac{E_{elas}}{k_B T} = 0, d \leq h \quad (S11)$$

$$\frac{E_{elas}}{k_B T} = \frac{2\pi R}{M_W} \Phi_{NOM} d^2 \rho_{NOM} \left[ \frac{2}{3} - \frac{1}{6} \left(\frac{h}{d}\right)^3 - \left(\frac{h}{2d}\right) + \left(\frac{h}{d}\right) \ln\left(\frac{h}{d}\right) \right], d > h \quad (S12)$$

where  $M_W$  (Da) is the molecular weight of NOM.[501] The MWs of bulk NOM and its fractions were estimated as follows: bulk NOM at 12,000 Da, NOM (> 30 kDa) at 50,000 Da, NOM (10–30 kDa) at 20,000 Da, NOM (3–10 kDa) at 6,500 Da, and NOM (< 3 kDa) at 1,500 Da.

Kuhl et al. also developed a steric repulsion model and the equation of  $E_S$  could be expressed as follows [504]:

$$E_S = \frac{16\pi K T d R}{35s^3} \left( 56 \left(\frac{2d}{h}\right)^{\frac{1}{4}} - \frac{40}{11} \left(\frac{h}{2d}\right)^{\frac{11}{4}} + 24 \frac{h}{2d} - \frac{840}{11} \right) \quad (S13)$$

Where  $s$  (nm) is the mean distance between anchoring (or grafting) sites on the surface ([Table S11](#)) [347].  $s$  could be calculated using following equation:

$$s = \sqrt{\frac{M_W}{NA \times Q}} \quad (S14)$$

where  $M_W$  (Da) is the molecular weight of NOM,  $NA$  is the Avogadro constant (6.02×10<sup>23</sup> mol<sup>-1</sup>),  $Q$  (mg/m<sup>2</sup>) is the adsorbed amount of NOM on NP surface ([Table S8](#)). The corresponding surface coverage (%) of NOM on NPs was shown in [Table S9](#).

Both steric repulsion models could predict the stabilization of pristine NPs by NOM. The calculated interaction energies based on osmotic pressure and elastic repulsion were much

higher than those from the secondary steric model by Kuhl et al. Additionally, since the secondary steric repulsion model shared the same parameters as the polymer bridging model, the secondary steric model was used in this study.

**Polymer Bridging.** Attractive polymer-mediated interactions (i.e. polymer bridging) occur when the polymer's affinity for another surface surpasses a certain threshold. The bridging adhesion energy ( $E_B$ ) is calculated as follows [371]:

$$E_B = \frac{2\pi R}{s^2 l} \left( l_c h - \frac{h^2}{2} - \frac{l_c^2}{2} \right) \quad (\text{S15})$$

where  $l$  (nm) is a segment length is considered as twice the C-C bond length (0.304 nm),  $l_c$  is the polymer contour length (Table S2),  $\epsilon$  (kT) is the bonding energy per segment (assumed to be 0.3 kT) and  $s$  (nm) is the mean distance between anchoring (or grafting) sites on the surface (Table S10) [347].

**Combination of DLVO and Steric Model.** Conventional DLVO theory considers interactions between "hard" particle surfaces. Some studies have integrated the steric model with the conventional DLVO theory by using the apparent zeta potential for calculations, which is suitable at low ionic strengths [502, 505]. In such conditions, the adsorbed layer thickness is smaller than the Debye length, so adsorbed polymers do not substantially distort the electrical potential distribution in the ionic diffuse layer. However, at high ionic strength, the adsorbed layer thickness may exceed the Debye length, making conventional DLVO theory inapplicable, as it would suggest that electrostatic interactions occur after the contact of adsorbed layers.

Ohshima's electrophoretic theory proposes that the outer surface potential (of the adsorbed layer) is the appropriate electrical potential for predicting electrostatic interactions between "soft" particles coated by polymers [506, 507]. However, Ohshima's theory applies DLVO principles to adsorbed layers and sometimes fails to accurately describe colloidal interactions of polymer-coated particles [506, 508]. Additionally, Ohshima's theory addresses pre-contact DLVO interactions between adsorbed layers, while the steric model describes post-contact particle interactions. Integrating the steric model with Ohshima's DLVO theory is difficult as they start from different zero separation distances.

Therefore, combining the steric model with both conventional DLVO theory and Ohshima's theory at high ionic strengths poses a challenge. Studies have indicated that, at high ionic strength, the effective distance of electrical double layer repulsion between approaching particles may be governed by the adsorbed layer thickness rather than the Debye length [385]. To address this, we used a modified Debye length (effective electrical double layer) in the conventional DLVO theory in this study. The modified Debye length was assumed to be the sum of the NOM adsorption layer thickness and the theoretical  $k^{-1}$  [509, 510].

**Table S7.** The  $d$  and  $L_c$  (nm) of bulk NOM and NOM fractions (2 mg/L) on pristine and photoaged NPs, estimated as half of the difference in the hydrodynamic size of NPs before and after NOM adsorption in 100 mM NaCl (Figure 2d).  $d$  and  $L_c$  (nm) in 500 mM NaCl were assumed to be the same.

d or $L_c$ (nm)	Bulk	> 30 kDa	10-30 kDa	3-10 kDa	< 3 kDa
PS <sub>0</sub>	2.81	6.07	4.82	4.29	2.02
PS <sub>2</sub>	4.19	6.62	3.87	3.22	1.58
PS <sub>4</sub>	4.23	6.92	4.77	4.05	2.95
PS <sub>8</sub>	3.63	5.91	4.17	2.92	2.33

**Table S8.** Adsorption capacity ( $Q$ , mg/m<sup>2</sup>) of bulk NOM and NOM fractions (2 mg/L) on pristine and photoaged NPs, as estimated based on NOM removal conducted in 100 mM NaCl (Figure 2a), and particle size of NPs (Figure 2c).  $Q$  in 500 mM NaCl were assumed to be the same.

$Q$ (mg/m <sup>2</sup> )	Bulk	> 30 kDa	10-30 kDa	3-10 kDa	< 3 kDa
PS <sub>0</sub>	3.35	2.94	2.79	2.72	2.28
PS <sub>2</sub>	3.22	2.88	2.86	2.71	2.24
PS <sub>4</sub>	2.97	2.78	2.92	2.81	2.1
PS <sub>8</sub>	2.51	2.48	3.03	2.84	2.14

**Table S9.** Surface coverage (%) of bulk NOM and NOM fractions (2 mg/L) on pristine and photoaged NPs, as estimated based on NOM density (assumed to be 1.5 g/cm<sup>3</sup>), molecular size, and adsorption amount. NOM molecules were assumed to have a spherical geometry, with their molecular sizes calculated using the online Molecular Weight to Size Calculator (<https://nanocomposix.com/pages/molecular-weight-to-size-calculator>).

Coverage (%)	Bulk	> 30 kDa	10-30 kDa	3-10 kDa	< 3 kDa
PS <sub>0</sub>	114.2	62.1	80.1	113.7	155.2
PS <sub>2</sub>	102.9	57.0	77.0	106.0	143.2
PS <sub>4</sub>	88.6	51.6	73.6	102.8	125.5
PS <sub>8</sub>	72.3	44.4	73.5	100.2	123.3

**Table S10.** The distance between anchoring sites (*s*, nm) of bulk NOM and NOM fractions (2 mg/L) on pristine and photoaged NPs, as estimated based on Equation S14. The MWs of bulk NOM and its fractions were estimated as follows: bulk NOM at 12,000 Da, NOM (> 30 kDa) at 50,000 Da, NOM (10–30 kDa) at 20,000 Da, NOM (3–10 kDa) at 6,500 Da, and NOM (< 3 kDa) at 1,500 Da. *s* in 500 mM NaCl were assumed to be the same.

<i>s</i> (nm)	Bulk	> 30 kDa	10-30 kDa	3-10 kDa	< 3 kDa
PS <sub>0</sub>	1.51	5.31	3.45	1.99	1.04
PS <sub>2</sub>	2.48	5.37	3.41	2.00	1.05
PS <sub>4</sub>	2.59	5.48	3.37	1.96	1.09
PS <sub>8</sub>	2.82	5.78	3.31	1.95	1.08

*Table S11. Functional groups of pristine and photoaged PS NPs at their respective wavenumbers measured using FTIR.*

Wavenumber (cm <sup>-1</sup> )	Functional groups	References
696, 753, and 1028	C–H in-plane bending/aromatic C–H bending	[128, 130, 511, 512]
1452	aromatic ring movement or –CH <sub>2</sub> – vibration	[511-514]
1493 and 1601	C=C stretching of the aromatic ring	
2850	C–H stretching vibration of the –CH group in the aliphatic segments	[225, 512, 513, 515-517]
2920	C–H stretching vibration of –CH <sub>2</sub> – group in the aliphatic segments	
3026	C–H vibration of the aromatic ring	
1717	C=O group	[372]
3453	–OH group	

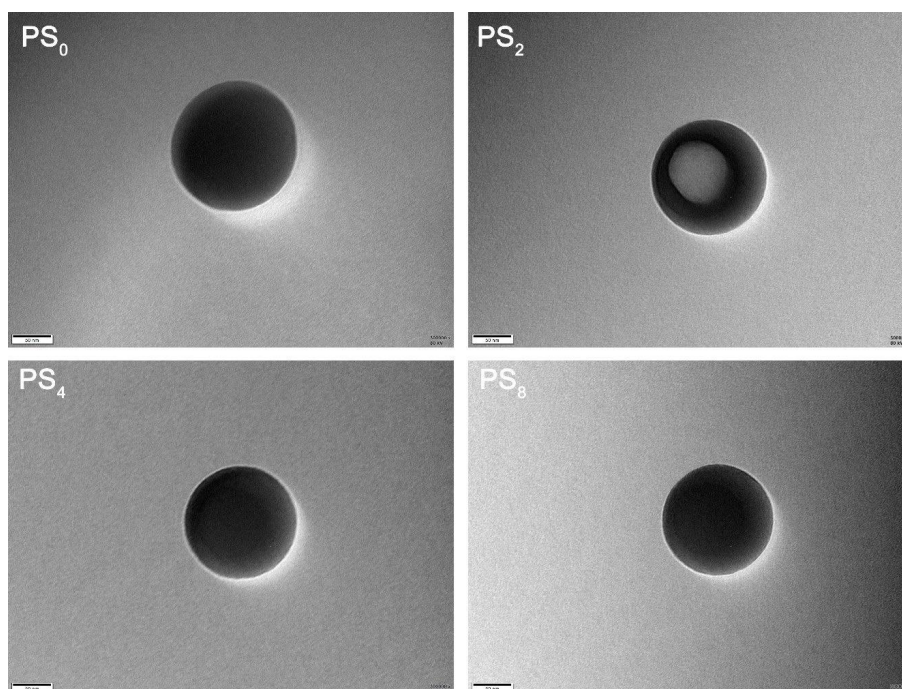


*Figure S6. TEM images of pristine and photoaged NPs*

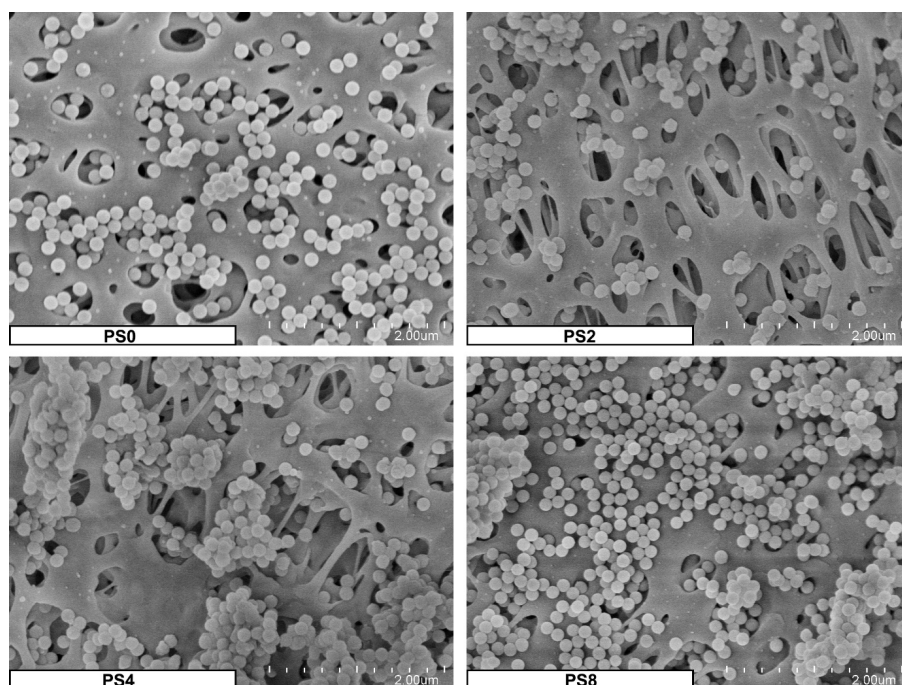


*Figure S7. SEM images of pristine and photoaged NPs (NPs were obtained by filtration on membranes and gold sputtering was conducted prior to measurement).*

*Table S12. Functional groups of bulk NOM and NOM fractions at their respective wavenumbers measured using FTIR.*

Wavenumber (cm <sup>-1</sup> )	Functional groups	References
1042 and 1112	C–O stretching of alcohols or carbohydrates	[367, 375]
1388	OH deformation, C–O stretching of phenolic OH, or deprotonated carboxyl groups (COO <sup>-</sup> ) asymmetric stretching	[375, 518]
1574	aromatic alkenes, conjugated carbonyl, or COO <sup>-</sup> asymmetric stretching	[519]
1747	C=O stretch of amide, quinone, or protonated carboxylic acids (COOH)	[355, 520]
3300	–OH stretching	[355, 375, 376]

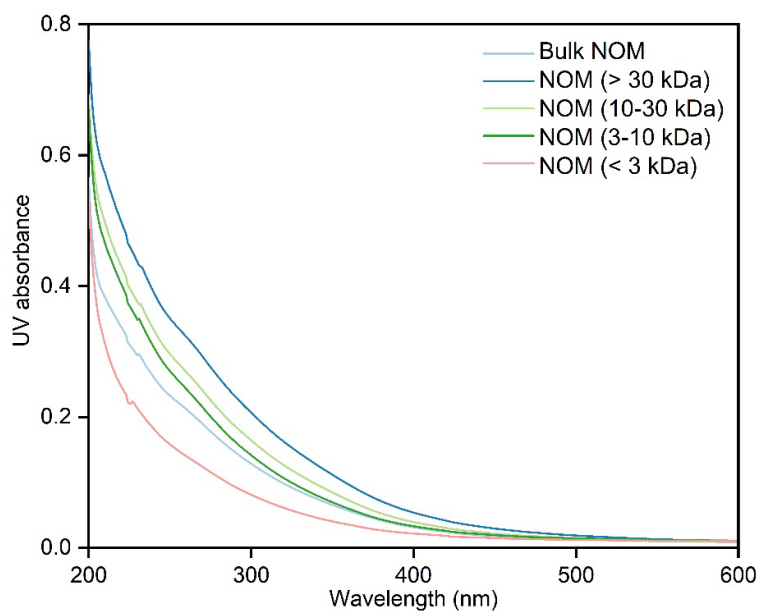


*Figure S8. UV absorbance of bulk NOM and different NOM fractions (4 mg C/L).*

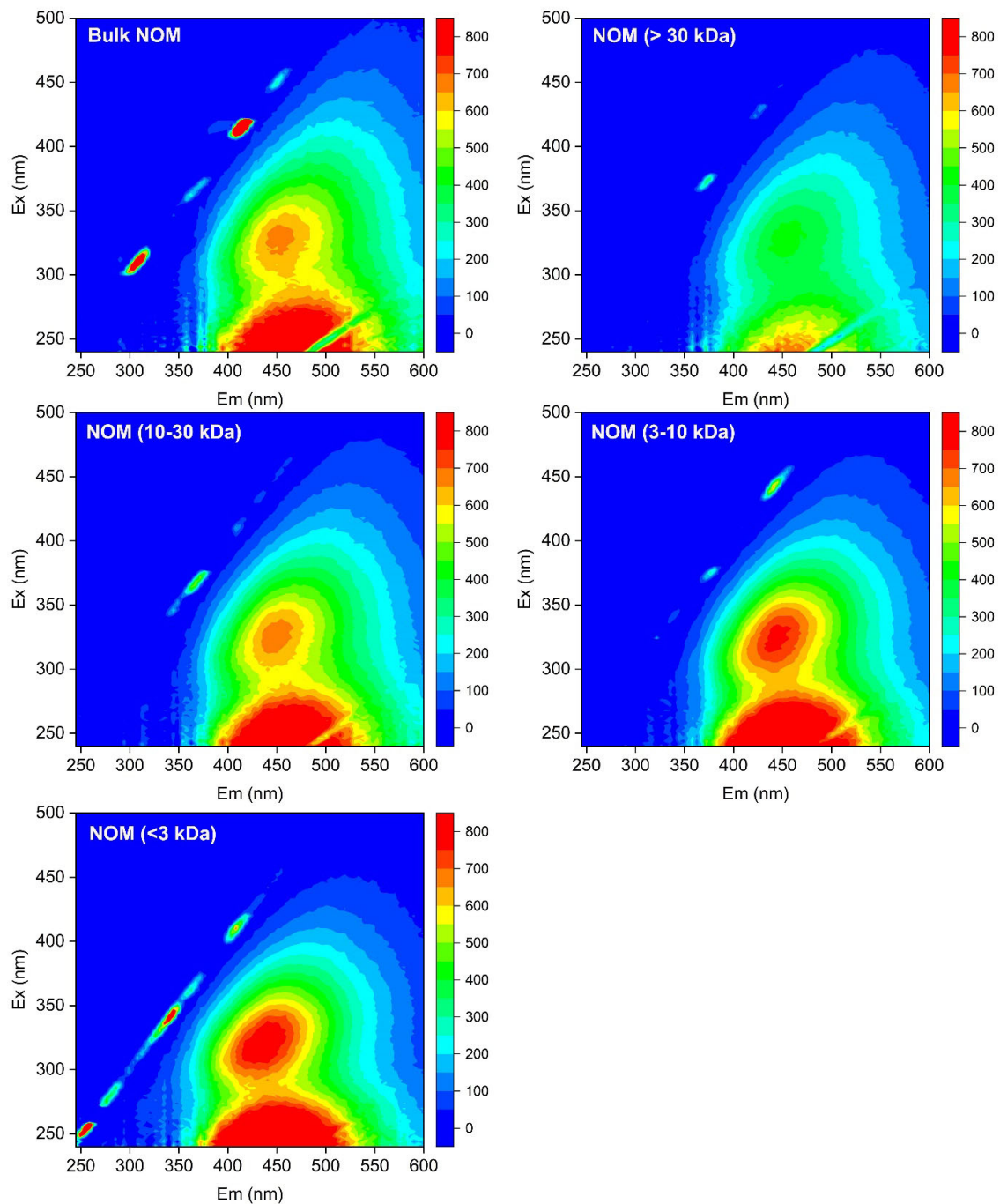
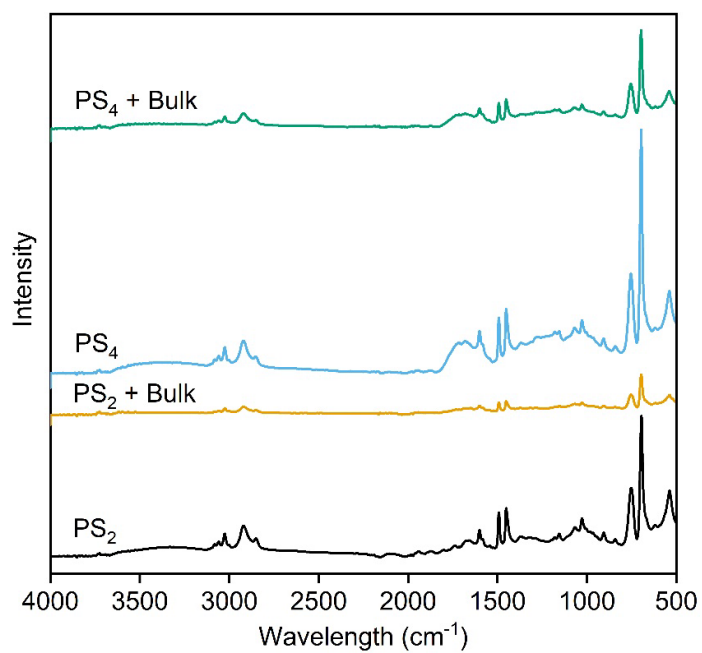


Figure S9. 3D-EEM spectra of bulk NOM and different NOM fractions



*Figure S10. FTIR spectra of PS<sub>2</sub> and PS<sub>4</sub> before and after adsorption with bulk NOM in 100 mM NaCl.*

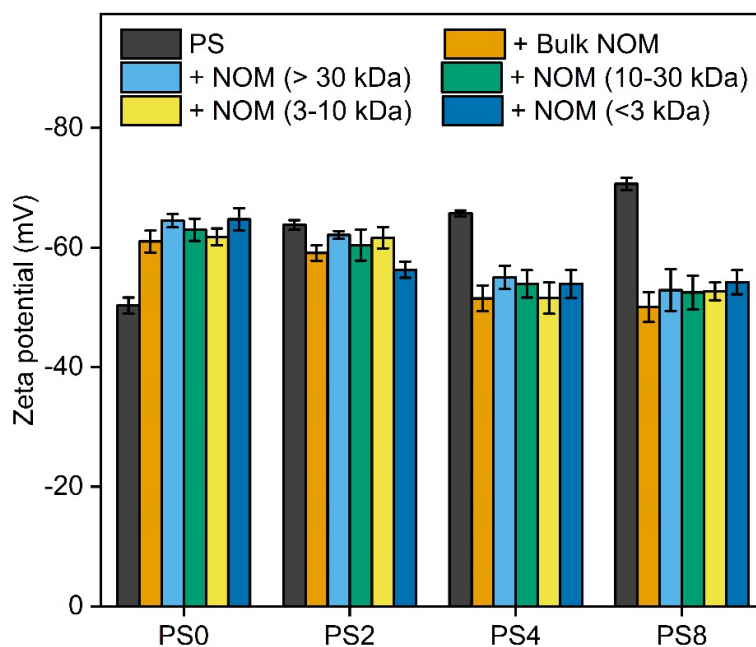


Figure S11. The zeta potential of pristine and photoaged NPs with and without bulk NOM and NOM fractions in 10 mM NaCl. Error bars represent the mean  $\pm$  1.96 SE (n = 10).

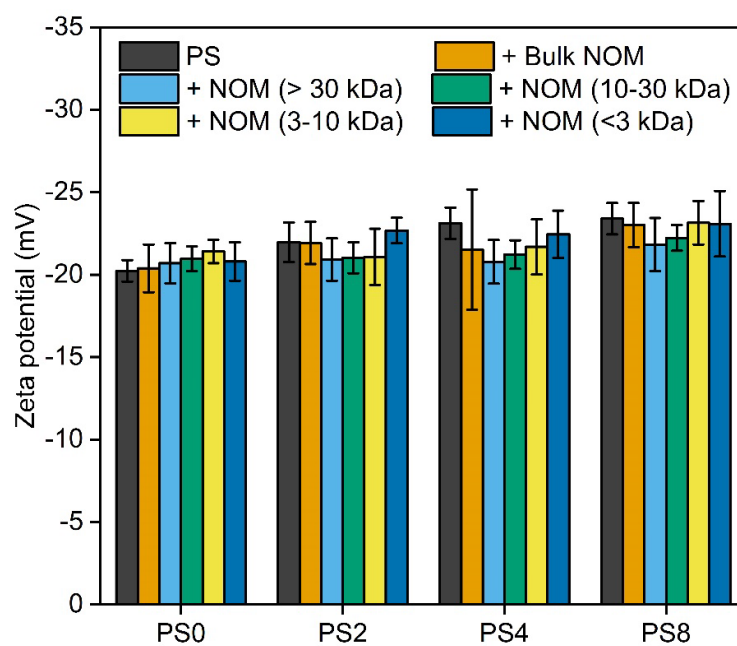
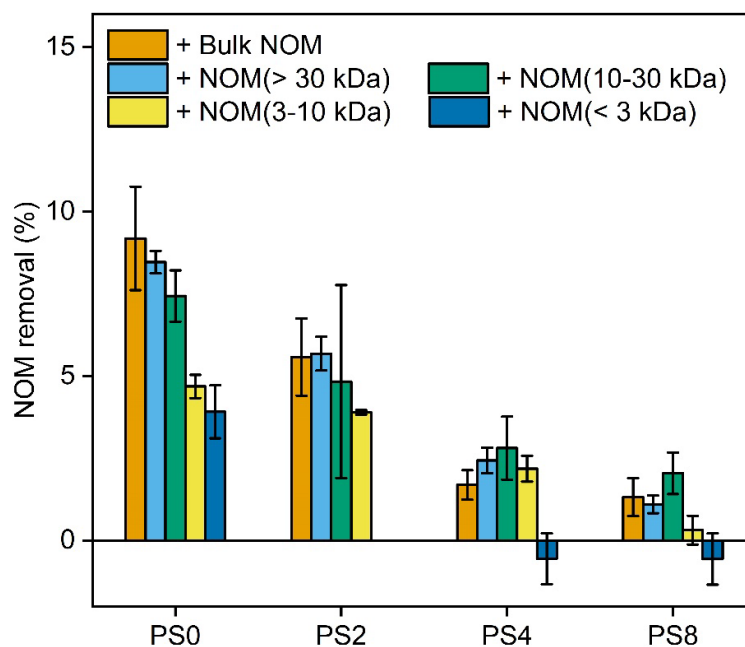
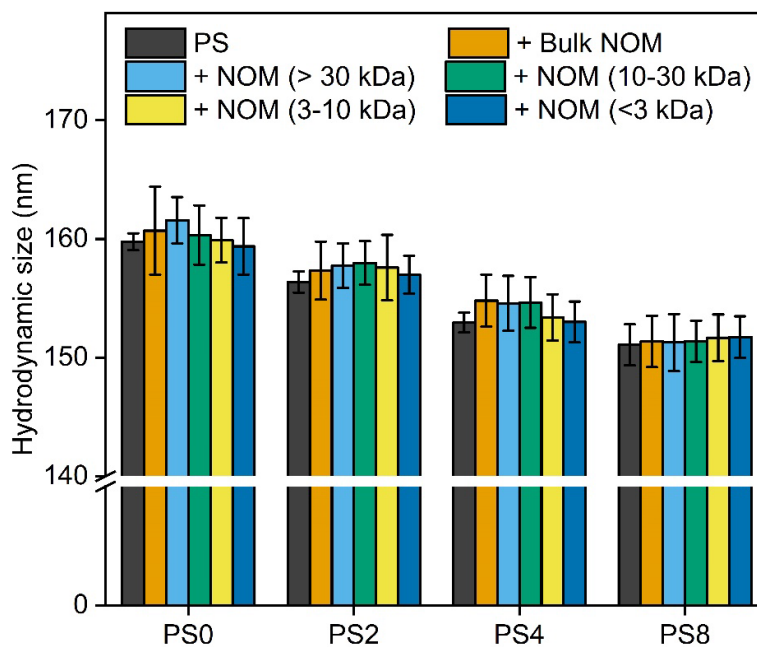


Figure S12. The zeta potential of pristine and photoaged NPs with and without bulk NOM and NOM fractions in 500 mM NaCl. Error bars represent the mean  $\pm$  1.96 SE (n = 10).



**Figure S13.** The reduction in UV280 (NOM removal) of bulk NOM and NOM fractions after adsorption on pristine and photoaged NPs in 10 mM NaCl. Error bars represent the mean  $\pm$  1.96 SE ( $n = 2$ ).



**Figure S14.** The hydrodynamic size of pristine and photoaged NPs with and without bulk NOM and NOM fractions in 10 mM NaCl. Error bars represent the mean  $\pm$  1.96 SE ( $n = 10$ ).

Result							
Name	Status	Repetition	Start time	Temperature °C	Focus position mm	Processed runs	
N-100 1	Failed	1	08:53:35	25	-0.8	3	
N-100 2	Failed	2	08:55:49	25	-0.8	3	
N-100 3	Failed	3	08:56:34	25	-0.8	3	
N-100 4	Failed	4	08:57:19	25	-0.8	3	
N-100 5	Failed	5	08:58:05	25	-0.8	3	
N-100 6	Failed	6	08:58:50	25	-0.8	3	
N-100 7	Failed	7	08:59:35	25	-0.8	3	
N-100 8	Failed	8	09:00:20	25	-0.8	3	
N-100 9	Failed	9	09:01:05	25	-0.8	3	
N-100 10	Failed	10	09:01:50	25	-0.8	3	
N-100 11	Failed	11	09:02:35	25	-0.8	3	
N-100 12	Failed	12	09:03:20	25	-0.8	3	
N-100 13	Canceled	13	09:04:03	25	-0.8	2	
Average							
St.Dev.							
RSD%							

Result							
Name	Status	Repetition	Start time	Temperature °C	Focus position mm	Processed runs	
N-500 1	Failed	1	09:49:33	25	-0.4	3	
N-500 2	Failed	2	09:51:47	25	-0.4	3	
N-500 3	Failed	3	09:52:32	25	-0.4	3	
N-500 4	Failed	4	09:53:17	25	-0.4	3	
N-500 5	Failed	5	09:54:02	25	-0.4	3	
N-500 6	Failed	6	09:54:47	25	-0.4	3	
N-500 7	Failed	7	09:55:32	25	-0.4	3	
N-500 8	Failed	8	09:56:17	25	-0.4	3	
N-500 9	Failed	9	09:57:02	25	-0.4	3	
N-500 10	Failed	10	09:57:48	25	-0.4	3	
N-500 11	Canceled	11	09:58:34	25	-0.4	1	
Average							
St.Dev.							
RSD%							

*Figure S15. The size characterization results of bulk NOM (10 mg/L) over time at 100 mM and 500 mM NaCl.*

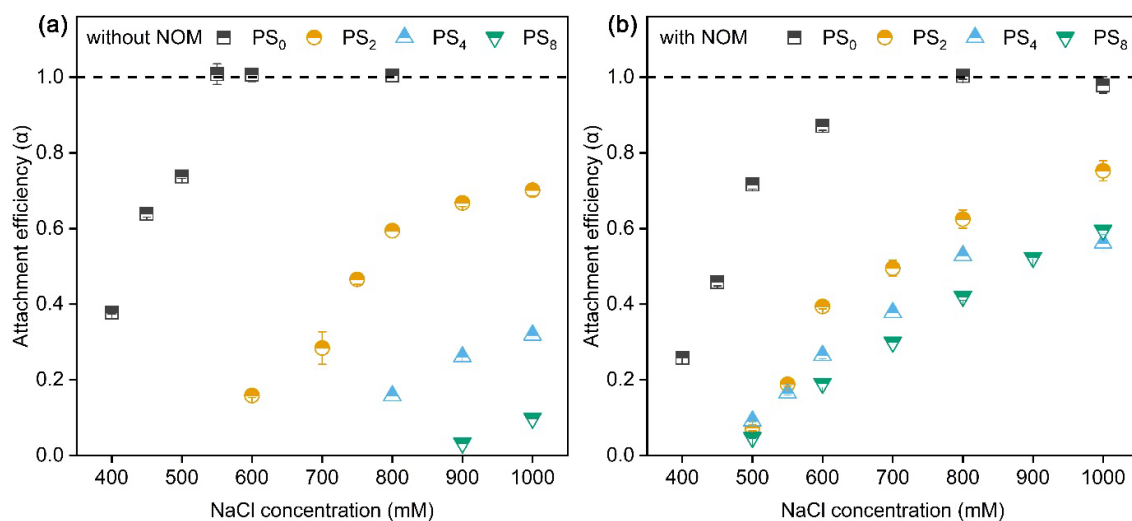


Figure S16. The aggregation kinetics of pristine and photoaged NPs without NOM (a) and with bulk NOM (b). Error bars represent the mean  $\pm$  SD ( $n = 2$  or  $3$ ).

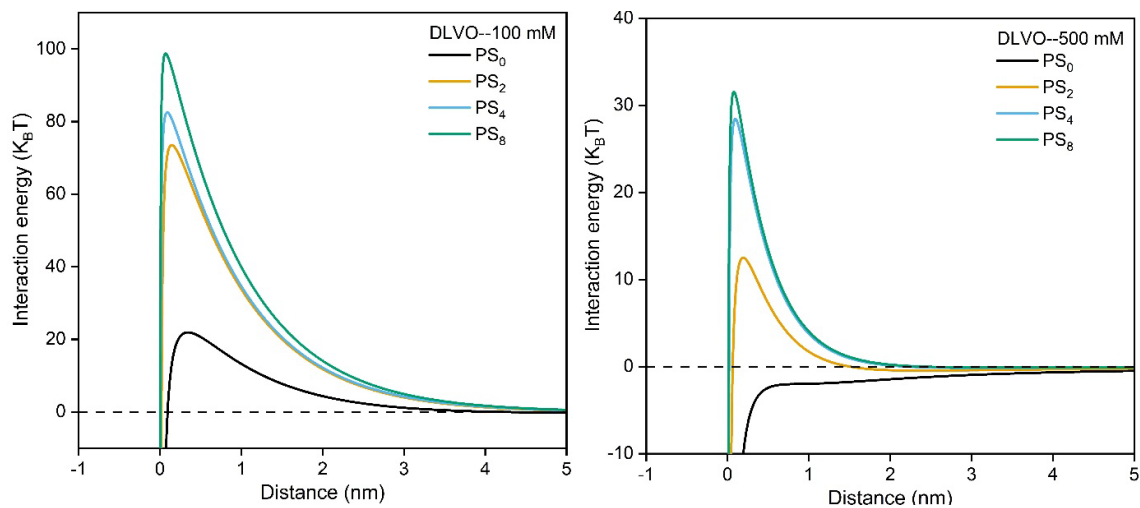
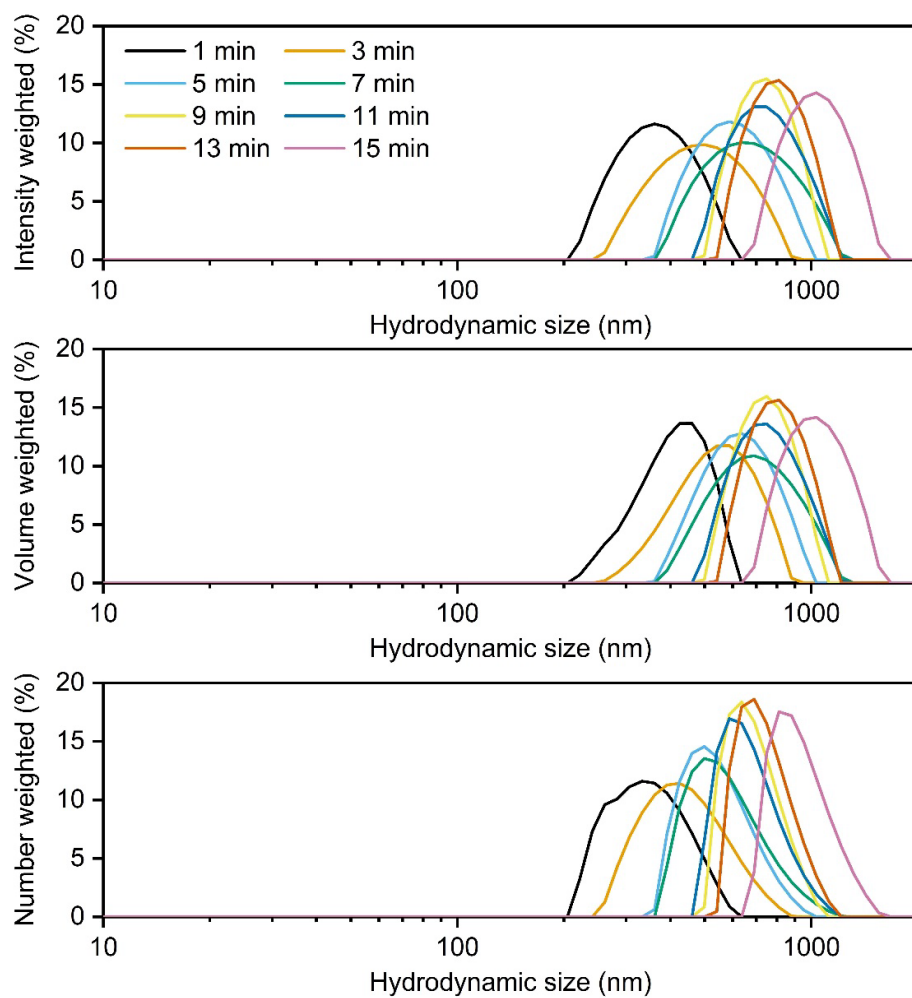
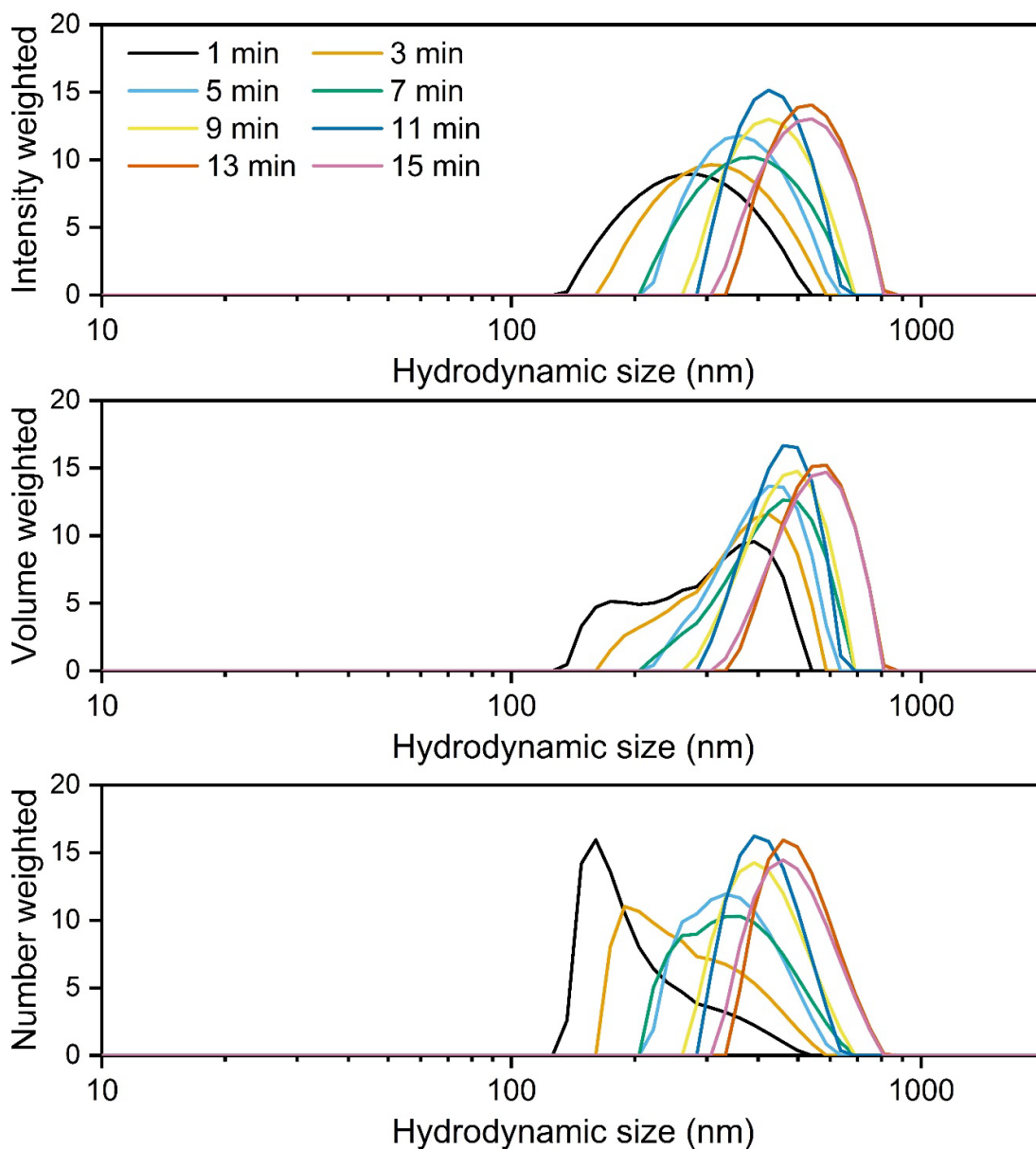


Figure S17. DLVO interaction energy of pristine and photoaged NPs at 100 and 500 mM NaCl solutions.



*Figure S18. The intensity, volume, and number-weighted size distributions of pristine NPs at 500 mM NaCl over time.*



*Figure S19. The intensity, volume, and number-weighted size distributions (%) of pristine NPs in the presence of bulk NOM (10 mg/L) at 500 mM NaCl over time.*

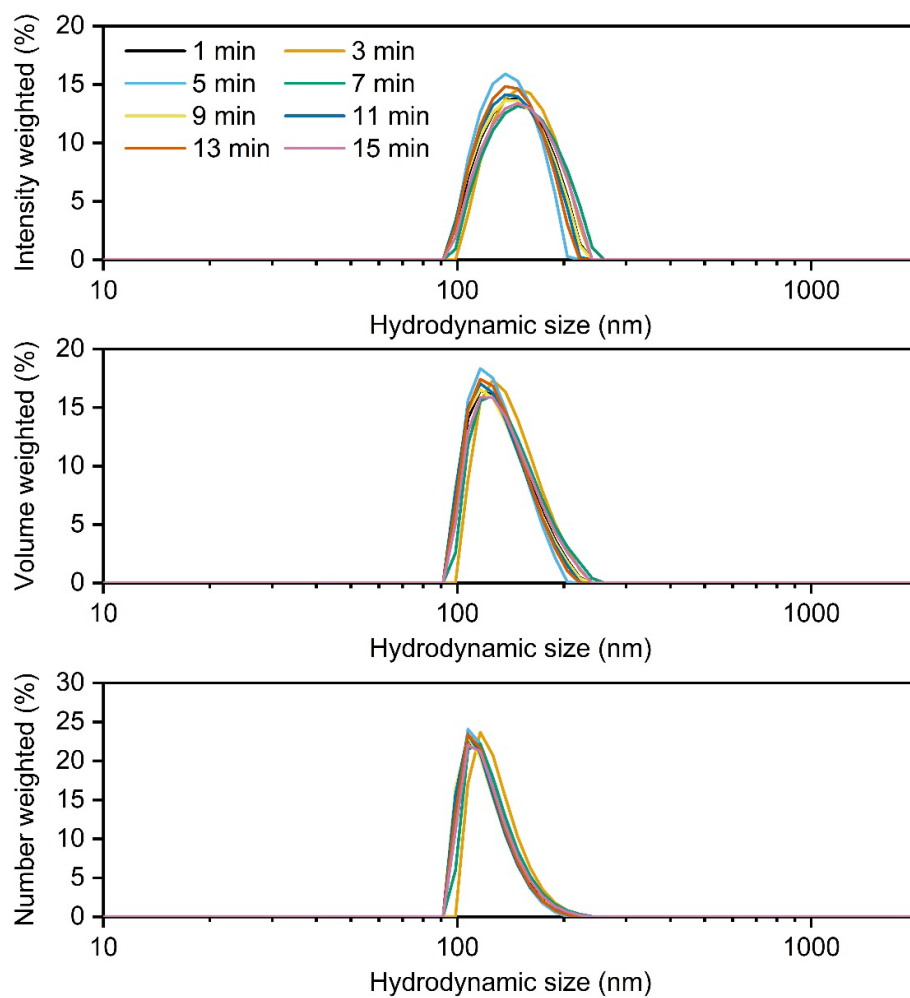


*Figure S20. The intensity, volume, and number-weighted size distributions of photoaged NPs (PS<sub>4</sub>) at 500 mM NaCl over time.*

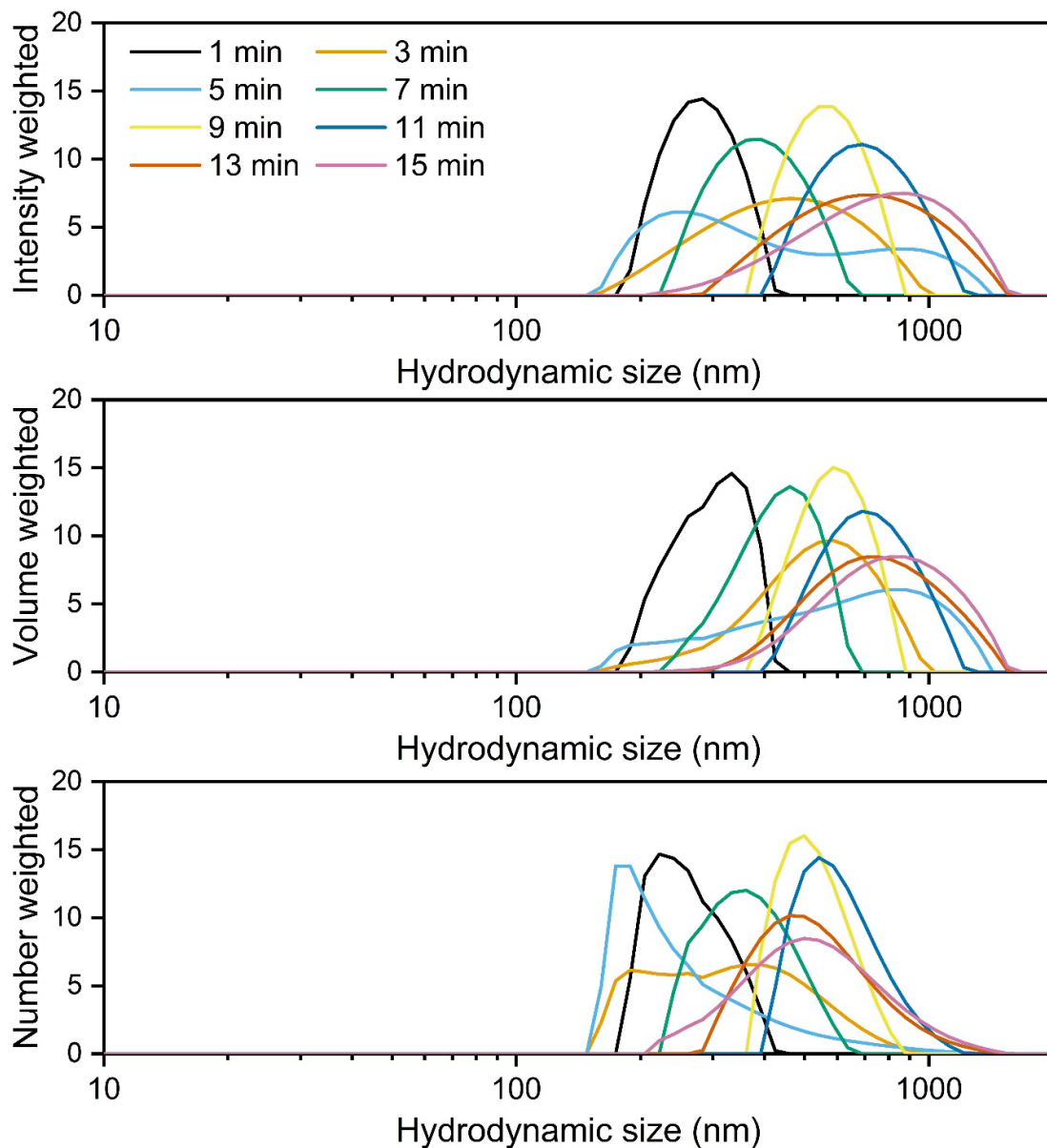


*Figure S21. The intensity, volume, and number-weighted size distributions (%) of photoaged NPs (PS<sub>4</sub>) in the presence of bulk NOM (10 mg/L) at 500 mM NaCl over time.*

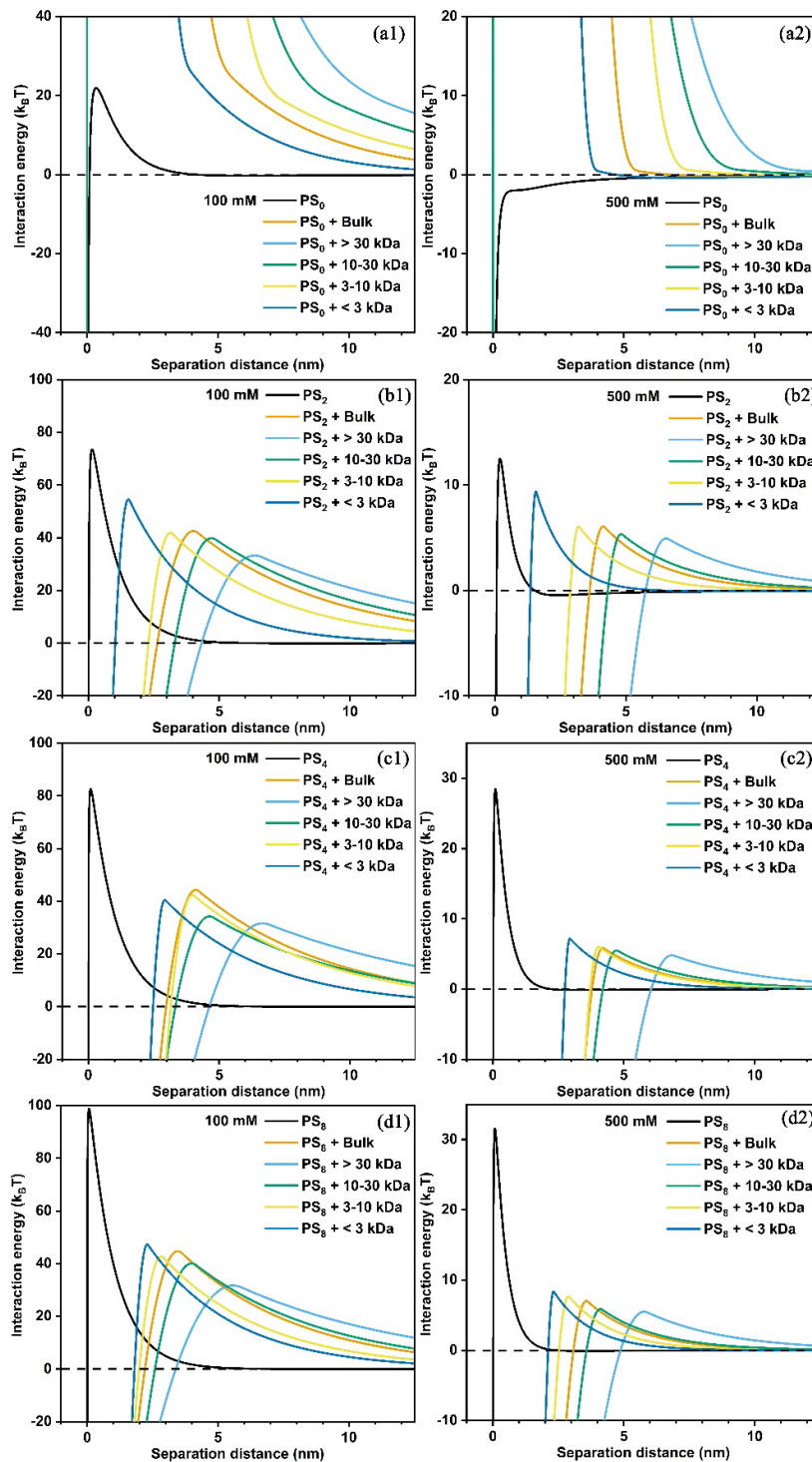


*Figure S22. DLVO and steric interaction energy of PS0 (a), PS2 (b), PS4 (c) and PS8 (d) in the absence and presence of bulk NOM and NOM fractions at 100 and 500 mM NaCl solutions.*

*Text S5. Adsorption and Desorption of NPs on sand*

Controls showed no obvious UV reduction of NPs following agitation for 48 hours (*Figure S24*). However, blanks indicated that agitation caused the fragmentation and release of suspended tiny sands, which interfered with the UV absorbance of NPs (*Figure S25*). Therefore, while the adsorption results were not highly precise, they provided valuable insights into NP adsorption. The UV absorbance of NPs was corrected by subtracting the blank UV absorbance measured at the same time, and the results are presented in *Figure S25c* and *Figure S25d*. The results showed rapid adsorption of pristine NPs within the initial 10 minutes, followed by slower adsorption over an extended period. This suggested the presence of both instantaneous equilibrium adsorption and time-dependent kinetic adsorption. UV-weathering obviously reduced NP adsorption, with the adsorption capacity decreasing as the aging time increased. In the presence of NOM, the adsorption of both non-weathered and UV-weathered NPs was negligible due to background interference. The desorption experiment demonstrated that some adsorbed NPs could be released, but not all were desorbed, indicating the presence of irreversible and reversible adsorption sites.



Figure S23. Photograph of the experimental setup used for NP transport experiments.

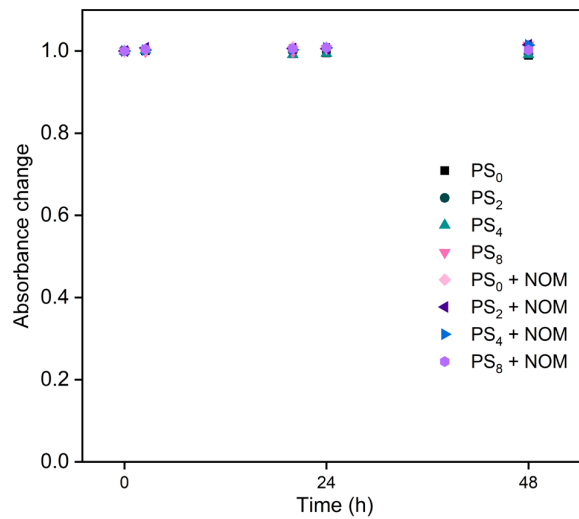
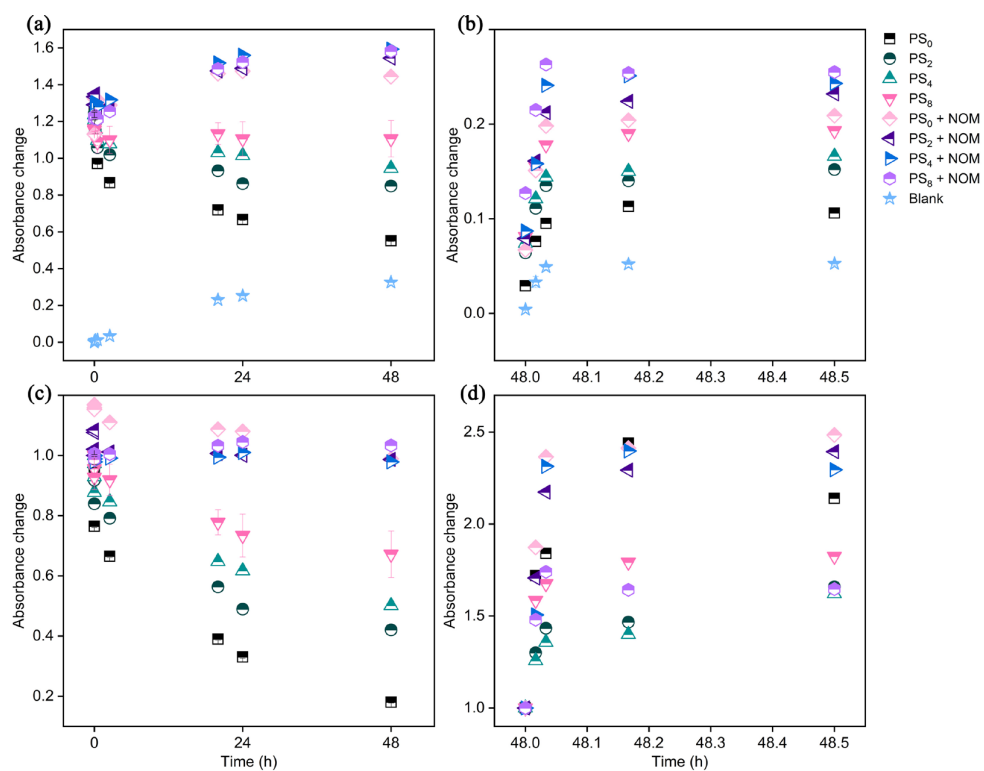


Figure S24. The UV289 change of non-weathered and weathered NPs following 48 hours of agitation (no sand).



**Figure S25.** The UV289 change of non-weathered and weathered NPs after adsorption (a and c) and desorption (b and d) on sand. The UV289 change in c and d was corrected by subtracting the blank UV absorbance.

### Text S6. DLVO and XDLVO interaction energy between NPs and sand

The classical Derjaguin-Landau-Verwey-Overbeek (DLVO) theory includes van der Waals and electrostatic double layer interactions [188, 370]. The total interaction energy ( $E_{DLVO}$ ) defined as the sum of the van der Waals interaction energy ( $E_{vdW}$ ) and electric double layer interaction energy ( $E_{EDL}$ ). In the presence of NOM, the extend DLVO (XDLVO) considering a steric repulsion was used to investigate interaction energies.

**DLVO.** The equations of  $E_{DLVO}$ ,  $E_{vdW}$  and  $E_{EDL}$  are given as follows:

$$E_{DLVO} = E_{vdW} + E_{EDL} \quad (S16)$$

$$E_{vdW} = -\frac{A_{121}R}{12h(1+\frac{14h}{\lambda_0})} \quad (S17)$$

$$E_{EDL} = 64\pi\epsilon_0\epsilon_rR_0(k_B T/ze)^2 \tanh\left(\frac{\Psi_1}{4k_B T/ze}\right) \tanh\left(\frac{\Psi_2}{4k_B T/ze}\right) \exp(-\kappa h) \quad (S18)$$

where  $A_{121}$  (J) is the Hamaker constant of NP-water-NP system.  $A_{121} \approx ((A_{11})^{1/2} - (A_{22})^{1/2})^2$ , where  $A_{11}$  and  $A_{22}$  denote the Hamaker constants of NPs and water ( $A_{22} \approx 3.7 \times 10^{-20}$  J) in a vacuum. The Hamaker constants of PS<sub>0</sub>, PS<sub>2</sub>, PS<sub>4</sub>, and PS<sub>8</sub> were estimated to be  $5.1 \times 10^{-21}$  J,  $1.2 \times 10^{-21}$  J,  $5.0 \times 10^{-22}$  J, and  $3.5 \times 10^{-22}$  J based on our previous study [425].  $R_0$  (nm) is the particle radius.  $h$  (nm) is the separation distance.  $\epsilon_0$  and  $\epsilon_r$  are the permittivity of the vacuum ( $8.854 \times 10^{-12}$  C/(V·m)) and the relative dielectric constant of the liquid (78.5), respectively.  $k_B$  is the Boltzman constant ( $1.381 \times 10^{-23}$  J/K).  $T$  is absolute temperature (298 K),  $z$  is the valence state of ion.  $e$  is the electron charge ( $1.602 \times 10^{-19}$  C).  $\Psi_1$  and  $\Psi_2$  are the potential of NPs and sand, respectively.  $\kappa$  is the inverse Debye length.

$$\kappa^{-1} = \sqrt{\frac{\epsilon_r\epsilon_0k_B T}{2NAIe^2}} \quad (S19)$$

where  $NA$  is the Avogadro constant ( $6.02 \times 10^{23}$  mol<sup>-1</sup>), and  $I$  is the ionic strength of the solutions,  $I = 0.5 \sum c_i z_i^2$ ,  $c_i$  is the molarity of ion. The Debye length or ionic diffuse layer is a measure of the range of electrostatic interactions.  $\kappa^{-1}$  is calculated as 3.04 nm in 10 mM NaCl.

**Steric Repulsion.** The adsorbed polymer layer on NPs can lead to an increase in osmotic pressure and elastic repulsion. The repulsive steric interaction energy ( $E_s$ ) is defined as the sum of osmotic ( $E_{osm}$ ) and elastic repulsive energies ( $E_{elas}$ ). Assuming that only the surfaces of NPs are coated by polymers, the osmotic repulsion energy  $E_{osm}$  could be expressed as follows [521]:

$$\frac{E_{osm}}{k_B T} = 0, \quad d \leq h \quad (S20)$$

$$\frac{E_{osm}}{k_B T} = \frac{4\pi R_0}{v_1} \Phi_{NOM}^2 \left(\frac{1}{2} - \chi\right) (h - d)^2, \quad h \leq d \quad (S21)$$

where  $v_1$  is the volume of one solvent molecule (0.03 nm<sup>3</sup>),  $\chi$  is the Flory-Huggins solvency parameter (0.45),  $d$  (nm) is the thickness of adsorbed NOM.  $\phi_{NOM}$  is the effective volume fraction of the adsorbed NOM layer and can be expressed as follows:

$$\Phi_{NOM} = 3 \frac{QR_0^2}{\rho_{NOM}[(d+R_0)^3 - R_0^3]} \quad (S22)$$

where  $Q$  (mg/m<sup>2</sup>) is the maximum adsorbed amount of NOM on NP surface, estimated based on the adsorption results (Figure S4).  $\rho_{NOM}$  is the density of NOM (assumed to be 1.5 g/cm<sup>3</sup>) [502].

The equation of  $E_{elas}$  could be expressed as follows [503, 521]:

$$\frac{E_{elas}}{k_B T} = 0, d \leq h \quad (S23)$$

$$\frac{E_{elas}}{k_B T} = \frac{2\pi R_0}{M_W} \Phi_{NOM} d^2 \rho_{NOM} \left[ \frac{2}{3} - \frac{1}{6} \left( \frac{h}{d} \right)^3 - \left( \frac{h}{2d} \right) + \left( \frac{h}{d} \right) \ln \left( \frac{h}{d} \right) \right], d > h \quad (S24)$$

where  $M_W$  (Da) is the molecular weight of NOM [501]. The MWs of bulk NOM and its fractions were estimated as follows: bulk NOM at 12,000 Da, NOM (> 30 kDa) at 50,000 Da, NOM (10–30 kDa) at 20,000 Da, NOM (3–10 kDa) at 6,500 Da, and NOM (< 3 kDa) at 1,500 Da. The adsorption thickness ( $d$ , nm) of NOM was negligible in some cases (Figure S13 and Figure S14), leading to an underestimation of steric repulsion. In this study,  $d$  was assumed to correspond to the molecular size of NOM, considering that the interplay distance of steric repulsion is related to NOM size. By assuming spherical geometry, the molecular sizes of NOM were calculated using the Molecular Weight to Size Calculator (<https://nanocomposix.com/pages/molecular-weight-to-size-calculator>). The estimated sizes were 2.938 nm for bulk NOM, 4.728 nm for NOM (> 30 kDa), 3.484 nm for NOM (10–30 kDa), 2.395 nm for NOM (3–10 kDa), and 1.469 nm for NOM (< 3 kDa), which were used to refine the XDLVO interaction calculations.

**Influence of surface roughness.** Based on previous studies [433, 434], surface roughness was modeled as hemispherical asperities on flat surfaces to account for nanoscale irregularities. Two cases were considered to account for surface roughness effects: (1) NPs deposited on convex asperities and (2) NPs deposited in concave valleys between asperities (Figure S26). The total interaction energy in both cases was estimated as the sum of the NP–surface interaction (particle–plate) and the NP–asperity interaction (particle–particle), which can be expressed as follows [434]:

$$E_{p-a} = E_{p-p}(h) + E_{p-s}(h+r) \quad (S25)$$

$$E_{p-v-1} = nE_{p-p}(h) + E_{p-s}(\sqrt{(h+r+R)^2 - (r+D)^2} - R) \quad (S26)$$

$$E_{p-v-2} = nE_{p-p}(\sqrt{(H+R)^2 + (r+D)^2} - r - R) + E_{p-s}(H) \quad (\text{S27})$$

Where  $E_{p-a}$  is the total interaction energy between NPs and a convex asperity on the sand, while  $E_{p-v-1}$  and  $E_{p-v-2}$  represent the interaction energy between NPs and a concave valley on the sand.  $E_{p-p}$  and  $E_{p-s}$  denote the particle-particle interaction energy between an NP and an asperity and the particle-surface interaction between NPs and the sand, respectively.  $h$  and  $H$  are the surface-to-surface separation distance between NP–asperity and NP–surface, respectively.  $R$  and  $r$  represent the radii of the NPs and the asperities, respectively. For the particle-particle interaction energy calculation, the  $R_0$  in equation (2), (3), (6) and (9), is calculated as  $rR/(r+R)$ . The choice between Equations (2) and (3) depends on the surface-to-surface distance ( $D$ ) between asperities. When  $D$  is large enough such that  $H < h$ , Equation (3) is applied. Conversely, when  $h \leq H$ , Equation (2) is used. In this study,  $D$  was selected to ensure  $h$  is approximately equal to  $H$ .  $n$  represents the estimated maximum number of asperities that can be arranged in a circle and is expressed as:

$$n = \frac{\pi}{\text{Arcsin}(\frac{r}{r+D})} \quad (\text{S28})$$

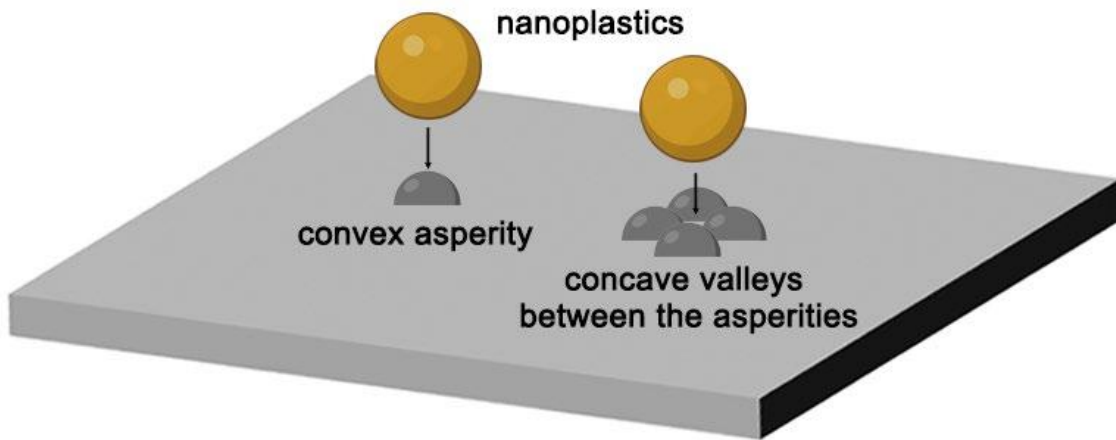


**Figure S26.** Schematic of interactions between NPs with a convex asperity and a concave valley between the asperities.

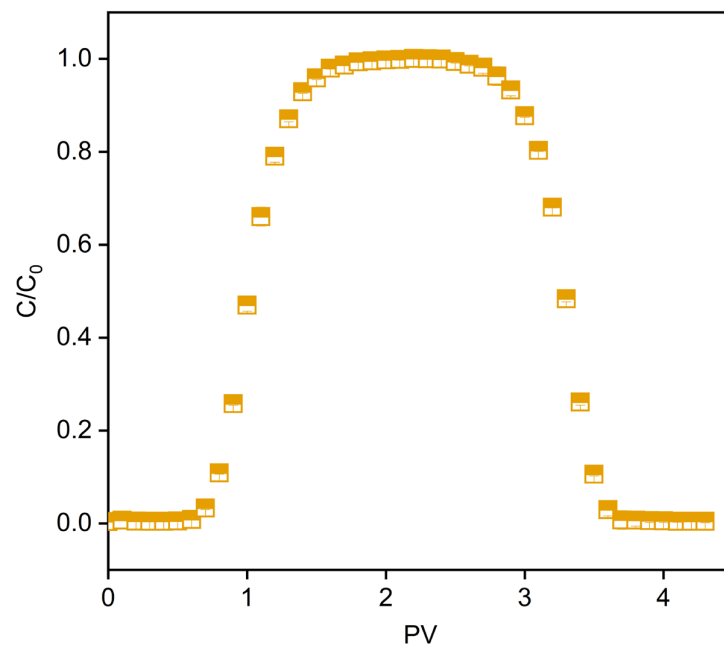


Figure S27. The BTC of tracer (10 mM NaCl) in porous media (vidaXL sand).

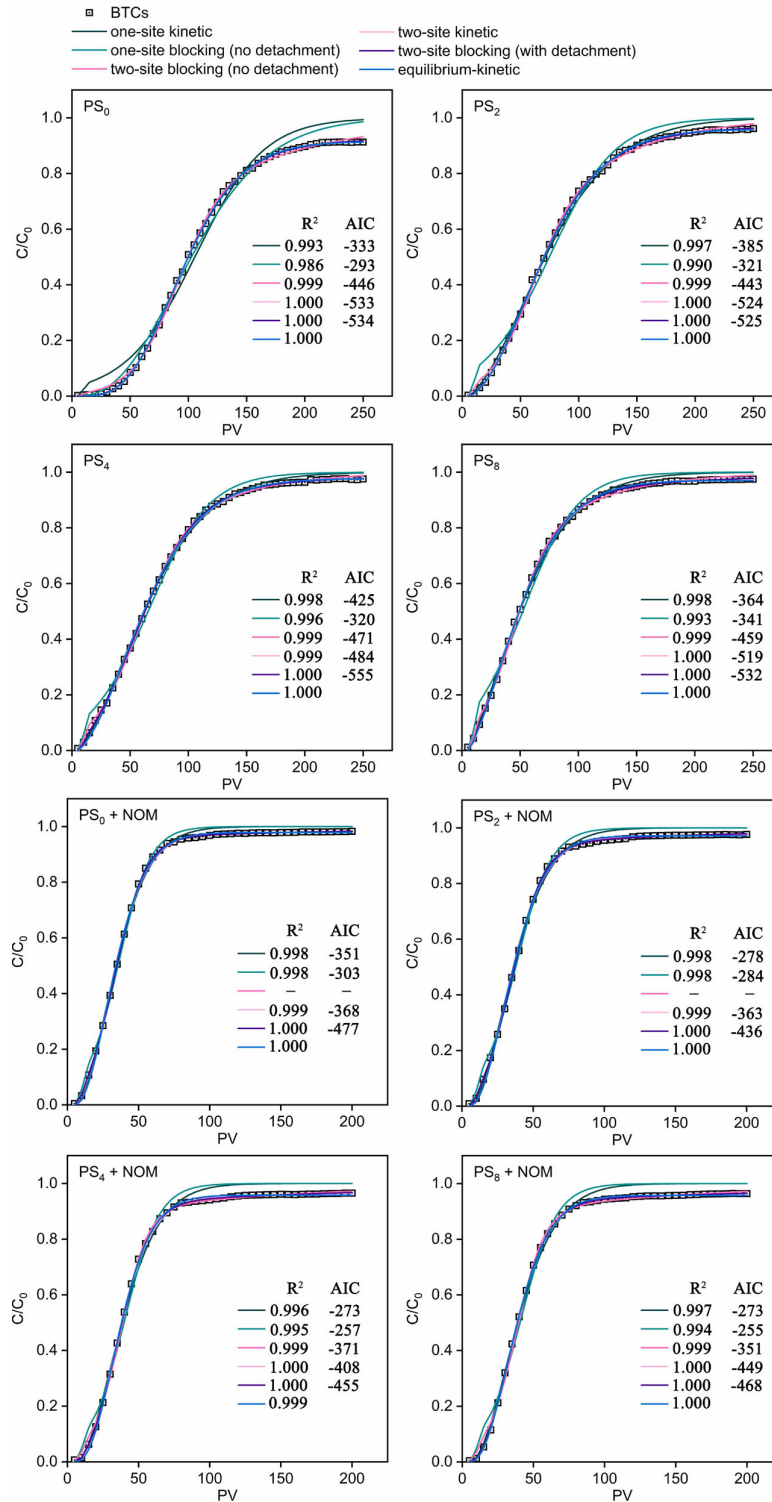
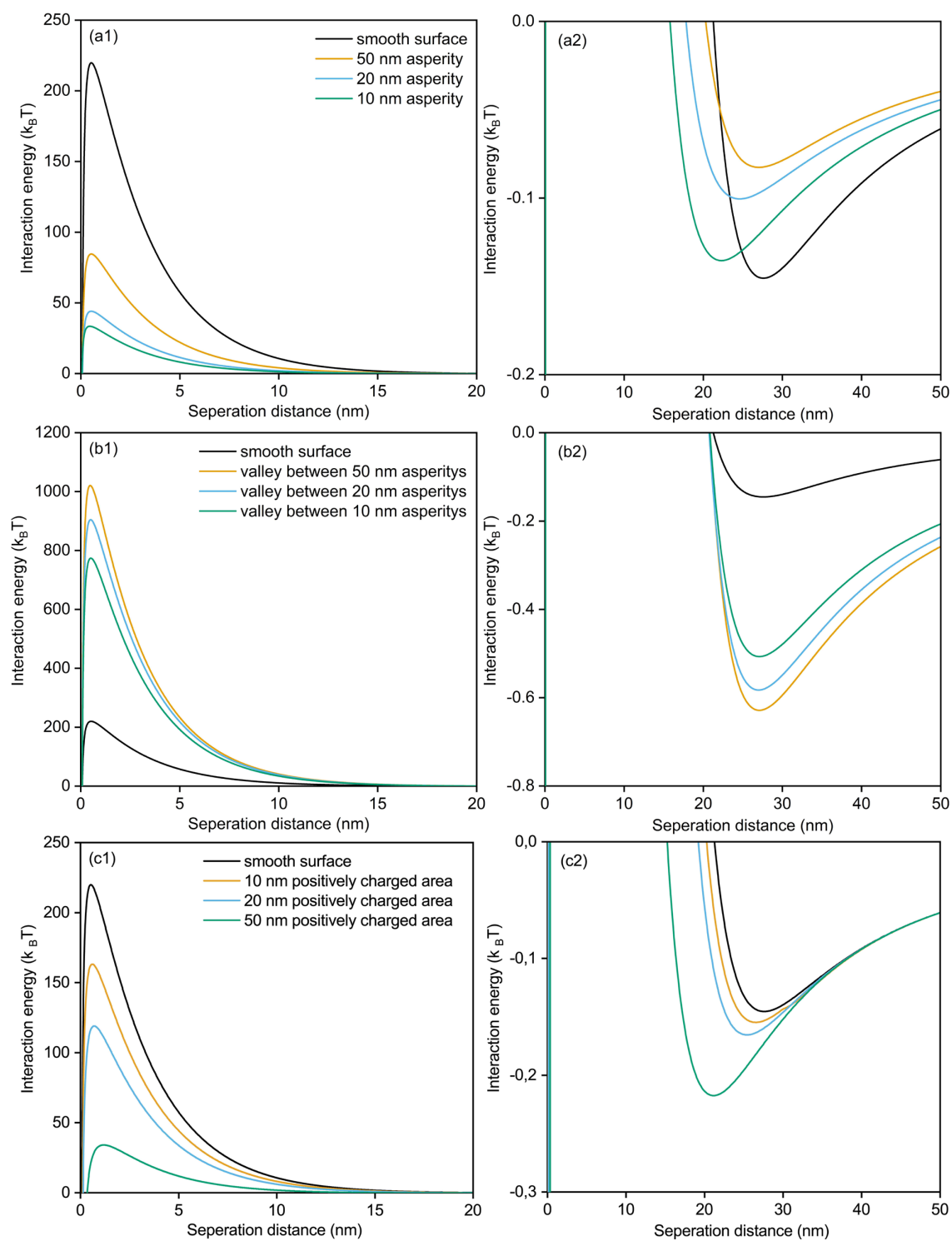


Figure S28. Fitting results of the BTCs for non-weathered and weathered NPs using different models.



**Figure S29.** Effects of a convex asperity (a), a concave valley (b) and a positively charged area (+ 20 mV) on the DLVO energy barrier (1) and the secondary energy minimum (2).

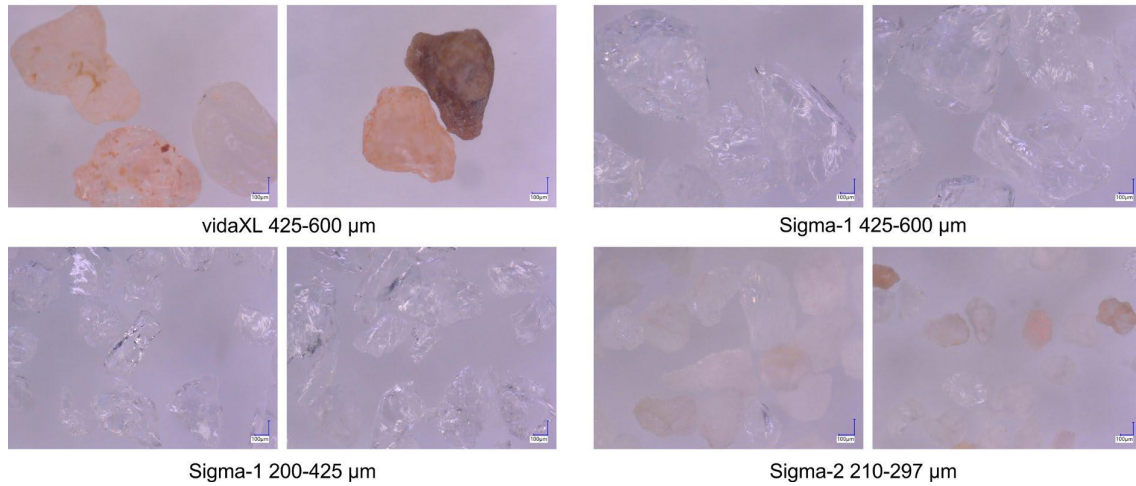


Figure S30. Microscopic images of vidaXL sand and Sigma-1 and Sigma-2 sand.

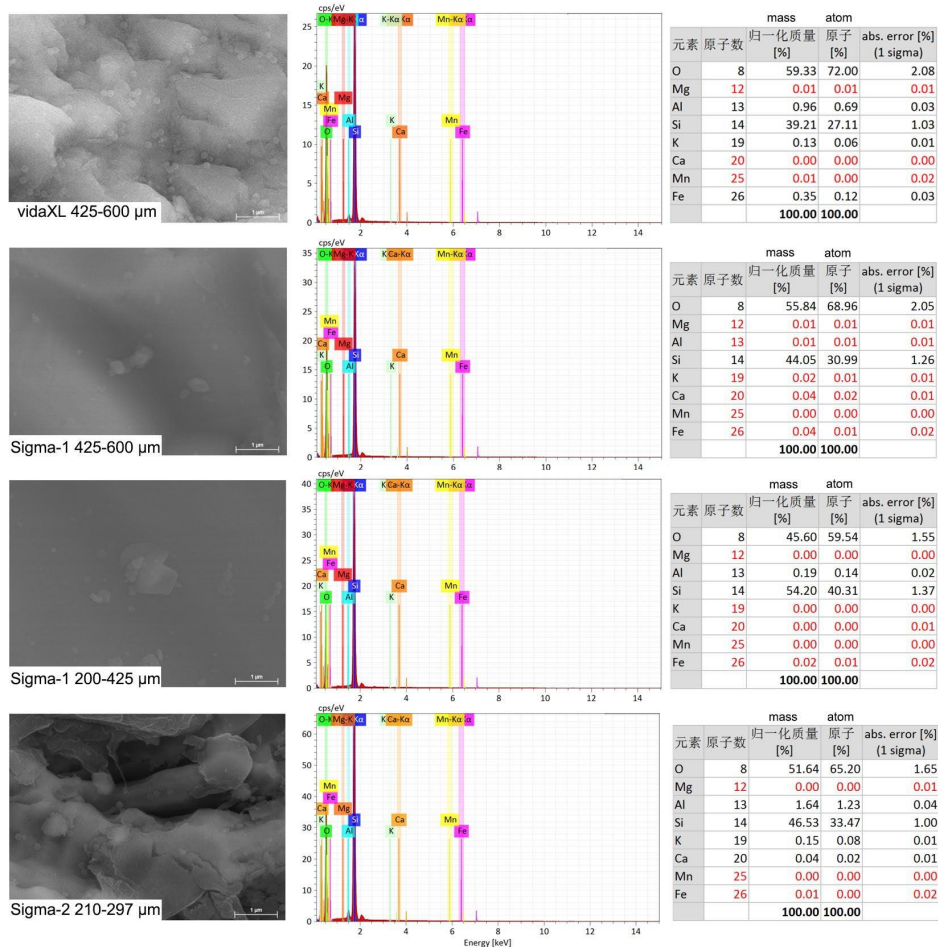
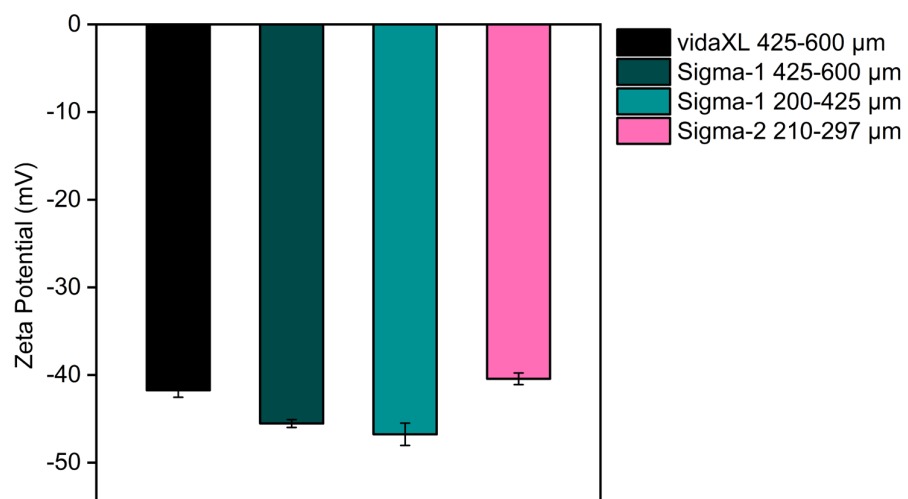


Figure S31. SEM-EDS results of vidaXL, Sigma-1 and Sigma-2 sand.



*Figure S32. Zeta potential of vidaXL sand and Sigma-1 and Sigma-2 sand.*

**Table S13.** The DLVO and XDLVO energy barrier ( $E_{max}$ ,  $k_B T$ ) and the secondary minimum ( $|E_{2-min}|$ ,  $k_B T$ ) for NP-asperity, NP-valley, and NP-positively charged area on heterogeneous surface and NP-plate on homogeneous surface.

NP-Sand	Heterogeneous Surface						Homogeneous Surface	
	NP-asperity		NP-valley		NP-positively charged area		NP-plate	
	$E_{max}$	$ E_{2-min} $	$E_{max}$	$ E_{2-min} $	$E_{max}$	$ E_{2-min} $	$E_{max}$	$ E_{2-min} $
PS <sub>0</sub>	33.5	0.135	774	0.507	34.1	0.217	220	0.145
PS <sub>0</sub> + bulk	177	0.131	3900	0.487	1216	0.206	1480	0.140
PS <sub>0</sub> + > 30 kDa	348	0.129	7761	0.483	2737	0.203	3013	0.138
PS <sub>0</sub> + 10-30 kDa	170	0.130	3759	0.485	1145	0.205	1414	0.139
PS <sub>0</sub> + 3-10 kDa	61.7	0.130	1381	0.486	197	0.206	450	0.140
PS <sub>0</sub> + < 3 kDa	47.4	0.129	1078	0.482	66.8	0.203	320	0.138
PS <sub>2</sub>	46.1	0.053	1063	0.196	54.2	0.079	300	0.056
PS <sub>2</sub> + bulk	98.4	0.054	2186	0.199	508	0.081	762	0.057
PS <sub>2</sub> + > 30 kDa	201	0.053	4461	0.197	1392	0.080	1659	0.056
PS <sub>2</sub> + 10-30 kDa	103	0.054	2301	0.198	546	0.080	804	0.056
PS <sub>2</sub> + 3-10 kDa	62.4	0.053	1403	0.197	186	0.080	443	0.056
PS <sub>2</sub> + < 3 kDa	46.9	0.054	1063	0.200	81.3	0.082	316	0.057
PS <sub>4</sub>	49.0	0.031	1120	0.113	57.3	0.045	315	0.032
PS <sub>4</sub> + bulk	58.0	0.032	1296	0.117	189	0.047	411	0.033
PS <sub>4</sub> + > 30 kDa	71.2	0.032	1592	0.116	286	0.047	520	0.033
PS <sub>4</sub> + 10-30 kDa	61.9	0.032	1386	0.117	211	0.047	441	0.033
PS <sub>4</sub> + 3-10 kDa	46.7	0.032	939	0.118	96.2	0.047	314	0.033
PS <sub>4</sub> + < 3 kDa	42.9	0.032	976	0.117	56.4	0.047	279	0.033
PS <sub>8</sub>	52.4	0.024	1195	0.090	60.6	0.035	335	0.025
PS <sub>8</sub> + bulk	57.5	0.026	1281	0.095	189	0.038	405	0.027
PS <sub>8</sub> + > 30 kDa	62.4	0.025	1394	0.094	218	0.037	443	0.027
PS <sub>8</sub> + 10-30 kDa	58.9	0.026	1316	0.094	189	0.037	414	0.027
PS <sub>8</sub> + 3-10 kDa	43.1	0.025	947	0.096	61.3	0.037	279	0.027
PS <sub>8</sub> + < 3 kDa	42.1	0.025	922	0.095	48.6	0.037	269	0.026

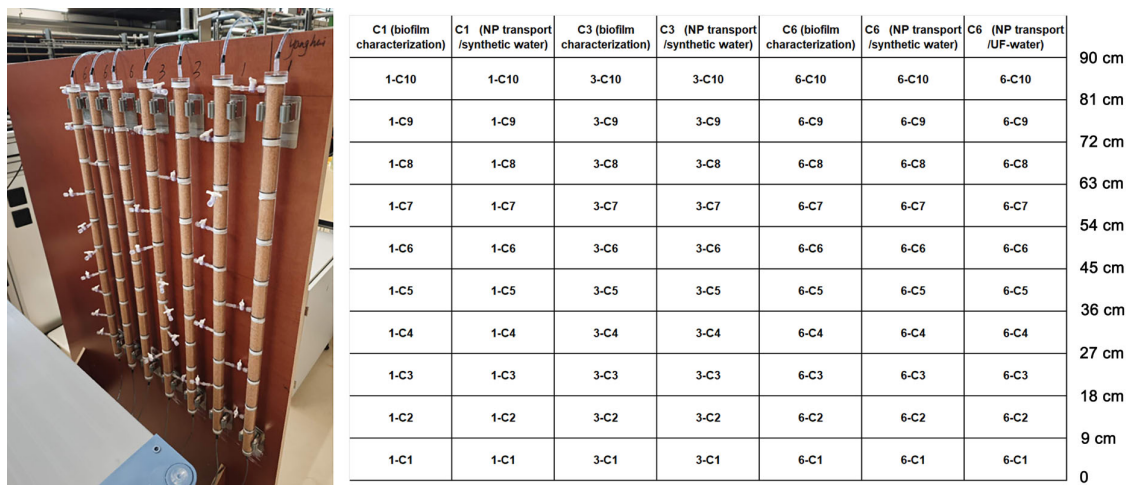


*Figure S33. Photograph and column design of the simulated RBF experimental setup.*

*Table S14. Water quality parameters of river water collected from a RBF site and synthetic water prepared to simulate the ion composition of the river water. The synthetic water was formulated using  $\text{CaSO}_4 \cdot 2\text{H}_2\text{O}$ ,  $\text{CaCl}_2 \cdot 2\text{H}_2\text{O}$ ,  $\text{CaCO}_3$ ,  $\text{MgCl}_2 \cdot 6\text{H}_2\text{O}$ ,  $\text{NaNO}_3$ ,  $\text{NaHCO}_3$ , and  $\text{KHCO}_3$ , and freshly prepared prior to the transport experiments. Ion concentrations were measured using ion chromatography (IC).*

Parameter	$\text{Ca}^{2+}$ (mg/L)	$\text{Mg}^{2+}$ (mg/L)	$\text{Na}^+$ (mg/L)	$\text{K}^+$ (mg/L)	$\text{SO}_4^{2-}$ (mg/L)	$\text{Cl}^-$ (mg/L)	$\text{NO}_3^-$ (mg/L)	pH	$\text{O}_2$ (mg/L)
river water-1	66.5	10.7	26.4	3.7	49.4	45.1	9.6	8.1	7.5
river water-2	69.1	13.1	23.4	4.6	52.5	43.2	7.3	8.2	7.2
synthetic water	66.6	10.3	26.1	3.5	49.0	44.6	9.3	8.0	8.1

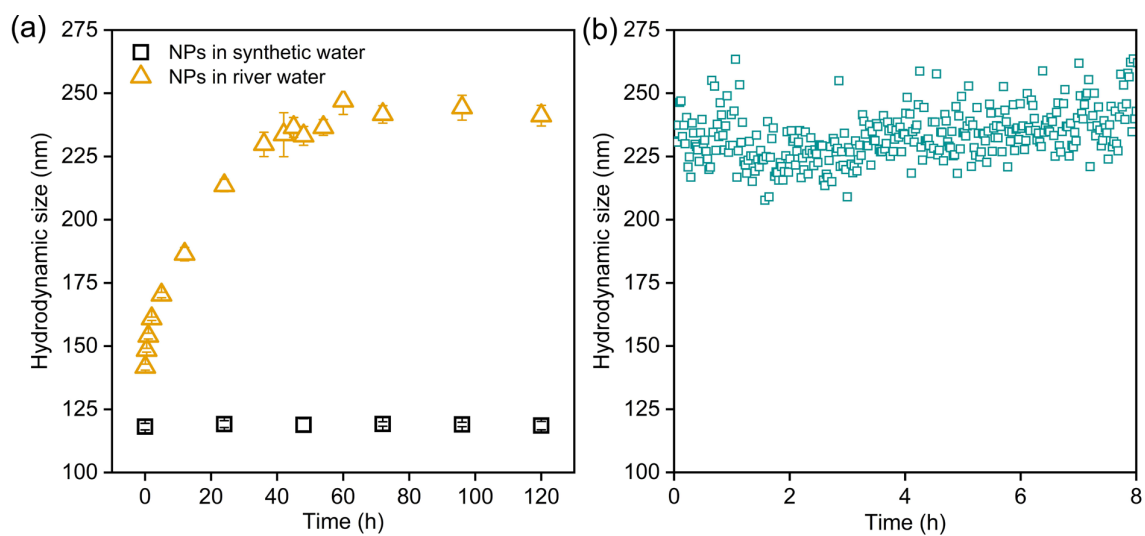


**Figure S34.** (a) Size evolution of NPs in synthetic water and river water (< 100 kDa) over time; (b) detailed size change of NPs in river water (< 100 kDa) monitored over 8 hours after 2 days of incubation.

*Text S7. The adsorption of DOM by NPs*

30 mg/L PS NPs were added to 50 mL of river water (< 100 kDa) and incubated for 2 days. After incubation, the suspension was filtered through a 0.1 µm PES membrane (pre-washed with 100 mL of ultrapure water) to separate the NPs from the dissolved organic matter (DOM). For each sample, the first 5 mL of filtrate was discarded to minimize contamination, and the remaining filtrate was collected for DOM analysis. The TOC, TN, UV270, and UV254 values of the DOM before and after adsorption were measured. Duplicates were conducted. The results are presented in [Table S15](#).

*Table S15. The parameter changes of DOM and NPs after adsorption.*

	DOM				NPs		
	TOC (mg/L)	TN (mg/L)	UV254	UV270	hydrodynamic size (nm)	zeta potential (mV)	Water contact angle (°)
Before adsorption	4.6	2.0	0.080	0.067	118.2	-29.0	101.6
After adsorption	3.9	1.9	0.080	0.067	233.2	-20.0	47.8

*Text S8. XDLVO interaction energy between NPs and sand/biofilm*

The classical Derjaguin–Landau–Verwey–Overbeek (DLVO) theory accounts for van der Waals and electrostatic double layer interactions [188, 370]. To incorporate the influence of hydrophobic interactions, the extended DLVO (XDLVO) framework was applied by including Lewis acid–base interactions.

**XDLVO.** The equations of  $E_{XDLVO}$ ,  $E_{vdW}$  and  $E_{EDL}$  and  $E_{AB}$  are given as follows:

$$E_{XDLVO} = E_{vdw} + E_{EDL} + E_{AB} \quad (S29)$$

$$E_{vdw} = -\frac{A_{121}R}{12h(1+\frac{14h}{\lambda_0})} \quad (S30)$$

$$E_{EDL} = 64\pi\epsilon_0\epsilon_r R(k_B T/ze)^2 \tanh\left(\frac{\psi_1}{4k_B T/ze}\right) \tanh\left(\frac{\psi_2}{4k_B T/ze}\right) \exp(-\kappa h) \quad (S31)$$

$$E_{AB} = 2\pi R\lambda_{AB}\Phi_{AB} \exp\left(\frac{h_0-h}{\lambda_{AB}}\right) \quad (S32)$$

where  $A_{121}$  (J) is the Hamaker constant of NP-water-NP system.  $A_{121} \approx ((A_{11})^{1/2} - (A_{22})^{1/2})^2$ , where  $A_{11}$  and  $A_{22}$  denote the Hamaker constants of NPs and water ( $A_{22} \approx 3.7 \times 10^{-20}$  J) in a vacuum. The Hamaker constants of PS were estimated to be  $5.1 \times 10^{-21}$  J based on our previous study [425]. The Hamaker constants of eco-corona-coated PS NPs was estimated to be  $1.2 \times 10^{-21}$  J. The Hamaker constants of silica surface and biofilm were estimated to be  $6.0 \times 10^{-21}$  J and  $1.0 \times 10^{-20}$  J, respectively [522, 523].  $R$  (nm) is the particle radius.  $h$  (nm) is the separation distance.  $\epsilon_0$  and  $\epsilon_r$  are the permittivity of the vacuum ( $8.854 \times 10^{-12}$  C/(V·m)) and the relative dielectric constant of the liquid (78.5), respectively.  $k_B$  is the Boltzman constant ( $1.381 \times 10^{-23}$  J/K).  $T$  is absolute temperature (298 K),  $z$  is the valence state of ion.  $e$  is the electron charge ( $1.602 \times 10^{-19}$  C).  $\psi_1$  and  $\psi_2$  are the potential of NPs and sand, respectively. The inverse Debye length ( $k^{-1}$ ) is estimated as 3.92 nm in synthetic water.  $\lambda_{AB}$  is the characteristic decay length of AB interactions in water (0.6 nm) [524].  $h_0$  is the distance of the closet approach (0.158 nm) [472].  $\Phi_{AB}$  is calculated as follows [472]:

$$\Phi_{AB} = -\frac{K_{123}}{2\pi h_0 \lambda_{AB}} \quad (S33)$$

where  $K_{123}$  is the hydrophobic force constant, which is determined as follows:

$$K_{123} = -7\left(\frac{\cos\beta_1 + \cos\beta_2}{2}\right) - 18 \quad (S34)$$

where  $\beta_1$  and  $\beta_2$  are the water contact angle of NPs and collector surface, respectively.

In river water, the formation of a thick eco-corona layer importantly altered the surface characteristics of NPs, thereby modifying their interaction energy profiles. In our modeling, we

focused on the pre-contact interactions between eco-corona-coated NPs and the collector surface. It is important to note that steric repulsion, which is a post-contact interaction, was not included in this analysis. Ohshima's electrophoretic theory proposes that the outer surface potential (of the adsorbed layer) is the appropriate electrical potential for predicting electrostatic interactions between "soft" particles coated by polymers [506, 507]. The outer surface potential ( $\Psi_{soft}$ ) is estimated as follows [506]:

$$\Psi_{soft} = \frac{1}{2} \Psi_1 \left( 1 - \frac{1}{\kappa R} + \frac{(1-\kappa R)(1+\kappa R_{soft})}{(1+\kappa R)\kappa R_{soft}} e^{-2\kappa\delta} \right) \quad (\text{S35})$$

where  $R_{soft}$  is the radius of eco-corona-coated NPs,  $\delta$  is the thickness of eco-corona.

**Influence of surface roughness.** Based on previous studies [433, 434], surface roughness was modeled as hemispherical asperities on flat surfaces to account for nanoscale irregularities. Two cases were considered to account for surface roughness effects: (1) NPs deposited on convex asperities and (2) NPs deposited in concave valleys between asperities. The total interaction energy in both cases was estimated as the sum of the NP–surface interaction (particle–plate) and the NP–asperity interaction (particle–particle), which can be expressed as follows [434]:

$$E_{p-a} = E_{p-p}(h) + E_{p-s}(h+r) \quad (\text{S36})$$

$$E_{p-v-1} = nE_{p-p}(h) + E_{p-s}(\sqrt{(h+r+R)^2 - (r+D)^2} - R) \quad (\text{S37})$$

$$E_{p-v-2} = nE_{p-p}(\sqrt{(H+R)^2 + (r+D)^2} - r - R) + E_{p-s}(H) \quad (\text{S38})$$

Where  $E_{p-a}$  is the total interaction energy between NPs and a convex asperity on the sand, while  $E_{p-v-1}$  and  $E_{p-v-2}$  represent the interaction energy between NPs and a concave valley on the sand.  $E_{p-p}$  and  $E_{p-s}$  denote the particle-particle interaction energy between an NP and an asperity and the particle-surface interaction between NPs and the sand, respectively.  $h$  and  $H$  are the surface-to-surface separation distance between NP–asperity and NP–surface, respectively.  $R$  and  $r$  represent the radii of the NPs and the asperities, respectively. For the particle-particle interaction energy calculation, the  $R$  in equations is calculated as  $rR/(r+R)$ . The choice between Equations (9) and (10) depends on the surface-to-surface distance ( $D$ ) between asperities. When  $D$  is large enough such that  $H < h$ , Equation (9) is applied. Conversely, when  $h \leq H$ , Equation (10) is used. In this study,  $D$  was selected to ensure  $h$  is approximately equal to  $H$ .  $n$  represents the estimated maximum number of asperities that can be arranged in a circle and is expressed as:

$$n = \frac{\pi}{\text{Arcsin}\left(\frac{r}{r+D}\right)} \quad (\text{SS39})$$

Here is schematic of interactions between NPs with a convex asperity and a concave valley between the asperities.

**Influence of surface charge or hydrophobicity heterogeneity.** We assume the presence of a positively charged or hydrophobic area (i.e., a heterogeneous patch) on an otherwise homogeneous flat surface. The interaction between NPs and these heterogeneous regions is approximated as the interaction between the NP and a positively charged particle or a hydrophobic particle, respectively. The total interaction energy between the NP and the heterogeneous surface, denoted as follows:

$$E_{p-c} = E_{p-s}(h) - E_{p-p1}(h) + E_{p-p2}(h) \quad (\text{S40})$$

Where  $E_{p-c}$  is the total interaction energy between NPs and a charge heterogeneity on a homogeneous surface.  $E_{p-s}$  is the particle-surface interaction energy between NPs and the original homogeneous surface.  $E_{p-p1}$  is interaction energy between the NP and the original surface region that has been replaced (homogeneous, patch 1), and  $E_{p-p2}$  denote interaction energy between the NP and the heterogeneous patch (positively charged or hydrophobic, patch 2).

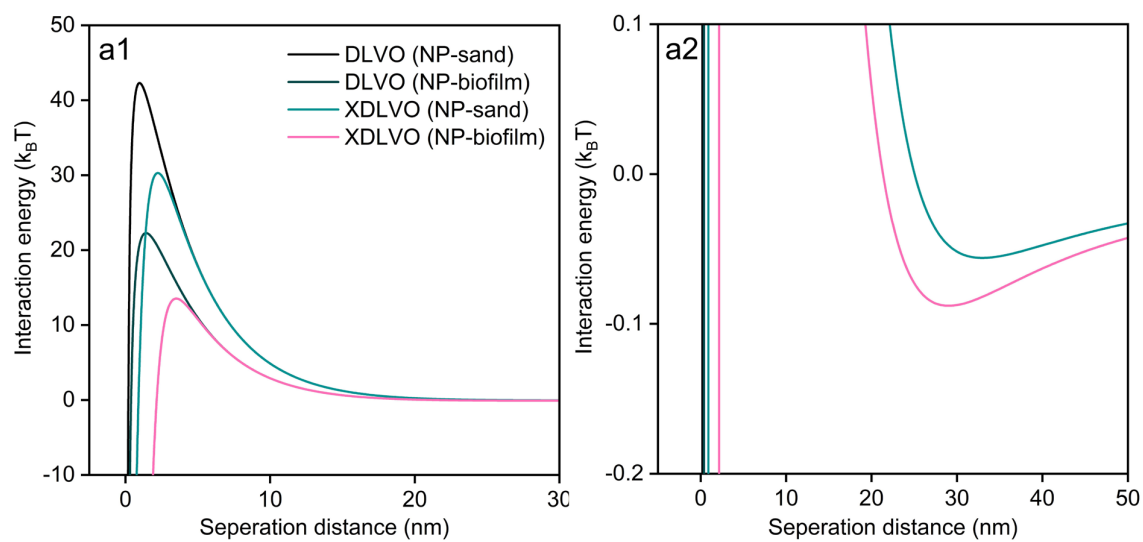


Figure S35. DLVO and XDLVO interaction energy of NP-sand and NP-biofilm.

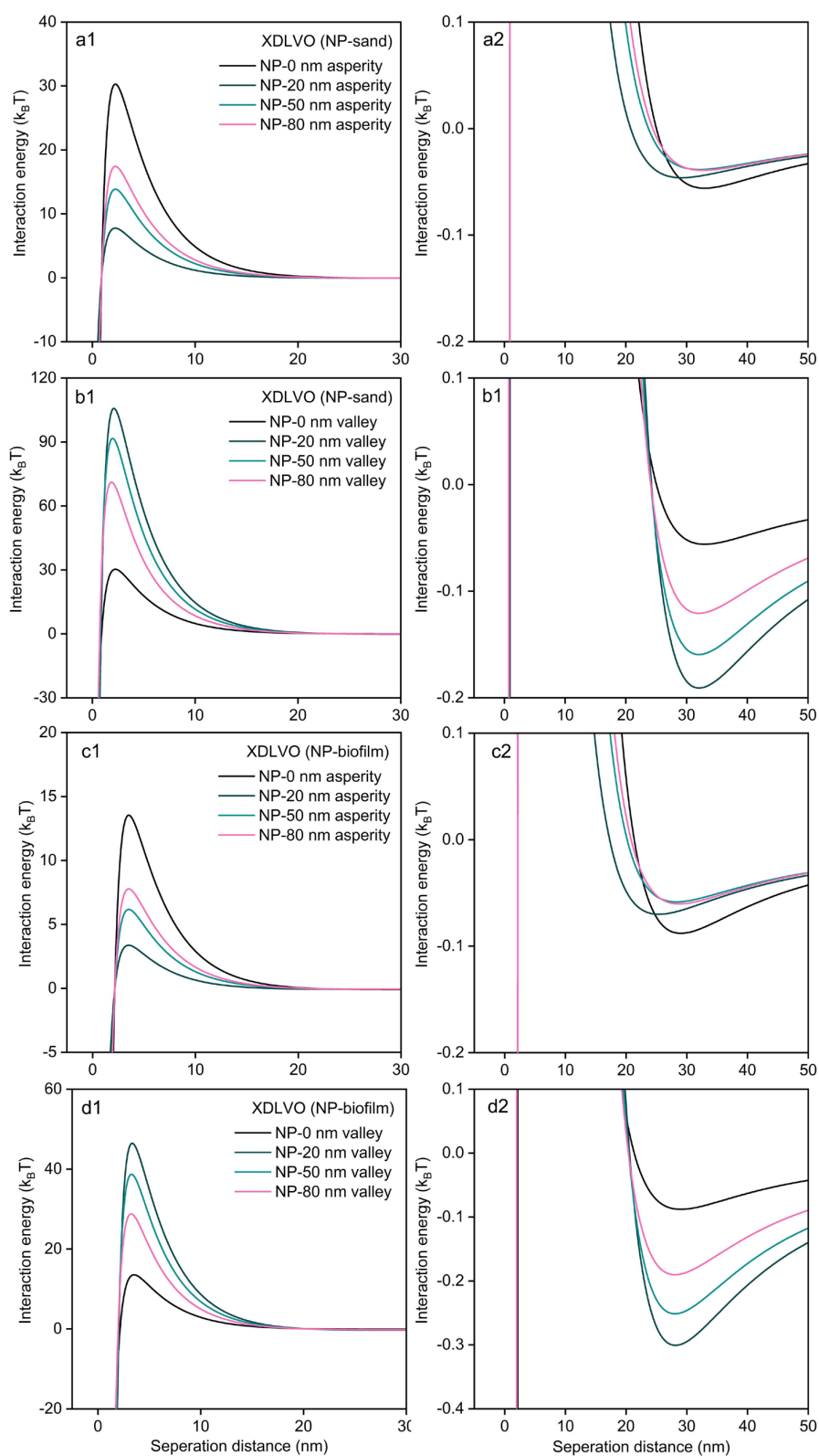
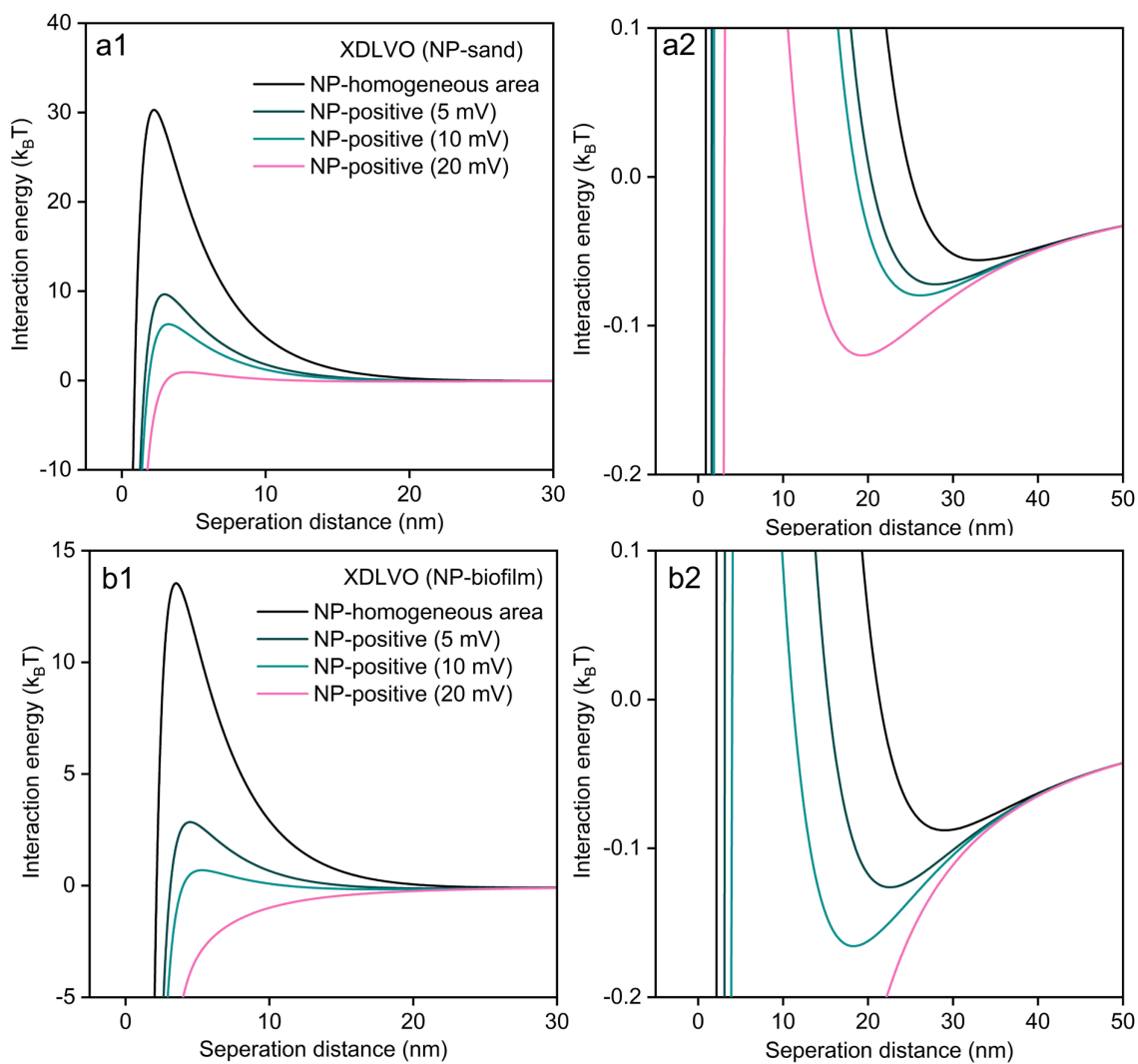
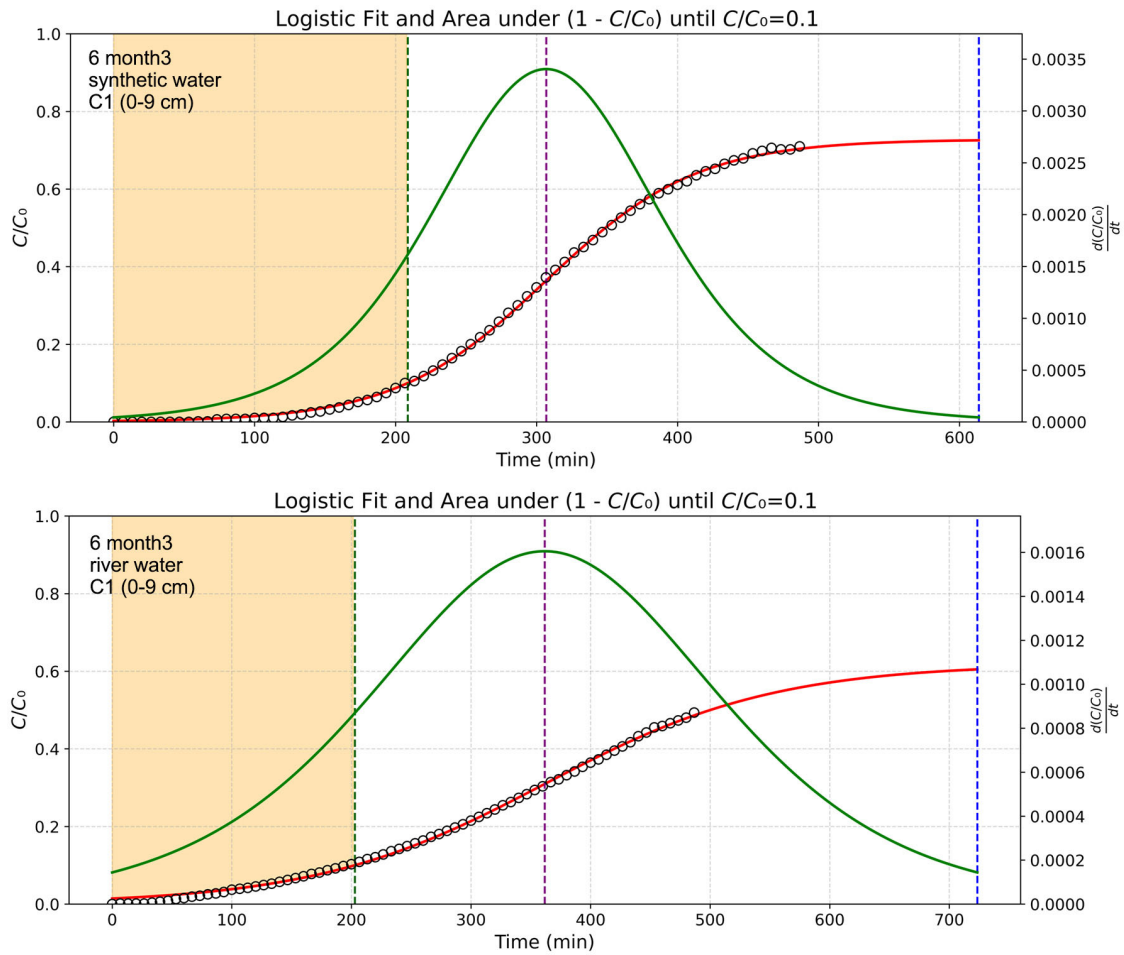


Figure S36. Effects of surface roughness on the energy barrier (1) and secondary energy minimum (2) (a and b) and NP-biofilm (c and d).



**Figure S37.** Effect of charge heterogeneity (50 nm) on the energy barrier (1) and secondary energy minimum (2) of NP-sand (a) and NP-biofilm (b).



*Figure S38. Representative logistic model fittings of BTCs of NPs in column C1 (0–9 cm) using synthetic water and river water after 6 months biofilm formation.*

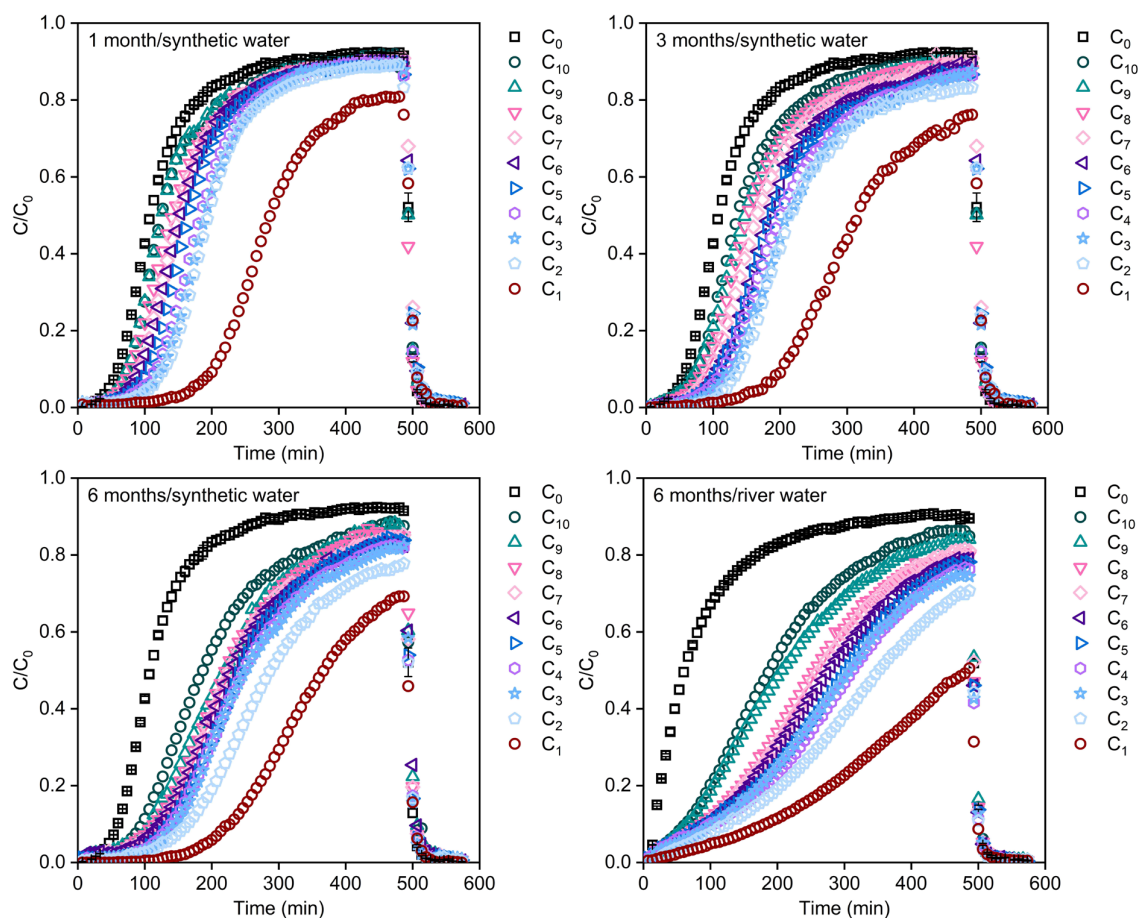


**Figure S39.** The BTCs of NPs in clean sand and in clean sand and in biofilm-coated sand segments after 1, 3, and 6 months of cultivation at different depths.

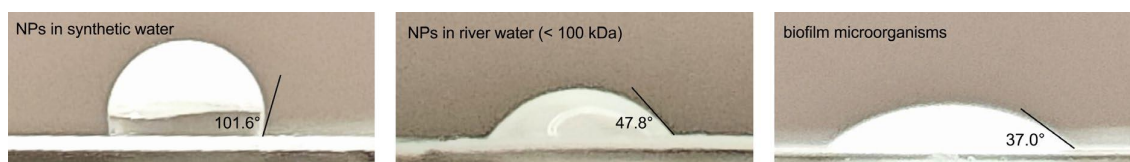


**Figure S40.** Water contact angles of NPs in synthetic water and river water (filtered onto  $0.1 \mu\text{m}$  membranes), and of biofilm microorganisms (sonicated and filtered onto  $0.1 \mu\text{m}$  membranes). For comparison, the water contact angle of a silica surface ( $13.7^\circ$ ) was obtained from literature [525].

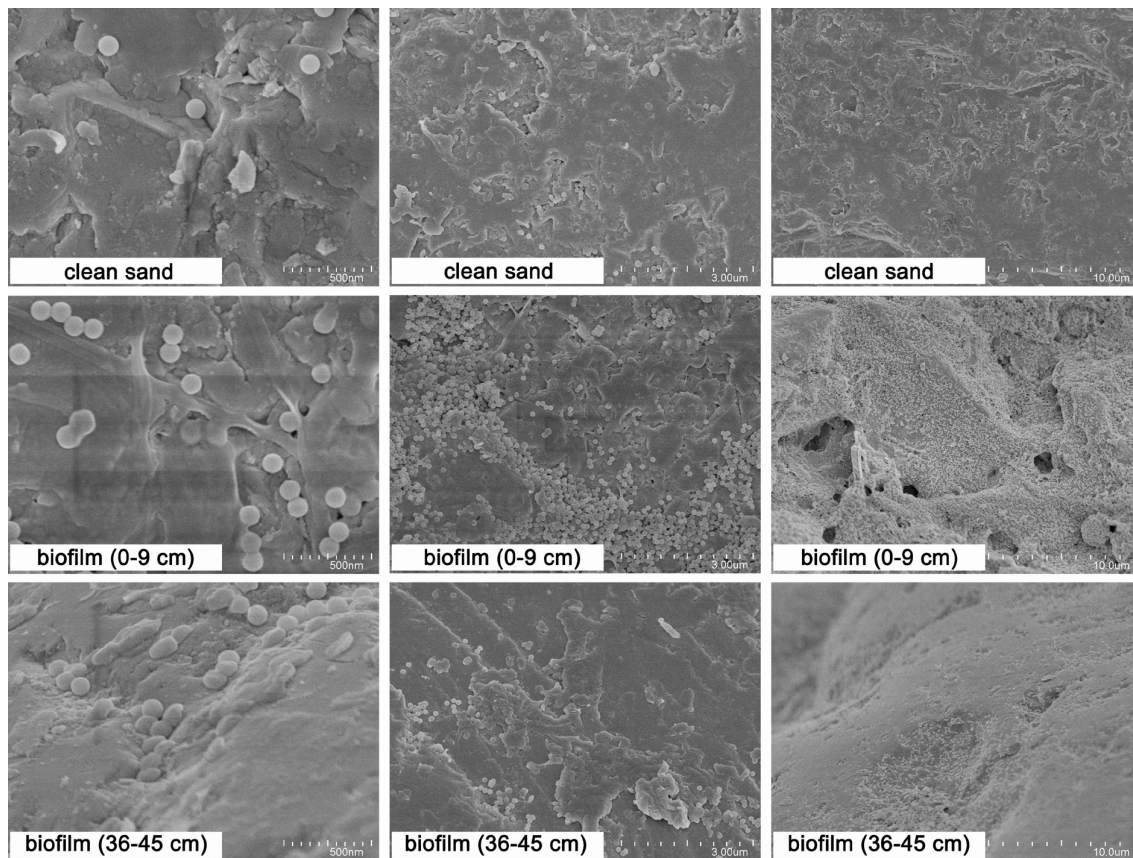


*Figure S41. SEM images showing the deposition of NPs on bare sand and biofilm-coated sand at two depths: 0–9 cm and 36–45 cm.*

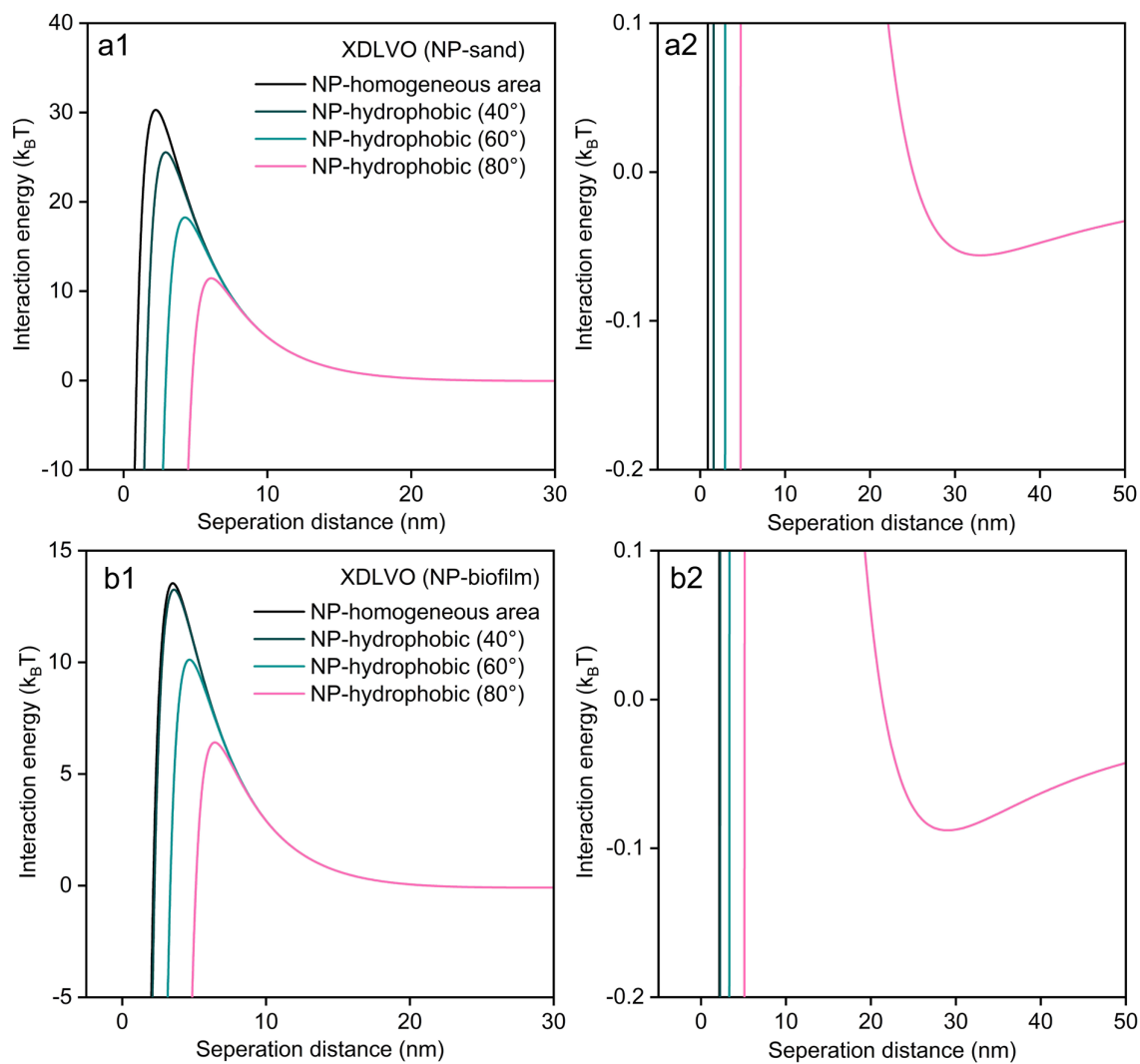
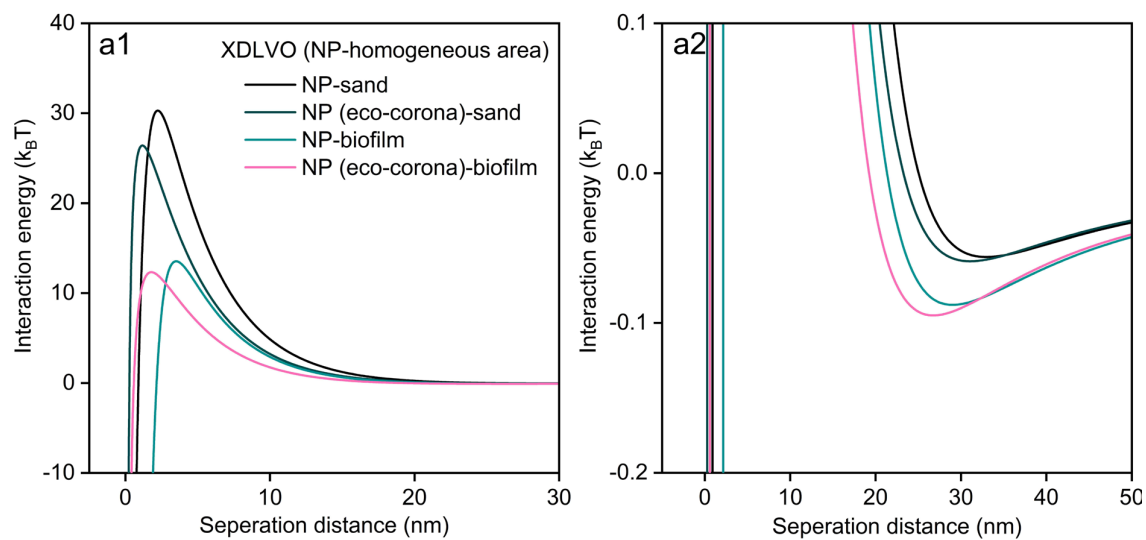
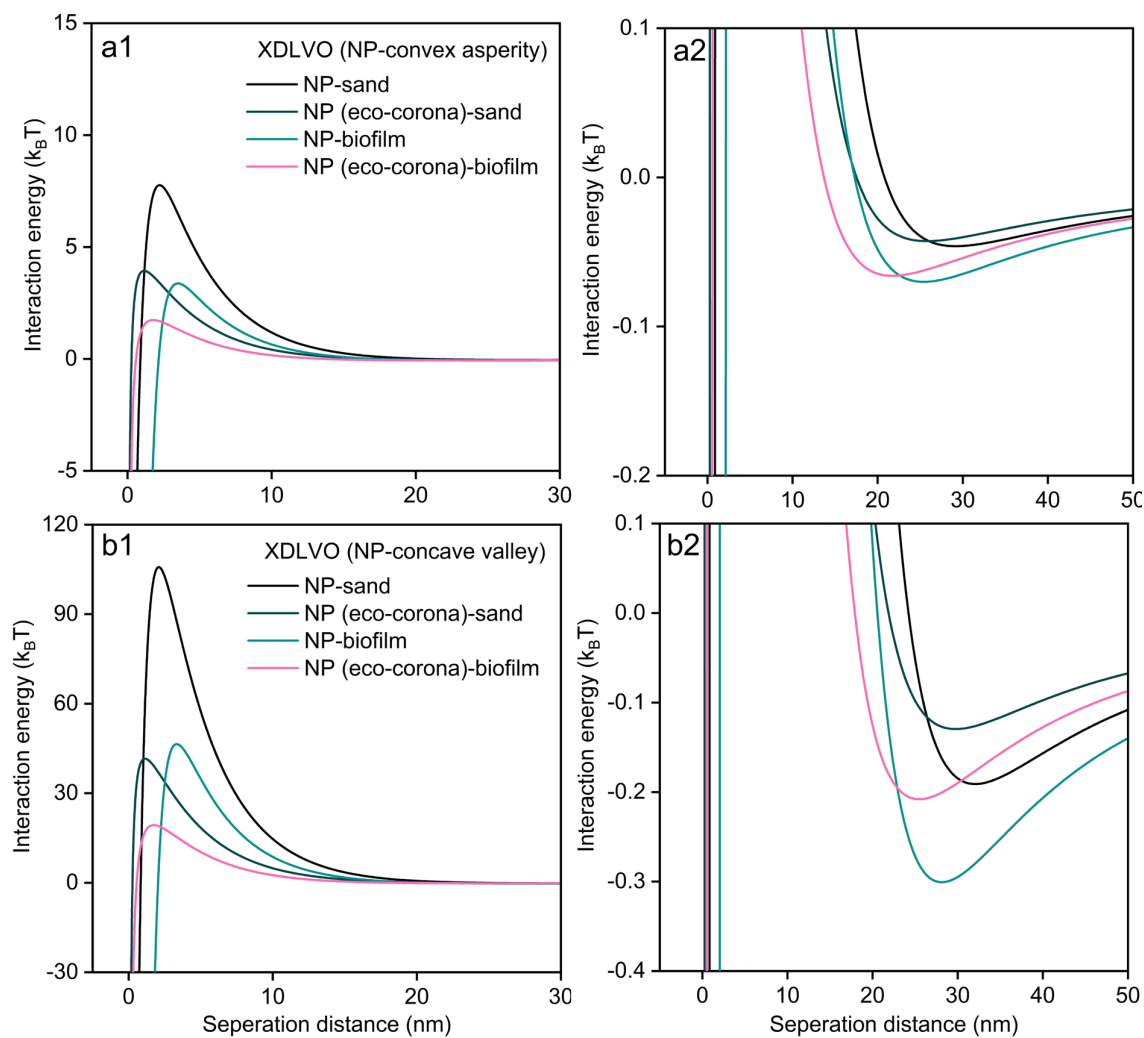


Figure S42. Effect of hydrophobicity heterogeneity (50 nm) on the energy barrier (1) and secondary energy minimum (2) of NP-sand (a) and NP-biofilm (b).



**Figure S43.** Effect of eco-corona on the XDLVO interaction energy profiles illustrating the energy barriers and secondary minima for NP deposition on homogeneous surfaces of sand and biofilm surfaces.



**Figure S44.** Effect of eco-corona on the XDLVO interaction energy profiles illustrating the energy barriers and secondary minima for NP deposition on (a) a surface with a 20 nm asperity and (b) a valley between 20 nm asperities.

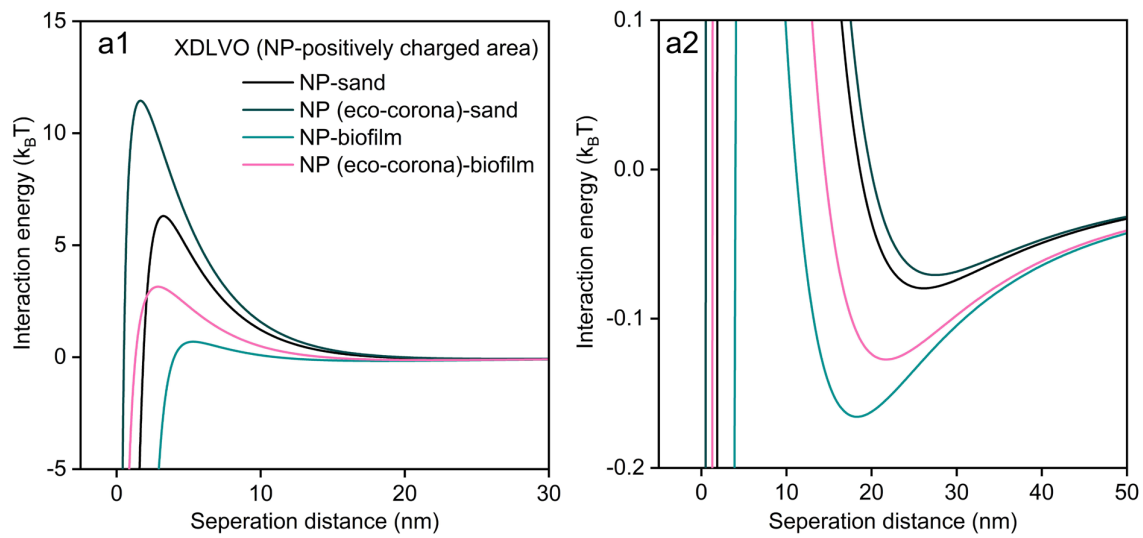


**Figure S45.** Effect of eco-corona on the XDLVO interaction energy profiles illustrating the energy barriers and secondary minima for NP deposition on an 50 nm positively charged area (10 mV).

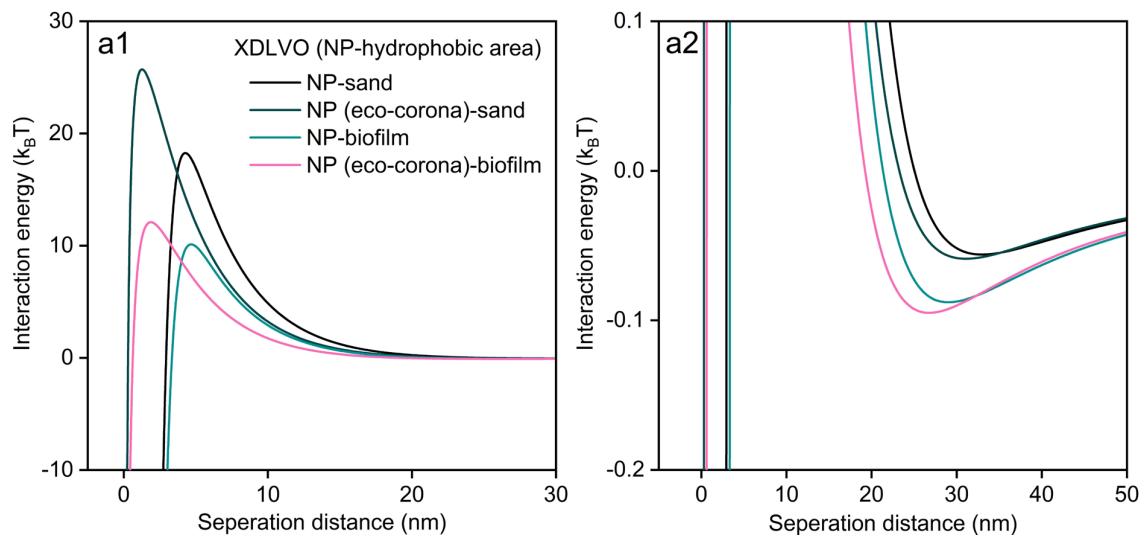


**Figure S46.** Effect of eco-corona on the XDLVO interaction energy profiles illustrating the energy barriers and secondary minima for NP deposition on an 50 nm hydrophobic area with a contact angle of 60°.



## Bibliography

1. Syberg, K., et al., *Regulation of plastic from a circular economy perspective*. Current opinion in green sustainable chemistry, 2021. **29**: p. 100462.
2. AlMaadeed, M.A.A., D. Ponnamma, and A.A. El-Samak, *Polymers to improve the world and lifestyle: physical, mechanical, and chemical needs*, in *Polymer Science and Innovative Applications*. 2020, Elsevier. p. 1-19.
3. Piyathilaka, P. and K. Sirisena, *Sustainable Management for Urban Plastic Waste Generation*, in *Sustainable Management of Urban Plastic Waste Through Circular Economic Approaches*. 2024, CRC Press. p. 104-147.
4. Amobonye, A., et al., *Plastic biodegradation: Frontline microbes and their enzymes*. Science of the Total Environment, 2021. **759**: p. 143536.
5. Hartmann, N.B., et al., *Are we speaking the same language? Recommendations for a definition and categorization framework for plastic debris*. 2019, ACS Publications. p. 1039-1047.
6. Thompson, R.C., et al., *Lost at sea: where is all the plastic?* Science, 2004. **304**(5672): p. 838-838.
7. Dawson, A.L., et al., *Turning microplastics into nanoplastics through digestive fragmentation by Antarctic krill*. Nature communications, 2018. **9**(1): p. 1001.
8. Yang, L., et al., *Microplastics in freshwater sediment: A review on methods, occurrence, and sources*. Sci Total Environ, 2021. **754**: p. 141948.
9. Wong, J.K.H., et al., *Microplastics in the freshwater and terrestrial environments: Prevalence, fates, impacts and sustainable solutions*. Sci Total Environ, 2020. **719**: p. 137512.
10. Xu, Y., et al., *Identification and Quantification of Nanoplastics in Surface Water and Groundwater by Pyrolysis Gas Chromatography-Mass Spectrometry*. Environ Sci Technol, 2022. **56**(8): p. 4988-4997.
11. Di, M. and J. Wang, *Microplastics in surface waters and sediments of the Three Gorges Reservoir, China*. Science of the Total Environment, 2018. **616**: p. 1620-1627.
12. Gao, S., et al., *A review on microplastics in major European rivers*. WIREs Water, 2024. **11**(3).
13. Fath, A., *Mikroplastik*, in *Mikroplastik: Verbreitung, Vermeidung, Verwendung*. 2019, Springer. p. 15-242.
14. Hildebrandt, L., et al., *Comparison and uncertainty evaluation of two centrifugal separators for microplastic sampling*. Journal of hazardous materials, 2021. **414**: p. 125482.
15. Materić, D., et al., *Presence of nanoplastics in rural and remote surface waters*. Environmental Research Letters, 2022. **17**(5).
16. Bouwman, H., et al., *Microplastics in freshwater environments*. Water research Commission. Report No. /1/18https, 2018.
17. Mintenig, S.M., et al., *Low numbers of microplastics detected in drinking water from ground water sources*. Science of The Total Environment, 2019. **648**: p. 631-635.
18. Panno, S.V., et al., *Microplastic contamination in karst groundwater systems*. Groundwater, 2019. **57**(2): p. 189-196.
19. Bäuerlein, P.S., et al., *Fate of microplastics in the drinking water production*. Water Research, 2022. **221**: p. 118790.
20. Burns, E.E. and A.B. Boxall, *Microplastics in the aquatic environment: Evidence for or against adverse impacts and major knowledge gaps*. Environmental toxicology chemistry, 2018. **37**(11): p. 2776-2796.
21. da Costa, J.P., A.C. Duarte, and T.A. Rocha-Santos, *Microplastics—occurrence, fate and behaviour in the environment*, in *Comprehensive analytical chemistry*. 2017, Elsevier. p. 1-24.
22. Lambert, S., C. Sinclair, and A. Boxall, *Occurrence, degradation, and effect of polymer-based materials in the environment*. Reviews of Environmental Contamination Toxicology, 2013. **227**: p. 1-53.
23. Bolívar-Subirats, G., et al., *Occurrence, toxicity and risk assessment of plastic additives in Besos river, Spain*. Chemosphere, 2021. **263**: p. 128022.
24. Tyree, C. and D. Morrison, *Invisibles: The plastic inside us*. Orb Media, 2017.
25. Okoye, C.O., et al., *Toxic chemicals and persistent organic pollutants associated with micro- and nanoplastics pollution*. Chemical Engineering Journal Advances, 2022. **11**: p. 100310.
26. Wang, T., et al., *Interactions between microplastics and organic pollutants: Effects on toxicity, bioaccumulation, degradation, and transport*. Science of The Total Environment, 2020. **748**: p. 142427.
27. Koelmans, B., et al., *A scientific perspective on microplastics in nature and society*. 2019: SAPEA.
28. Wright, S.L. and F.J. Kelly, *Plastic and human health: a micro issue?* Environmental science technology, 2017. **51**(12): p. 6634-6647.

29. Brown, D.M., et al., *Size-dependent proinflammatory effects of ultrafine polystyrene particles: a role for surface area and oxidative stress in the enhanced activity of ultrafines*. Toxicology applied pharmacology, 2001. **175**(3): p. 191-199.
30. Dong, X., et al., *From natural environment to animal tissues: A review of microplastics (nanoplastics) translocation and hazards studies*. Science of the Total Environment, 2023. **855**: p. 158686.
31. Sun, N., et al., *Combined toxicity of micro/nanoplastics loaded with environmental pollutants to organisms and cells: Role, effects, and mechanism*. Environment international, 2023. **171**: p. 107711.
32. González-Soto, N., et al., *Impacts of dietary exposure to different sized polystyrene microplastics alone and with sorbed benzo [a] pyrene on biomarkers and whole organism responses in mussels *Mytilus galloprovincialis**. Science of the Total Environment, 2019. **684**: p. 548-566.
33. Ali, N., et al., *The potential impacts of micro-and-nano plastics on various organ systems in humans*. EBioMedicine, 2024. **99**.
34. Santillo, D., K. Miller, and P. Johnston, *Microplastics as contaminants in commercially important seafood species*. Integrated environmental assessment management, 2017. **13**(3): p. 516-521.
35. Karami, A., et al., *The presence of microplastics in commercial salts from different countries*. Scientific Reports, 2017. **7**(1): p. 46173.
36. Mason, S.A., V.G. Welch, and J. Neratko, *Synthetic polymer contamination in bottled water*. Frontiers in chemistry, 2018. **6**: p. 389699.
37. González-Pleiter, M., et al., *Secondary nanoplastics released from a biodegradable microplastic severely impact freshwater environments*. Environmental Science: Nano, 2019. **6**(5): p. 1382-1392.
38. Landeros, L., et al., *A review of the origins of microplastics arriving at wastewater treatment plants*. Detritus, 2022. **20**: p. 41-55.
39. An, L., et al., *Sources of microplastic in the environment*. Microplastics in terrestrial environments: Emerging contaminants major challenges, 2020: p. 143-159.
40. Fendall, L.S. and M.A. Sewell, *Contributing to marine pollution by washing your face: Microplastics in facial cleansers*. Marine Pollution Bulletin, 2009. **58**(8): p. 1225-1228.
41. Anagnosti, L., et al., *Worldwide actions against plastic pollution from microbeads and microplastics in cosmetics focusing on European policies. Has the issue been handled effectively?* Marine Pollution Bulletin, 2021. **162**: p. 111883.
42. Essel, R., et al., *Sources of microplastics relevant to marine protection in Germany*. Texte, 2015. **64**(2015): p. 1219-1226.
43. Alimi, O.S., et al., *Microplastics and Nanoplastics in Aquatic Environments: Aggregation, Deposition, and Enhanced Contaminant Transport*. Environ Sci Technol, 2018. **52**(4): p. 1704-1724.
44. Amaral-Zettler, L.A., E.R. Zettler, and T.J. Mincer, *Ecology of the plastisphere*. Nat Rev Microbiol, 2020. **18**(3): p. 139-151.
45. Enfrin, M., et al., *Release of hazardous nanoplastic contaminants due to microplastics fragmentation under shear stress forces*. J Hazard Mater, 2020. **384**: p. 121393.
46. Liu, P., et al., *New Insights into the Aging Behavior of Microplastics Accelerated by Advanced Oxidation Processes*. Environ Sci Technol, 2019. **53**(7): p. 3579-3588.
47. Roager, L. and E.C. Sonnenschein, *Bacterial Candidates for Colonization and Degradation of Marine Plastic Debris*. Environ Sci Technol, 2019. **53**(20): p. 11636-11643.
48. Roweczyk, L., et al., *Microstructure Characterization of Oceanic Polyethylene Debris*. Environ Sci Technol, 2020. **54**(7): p. 4102-4109.
49. Enfrin, M., et al., *Release of hazardous nanoplastic contaminants due to microplastics fragmentation under shear stress forces*. Journal of Hazardous Materials, 2020. **384**: p. 121393.
50. Pielichowski, K., J. Njuguna, and T.M. Majka, *Thermal degradation of polymeric materials*. 2022: Elsevier.
51. Urban-Malinga, B., et al., *Microplastics on sandy beaches of the southern Baltic Sea*. Marine Pollution Bulletin, 2020. **155**: p. 111170.
52. Andrady, A.L., *Microplastics in the marine environment*. Marine pollution bulletin, 2011. **62**(8): p. 1596-1605.
53. Song, Y.K., et al., *Combined Effects of UV Exposure Duration and Mechanical Abrasion on Microplastic Fragmentation by Polymer Type*. Environ Sci Technol, 2017. **51**(8): p. 4368-4376.

54. Muenmee, S., W. Chiemchaisri, and C. Chiemchaisri, *Microbial consortium involving biological methane oxidation in relation to the biodegradation of waste plastics in a solid waste disposal open dump site*. International Biodeterioration & Biodegradation, 2015. **102**: p. 172-181.
55. Yang, Y., et al., *Biodegradation and mineralization of polystyrene by plastic-eating mealworms: part 2. Role of gut microorganisms*. Environmental science technology, 2015. **49**(20): p. 12087-12093.
56. Zhao, J., et al., *Microplastic fragmentation by rotifers in aquatic ecosystems contributes to global nanoplastic pollution*. Nature Nanotechnology, 2024. **19**(3): p. 406-414.
57. Tian, R., et al., *Characterization Techniques of Polymer Aging: From Beginning to End*. Chemical Reviews, 2023. **123**(6): p. 3007-3088.
58. Sun, Y., et al., *Laboratory simulation of microplastics weathering and its adsorption behaviors in an aqueous environment: A systematic review*. Environ Pollut, 2020. **265**(Pt B): p. 114864.
59. Brandon, J., M. Goldstein, and M.D. Ohman, *Long-term aging and degradation of microplastic particles: Comparing in situ oceanic and experimental weathering patterns*. Marine Pollution Bulletin, 2016. **110**(1): p. 299-308.
60. Ren, Z., et al., *Microplastics in the soil-groundwater environment: Aging, migration, and co-transport of contaminants - A critical review*. J Hazard Mater, 2021. **419**: p. 126455.
61. Tang, K.H.D. and R. Li, *The effects of plastisphere on the physicochemical properties of microplastics*. Bioprocess and Biosystems Engineering, 2025. **48**(1): p. 1-15.
62. Behera, S. and S. Das, *Environmental impacts of microplastic and role of plastisphere microbes in the biodegradation and upcycling of microplastic*. Chemosphere, 2023. **334**: p. 138928.
63. Van Melkebeke, M., C. Janssen, and S. De Meester, *Characteristics and Sinking Behavior of Typical Microplastics Including the Potential Effect of Biofouling: Implications for Remediation*. Environmental Science & Technology, 2020. **54**(14): p. 8668-8680.
64. Kooi, M., et al., *Ups and Downs in the Ocean: Effects of Biofouling on Vertical Transport of Microplastics*. Environmental Science & Technology, 2017. **51**(14): p. 7963-7971.
65. Junaid, M. and J. Wang, *Interaction of nanoplastics with extracellular polymeric substances (EPS) in the aquatic environment: A special reference to eco-corona formation and associated impacts*. Water Res, 2021. **201**: p. 117319.
66. Saavedra, J., S. Stoll, and V.I. Slaveykova, *Influence of nanoplastic surface charge on eco-corona formation, aggregation and toxicity to freshwater zooplankton*. Environmental Pollution, 2019. **252**: p. 715-722.
67. Zhu, M., et al., *Eco-Corona Dictates Mobility of Nanoplastics in Saturated Porous Media: The Critical Role of Preferential Binding of Macromolecules*. Environ Sci Technol, 2022.
68. Kumar, R., et al., *Effect of Physical Characteristics and Hydrodynamic Conditions on Transport and Deposition of Microplastics in Riverine Ecosystem*. Water, 2021. **13**(19): p. 2710.
69. Waldschläger, K. and H. Schüttrumpf, *Effects of particle properties on the settling and rise velocities of microplastics in freshwater under laboratory conditions*. Environmental science technology, 2019. **53**(4): p. 1958-1966.
70. Lenaker, P.L., et al., *Vertical distribution of microplastics in the water column and surficial sediment from the Milwaukee River Basin to Lake Michigan*. Environmental science technology, 2019. **53**(21): p. 12227-12237.
71. Gigault, J., et al., *Nanoplastics are neither microplastics nor engineered nanoparticles*. Nature Nanotechnology, 2021. **16**(5): p. 501-507.
72. Yu, Y. and M. Flury, *Current understanding of subsurface transport of micro- and nanoplastics in soil*. Vadose Zone Journal, 2021. **20**(2).
73. O'Connor, D., et al., *Microplastics undergo accelerated vertical migration in sand soil due to small size and wet-dry cycles*. Environmental Pollution, 2019. **249**: p. 527-534.
74. Tufenkji, N. and M. Elimelech, *Correlation equation for predicting single-collector efficiency in physicochemical filtration in saturated porous media*. Environmental science technology, 2004. **38**(2): p. 529-536.
75. Pradel, A., et al., *Deposition of environmentally relevant nanoplastic models in sand during transport experiments*. Chemosphere, 2020. **255**: p. 126912.
76. Wang, J., et al., *Aggregation and stability of sulfate-modified polystyrene nanoplastics in synthetic and natural waters*. Environ Pollut, 2021. **268**(Pt A): p. 114240.
77. Yu, S., et al., *Aggregation kinetics of different surface-modified polystyrene nanoparticles in monovalent and divalent electrolytes*. Environ Pollut, 2019. **255**(Pt 2): p. 113302.
78. Lee, C.-H. and J.K.-H. Fang, *Effects of temperature and particle concentration on aggregation of nanoplastics in freshwater and seawater*. Science of the Total Environment, 2022. **817**: p. 152562.

79. Dong, Z., et al., *Role of surface functionalities of nanoplastics on their transport in seawater-saturated sea sand*. Environmental Pollution, 2019. **255**: p. 113177.
80. Wheeler, K.E., et al., *Environmental dimensions of the protein corona*. Nature Nanotechnology, 2021. **16**: p. 617–629.
81. Shams, M., I. Alam, and I. Chowdhury, *Aggregation and stability of nanoscale plastics in aquatic environment*. Water Res, 2020. **171**: p. 115401.
82. Liu, Y., et al., *Influence of environmental and biological macromolecules on aggregation kinetics of nanoplastics in aquatic systems*. Water Res, 2020. **186**: p. 116316.
83. Xu, Y., et al., *Combined effects of photoaging and natural organic matter on the colloidal stability of nanoplastics in aquatic environments*. Water Research, 2022. **226**: p. 119313.
84. Zhang, F., et al., *Aquatic behavior and toxicity of polystyrene nanoplastic particles with different functional groups: Complex roles of pH, dissolved organic carbon and divalent cations*. Chemosphere, 2019. **228**: p. 195-203.
85. Singh, N., et al., *Understanding the stability of nanoplastics in aqueous environments: effect of ionic strength, temperature, dissolved organic matter, clay, and heavy metals*. Environmental Science: Nano, 2019. **6**(10): p. 2968-2976.
86. Zhang, Y., et al., *Charge mediated interaction of polystyrene nanoplastic (PSNP) with minerals in aqueous phase*. Water Research, 2020. **178**: p. 115861.
87. Ling, X., Z. Yan, and G. Lu, *Vertical transport and retention behavior of polystyrene nanoplastics in simulated hyporheic zone*. Water Res, 2022. **219**: p. 118609.
88. Tan, M., et al., *Effects of solution chemistry and humic acid on the transport of polystyrene microplastics in manganese oxides coated sand*. J Hazard Mater, 2021. **413**: p. 125410.
89. Dong, Z., et al., *Protein corona-mediated transport of nanoplastics in seawater-saturated porous media*. Water Res, 2020. **182**: p. 115978.
90. He, L., et al., *Bacteria have different effects on the transport behaviors of positively and negatively charged microplastics in porous media*. J Hazard Mater, 2021. **415**: p. 125550.
91. Wu, X., et al., *Transport of polystyrene nanoplastics in natural soils: Effect of soil properties, ionic strength and cation type*. Science of The Total Environment, 2020. **707**: p. 136065.
92. Quevedo, I.R. and N. Tufenkji, *Mobility of functionalized quantum dots and a model polystyrene nanoparticle in saturated quartz sand and loamy sand*. Environmental science technology, 2012. **46**(8): p. 4449-4457.
93. Lu, T., et al., *Relevance of iron oxyhydroxide and pore water chemistry on the mobility of nanoplastic particles in water-saturated porous media environments*. Water, Air, Soil Pollution, 2021. **232**: p. 1-13.
94. Ma, J., et al., *Effect of Agricultural Organic Inputs on Nanoplastics Transport in Saturated Goethite-Coated Porous Media: Particle Size Selectivity and Role of Dissolved Organic Matter*. environmental science & technology, 2022. **56**: p. 3524-3534.
95. Dong, S., et al., *Transport and retention patterns of fragmental microplastics in saturated and unsaturated porous media: A real-time pore-scale visualization*. Water Research, 2022. **214**: p. 118195.
96. Li, S., et al., *Adsorption of microplastics on aquifer media: Effects of the action time, initial concentration, ionic strength, ionic types and dissolved organic matter*. Environmental Pollution, 2022. **308**: p. 119482.
97. He, L., et al., *Influence of biofilm on the transport and deposition behaviors of nano- and microplastic particles in quartz sand*. Water Res, 2020. **178**: p. 115808.
98. Mitzel, M.R., et al., *Hydrophobicity of biofilm coatings influences the transport dynamics of polystyrene nanoparticles in biofilm-coated sand*. Water Res, 2016. **92**: p. 113-20.
99. Li, D., et al., *Microbial community evolution during simulated managed aquifer recharge in response to different biodegradable dissolved organic carbon (BDOC) concentrations*. Water Res, 2013. **47**(7): p. 2421-30.
100. Maeng, S.K., et al., *Role of biodegradation in the removal of pharmaceutically active compounds with different bulk organic matter characteristics through managed aquifer recharge: batch and column studies*. Water Res, 2011. **45**(16): p. 4722-36.
101. Tufenkji, N., J.N. Ryan, and M. Elimelech, *The promise of bank filtration*. Environmental Science and Technology, 2002. **36**(21): p. 422A-428A.
102. van der Hoek, J.P., et al., *Drinking water treatment technologies in Europe: state of the art – challenges – research needs*. Journal of Water Supply: Research and Technology-Aqua, 2014. **63**(2): p. 124-130.
103. Ray, C., et al., *A Perspective of Riverbank Filtration*. Journal - American Water Works Association, 2002. **94**(4): p. 149-160.

104. Sandhu, C., et al., *Potential for Riverbank filtration in India*. Clean Technologies and Environmental Policy, 2010. **13**(2): p. 295-316.
105. Bertelkamp, C., et al., *Sorption and biodegradation of organic micropollutants during river bank filtration: a laboratory column study*. Water Res, 2014. **52**: p. 231-41.
106. Rudolf von Rohr, M., et al., *Column studies to assess the effects of climate variables on redox processes during riverbank filtration*. Water Res, 2014. **61**: p. 263-75.
107. Knabe, D., et al., *Uncertainty Analysis and Identification of Key Parameters Controlling Bacteria Transport Within a Riverbank Filtration Scenario*. Water Resources Research, 2021. **57**(4).
108. Metge, D.W., et al., *Influence of organic carbon loading, sediment associated metal oxide content and sediment grain size distributions upon Cryptosporidium parvum removal during riverbank filtration operations, Sonoma County, CA*. Water Res, 2010. **44**(4): p. 1126-37.
109. Degenkolb, L., et al., *The fate of silver nanoparticles in riverbank filtration systems - The role of biological components and flow velocity*. Sci Total Environ, 2020. **699**: p. 134387.
110. Faulkner, B.R., et al., *Removal efficiencies and attachment coefficients for Cryptosporidium in sandy alluvial riverbank sediment*. Water Res, 2010. **44**(9): p. 2725-34.
111. Degenkolb, L., et al., *Retention and remobilization mechanisms of environmentally aged silver nanoparticles in an artificial riverbank filtration system*. Sci Total Environ, 2018. **645**: p. 192-204.
112. Velis, C.A. and E. Cook, *Mismanagement of Plastic Waste through Open Burning with Emphasis on the Global South: A Systematic Review of Risks to Occupational and Public Health*. Environ Sci Technol, 2021. **55**(11): p. 7186-7207.
113. Borrelle, S.B., et al., *Predicted growth in plastic waste exceeds efforts to mitigate plastic pollution*. Science, 2020. **369**: p. 1515-1518.
114. Jahnke, A., et al., *Reducing Uncertainty and Confronting Ignorance about the Possible Impacts of Weathering Plastic in the Marine Environment*. Environmental Science & Technology Letters, 2017. **4**(3): p. 85-90.
115. Gigault, J., et al., *Nanoplastics are neither microplastics nor engineered nanoparticles*. Nat Nanotechnol, 2021. **16**(5): p. 501-507.
116. Mitrano, D.M., P. Wick, and B. Nowack, *Placing nanoplastics in the context of global plastic pollution*. Nat Nanotechnol, 2021. **16**(5): p. 491-500.
117. Duan, J., et al., *Weathering of microplastics and interaction with other coexisting constituents in terrestrial and aquatic environments*. Water Res, 2021. **196**: p. 117011.
118. Mao, R., et al., *Aging mechanism of microplastics with UV irradiation and its effects on the adsorption of heavy metals*. J Hazard Mater, 2020. **393**: p. 122515.
119. Zhu, K., et al., *Long-term phototransformation of microplastics under simulated sunlight irradiation in aquatic environments: Roles of reactive oxygen species*. Water Res, 2020. **173**: p. 115564.
120. Miranda, M.N., et al., *Aging assessment of microplastics (LDPE, PET and uPVC) under urban environment stressors*. Sci Total Environ, 2021. **796**: p. 148914.
121. Chen, C., et al., *Organotin Release from Polyvinyl Chloride Microplastics and Concurrent Photodegradation in Water: Impacts from Salinity, Dissolved Organic Matter, and Light Exposure*. Environ Sci Technol, 2019. **53**(18): p. 10741-10752.
122. Ding, L., et al., *The photodegradation processes and mechanisms of polyvinyl chloride and polyethylene terephthalate microplastic in aquatic environments: Important role of clay minerals*. Water Res, 2022. **208**: p. 117879.
123. Yu, X., et al., *New insights on metal ions accelerating the aging behavior of polystyrene microplastics: Effects of different excess reactive oxygen species*. Sci Total Environ, 2022. **821**: p. 153457.
124. Zhu, K., et al., *Inorganic anions influenced the photoaging kinetics and mechanism of polystyrene microplastic under the simulated sunlight: Role of reactive radical species*. Water Res, 2022. **216**: p. 118294.
125. Liu, P., et al., *Critical effect of iron red pigment on photoaging behavior of polypropylene microplastics in artificial seawater*. J Hazard Mater, 2021. **404**(Pt B): p. 124209.
126. Wu, X., et al., *Humic Acid and Fulvic Acid Hinder Long-Term Weathering of Microplastics in Lake Water*. Environ Sci Technol, 2021. **55**(23): p. 15810-15820.
127. Wu, X., et al., *Photo aging of polypropylene microplastics in estuary water and coastal seawater: Important role of chlorine ion*. Water Res, 2021. **202**: p. 117396.
128. Liu, Y., et al., *Aggregation kinetics of UV irradiated nanoplastics in aquatic environments*. Water Res, 2019. **163**: p. 114870.
129. Ren, Z., et al., *Chemical and photo-initiated aging enhances transport risk of microplastics in saturated soils: Key factors, mechanisms, and modeling*. Water Res, 2021. **202**: p. 117407.

130. Mao, Y., et al., *Nanoplastics display strong stability in aqueous environments: Insights from aggregation behaviour and theoretical calculations*. Environ Pollut, 2020. **258**: p. 113760.
131. Xi, X., et al., *Interactions of pristine and aged nanoplastics with heavy metals: Enhanced adsorption and transport in saturated porous media*. Journal of Hazardous Materials, 2022. **437**: p. 129311.
132. Wang, X., et al., *UV-induced aggregation of polystyrene nanoplastics: effects of radicals, surface functional groups and electrolyte*. Environmental Science: Nano, 2020. **7**(12): p. 3914-3926.
133. Li, X., et al., *UV/ozone induced physicochemical transformations of polystyrene nanoparticles and their aggregation tendency and kinetics with natural organic matter in aqueous systems*. J Hazard Mater, 2022. **433**: p. 128790.
134. Zhang, Y., et al., *Aging significantly increases the interaction between polystyrene nanoplastic and minerals*. Water Res, 2022. **219**: p. 118544.
135. Kim, T.K., M. Jang, and Y.S. Hwang, *Adsorption of benzalkonium chlorides onto polyethylene microplastics: Mechanism and toxicity evaluation*. J Hazard Mater, 2022. **426**: p. 128076.
136. Liu, J., et al., *Aging Significantly Affects Mobility and Contaminant-Mobilizing Ability of Nanoplastics in Saturated Loamy Sand*. Environ Sci Technol, 2019. **53**(10): p. 5805-5815.
137. Zhang, X., et al., *Effects and mechanisms of aged polystyrene microplastics on the photodegradation of sulfamethoxazole in water under simulated sunlight*. J Hazard Mater, 2022. **433**: p. 128813.
138. Chen, M., et al., *Addition of biodegradable microplastics alters the quantity and chemodiversity of dissolved organic matter in latosol*. Sci Total Environ, 2022. **816**: p. 151960.
139. Zhang, P., et al., *The interaction of micro/nano plastics and the environment: Effects of ecological corona on the toxicity to aquatic organisms*. Ecotoxicol Environ Saf, 2022. **243**: p. 113997.
140. Tong, L., et al., *Zinc oxide nanoparticles dissolution and toxicity enhancement by polystyrene microplastics under sunlight irradiation*. Chemosphere, 2022. **299**: p. 134421.
141. Tong, L., et al., *Polystyrene microplastics sunlight-induce oxidative dissolution, chemical transformation and toxicity enhancement of silver nanoparticles*. Sci Total Environ, 2022. **827**: p. 154180.
142. Rummel, C.D., et al., *Conditioning Film and Early Biofilm Succession on Plastic Surfaces*. Environ Sci Technol, 2021. **55**(16): p. 11006-11018.
143. Romera-Castillo, C., et al., *Dissolved organic carbon leaching from plastics stimulates microbial activity in the ocean*. Nat Commun, 2018. **9**(1): p. 1430.
144. Sheridan, E.A., et al., *Plastic pollution fosters more microbial growth in lakes than natural organic matter*. Nat Commun, 2022. **13**(1): p. 4175.
145. Chen, M., et al., *Aging behavior of microplastics affected DOM in riparian sediments: From the characteristics to bioavailability*. J Hazard Mater, 2022. **431**: p. 128522.
146. Choi, H.-J., W.J. Ju, and J. An, *Impact of the Virgin and Aged Polystyrene and Polypropylene Microfibers on the Soil Enzyme Activity and the Microbial Community Structure*. Water, Air, & Soil Pollution, 2021. **232**(8): p. 322.
147. Cheng, F., et al., *Non-Negligible Effects of UV Irradiation on Transformation and Environmental Risks of Microplastics in the Water Environment*. J Xenobiot, 2021. **12**(1): p. 1-12.
148. Liu, P., et al., *Effect of weathering on environmental behavior of microplastics: Properties, sorption and potential risks*. Chemosphere, 2020. **242**: p. 125193.
149. Luo, H., et al., *Environmental behaviors of microplastics in aquatic systems: A systematic review on degradation, adsorption, toxicity and biofilm under aging conditions*. J Hazard Mater, 2022. **423**(Pt A): p. 126915.
150. Ding, L., et al., *Insight into the Photodegradation of Microplastics Boosted by Iron (Hydr)oxides*. Environ Sci Technol, 2022. **56**(24): p. 17785-17794.
151. Jiang, Z., et al., *Contrasting effects of microplastic aging upon the adsorption of sulfonamides and its mechanism*. Chemical Engineering Journal, 2022. **430**: p. 132939.
152. Liu, X., et al., *Insight into the characteristics and sorption behaviors of aged polystyrene microplastics through three type of accelerated oxidation processes*. J Hazard Mater, 2021. **407**: p. 124836.
153. Liu, P., et al., *Polystyrene microplastics accelerated photodegradation of co-existed polypropylene via photosensitization of polymer itself and released organic compounds*. Water Res, 2022. **214**: p. 118209.
154. Yin, L., et al., *Insight into the photodegradation and universal interactive products of 2,2',4,4'-tetrabromodiphenyl ether on three microplastics*. J Hazard Mater, 2022. **445**: p. 130475.

155. Zhu, J., et al., *Microplastic particles alter wheat rhizosphere soil microbial community composition and function*. J Hazard Mater, 2022. **436**: p. 129176.
156. Ainali, N.M., D.N. Bikiaris, and D.A. Lambropoulou, *Aging effects on low- and high-density polyethylene, polypropylene and polystyrene under UV irradiation: An insight into decomposition mechanism by Py-GC/MS for microplastic analysis*. Journal of Analytical and Applied Pyrolysis, 2021. **158**: p. 105207.
157. Alimi, O.S., et al., *Weathering pathways and protocols for environmentally relevant microplastics and nanoplastics: What are we missing?* J Hazard Mater, 2022. **423**(Pt A): p. 126955.
158. Duan, J., et al., *ROS-mediated photoaging pathways of nano- and micro-plastic particles under UV irradiation*. Water Res, 2022. **216**: p. 118320.
159. Lindsey, R., *Climate and Earth's Energy Budget*. earthobservatory.nasa.gov., 2009.
160. Zhu, K., et al., *The First Observation of the Formation of Persistent Aminoxyl Radicals and Reactive Nitrogen Species on Photoirradiated Nitrogen-Containing Microplastics*. Environ Sci Technol, 2022. **56**(2): p. 779-789.
161. Zhu, K., et al., *Formation of Environmentally Persistent Free Radicals on Microplastics under Light Irradiation*. Environ Sci Technol, 2019. **53**(14): p. 8177-8186.
162. Gewert, B., M.M. Plassmann, and M. MacLeod, *Pathways for degradation of plastic polymers floating in the marine environment*. Environ Sci Process Impacts, 2015. **17**(9): p. 1513-21.
163. Chamas, A., et al., *Degradation Rates of Plastics in the Environment*. ACS Sustainable Chemistry & Engineering, 2020. **8**(9): p. 3494-3511.
164. Gewert, B., et al., *Identification of Chain Scission Products Released to Water by Plastic Exposed to Ultraviolet Light*. Environmental Science & Technology Letters, 2018. **5**(5): p. 272-276.
165. Ward, C.P., et al., *Sunlight Converts Polystyrene to Carbon Dioxide and Dissolved Organic Carbon*. Environmental Science & Technology Letters, 2019. **6**(11): p. 669-674.
166. Lin, J., et al., *Ultraviolet-C and vacuum ultraviolet inducing surface degradation of microplastics*. Water Research, 2020. **186**: p. 116360.
167. Liu, P., et al., *Effect of aging on adsorption behavior of polystyrene microplastics for pharmaceuticals: Adsorption mechanism and role of aging intermediates*. J Hazard Mater, 2020. **384**: p. 121193.
168. Wang, Q., et al., *The adsorption behavior of metals in aqueous solution by microplastics effected by UV radiation*. J Environ Sci (China), 2020. **87**: p. 272-280.
169. Gao, L., et al., *Microplastics aged in various environmental media exhibited strong sorption to heavy metals in seawater*. Mar Pollut Bull, 2021. **169**: p. 112480.
170. Liu, G., et al., *Sorption behavior and mechanism of hydrophilic organic chemicals to virgin and aged microplastics in freshwater and seawater*. Environ Pollut, 2019. **246**: p. 26-33.
171. Yang, J., et al., *Effects of soil environmental factors and UV aging on Cu(2+) adsorption on microplastics*. Environ Sci Pollut Res Int, 2019. **26**(22): p. 23027-23036.
172. Wang, Y., et al., *Behavior and mechanism of atrazine adsorption on pristine and aged microplastics in the aquatic environment: Kinetic and thermodynamic studies*. Chemosphere, 2022. **292**: p. 133425.
173. Huffer, T. and T. Hofmann, *Sorption of non-polar organic compounds by micro-sized plastic particles in aqueous solution*. Environ Pollut, 2016. **214**: p. 194-201.
174. Muller, A., et al., *The effect of polymer aging on the uptake of fuel aromatics and ethers by microplastics*. Environ Pollut, 2018. **240**: p. 639-646.
175. Xu, Y., et al., *Influence of dissolved black carbon on the aggregation and deposition of polystyrene nanoplastics: Comparison with dissolved humic acid*. Water Res, 2021. **196**: p. 117054.
176. Zhang, H., et al., *Enhanced adsorption of oxytetracycline to weathered microplastic polystyrene: Kinetics, isotherms and influencing factors*. Environ Pollut, 2018. **243**(Pt B): p. 1550-1557.
177. Fan, X., et al., *Investigation on the adsorption and desorption behaviors of antibiotics by degradable MPs with or without UV ageing process*. J Hazard Mater, 2021. **401**: p. 123363.
178. Fan, X., et al., *Investigation on the adsorption and desorption behaviors of heavy metals by tire wear particles with or without UV ageing processes*. Environ Res, 2021. **195**: p. 110858.
179. Guan, Y., et al., *The effect of UV exposure on conventional and degradable microplastics adsorption for Pb (II) in sediment*. Chemosphere, 2022. **286**(Pt 2): p. 131777.
180. Huang, X., et al., *Competitive heavy metal adsorption onto new and aged polyethylene under various drinking water conditions*. J Hazard Mater, 2020. **385**: p. 121585.

181. Zhou, Z., et al., *Adsorption behavior of Cu(II) and Cr(VI) on aged microplastics in antibiotics-heavy metals coexisting system*. Chemosphere, 2022. **291**(Pt 1): p. 132794.
182. Xue, X.D., C.R. Fang, and H.F. Zhuang, *Adsorption behaviors of the pristine and aged thermoplastic polyurethane microplastics in Cu(II)-OTC coexisting system*. J Hazard Mater, 2021. **407**: p. 124835.
183. Li, X., et al., *The crucial role of a protein corona in determining the aggregation kinetics and colloidal stability of polystyrene nanoplastics*. Water Res, 2021. **190**: p. 116742.
184. Zhang, Y.N., et al., *Dissolved Organic Matter Enhanced the Aggregation and Oxidation of Nanoplastics under Simulated Sunlight Irradiation in Water*. Environ Sci Technol, 2022. **56**(5): p. 3085-3095.
185. Zhang, J., et al., *Polystyrene microplastics reduce Cr(VI) and decrease its aquatic toxicity under simulated sunlight*. J Hazard Mater, 2022. **445**: p. 130483.
186. Tian, L., et al., *A carbon-14 radiotracer-based study on the phototransformation of polystyrene nanoplastics in water versus in air*. Environmental Science: Nano, 2019. **6**(9): p. 2907-2917.
187. Zhang, L., L. Luo, and S. Zhang, *Integrated investigations on the adsorption mechanisms of fulvic and humic acids on three clay minerals*. Colloids and Surfaces A: Physicochemical and Engineering Aspects, 2012. **406**: p. 84-90.
188. Huangfu, X., et al., *A review on the interactions between engineered nanoparticles with extracellular and intracellular polymeric substances from wastewater treatment aggregates*. Chemosphere, 2019. **219**: p. 766-783.
189. Giri, S. and A. Mukherjee, *Ageing with algal EPS reduces the toxic effects of polystyrene nanoplastics in freshwater microalgae Scenedesmus obliquus*. Journal of Environmental Chemical Engineering, 2021. **9**(5): p. 105978.
190. Sun, L., et al., *Sunlight induced aggregation of dissolved organic matter: Role of proteins in linking organic carbon and nitrogen cycling in seawater*. Science of The Total Environment, 2019. **654**: p. 872-877.
191. Lenaker, P.L., et al., *Vertical Distribution of Microplastics in the Water Column and Surficial Sediment from the Milwaukee River Basin to Lake Michigan*. Environ Sci Technol, 2019. **53**(21): p. 12227-12237.
192. Xu, Q., et al., *Microplastics in sediments from an interconnected river-estuary region*. Sci Total Environ, 2020. **729**: p. 139025.
193. Li, M., et al., *Cotransport and Deposition of Iron Oxides with Different-Sized Plastic Particles in Saturated Quartz Sand*. Environ Sci Technol, 2019. **53**(7): p. 3547-3557.
194. Schipperski, F., J. Zirlewagen, and T. Scheytt, *Transport and Attenuation of Particles of Different Density and Surface Charge: A Karst Aquifer Field Study*. Environ Sci Technol, 2016. **50**(15): p. 8028-35.
195. Waldschlager, K. and H. Schuttrumpf, *Infiltration Behavior of Microplastic Particles with Different Densities, Sizes, and Shapes-From Glass Spheres to Natural Sediments*. Environ Sci Technol, 2020. **54**(15): p. 9366-9373.
196. Liu, J., et al., *Polystyrene Nanoplastics-Enhanced Contaminant Transport: Role of Irreversible Adsorption in Glassy Polymeric Domain*. Environ Sci Technol, 2018. **52**(5): p. 2677-2685.
197. Yao, J., et al., *Cotransport of thallium(I) with polystyrene plastic particles in water-saturated porous media*. J Hazard Mater, 2022. **422**: p. 126910.
198. Dahirel, V., M.J.C.O.i.C. Jardat, and I. Science, *Effective interactions between charged nanoparticles in water: What is left from the DLVO theory?* 2010. **15**(1-2): p. 2-7.
199. Chen, G., X. Liu, and C.J.L. Su, *Transport and retention of TiO<sub>2</sub> rutile nanoparticles in saturated porous media under low-ionic-strength conditions: measurements and mechanisms*. 2011. **27**(9): p. 5393-5402.
200. Fan, W., et al., *Effects of surfactants on graphene oxide nanoparticles transport in saturated porous media*. 2015. **35**: p. 12-19.
201. Shi, Y., et al., *Insight into chain scission and release profiles from photodegradation of polycarbonate microplastics*. Water Res, 2021. **195**: p. 116980.
202. Feng, Q., et al., *Transport of Microplastics in Shore Substrates over Tidal Cycles: Roles of Polymer Characteristics and Environmental Factors*. Environ Sci Technol, 2022. **56**(12): p. 8187-8196.
203. Hu, B., et al., *Influence of microplastics occurrence on the adsorption of 17beta-estradiol in soil*. J Hazard Mater, 2020. **400**: p. 123325.
204. Gardette, M., et al., *Photo- and thermal-oxidation of polyethylene: Comparison of mechanisms and influence of unsaturation content*. Polymer Degradation and Stability, 2013. **98**(11): p. 2383-2390.

205. Yousif, E., Haddad, R., *Photodegradation and photostabilization of polymers, especially polystyrene: review*. SpringerPlus, 2013. **2**(1): p. 398.
206. Chen, X., et al., *Cotransformation of Carbon Dots and Contaminant under Light in Aqueous Solutions: A Mechanistic Study*. Environ Sci Technol, 2019. **53**(11): p. 6235-6244.
207. Awfa, D., et al., *Photocatalytic degradation of organic micropollutants: Inhibition mechanisms by different fractions of natural organic matter*. 2020. **174**: p. 115643.
208. Berg, S.M., et al., *Dissolved organic matter photoreactivity is determined by its optical properties, redox activity, and molecular composition*. 2023. **57**(16): p. 6703-6711.
209. Klapstein, S.J., et al., *Quantifying the effects of photoreactive dissolved organic matter on methylmercury photodemethylation rates in freshwaters*. 2017. **36**(6): p. 1493-1502.
210. Cai, L., et al., *Observation of the degradation of three types of plastic pellets exposed to UV irradiation in three different environments*. Sci Total Environ, 2018. **628-629**: p. 740-747.
211. Ranjan, V.P. and S. Goel, *Degradation of Low-Density Polyethylene Film Exposed to UV Radiation in Four Environments*. J. Hazard. Toxic Radioact. Waste, 2019. **23**(4): p. 04019015.
212. Bai, X., et al., *Photon-induced redox chemistry on pyrite promotes photoaging of polystyrene microplastics*. Sci Total Environ, 2022. **829**: p. 154441.
213. Bai, Y., et al., *Indirect photodegradation of sulfadiazine in the presence of DOM: Effects of DOM components and main seawater constituents*. 2021. **268**: p. 115689.
214. Wang, J., et al., *Disparate effects of DOM extracted from coastal seawaters and freshwaters on photodegradation of 2, 4-Dihydroxybenzophenone*. 2019. **151**: p. 280-287.
215. Qiu, X., et al., *Dissolved Organic Matter Promotes the Aging Process of Polystyrene Microplastics under Dark and Ultraviolet Light Conditions: The Crucial Role of Reactive Oxygen Species*. Environ Sci Technol, 2022. **56**(14): p. 10149-10160.
216. Cao, R., et al., *Opposite impact of DOM on ROS generation and photoaging of aromatic and aliphatic nano- and micro-plastic particles*. Environ Pollut, 2022. **315**: p. 120304.
217. Wang, J., et al., *Photochemical degradation of nebulol in different natural organic matter solutions under simulated sunlight irradiation: Kinetics, mechanism and degradation pathway*. Water Res, 2020. **173**: p. 115524.
218. Trubetskoi, O.A., S.V. Patsaeva, and O.E. Trubetskaya, *Photochemical Degradation of Organic Pollutants in Solutions of Soil Humic Acids*. Eurasian Soil Science, 2019. **52**(9): p. 1075-1080.
219. Dong, Y., et al., *Photochemical origin of reactive radicals and halogenated organic substances in natural waters: A review*. J Hazard Mater, 2021. **401**: p. 123884.
220. Yang, W., et al., *Photolysis of Nitroaromatic Compounds under Sunlight: A Possible Daytime Photochemical Source of Nitrous Acid? Environmental Science & Technology Letters*, 2021. **8**(9): p. 747-752.
221. Chen, M., et al., *Roles of microplastic-derived dissolved organic matter on the photodegradation of organic micropollutants*. J Hazard Mater, 2022. **440**: p. 129784.
222. Huang, J., et al., *Influence of polystyrene microplastics on the volatilization, photodegradation and photoinduced toxicity of anthracene and pyrene in freshwater and artificial seawater*. Sci Total Environ, 2022. **819**: p. 152049.
223. Chen, C., et al., *Impacts of microplastics on organotins' photodegradation in aquatic environments*. Environ Pollut, 2020. **267**: p. 115686.
224. Wang, H.J., et al., *Photoaged polystyrene microplastics serve as photosensitizers that enhance cimetidine photolysis in an aqueous environment*. Chemosphere, 2022. **290**: p. 133352.
225. Ding, R., et al., *What are the drivers of tetracycline photolysis induced by polystyrene microplastic? Chemical Engineering Journal*, 2022. **435**: p. 134827.
226. Wang, H., et al., *Enhanced phototransformation of atorvastatin by polystyrene microplastics: Critical role of aging*. J Hazard Mater, 2021. **408**: p. 124756.
227. Wang, C., et al., *Structure-dependent surface catalytic degradation of cephalosporin antibiotics on the aged polyvinyl chloride microplastics*. Water Res, 2021. **206**: p. 117732.
228. Zhang, W., et al., *Role of polystyrene microplastics in sunlight-mediated transformation of silver in aquatic environments: Mechanisms, kinetics and toxicity*. J Hazard Mater, 2021. **419**: p. 126429.
229. Huang, Y., et al., *Weathered Microplastics Induce Silver Nanoparticle Formation*. Environmental Science & Technology Letters, 2021. **9**(2): p. 179-185.
230. Gao, Z., et al., *Oxidative Roles of Polystyrene-Based Nanoplastics in Inducing Manganese Oxide Formation under Light Illumination*. ACS Nano, 2022. **16**: p. 20238-20250.
231. Zhang, X., et al., *Photoaging enhanced the adverse effects of polyamide microplastics on the growth, intestinal health, and lipid absorption in developing zebrafish*. Environ Int, 2022. **158**: p. 106922.

232. Zhang, X., et al., *Photolytic degradation elevated the toxicity of polylactic acid microplastics to developing zebrafish by triggering mitochondrial dysfunction and apoptosis*. J Hazard Mater, 2021. **413**: p. 125321.
233. Wang, Q., et al., *The toxicity of virgin and UV-aged PVC microplastics on the growth of freshwater algae Chlamydomonas reinhardtii*. Sci Total Environ, 2020. **749**: p. 141603.
234. Fu, D., et al., *Aged microplastics polyvinyl chloride interact with copper and cause oxidative stress towards microalgae Chlorella vulgaris*. Aquat Toxicol, 2019. **216**: p. 105319.
235. Zou, W., et al., *Photo-Oxidative Degradation Mitigated the Developmental Toxicity of Polyamide Microplastics to Zebrafish Larvae by Modulating Macrophage-Triggered Proinflammatory Responses and Apoptosis*. Environ Sci Technol, 2020. **54**(21): p. 13888-13898.
236. Wang, X., et al., *Photodegradation Elevated the Toxicity of Polystyrene Microplastics to Grouper (Epinephelus moara) through Disrupting Hepatic Lipid Homeostasis*. Environ Sci Technol, 2020. **54**(10): p. 6202-6212.
237. Liu, Z., et al., *Generation of environmental persistent free radicals (EPFRs) enhances ecotoxicological effects of the disposable face mask waste with the COVID-19 pandemic*. Environ Pollut, 2022. **301**: p. 119019.
238. Zhu, K., et al., *Enhanced cytotoxicity of photoaged phenol-formaldehyde resins microplastics: Combined effects of environmentally persistent free radicals, reactive oxygen species, and conjugated carbonyls*. Environ Int, 2020. **145**: p. 106137.
239. Bejgarn, S., et al., *Toxicity of leachate from weathering plastics: An exploratory screening study with Nitocra spinipes*. Chemosphere, 2015. **132**: p. 114-9.
240. Rummel, C.D., et al., *Effects of Leachates from UV-Weathered Microplastic in Cell-Based Bioassays*. Environ Sci Technol, 2019. **53**(15): p. 9214-9223.
241. Luo, H., et al., *Effects of accelerated aging on characteristics, leaching, and toxicity of commercial lead chromate pigmented microplastics*. Environ Pollut, 2020. **257**: p. 113475.
242. Mei, W., et al., *Interactions between microplastics and organic compounds in aquatic environments: A mini review*. Sci Total Environ, 2020. **736**: p. 139472.
243. Guan, J., et al., *Microplastics as an emerging anthropogenic vector of trace metals in freshwater: Significance of biofilms and comparison with natural substrates*. Water Res, 2020. **184**: p. 116205.
244. Wang, Z., et al., *Aged microplastics decrease the bioavailability of coexisting heavy metals to microalga Chlorella vulgaris*. Ecotoxicol Environ Saf, 2021. **217**: p. 112199.
245. Davarpanah, E. and L. Guilhermino, *Single and combined effects of microplastics and copper on the population growth of the marine microalgae Tetraselmis chuii*. Estuarine, Coastal and Shelf Science, 2015. **167**: p. 269-275.
246. Zhang, P., et al., *Metagenomic analysis explores the interaction of aged microplastics and roxithromycin on gut microbiota and antibiotic resistance genes of Carassius auratus*. J Hazard Mater, 2022. **425**: p. 127773.
247. Huang, Y., et al., *Interactive effects of microplastics and selected pharmaceuticals on red tilapia: Role of microplastic aging*. Sci Total Environ, 2021. **752**: p. 142256.
248. Zhang, X., et al., *Aging relieves the promotion effects of polyamide microplastics on parental transfer and developmental toxicity of TDCIPP to zebrafish offspring*. J Hazard Mater, 2022. **437**: p. 129409.
249. Li, W., et al., *Colonization Characteristics of Bacterial Communities on Plastic Debris Influenced by Environmental Factors and Polymer Types in the Haihe Estuary of Bohai Bay, China*. Environ Sci Technol, 2019. **53**(18): p. 10763-10773.
250. Rummel, C.D., et al., *Impacts of Biofilm Formation on the Fate and Potential Effects of Microplastic in the Aquatic Environment*. Environmental Science & Technology Letters, 2017. **4**(7): p. 258-267.
251. Wright, R.J., et al., *Marine Plastic Debris: A New Surface for Microbial Colonization*. Environ Sci Technol, 2020. **54**(19): p. 11657-11672.
252. Yang, Y., et al., *Microplastics provide new microbial niches in aquatic environments*. Appl Microbiol Biotechnol, 2020. **104**(15): p. 6501-6511.
253. Hossain, M.R., et al., *Microplastic surface properties affect bacterial colonization in freshwater*. J Basic Microbiol, 2019. **59**(1): p. 54-61.
254. Shan, E., et al., *Incubation habitats and aging treatments affect the formation of biofilms on polypropylene microplastics*. Sci Total Environ, 2022. **831**: p. 154769.
255. Bao, R., et al., *Secondary microplastics formation and colonized microorganisms on the surface of conventional and degradable plastic granules during long-term UV aging in various environmental media*. Journal of Hazardous Materials, 2022. **439**: p. 129686.

256. Gong, M., et al., *Microbial biofilm formation and community structure on low-density polyethylene microparticles in lake water microcosms*. Environ Pollut, 2019. **252**(Pt A): p. 94-102.
257. Sun, Y., et al., *Selection of antibiotic resistance genes on biodegradable and non-biodegradable microplastics*. J Hazard Mater, 2021. **409**: p. 124979.
258. Wu, X., et al., *Selective enrichment of bacterial pathogens by microplastic biofilm*. Water Res, 2019. **165**: p. 114979.
259. Yuan, Q., et al., *UV-aging of microplastics increases proximal ARG donor-recipient adsorption and leaching of chemicals that synergistically enhance antibiotic resistance propagation*. J Hazard Mater, 2022. **427**: p. 127895.
260. Lee, Y.K., K.R. Murphy, and J. Hur, *Fluorescence Signatures of Dissolved Organic Matter Leached from Microplastics: Polymers and Additives*. Environ Sci Technol, 2020. **54**(19): p. 11905-11914.
261. Lee, Y.K., et al., *Characteristics of microplastic polymer-derived dissolved organic matter and its potential as a disinfection byproduct precursor*. Water Res, 2020. **175**: p. 115678.
262. Zhu, L., et al., *Photochemical dissolution of buoyant microplastics to dissolved organic carbon: Rates and microbial impacts*. J Hazard Mater, 2020. **383**: p. 121065.
263. Eyheraguibel, B., et al., *Environmental scenarii for the degradation of oxo-polymers*. Chemosphere, 2018. **198**: p. 182-190.
264. Tetu, S.G., et al., *Plastic leachates impair growth and oxygen production in Prochlorococcus, the ocean's most abundant photosynthetic bacteria*. Commun Biol, 2019. **2**: p. 184.
265. Peller, J.R., J.P. McCool, and M. Watters, *Microplastics in Soils and Sediment: Sources, Methodologies, and Interactions with Microorganisms*, in *Handbook of Microplastics in the Environment*. 2020. p. 1-31.
266. Zhang, X., et al., *Systematical review of interactions between microplastics and microorganisms in the soil environment*. J Hazard Mater, 2021. **418**: p. 126288.
267. Rong, L., et al., *LDPE microplastics affect soil microbial communities and nitrogen cycling*. Sci Total Environ, 2021. **773**: p. 145640.
268. Yi, M., et al., *The effects of three different microplastics on enzyme activities and microbial communities in soil*. Water Environ Res, 2021. **93**(1): p. 24-32.
269. Fei, Y., et al., *Response of soil enzyme activities and bacterial communities to the accumulation of microplastics in an acid cropped soil*. Sci Total Environ, 2020. **707**: p. 135634.
270. Ding, J., et al., *Leachable Additives of Tire Particles Explain the Shift in Microbial Community Composition and Function in Coastal Sediments*. Environ Sci Technol, 2022. **56**(17): p. 12257-12266.
271. Hope, J.A., G. Coco, and S.F. Thrush, *Effects of Polyester Microfibers on Microphytobenthos and Sediment-Dwelling Infauna*. Environ Sci Technol, 2020. **54**(13): p. 7970-7982.
272. Matjasic, T., et al., *Presence of polyethylene terephthalate (PET) fibers in hyporheic zone alters colonization patterns and seasonal dynamics of biofilm metabolic functioning*. Water Res, 2021. **203**: p. 117455.
273. Seeley, M.E., et al., *Microplastics affect sedimentary microbial communities and nitrogen cycling*. Nat Commun, 2020. **11**(1): p. 2372.
274. Yu, H., et al., *Polyethylene microplastics interfere with the nutrient cycle in water-plant-sediment systems*. Water Res, 2022. **214**: p. 118191.
275. Yu, H., et al., *Microplastic residues in wetland ecosystems: Do they truly threaten the plant-microbe-soil system?* Environ Int, 2021. **156**: p. 106708.
276. de Souza Machado, A.A., et al., *Impacts of Microplastics on the Soil Biophysical Environment*. Environ Sci Technol, 2018. **52**(17): p. 9656-9665.
277. Rillig, M.C. and A.J.S. Lehmann, *Microplastic in terrestrial ecosystems*. 2020. **368**(6498): p. 1430-1431.
278. Lehmann, A., K. Fitschen, and M. Rillig, *Abiotic and Biotic Factors Influencing the Effect of Microplastic on Soil Aggregation*. Soil Systems, 2019. **3**(1): p. 21.
279. Boots, B., C.W. Russell, and D.S. Green, *Effects of Microplastics in Soil Ecosystems: Above and Below Ground*. Environ Sci Technol, 2019. **53**(19): p. 11496-11506.
280. Zhang, G.S. and Y.F. Liu, *The distribution of microplastics in soil aggregate fractions in southwestern China*. Sci Total Environ, 2018. **642**: p. 12-20.
281. de Souza Machado, A.A., et al., *Microplastics Can Change Soil Properties and Affect Plant Performance*. Environ Sci Technol, 2019. **53**(10): p. 6044-6052.
282. Lozano, Y.M. and M.C. Rillig, *Effects of Microplastic Fibers and Drought on Plant Communities*. Environ Sci Technol, 2020. **54**(10): p. 6166-6173.

283. Zhang, M., et al., *Microplastics from mulching film is a distinct habitat for bacteria in farmland soil*. *Sci Total Environ*, 2019. **688**: p. 470-478.
284. Zhang, X., et al., *Time-dependent effects of microplastics on soil bacteriome*. *J Hazard Mater*, 2023. **447**: p. 130762.
285. Dong, Y., et al., *Effect of microplastics and arsenic on nutrients and microorganisms in rice rhizosphere soil*. *Ecotoxicol Environ Saf*, 2021. **211**: p. 111899.
286. Wang, J., et al., *Effects of co-loading of polyethylene microplastics and ciprofloxacin on the antibiotic degradation efficiency and microbial community structure in soil*. *Sci Total Environ*, 2020. **741**: p. 140463.
287. Liu, Y., et al., *Toxicity of tire wear particles and the leachates to microorganisms in marine sediments*. *Environ Pollut*, 2022. **309**: p. 119744.
288. Li, S., et al., *Polystyrene microplastics trigger hepatocyte apoptosis and abnormal glycolytic flux via ROS-driven calcium overload*. 2021. **417**: p. 126025.
289. Yu, P., et al., *Accumulation of polystyrene microplastics in juvenile *Eriocheir sinensis* and oxidative stress effects in the liver*. 2018. **200**: p. 28-36.
290. Miao, L., et al., *Acute effects of nanoplastics and microplastics on periphytic biofilms depending on particle size, concentration and surface modification*. 2019. **255**: p. 113300.
291. Nantapong, N., et al., *The effect of reactive oxygen species (ROS) and ROS-scavenging enzymes, superoxide dismutase and catalase, on the thermotolerant ability of *Corynebacterium glutamicum**. 2019. **103**: p. 5355-5366.
292. Attri, P. and E.H.J.P.o. Choi, *Influence of reactive oxygen species on the enzyme stability and activity in the presence of ionic liquids*. 2013. **8(9)**: p. e75096.
293. Semenov, A.M.J.M.e., *Physiological bases of oligotrophy of microorganisms and the concept of microbial community*. 1991. **22**: p. 239-247.
294. Rillig, M.C., E. Leifheit, and J. Lehmann, *Microplastic effects on carbon cycling processes in soils*. *PLoS Biol*, 2021. **19(3)**: p. e3001130.
295. Yu, Y., et al., *Polyethylene microplastics alter the microbial functional gene abundances and increase nitrous oxide emissions from paddy soils*. *J Hazard Mater*, 2022. **432**: p. 128721.
296. Zhang, Y., et al., *Effects of microplastics on soil carbon dioxide emissions and the microbial functional genes involved in organic carbon decomposition in agricultural soil*. *Sci Total Environ*, 2022. **806(Pt 3)**: p. 150714.
297. Allouzi, M.M.A., et al., *Micro (nano) plastic pollution: The ecological influence on soil-plant system and human health*. *Sci Total Environ*, 2021. **788**: p. 147815.
298. Khalid, N., M. Aqeel, and A. Noman, *Microplastics could be a threat to plants in terrestrial systems directly or indirectly*. *Environ Pollut*, 2020. **267**: p. 115653.
299. Bosker, T., et al., *Microplastics accumulate on pores in seed capsule and delay germination and root growth of the terrestrial vascular plant *Lepidium sativum**. *Chemosphere*, 2019. **226**: p. 774-781.
300. Jiang, X., et al., *Ecotoxicity and genotoxicity of polystyrene microplastics on higher plant *Vicia faba**. *Environ Pollut*, 2019. **250**: p. 831-838.
301. Li, L., et al., *Effective uptake of submicrometre plastics by crop plants via a crack-entry mode*. *Nature Sustainability*, 2020. **3(11)**: p. 929-937.
302. Li, L., et al., *Confocal measurement of microplastics uptake by plants*. *MethodsX*, 2020. **7**: p. 100750.
303. Wang, C., et al., *Toxic effects of microplastics and nanoplastics on plants: A global meta-analysis*. *Environ Pollut*, 2023. **337**: p. 122593.
304. Giorgetti, L., et al., *Exploring the interaction between polystyrene nanoplastics and *Allium cepa* during germination: Internalization in root cells, induction of toxicity and oxidative stress*. *Plant Physiol Biochem*, 2020. **149**: p. 170-177.
305. Spielman-Sun, E., et al., *Impact of Surface Charge on Cerium Oxide Nanoparticle Uptake and Translocation by Wheat (*Triticum aestivum*)*. *Environ Sci Technol*, 2017. **51(13)**: p. 7361-7368.
306. Kibbey, T.C.G. and K.A. Strevett, *The effect of nanoparticles on soil and rhizosphere bacteria and plant growth in lettuce seedlings*. *Chemosphere*, 2019. **221**: p. 703-707.
307. Sun, X.D., et al., *Differentially charged nanoplastics demonstrate distinct accumulation in *Arabidopsis thaliana**. *Nat Nanotechnol*, 2020. **15(9)**: p. 755-760.
308. Sun, H., et al., *Foliar uptake and leaf-to-root translocation of nanoplastics with different coating charge in maize plants*. *J Hazard Mater*, 2021. **416**: p. 125854.
309. Pflugmacher, S., et al., *The Influence of New and Artificial Aged Microplastic and Leachates on the Germination of *Lepidium sativum* L.* *Plants (Basel)*, 2020. **9(3)**: p. 339.

310. Li, Z., et al., *Physiological response of cucumber (*Cucumis sativus* L.) leaves to polystyrene nanoplastics pollution*. Chemosphere, 2020. **255**: p. 127041.
311. Luo, H., et al., *Aging of microplastics affects their surface properties, thermal decomposition, additives leaching and interactions in simulated fluids*. 2020. **714**: p. 136862.
312. Luo, H., et al., *Leaching behavior of fluorescent additives from microplastics and the toxicity of leachate to *Chlorella vulgaris**. 2019. **678**: p. 1-9.
313. Vejerano, E.P., et al., *Environmentally Persistent Free Radicals: Insights on a New Class of Pollutants*. Environ Sci Technol, 2018. **52**(5): p. 2468-2481.
314. Ruan, X., et al., *Formation, characteristics, and applications of environmentally persistent free radicals in biochars: A review*. Bioresour Technol, 2019. **281**: p. 457-468.
315. Pan, B., et al., *Environmentally persistent free radicals: Occurrence, formation mechanisms and implications*. Environ Pollut, 2019. **248**: p. 320-331.
316. Wen, X., et al., *Microplastics can affect soil properties and chemical speciation of metals in yellow-brown soil*. 2022. **243**: p. 113958.
317. Zhao, T., Y.M. Lozano, and M.C. Rillig, *Microplastics Increase Soil pH and Decrease Microbial Activities as a Function of Microplastic Shape, Polymer Type, and Exposure Time*. Frontiers in Environmental Science, 2021. **9**: p. 675803.
318. Zhang, Q., et al., *Influences of microplastics types and size on soil properties and cadmium adsorption in paddy soil after one rice season*. Resources, Environment and Sustainability, 2023. **11**: p. 100102.
319. Wang, F., et al., *Interactions of microplastics and cadmium on plant growth and arbuscular mycorrhizal fungal communities in an agricultural soil*. Chemosphere, 2020. **254**: p. 126791.
320. Qi, Y., et al., *Effects of plastic mulch film residues on wheat rhizosphere and soil properties*. J Hazard Mater, 2020. **387**: p. 121711.
321. Rousk, J., P.C. Brookes, and E. Baath, *Contrasting soil pH effects on fungal and bacterial growth suggest functional redundancy in carbon mineralization*. Appl Environ Microbiol, 2009. **75**(6): p. 1589-96.
322. Chen, Y., et al., *Adsorption of tetracyclines onto polyethylene microplastics: A combined study of experiment and molecular dynamics simulation*. 2021. **265**: p. 129133.
323. Qiu, Y., et al., *Predicting aqueous sorption of organic pollutants on microplastics with machine learning*. Water Res, 2023. **244**: p. 120503.
324. Astray, G., et al., *Machine Learning to Predict the Adsorption Capacity of Microplastics*. Nanomaterials (Basel), 2023. **13**(6): p. 1061.
325. Jatav, N., et al., *AgI/CuWO<sub>4</sub> Z-scheme photocatalyst for the degradation of organic pollutants: Experimental and molecular dynamics studies*. 2021. **599**: p. 717-729.
326. Jiang, Z., et al., *A Novel Machine Learning Model to Predict the Photo-Degradation Performance of Different Photocatalysts on a Variety of Water Contaminants*. Catalysts, 2021. **11**(9): p. 1107.
327. Navidpour, A.H., et al., *Application of machine learning algorithms in predicting the photocatalytic degradation of perfluorooctanoic acid*. Catalysis Reviews, 2022: p. 1-26.
328. Dell'Anno, F., et al., *Degradation of Hydrocarbons and Heavy Metal Reduction by Marine Bacteria in Highly Contaminated Sediments*. Microorganisms, 2020. **8**(9): p. 1402.
329. Liu, C., et al., *Reduction kinetics of Fe(III), Co(III), U(VI), Cr(VI), and Tc(VII) in cultures of dissimilatory metal-reducing bacteria*. Biotechnol Bioeng, 2002. **80**(6): p. 637-49.
330. Field, J.A., et al., *Role of quinones in the biodegradation of priority pollutants: a review*. Water Sci Technol, 2000. **42**(5-6): p. 215-222.
331. Zhu, T.T., et al., *Unexpected role of electron-transfer hub in direct degradation of pollutants by exoelectrogenic bacteria*. Environ Microbiol, 2022. **24**(4): p. 1838-1848.
332. Roden, E.E., et al., *Extracellular electron transfer through microbial reduction of solid-phase humic substances*. Nature Geoscience, 2010. **3**(6): p. 417-421.
333. Xu, S., et al., *Polystyrene Nanoplastics Inhibit the Transformation of Tetrabromobisphenol A by the Bacterium *Rhodococcus jostii**. ACS Nano, 2021. **16**(1): p. 405-414.
334. Wang, C., et al., *Natural Solar Irradiation Produces Fluorescent and Biodegradable Nanoplastics*. Environ Sci Technol, 2023. **57**(16): p. 6626-6635.
335. Eerkes-Medrano, D., R.C. Thompson, and D.C. Aldridge, *Microplastics in freshwater systems: a review of the emerging threats, identification of knowledge gaps and prioritisation of research needs*. Water Res, 2015. **75**: p. 63-82.
336. Erni-Cassola, G., et al., *Lost, but Found with Nile Red: A Novel Method for Detecting and Quantifying Small Microplastics (1 mm to 20 μm) in Environmental Samples*. Environ Sci Technol, 2017. **51**(23): p. 13641-13648.

337. Jia, T., et al., *Deep learning for detecting macroplastic litter in water bodies: A review*. *Water Res*, 2023. **231**: p. 119632.
338. Mao, Y., et al., *Phytoplankton response to polystyrene microplastics: Perspective from an entire growth period*. *Chemosphere*, 2018. **208**: p. 59-68.
339. Mao, Y., et al., *Distribution and characteristics of microplastics in the Yulin River, China: Role of environmental and spatial factors*. *Environ Pollut*, 2020. **265**(Pt A): p. 115033.
340. Xu, Y., et al., *Are Micro- or Nanoplastics Leached from Drinking Water Distribution Systems?* *Environ Sci Technol*, 2019. **53**(16): p. 9339-9340.
341. Wu, J., et al., *Effect of salinity and humic acid on the aggregation and toxicity of polystyrene nanoplastics with different functional groups and charges*. *Environ Pollut*, 2019. **245**: p. 836-843.
342. Zhang, Y., et al., *Charge mediated interaction of polystyrene nanoplastic (PSNP) with minerals in aqueous phase*. *Water Res*, 2020. **178**: p. 115861.
343. Xu, Y., et al., *Photo-oxidation of Micro- and Nanoplastics: Physical, Chemical, and Biological Effects in Environments*. *Environ Sci Technol*, 2024. **58**(2): p. 991-1009.
344. Borgnino, L., *Experimental determination of the colloidal stability of Fe(III)-montmorillonite: Effects of organic matter, ionic strength and pH conditions*. *Colloids and Surfaces A: Physicochemical and Engineering Aspects*, 2013. **423**: p. 178-187.
345. Romanello, M.B. and M.M. Fidalgo de Cortalezzi, *An experimental study on the aggregation of TiO<sub>2</sub> nanoparticles under environmentally relevant conditions*. *Water Res*, 2013. **47**(12): p. 3887-3898.
346. Kim, G., et al., *Application of Depletion Attraction in Mineral Flotation: II. Effects of Depletant Concentration*. *Minerals*, 2018. **8**(10): p. 450.
347. Ji, Y., et al., *Effect of solution salinity on settling of mineral tailings by polymer flocculants*. *Colloids and Surfaces A: Physicochemical and Engineering Aspects*, 2013. **430**: p. 29-38.
348. Zhao, C., et al., *Macrogel induced by microgel: bridging and depletion mechanisms*. *Soft Matter*, 2012. **8**(26): p. 7036.
349. Xing, X., L. Hua, and T. Ngai, *Depletion versus stabilization induced by polymers and nanoparticles: The state of the art*. *Current Opinion in Colloid & Interface Science*, 2015. **20**(1): p. 54-59.
350. Yu, S., et al., *Interactions between engineered nanoparticles and dissolved organic matter: A review on mechanisms and environmental effects*. *J Environ Sci (China)*, 2018. **63**: p. 198-217.
351. Choi, J., et al., *Application of Depletion Attraction in Mineral Flotation: I. Theory*. *Minerals*, 2018. **8**(10): p. 451.
352. Pradel, A., C. Catrouillet, and J. Gigault, *The environmental fate of nanoplastics: What we know and what we need to know about aggregation*. *NanoImpact*, 2023. **29**: p. 100453.
353. Pradel, A., et al., *Stabilization of Fragmental Polystyrene Nanoplastic by Natural Organic Matter: Insight into Mechanisms*. *ACS ES&T Water*, 2021. **1**(5): p. 1198-1208.
354. Nason, J.A., S.A. McDowell, and T.W. Callahan, *Effects of natural organic matter type and concentration on the aggregation of citrate-stabilized gold nanoparticles*. *J Environ Monit*, 2012. **14**(7): p. 1885-1892.
355. Li, Z., et al., *Natural Organic Matter (NOM) Imparts Molecular-Weight-Dependent Steric Stabilization or Electrostatic Destabilization to Ferrihydrite Nanoparticles*. *Environ Sci Technol*, 2020. **54**(11): p. 6761-6770.
356. Loosli, F., P. Le Coustumer, and S. Stoll, *TiO<sub>2</sub> nanoparticles aggregation and disaggregation in presence of alginate and Suwannee River humic acids. pH and concentration effects on nanoparticle stability*. *Water Res*, 2013. **47**(16): p. 6052-6063.
357. Zhang, Y., et al., *Impact of natural organic matter and divalent cations on the stability of aqueous nanoparticles*. *Water research*, 2009. **43**(17): p. 4249-4257.
358. Shen, M.-H., et al., *Effects of molecular weight-dependent physicochemical heterogeneity of natural organic matter on the aggregation of fullerene nanoparticles in mono- and di-valent electrolyte solutions*. *Water Research*, 2015. **71**: p. 11-20.
359. Xiaoli, C., et al., *Fluorescence excitation-emission matrix combined with regional integration analysis to characterize the composition and transformation of humic and fulvic acids from landfill at different stabilization stages*. *Waste Manag*, 2012. **32**(3): p. 438-447.
360. Schefer, R.B., A. Armanious, and D.M. Mitrano, *Eco-Corona Formation on Plastics: Adsorption of Dissolved Organic Matter to Pristine and Photochemically Weathered Polymer Surfaces*. *Environ Sci Technol*, 2023: p. 14707-14716.
361. Cai, N., D. Peak, and P. Larese-Casanova, *Factors influencing natural organic matter sorption onto commercial graphene oxides*. *Chemical Engineering Journal*, 2015. **273**: p. 568-579.

362. Mwaanga, P., E.R. Carraway, and M.A. Schlautman, *Preferential sorption of some natural organic matter fractions to titanium dioxide nanoparticles: influence of pH and ionic strength*. Environ Monit Assess, 2014. **186**(12): p. 8833-8844.
363. Louie, S.M., et al., *Correlation of the physicochemical properties of natural organic matter samples from different sources to their effects on gold nanoparticle aggregation in monovalent electrolyte*. Environ Sci Technol, 2015. **49**(4): p. 2188-2198.
364. Xu, Y., et al., *Key factors in the adsorption of natural organic matter to metal (hydr)oxides: Fractionation and conformational change*. Chemosphere, 2022. **308**(Pt 1): p. 136129.
365. Taniguchi, M., J.E. Kilduff, and G. Belfort, *Modes of Natural Organic Matter Fouling during Ultrafiltration*. Environ. Sci. Technol., 2003. **37**(8): p. 1676-1683.
366. Guo, J., et al., *Ultrafiltration performance of EFOM and NOM under different MWCO membranes: Comparison with fluorescence spectroscopy and gel filtration chromatography*. Desalination, 2014. **344**: p. 129-136.
367. Li, Y., et al., *High molecular weight fractions of dissolved organic matter (DOM) determined the adsorption and electron transfer capacity of DOM on iron minerals*. Chemical Geology, 2022. **604**: p. 120907.
368. Rodriguez, F.J., P. Schlenger, and M. Garcia-Valverde, *Monitoring changes in the structure and properties of humic substances following ozonation using UV-Vis, FTIR and (1)H NMR techniques*. Sci Total Environ, 2016. **541**: p. 623-637.
369. Qu, i., et al., *UV Irradiation and humic acid mediate aggregation of aqueous fullerene (nC(60)) nanoparticles*. Environ. Sci. Technol., 2010. **44**(20): p. 7821-7826.
370. Xu, Y., et al., *Aggregation and deposition behaviors of dissolved black carbon with coexisting heavy metals in aquatic solution*. Environmental Science: Nano, 2020: p. 2773-2784.
371. Israelachvili, J.N., *Intermolecular and surface forces*. 2011: Academic press. 663.
372. Ou, Q., et al., *Deposition behavior of dissolved black carbon on representative surfaces: Role of molecular conformation*. Journal of Environmental Chemical Engineering, 2021. **9**(5): p. 105921.
373. Luo, J., et al., *Synthesis of stable aqueous dispersion of graphene/polyaniline composite mediated by polystyrene sulfonic acid*. Journal of Polymer Science Part A: Polymer Chemistry, 2012. **50**(23): p. 4888-4894.
374. Su, J., et al., *Differential Photoaging Effects on Colored Nanoplastics in Aquatic Environments: Physicochemical Properties and Aggregation Kinetics*. Environ Sci Technol, 2023. **57**(41): p. 15656-15666.
375. Chen, W., et al., *Two-dimensional correlation spectroscopic analysis on the interaction between humic acids and TiO2 nanoparticles*. Environ Sci Technol, 2014. **48**(19): p. 11119-11126.
376. Coates, J., *Interpretation of infrared spectra, a practical approach*. Encyclopedia of analytical chemistry, 2000. **12**: p. 10815-10837.
377. Korak, J.A. and G. McKay, *Critical review of fluorescence and absorbance measurements as surrogates for the molecular weight and aromaticity of dissolved organic matter*. Environ Sci Process Impacts, 2024. **26**: p. 1663-1702.
378. Li, M., et al., *Effects of molecular weight-fractionated natural organic matter on the phytoavailability of silver nanoparticles*. Environmental Science: Nano, 2018. **5**(4): p. 969-979.
379. Senesi, N., et al., *Characterization, differentiation, and classification of humic substances by fluorescence spectroscopy*. Soil Science, 1991. **152**(4): p. 259-271.
380. Yin, Y., et al., *Particle coating-dependent interaction of molecular weight fractionated natural organic matter: impacts on the aggregation of silver nanoparticles*. Environ Sci Technol, 2015. **49**(11): p. 6581-6589.
381. Richard, C., et al., *Spectroscopic approach for elucidation of structural peculiarities of Andisol soil humic acid fractionated by SEC-PAGE setup*. Geoderma, 2007. **142**(1-2): p. 210-216.
382. Margenau, H., *Van der Waals forces*. Reviews of Modern Physics, 1939. **11**(1): p. 1.
383. Wang, X., et al., *Adsorption characteristics and mechanisms of water-soluble polymers (PVP and PEG) on kaolin and montmorillonite minerals*. J Hazard Mater, 2024. **466**: p. 133592.
384. Louie, S.M., R.D. Tilton, and G.V. Lowry, *Critical review: impacts of macromolecular coatings on critical physicochemical processes controlling environmental fate of nanomaterials*. Environmental Science: Nano, 2016. **3**(2): p. 283-310.
385. Tiller, C.L. and C.R. O'Melia, *Natural organic matter and colloidal stability: models and measurements*. Colloids and Surfaces A: Physicochemical and Engineering Aspects, 1993. **73**: p. 89-102.
386. Gregory, J. and S. Barany, *Adsorption and flocculation by polymers and polymer mixtures*. Adv Colloid Interface Sci, 2011. **169**(1): p. 1-12.

387. Pontoni, L., et al., *Supramolecular aggregation of colloidal natural organic matter masks priority pollutants released in water from peat soil*. Environ Res, 2021. **195**: p. 110761.
388. Conte, P. and A. Piccolo, *Conformational arrangement of dissolved humic substances. Influence of solution composition on association of humic molecules*. Environ Sci Technol, 1999. **33**(10): p. 1682-1690.
389. Avena, M.J. and L.K. Koopal, *Kinetics of humic acid adsorption at solid-water interfaces*. Environ Sci Technol, 1999. **33**(16): p. 2739-2744.
390. Wang, J., et al., *Elucidating the conformation effects within adsorption of natural organic matter on mesoporous graphitic carbon*. Chemical Engineering Journal, 2024. **480**: p. 148171.
391. Guan, X.-H., G.-H. Chen, and C. Shang, *Combining kinetic investigation with surface spectroscopic examination to study the role of aromatic carboxyl groups in NOM adsorption by aluminum hydroxide*. Journal of Colloid and Interface Science, 2006. **301**(2): p. 419-427.
392. Chowdhury, I., et al., *Interactions of graphene oxide nanomaterials with natural organic matter and metal oxide surfaces*. Environ Sci Technol, 2014. **48**(16): p. 9382-90.
393. Louie, S.M., R.D. Tilton, and G.V. Lowry, *Effects of molecular weight distribution and chemical properties of natural organic matter on gold nanoparticle aggregation*. Environ Sci Technol, 2013. **47**(9): p. 4245-4254.
394. Du, T., et al., *Aging of Nanoplastics Significantly Affects Protein Corona Composition Thus Enhancing Macrophage Uptake*. Environ Sci Technol, 2023. **57**(8): p. 3206-3217.
395. Ban, Z., et al., *Machine learning predicts the functional composition of the protein corona and the cellular recognition of nanoparticles*. Proc Natl Acad Sci U S A, 2020. **117**(19): p. 10492-10499.
396. Yu, S., et al., *Aggregation kinetics of different surface-modified polystyrene nanoparticles in monovalent and divalent electrolytes*. Environmental pollution, 2019. **255**: p. 113302.
397. Jia, T., et al., *Advancing deep learning-based detection of floating litter using a novel open dataset*. Frontiers in Water, 2023. **5**.
398. Geyer, R., J.R. Jambeck, and K.L. Law, *Production, use, and fate of all plastics ever made*. Science Advances, 2017. **3**(7): p. e1700782.
399. Simon-Sanchez, L., et al., *Can a Sediment Core Reveal the Plastic Age? Microplastic Preservation in a Coastal Sedimentary Record*. Environ Sci Technol, 2022. **56**(23): p. 16780-16788.
400. Liu, W., et al., *Ecotoxicoproteomic assessment of microplastics and plastic additives in aquatic organisms: A review*. Comp Biochem Physiol Part D Genomics Proteomics, 2020. **36**: p. 100713.
401. Zhou, Y., et al., *Nanoplastics alter ecosystem multifunctionality and may increase global warming potential*. Glob Chang Biol, 2023. **29**(14): p. 3895-3909.
402. Bhardwaj, L.K., P. Rath, and M. Choudhury, *A comprehensive review on the classification, uses, sources of nanoparticles (NPs) and their toxicity on health*. Aerosol Science Engineering, 2023. **7**(1): p. 69-86.
403. Shi, Y., et al., *Formation of Nano- and Microplastics and Dissolved Chemicals During Photodegradation of Polyester Base Fabrics with Polyurethane Coating*. Environ Sci Technol, 2023. **57**(5): p. 1894-1906.
404. Lehner, R., et al., *Emergence of Nanoplastic in the Environment and Possible Impact on Human Health*. Environmental Science & Technology, 2019. **53**(4): p. 1748-1765.
405. Babakhani, P., et al., *Continuum-based models and concepts for the transport of nanoparticles in saturated porous media: A state-of-the-science review*. Adv Colloid Interface Sci, 2017. **246**: p. 75-104.
406. Harvey, R.W. and S.P. Garabedian, *Use of colloid filtration theory in modeling movement of bacteria through a contaminated sandy aquifer*. Environmental science & technology, 1991. **25**(1): p. 178-185.
407. Shen, C., et al., *Role and importance of surface heterogeneities in transport of particles in saturated porous media*. Critical Reviews in Environmental Science and Technology, 2019. **50**(3): p. 244-329.
408. Adamczyk, Z. and P. Weroński, *Application of the DLVO theory for particle deposition problems. Advances in colloid interface science*, 1999. **83**(1-3): p. 137-226.
409. Shen, C., et al., *Kinetics of Coupled Primary- and Secondary-Minimum Deposition of Colloids under Unfavorable Chemical Conditions*. Environ. Sci. Technol., 2007. **41**: p. 6976-6982.
410. Tufenkji, N. and M. Elimelech, *Breakdown of Colloid Filtration Theory: Role of the Secondary Energy Minimum and Surface Charge Heterogeneities*. Langmuir, 2005. **21**: p. 841-852.
411. Tufenkji, N. and M. Elimelech, *Deviation from the classical colloid filtration theory in the presence of repulsive DLVO interactions*. Langmuir, 2004. **20**(25): p. 10818-10828.

412. Hu, Z., et al., *Transport and Deposition of Carbon Nanoparticles in Saturated Porous Media*. Energies, 2017. **10**(8).
413. Lim, M., et al., *Transport of citrate-coated silver nanoparticles in saturated porous media*. Environ Geochem Health, 2020. **42**(6): p. 1753-1766.
414. Sasidharan, S., et al., *Coupled effects of hydrodynamic and solution chemistry on long-term nanoparticle transport and deposition in saturated porous media*. Colloids and Surfaces A: Physicochemical and Engineering Aspects, 2014. **457**: p. 169-179.
415. El Badawy, A.M., et al., *Key factors controlling the transport of silver nanoparticles in porous media*. Environ Sci Technol, 2013. **47**(9): p. 4039-45.
416. Tufenkji, N., *Modeling microbial transport in porous media: Traditional approaches and recent developments*. Advances in water resources, 2007. **30**(6-7): p. 1455-1469.
417. Cameron, D.R. and A. Klute, *Convective dispersive solute transport with a combined equilibrium and kinetic adsorption model*. Water resources research, 1977. **13**(1): p. 183-188.
418. Praetorius, A., et al., *The road to nowhere: equilibrium partition coefficients for nanoparticles*. Environ. Sci.: Nano, 2014. **1**(4): p. 317-323.
419. Liang, Y., et al., *Micro- and nanoplastics retention in porous media exhibits different dependence on grain surface roughness and clay coating with particle size*. Water Res, 2022. **221**: p. 118717.
420. He, L., et al., *Influence of Nano- and Microplastic Particles on the Transport and Deposition Behaviors of Bacteria in Quartz Sand*. Environ Sci Technol, 2018. **52**(20): p. 11555-11563.
421. Zhang, G., et al., *Transport of polystyrene nanoplastics with different functional groups in goethite-coated saturated porous media: Effects of low molecular weight organic acids and physicochemical properties*. J Colloid Interface Sci, 2024. **653**(Pt A): p. 423-433.
422. Shaniv, D., I. Dror, and B. Berkowitz, *Effects of particle size and surface chemistry on plastic nanoparticle transport in saturated natural porous media*. Chemosphere, 2021. **262**: p. 127854.
423. Wu, Y., et al., *Quantification of two-site kinetic transport parameters of polystyrene nanoplastics in porous media*. Chemosphere, 2023. **338**: p. 139506.
424. Liu, Z., et al., *Quantifying the Dynamics of Polystyrene Microplastics UV-Aging Process*. Environmental Science & Technology Letters, 2021. **9**(1): p. 50-56.
425. Xu, Y., et al., *Natural Organic Matter Stabilizes Pristine Nanoplastics but Destabilizes Photochemical Weathered Nanoplastics in Monovalent Electrolyte Solutions*. Environmental Science & Technology, 2025. **59**(3): p. 1822–1834.
426. Chandel, A., F. Faizan, and V. and Shankar, *Assessment of column to particle diameter ratio on the hydraulic conductivity of porous media: Wall effect in Darcy Regime*. ISH Journal of Hydraulic Engineering, 2023. **29**(4): p. 437-445.
427. Liu, G., et al., *Transport of Pseudomonas aeruginosa in Porous Media Mediated by Low-Concentration Surfactants: The Critical Role of Surfactant to Change Cell Surface Hydrophobicity*. Water Resources Research, 2020. **56**(2).
428. Saiers, J.E., G.M. Hornberger, and L. Liang, *First- and second-order kinetics approaches for modeling the transport of colloidal particles in porous media*. Water Resources Research, 1994. **30**(9): p. 2499-2506.
429. Zhang, W., et al., *Transport and retention of biochar particles in porous media: effect of pH, ionic strength, and particle size*. Ecohydrology, 2010. **3**(4): p. 497-508.
430. Dale, A.L., G.V. Lowry, and E.A. Casman, *Much ado about  $\alpha$ : reframing the debate over appropriate fate descriptors in nanoparticle environmental risk modeling*. Environmental Science: Nano, 2015. **2**(1): p. 27-32.
431. He, F., et al., *Transport of carboxymethyl cellulose stabilized iron nanoparticles in porous media: column experiments and modeling*. J Colloid Interface Sci, 2009. **334**(1): p. 96-102.
432. Mattison, N.T., et al., *Impact of porous media grain size on the transport of multi-walled carbon nanotubes*. Environ Sci Technol, 2011. **45**(22): p. 9765-75.
433. Shen, C., et al., *Application of DLVO energy map to evaluate interactions between spherical colloids and rough surfaces*. Langmuir, 2012. **28**(41): p. 14681-92.
434. Shen, C., et al., *Role of Surface Roughness in Chemical Detachment of Colloids Deposited at Primary Energy Minima*. Vadose Zone Journal, 2012. **11**(1).
435. Bradford, S.A., et al., *Physical factors affecting the transport and fate of colloids in saturated porous media*. Water resources research, 2002. **38**(12): p. 63-1-63-12.
436. Raychoudhury, T., N. Tufenkji, and S. Ghoshal, *Aggregation and deposition kinetics of carboxymethyl cellulose-modified zero-valent iron nanoparticles in porous media*. Water Res, 2012. **46**(6): p. 1735-44.

437. Chowdhury, I., et al., *Mechanisms of TiO<sub>2</sub> nanoparticle transport in porous media: role of solution chemistry, nanoparticle concentration, and flowrate*. J Colloid Interface Sci, 2011. **360**(2): p. 548-55.
438. Kasel, D., et al., *Transport and retention of multi-walled carbon nanotubes in saturated porous media: effects of input concentration and grain size*. Water Res, 2013. **47**(2): p. 933-44.
439. Sun, P., et al., *Distinguishable transport behavior of zinc oxide nanoparticles in silica sand and soil columns*. Sci Total Environ, 2015. **505**: p. 189-98.
440. Cornelis, G., et al., *A method for determination of retention of silver and cerium oxide manufactured nanoparticles in soils*. Environmental Chemistry, 2010. **7**(3): p. 298-308.
441. Cornelis, G., et al., *Solubility and batch retention of CeO<sub>2</sub> nanoparticles in soils*. Environ. Sci. Technol., 2011. **45**(7): p. 2777-2782.
442. Bradford, S.A., S. Torkzaban, and A. Wiegmann, *Pore-scale simulations to determine the applied hydrodynamic torque and colloid immobilization*. Vadose Zone Journal, 2011. **10**(1): p. 252-261.
443. Bradford, S.A. and S. Torkzaban, *Colloid interaction energies for physically and chemically heterogeneous porous media*. Langmuir, 2013. **29**(11): p. 3668-76.
444. Liang, Y., et al., *Evidence for the critical role of nanoscale surface roughness on the retention and release of silver nanoparticles in porous media*. Environ Pollut, 2020. **258**: p. 113803.
445. Johnson, W.P., M. Tong, and X. Li, *On colloid retention in saturated porous media in the presence of energy barriers: The failure of  $\alpha$ , and opportunities to predict  $\eta$* . Water Resources Research, 2007. **43**(12): p. W12S13.
446. Xu, S., B. Gao, and J.E. Saiers, *Straining of colloidal particles in saturated porous media*. Water Resources Research, 2006. **42**(12): p. W12S16.
447. Torkzaban, S., et al., *Impacts of bridging complexation on the transport of surface-modified nanoparticles in saturated sand*. J Contam Hydrol, 2012. **136-137**: p. 86-95.
448. Fernandez, R., F. Martirena, and K.L. Scrivener, *The origin of the pozzolanic activity of calcined clay minerals: A comparison between kaolinite, illite and montmorillonite*. Cement and Concrete Research, 2011. **41**(1): p. 113-122.
449. Muller, S., et al., *Nanoplastic in aqueous environments: The role of chemo-electric properties for nanoplastic-mineral interaction*. Sci Total Environ, 2025. **964**: p. 178529.
450. Tombácz, E. and M. Szekeres, *Surface charge heterogeneity of kaolinite in aqueous suspension in comparison with montmorillonite*. Applied Clay Science, 2006. **34**(1-4): p. 105-124.
451. Ye, X., et al., *Effects of clay minerals on the transport of polystyrene nanoplastic in groundwater*. Water Res, 2022. **223**: p. 118978.
452. Lu, T., et al., *Effects of clay minerals on the transport of nanoplastics through water-saturated porous media*. Sci Total Environ, 2021. **796**: p. 148982.
453. Li, J., et al., *Effects of low-molecular weight organic acids on the transport of graphene oxide nanoparticles in saturated sand columns*. Sci Total Environ, 2019. **666**: p. 94-102.
454. Bales, R.C., et al., *Bacteriophage adsorption during transport through porous media: Chemical perturbations and reversibility*. Environmental Science & Technology, 1991. **25**(12): p. 2088-2095.
455. Li, T., et al., *Observed Dependence of Colloid Detachment on the Concentration of Initially Attached Colloids and Collector Surface Heterogeneity in Porous Media*. Environ Sci Technol, 2017. **51**(5): p. 2811-2820.
456. Shen, M., et al., *Insights into aggregation and transport of graphene oxide in aqueous and saturated porous media: complex effects of cations with different molecular weight fractionated natural organic matter*. 2019. **656**: p. 843-851.
457. Jiang, X., et al., *Influence of natural organic matter on the transport and deposition of zinc oxide nanoparticles in saturated porous media*. 2012. **386**(1): p. 34-43.
458. Kanel, S.R., et al., *Influence of natural organic matter on fate and transport of silver nanoparticles in saturated porous media: laboratory experiments and modeling*. 2015. **17**: p. 1-13.
459. Tan, M.-M., et al., *Interaction of Dissolved Organic Matters and Microplastics Regulates the Transport of Microplastics in Saturated Porous Media*. ACS ES&T Engineering, 2024. **4**(5): p. 1230-1239.
460. Chen, F., et al., *Effects of low-molecular-weight organic acids on the transport of polystyrene nanoplastics: An insight at the structure of organic acids*. Sci Total Environ, 2024. **949**: p. 175204.

461. Wang, D., et al., *Hyperexponential and nonmonotonic retention of polyvinylpyrrolidone-coated silver nanoparticles in an Ultisol*. J Contam Hydrol, 2014. **164**: p. 35-48.
462. Li, Y., Z. Wang, and B. Guan, *Separation and identification of nanoplastics in tap water*. Environmental Research, 2022. **204**: p. 112134.
463. Bottero, S., et al., *Biofilm development and the dynamics of preferential flow paths in porous media*. Biofouling, 2013. **29**(9): p. 1069-1086.
464. Jägevall, S., L. Rabe, and K. Pedersen, *Abundance and diversity of biofilms in natural and artificial aquifers of the Äspö Hard Rock Laboratory, Sweden*. Microbial Ecology, 2011. **61**: p. 410-422.
465. Xia, L., et al., *Influences of environmental factors on bacterial extracellular polymeric substances production in porous media*. Journal of hydrology, 2014. **519**: p. 3153-3162.
466. Bertelkamp, C., et al., *The effect of feed water dissolved organic carbon concentration and composition on organic micropollutant removal and microbial diversity in soil columns simulating river bank filtration*. Chemosphere, 2016. **144**: p. 932-9.
467. Xia, L., et al., *Effects of bacterial cells and two types of extracellular polymers on bioclogging of sand columns*. Journal of Hydrology, 2016. **535**: p. 293-300.
468. Perujo, N., et al., *Interaction between Physical Heterogeneity and Microbial Processes in Subsurface Sediments: A Laboratory-Scale Column Experiment*. Environ Sci Technol, 2017. **51**(11): p. 6110-6119.
469. Frølund, B., et al., *Extraction of extracellular polymers from activated sludge using a cation exchange resin*. Water research, 1996. **30**(8): p. 1749-1758.
470. de Oliveira, J.T., et al., *Experimental design and data prediction by Bayesian statistics for adsorption of tetracycline in a GAC fixed-bed column*. Separation and Purification Technology, 2023. **319**: p. 124097.
471. Hu, Q., et al., *Prediction of breakthrough behaviors using logistic, hyperbolic tangent and double exponential models in the fixed-bed column*. Separation and Purification Technology, 2019. **212**: p. 572-579.
472. Bergendahl, J. and D. Grasso, *Prediction of colloid detachment in a model porous media: Thermodynamics*. AIChE Journal, 1999. **45**(3): p. 475-484.
473. Tripathi, S., D. Champagne, and N. Tufenkji, *Transport behavior of selected nanoparticles with different surface coatings in granular porous media coated with Pseudomonas aeruginosa biofilm*. Environ Sci Technol, 2012. **46**(13): p. 6942-9.
474. Xiao, Y. and M.R. Wiesner, *Transport and retention of selected engineered nanoparticles by porous media in the presence of a biofilm*. Environmental science & technology, 2013. **47**(5): p. 2246-2253.
475. Bozorg, A., I.D. Gates, and A. Sen, *Impact of biofilm on bacterial transport and deposition in porous media*. Journal of contaminant hydrology, 2015. **183**: p. 109-120.
476. Lerner, R.N., et al., *The effects of biofilm on the transport of stabilized zerovalent iron nanoparticles in saturated porous media*. Water Research, 2012. **46**(4): p. 975-985.
477. Jiang, X., et al., *Initial transport and retention behaviors of ZnO nanoparticles in quartz sand porous media coated with Escherichia coli biofilm*. Environmental Pollution, 2013. **174**: p. 38-49.
478. Fulaz, S., et al., *Nanoparticle-Biofilm Interactions: The Role of the EPS Matrix*. Trends Microbiol, 2019. **27**(11): p. 915-926.
479. Xiao, Y. and M.R. Wiesner, *Transport and retention of selected engineered nanoparticles by porous media in the presence of a biofilm*. Environmental Science and Technology, 2013. **47**(5): p. 2246-2253.
480. Fu, J., et al., *Effects of biofilms on the retention and transport of PFOA in saturated porous media*. Journal of Hazardous Materials, 2023. **443**.
481. Harvey, R.W., et al., *Importance of the Colmation Layer in the Transport and Removal of Cyanobacteria, Viruses, and Dissolved Organic Carbon during Natural Lake-Bank Filtration*. J Environ Qual, 2015. **44**(5): p. 1413-23.
482. Bauer, R., et al., *Removal of bacterial fecal indicators, coliphages and enteric adenoviruses from waters with high fecal pollution by slow sand filtration*. Water Res, 2011. **45**(2): p. 439-52.
483. Li, X., et al., *The suspension stability of nanoplastics in aquatic environments revealed using meta-analysis and machine learning*. Journal of Hazardous Materials, 2024. **471**: p. 134426.
484. Wu, J., et al., *Effects of polymer aging on sorption of 2,2',4,4'-tetrabromodiphenyl ether by polystyrene microplastics*. Chemosphere, 2020. **253**: p. 126706.

485. Fu, J., et al., *Distinct chemical adsorption behaviors of sulfanilamide as a model antibiotic onto weathered microplastics in complex systems*. Colloids and Surfaces A: Physicochemical and Engineering Aspects, 2022. **648**.
486. Ding, L., et al., *Photodegradation of microplastics mediated by different types of soil: The effect of soil components*. Sci Total Environ, 2022. **802**: p. 149840.
487. Wang, C., et al., *Photo-aging of polyvinyl chloride microplastic in the presence of natural organic acids*. Water Res, 2020. **183**: p. 116082.
488. Khaled, A., et al., *Phototransformation of Plastic Containing Brominated Flame Retardants: Enhanced Fragmentation and Release of Photoproducts to Water and Air*. Environ Sci Technol, 2018. **52**(19): p. 11123-11131.
489. Wu, X., et al., *Photo aging and fragmentation of polypropylene food packaging materials in artificial seawater*. Water Res, 2021. **188**: p. 116456.
490. Ouyang, Z., et al., *Dissolved organic matter derived from biodegradable microplastic promotes photo-aging of coexisting microplastics and alters microbial metabolism*. Journal of Hazardous Materials, 2023. **445**.
491. Zhang, E., et al., *The photo-redox of chromium regulated by microplastics (MPs) and MPs-derived dissolved organic matter (MPs-DOM) and the CO<sub>2</sub> emission of MPs-DOM*. Fundamental Research, 2022.
492. Chen, H., et al., *Reproductive toxicity of UV-photodegraded polystyrene microplastics induced by DNA damage-dependent cell apoptosis in Caenorhabditis elegans*. Sci Total Environ, 2022. **811**: p. 152350.
493. Li, Z., et al., *Plastic leachates lead to long-term toxicity in fungi and promote biodegradation of heterocyclic dye*. Sci Total Environ, 2022. **806**(Pt 1): p. 150538.
494. Zhao, C., et al., *Exploring the toxicity of the aged styrene-butadiene rubber microplastics to petroleum hydrocarbon-degrading bacteria under compound pollution system*. Ecotoxicol Environ Saf, 2021. **227**: p. 112903.
495. Ter Halle, A., et al., *Nanoplastic in the North Atlantic Subtropical Gyre*. Environ Sci Technol, 2017. **51**(23): p. 13689-13697.
496. Chen, C. and W. Huang, *Aggregation kinetics of nanosized activated carbons in aquatic environments*. Chemical Engineering Journal, 2017. **313**: p. 882-889.
497. Yeap, S.P., et al., *Role of Particle-Particle Interaction Towards Effective Interpretation of Z-Average and Particle Size Distributions from Dynamic Light Scattering (DLS) Analysis*. J Nanosci Nanotechnol, 2018. **18**(10): p. 6957-6964.
498. Baalousha, M., et al., *Effect of monovalent and divalent cations, anions and fulvic acid on aggregation of citrate-coated silver nanoparticles*. Sci Total Environ, 2013. **454-455**: p. 119-31.
499. Fritz, G., et al., *Electrosteric Stabilization of Colloidal Dispersions*. Langmuir, 2002. **18**(16): p. 6381-6390.
500. Phenrat, T., et al., *Stabilization of aqueous nanoscale zerovalent iron dispersions by anionic polyelectrolytes: adsorbed anionic polyelectrolyte layer properties and their effect on aggregation and sedimentation*. Journal of Nanoparticle Research, 2008. **10**(5): p. 795-814.
501. Wang, D., Y. Jin, and D.P. Jaisi, *Effect of Size-Selective Retention on the Cotransport of Hydroxyapatite and Goethite Nanoparticles in Saturated Porous Media*. Environmental Science & Technology, 2015. **49**(14): p. 8461-8470.
502. Liang, W., et al., *Organic matters adsorbed on goethite inhibited the heterogeneous aggregation and adsorption of CdSe quantum dots: Experiments and extended DLVO theory*. J Hazard Mater, 2024. **467**: p. 133769.
503. Song, J.E., et al., *Hydrophobic Interactions Increase Attachment of Gum Arabic- and PVP-Coated Ag Nanoparticles to Hydrophobic Surfaces*. Environmental Science & Technology, 2011. **45**(14): p. 5988-5995.
504. Kuhl, T., et al., *Modulation of interaction forces between bilayers exposing short-chained ethylene oxide headgroups*. Biophysical Journal, 1994. **66**(5): p. 1479-1488.
505. Wang, D., Y. Jin, and D.P. Jaisi, *Effect of Size-Selective Retention on the Cotransport of Hydroxyapatite and Goethite Nanoparticles in Saturated Porous Media*. Environ Sci Technol, 2015. **49**(14): p. 8461-70.
506. Lin, S. and M.R. Wiesner, *Theoretical investigation on the interaction between a soft particle and a rigid surface*. Chemical Engineering Journal, 2012. **191**: p. 297-305.
507. Ohshima, H., *Electrophoretic mobility of soft particles*. Colloids Surfaces A: Physicochemical Engineering Aspects, 1995. **103**(3): p. 249-255.
508. Kerchova, A.J.d. and M. Elimelech, *Relevance of Electrokinetic Theory for "Soft" Particles to Bacterial Cells: Implications for Bacterial Adhesion*. Langmuir, 2005. **21**: p. 6462-6472.

509. Okubo, T., *Effect of Neutral Polymers on the Ordering of Monodispersed Polystyrene Spheres*. Journal of the Chemical Society, Faraday Transactions 1: Physical Chemistry in Condensed Phases, 1987. **83**(8): p. 2497-2504.
510. Piccinini, E., et al., *Pushing the Boundaries of Interfacial Sensitivity in Graphene FET Sensors: Polyelectrolyte Multilayers Strongly Increase the Debye Screening Length*. The Journal of Physical Chemistry C, 2018. **122**(18): p. 10181-10188.
511. Song, F., et al., *Molecular-level insights into the heterogeneous variations and dynamic formation mechanism of leached dissolved organic matter during the photoaging of polystyrene microplastics*. Water Res, 2023. **242**: p. 120114.
512. Chercoles Asensio, R., et al., *Analytical characterization of polymers used in conservation and restoration by ATR-FTIR spectroscopy*. Anal Bioanal Chem, 2009. **395**(7): p. 2081-96.
513. Ho, W.K., et al., *Effects of Weathering on the Sorption Behavior and Toxicity of Polystyrene Microplastics in Multi-solute Systems*. Water Res, 2020. **187**: p. 116419.
514. Liu, Y., et al., *Molecular assembly of extracellular polymeric substances regulating aggregation of differently charged nanoplastics and subsequent interactions with bacterial membrane*. J Hazard Mater, 2023. **457**: p. 131825.
515. Bhutto, A.A., D. Vesely, and B.J. Gabrys, *Miscibility and interactions in polystyrene and sodium sulfonated polystyrene with poly(vinyl methyl ether) PVME blends. Part II. FTIR*. Polymer, 2003. **44**(21): p. 6627-6631.
516. Jabbari, E. and N.A. Peppas, *Use of ATR-FTIR to study interdiffusion in polystyrene and poly(vinyl methyl ether)*. Macromolecules, 1993. **26**(9): p. 2175-2186.
517. Olmos, D., E.V. Martin, and J. Gonzalez-Benito, *New molecular-scale information on polystyrene dynamics in PS and PS-BaTiO<sub>3</sub> composites from FTIR spectroscopy*. Phys Chem Chem Phys, 2014. **16**(44): p. 24339-49.
518. Mudunkotuwa, I.A. and V.H. Grassian, *Biological and environmental media control oxide nanoparticle surface composition: the roles of biological components (proteins and amino acids), inorganic oxyanions and humic acid*. Environmental Science: Nano, 2015. **2**(5): p. 429-439.
519. Han, L., et al., *Different mechanisms driving the preferential adsorption of dissolved organic matter by goethite and montmorillonite*. Chemical Geology, 2021. **585**: p. 120560.
520. Chang, R., et al., *A comparison of the compositional differences between humic fractions isolated by the IHSS and exhaustive extraction procedures*. Naturwissenschaften, 2014. **101**: p. 197-209.
521. Xu, S., et al., *Mutually facilitated co-transport of two different viruses through reactive porous media*. Water Res, 2017. **123**: p. 40-48.
522. Hermansson, M., *The DLVO theory in microbial adhesion*. Colloids and surfaces B: Biointerfaces, 1999. **14**(1-4): p. 105-119.
523. Gregory, J., *Particles in water: properties and processes*. 2005: CRC Press.
524. Lin, T., Z. Lu, and W. Chen, *Interaction mechanisms and predictions on membrane fouling in an ultrafiltration system, using the XDLVO approach*. Journal of Membrane Science, 2014. **461**: p. 49-58.
525. Ou, Q., et al., *Interactions between activated sludge extracellular polymeric substances and model carrier surfaces in WWTPs: A combination of QCM-D, AFM and XDLVO prediction*. Chemosphere, 2020. **253**.

---

## Acknowledgement

Time flies. My PhD journey has come to an end. Since December 2021, when I first arrived in the Netherlands to begin this chapter, it has felt like a dream. Only now, as I write these words, do I truly grasp the magnitude of this experience, and the many people who made it possible.

First and foremost, I would like to express my deepest gratitude to my country and the China Scholarship Council (CSC) for the financial support. Without this opportunity, I would not have been able to pursue my doctoral studies abroad.

I would like to sincerely thank my supervisory team: my promotor Prof. Jan Peter van der Hoek, Prof. Luuk Rietveld, my daily supervisor Dr. Kim Maren Lompe, and Prof. Gang Liu. Jan Peter, thank you for your kindness and continuous support from the very beginning. You encouraged me to pursue my experiments with confidence and always responded promptly and thoughtfully to my questions, especially during the revision of my manuscripts. I still remember the encouragement you and Kim gave me at my first conference in Amsterdam. I wish you a full and speedy recovery and hope to see you back with us soon. Luuk, thank you for joining my supervisory team in the final year of my PhD. Although our time working together was relatively short, I deeply appreciate your critical and insightful comments on my last two papers and the productive discussions you facilitated with Kim and me. Your feedback strengthened both my research and this thesis.

I would also like to thank Kim for your critical thinking and timely guidance throughout my PhD. Your constructive critiques pushed me to refine my ideas and strengthen my arguments. I know we sometimes held different views, for instance when you advised me to stay focused on the original plan while I felt compelled to explore further. Yet I am grateful for your patience and willingness to engage and support me, even when you did not fully agree. Gang, thank you very much for your continuous support during my PhD. Without your help, I might not have been able to start this PhD journey. You always supported me to follow my own scientific curiosity, both in spirit and through financial support. Although you were often busy and could not always attend meetings, your trust and encouragement meant a lot to me. I would also like to thank Merle de Kreuk for her encouraging words and thoughtful feedback during my Go/No-Go meeting. My gratitude also goes to Jan Willem Foppen for engaging in deep discussions on colloid transport, offering critical insights on my results, and assisting me with transport modeling software.

Next, I would like to thank my colleagues in Kim's group. I thank Yana for her warm support during my early days in the Netherlands and for your help in the lab. I also thank Sevda, Akhilesh, Katherine, Anik, and Apoorva for being great colleagues. I truly enjoyed the time we spent sharing food and playing games during our group activities. I am grateful to the lab assistants Armand, Tenia, Bokuretsion, and Bright for their patient and reliable support, as well as to the secretaries Maureen and Linda for their always helpful assistance.

I am also grateful to my colleagues in Gang's group. A special thank you to Xintu, a student I mentored in Beijing, for his dedicated help with characterization experiments; this thesis would

not have been completed without his contributions. I also thank Lihua, Sijia, Jiaying, Xun, Anran, Mingchen, Yue, Qiming, Jialin, Yongfei, Jun, Ziyang, Keyu, Xuhan and Mengqing for your companionship, collaboration, and shared experiences during our time in Beijing and the Netherlands, including field sampling and the period at No. 18, Shuangqing Road. In particular, I would like to thank Xiangyu for your thoughtful guidance, suggestions, and friendship. Sharing a year together in the Netherlands was a truly special time.

Next, I would like to thank my Chinese friends in the Netherlands. Shuo, Dengxiao, Ned, Coco, Yang, and Yangco, Max, Ye, Na, Tianlong, Jingjing, Guangze, Xingzhou, Minglian, Yuke, and Yipeng, thank you for the countless hours we spent cooking, traveling, hiking, chatting, and playing games. Those moments brought lightness and joy to my life here, and I will carry them with me always. Hanbing, Yuanyuan, Bo, Chi, Ruopeng, and Xinyue, our unforgettable trip to Norway with Tianlong and Jingjing remains a cherished memory. Thank you for the adventure and the laughter. I also thank Zheyi and Nan for your care and support. A special note of gratitude to Shuo, Max, Ned, Xingzhou, Tianlong, Guangze, and Yipeng for helping transport samples, materials, or some daily necessities between China and the Netherlands.

Finally, I would like to thank my family. I am deeply grateful to my father, mother, uncle, my two sisters, and their children Bowen, Siwen, and Yunwen, for your love and the happiness you brought me through our video calls, even across great distance. My greatest thanks go to my wife, Qin. It has been a gift to build our life together here. Your love, companionship, encouragement, and patience carried me through both challenges and triumphs. I also thank Qin's family, especially her parents, for their trust, patience, and understanding.

I am sincerely thankful to everyone I encountered during my PhD journey; each of you, in your own way, made this path richer and more meaningful.

February 8, 2026

Delft

Yanghui Xu

---

## Curriculum Vitae

Family name: Xu (徐)

First name: Yanghui (仰辉)

Email: [xuyanghui111@163.com](mailto:xuyanghui111@163.com)



Yanghui Xu was born on December 24, 1994, in Anqing, Anhui Province, China. He completed his secondary education in 2013 at Qianshan Yezhai Middle School in Anhui Province and subsequently enrolled in the Bachelor's program in Water Science and Engineering at the Faculty of Urban Construction, Wuhan University of Science and Technology. He earned his BSc degree in 2017 and then he began his Master's studies in Municipal Engineering at the Faculty of Environment and Ecology, Chongqing University, graduating with an MSc degree in 2020. Following this, he was awarded a scholarship by the China Scholarship Council (CSC) to pursue doctoral research at Delft University of Technology in the Netherlands. Before going to the Netherlands, he spent one year as a Research Assistant at the Key Laboratory of Drinking Water Science and Technology, Research Center for Eco-Environmental Sciences, Chinese Academy of Sciences. In late 2021, he commenced his PhD in Sanitary Engineering within the Department of Water Management, Faculty of Civil Engineering and Geosciences at Delft University of Technology. His doctoral research is supervised by Jan Peter van der Hoek, Luuk Rietveld, Gang Liu, and Kim Maren Lompe. He specializes in combining laboratory-based experimental studies with modeling approaches to evaluate and predict key contaminant fate processes. By integrating advanced analytical techniques with a mechanistic understanding of contaminant behavior, his work enables more accurate environmental risk assessments and supports the development of sustainable water management strategies.

## List of Publications

### Peer-Reviewed Journal Papers

**Xu, Y.;** van der Hoek, J. P.; Rietveld, L.C.; Liu, G.; Lompe, K. M., Beyond classic colloid filtration: the role of biofilm spatial heterogeneity in nanoplastic transport and predictive modeling during riverbank filtration. In Submission.

**Xu, Y.;** van der Hoek, J. P.; Rietveld, L.C.; Liu, G.; Lompe, K. M., Weathering of Nanoplastics Reduces the Effect of Sand Surface Heterogeneity on Irreversible and Reversible Deposition in Saturated Porous Media. In Submission.

**Xu, Y.;** Wang, X.; van der Hoek, J. P.; Liu, G.; Lompe, K. M., Natural Organic Matter Stabilizes Pristine Nanoplastics but Destabilizes Photochemical Weathered Nanoplastics in Monovalent Electrolyte Solutions. *Environ Sci Technol* 2025, 59, (3), 1822–1834.

**Xu, Y.;** Ou, Q.; van der Hoek, J. P.; Liu, G.; Lompe, K. M., Photo-oxidation of Micro- and Nanoplastics: Physical, Chemical, and Biological Effects in Environments. *Environ Sci Technol* 2024, 58, (2), 991–1009.

**Xu, Y.;** Wang, X.; Ou, Q.; van der Hoek, J. P.; Liu, G., Appearance of Recalcitrant Dissolved Black Carbon and Dissolved Organic Sulfur in River Waters Following Wildfire Events. *Environ Sci Technol* 2024, 58, (16), 7165–7175.

**Xu, Y.;** Ou, Q.; Wang, X.; van der Hoek, J. P.; Liu, G., Mass Concentration and Removal Characteristics of Microplastics and Nanoplastics in a Drinking Water Treatment Plant. *ACS ES&T Water* 2024, 4, (8), 3348–3358.

**Xu, Y.;** Ou, Q.; Wang, X.; Hou, F.; Li, P.; van der Hoek, J. P.; Liu, G., Assessing the Mass Concentration of Microplastics and Nanoplastics in Wastewater Treatment Plants by Pyrolysis Gas Chromatography-Mass Spectrometry. *Environ Sci Technol* 2023, 57, (8), 3114–3123.

**Xu, Y.;** Ou, Q.; Jiao, M.; Liu, G.; van der Hoek, J. P., Identification and Quantification of Nanoplastics in Surface Water and Groundwater by Pyrolysis Gas Chromatography-Mass Spectrometry. *Environ Sci Technol* 2022, 56, (8), 4988-4997.

**Xu, Y.;** Ou, Q.; Li, X.; Wang, X.; van der Hoek, J. P.; Liu, G., Combined effects of photoaging and natural organic matter on the colloidal stability of nanoplastics in aquatic environments. *Water Research* 2022, 226, 119313.

Yang, T.; **Xu, Y.;** Liu, G.; Nowack, B., Oligomers are a major fraction of the submicrometre particles released during washing of polyester textiles. *Nature Water* 2024, 2, (2), 151-160.

Ou, Q.; **Xu, Y.;** Wang, X.; van der Hoek, J. P.; Yu, G.; Liu, G., Dissolved Black Carbon Facilitates the Photodegradation of Microplastics via Molecular Weight-Dependent Generation of Reactive Intermediates. *Environ Sci Technol* 2024, 58, (34), 15181–15193.

Wang, X.; **Xu, Y.**; Ou, Q.; Chen, W.; van der Meer, W.; Liu, G., Adsorption characteristics and mechanisms of water-soluble polymers (PVP and PEG) on kaolin and montmorillonite minerals. *J Hazard Mater* 2024, 466, 133592.

#### Conference Paper

**Xu, Y.**, van der Hoek, J. P., Liu, G., and Maren Lompe, K.: Biofilm heterogeneity affects the mobility of nanoplastics during riverbank filtration, EGU General Assembly 2025, Vienna, Austria, 27 Apr–2 May 2025, EGU25-10477.

#### Workshops, Conferences, and Forums

9. Invited report: “Migration mechanism and model prediction of nanoplastics during riverbank filtration,” The 2025 Ningbo Yongriver Forum, November 16–18, 2025.

8. Invited report: “Migration mechanism and model prediction of nanoplastics during riverbank filtration”, The Fourth ECAEE Young Scholars Forum, August 19, 2025

7. EGU 2025: “Biofilm heterogeneity affects nanoplastic mobility during riverbank filtration”, April 27– May 2, 2025 (poster presentation).

6. Invited report: “Quantitative analysis, transport, and fate of nanoplastics in aquatic environments,” The 12th Nanjing University Chengyao Young Scholars Forum, December 26–28, 2024.

5. Invited report: “Quantitative analysis, transport, and fate of nanoplastics in aquatic environments,” The 12th Global Young Scholars Forum of Sichuan University, November 16–18, 2024.

4. MICRO 2024: Plastic Pollution from macro to nano: “Natural organic matter stabilizes pristine nanoplastics but destabilizes photochemical weathered nanoplastics”, September 23–27, 2024 (oral presentation)

3. Microplastics workshop for early career researchers: Best practices and expert insights in 2024, Idstein, Germany, September 8–13, 2024.

2. Amsterdam International Water Week 2023: Effects of natural organic matter and photochemical weathering, November 6–9, 2023 (oral presentation).

1. The 10<sup>th</sup> national conference on environmental chemistry: Interactions between activated sludge extracellular polymeric substances and model carrier surfaces in WWTPs: A combination of QCM-D, AFM and XDLVO prediction, August 17, 2018 (oral presentation).

---

